FINITE SIMILITUDE THEORY FOR FRACTURE AND FAILURE

A thesis submitted to The University of Manchester for the degree of Doctor of Philosophy in the Faculty of Science and Engineering

2022

Jingwen Zhang

The University of Manchester

School of Engineering
Department of Mechanical, Aerospace and Civil Engineering

List of Content

List of Figures.

List of Tables.

Abstract

Fracture mechanics is concerned with the response of defect ridden components, which under scaling suffer a phenomenon known as *size effect*, where the response of a material is influenced by its size. It can be observed that a component can fail before the limiting loads indicated by a smaller version of the same material. The difference can be explained by the more significant defects in the larger model, leading to failure at a lower load. An affliction of current scaling theories founded on dimensional analysis is that they can only accommodate scale/size effects ad hoc. Dimensional analysis ignores them completely and is one of the principal reasons why scaling is not presently a fundamental approach for fracture investigations. To overcome this limitation, a new method of scaling called *finite similitude*, involving additional experiments at scale, is examined as a possible alternative approach. It is shown in the thesis how two scaled experiments, as opposed to one, can better represent the response of cracked components. The finite similitude theory provides the means to link information from the scaled experiments. The theory provides the means to couple fields like stress, strain, and displacement in fracture mechanics. Although initially tested in quasistatic fracture, its scope is expanded to different fields in dynamic fracture and impact processes. This research presented in the thesis presents evidence of the efficacy of the finite similitude theory in fracture mechanics. Several standard specimens, with crack propagation, under different loading scenarios are examined for different ductile metals. Dynamic fracture mechanics is also investigated by applying the theory to the Charpy impact test, which serves to select different materials in physical modelling for more practical studies. An example of this is presented with a dynamic impact study of a thin-walled pressure vessel further to confirm the approach's relevance to an industrial setting. Through different tests, loading conditions, materials, boundary conditions and investigations, it is demonstrated in the thesis how the two-experiment approach to fracture mechanics provides higher accuracy than a single-scaled experiment.

Declaration

The thesis and journals contained in the thesis have not been submitted to any university or higher education institution previously, as the research for the degree of diploma, to the best of my knowledge and belief.

Jingwen Zhang

Copyright Statement

Acknowledgments

Completing this research is not possible without help, support, and suggestion from numerous people in the project. So, I would sincerely express my appreciation to my supervisors, Dr Keith Davey, and Dr Rooholamin Darvizeh, for their professional guidance and advice, throughout the whole duration of my research, I am beneficial from the assistance and very grateful to them.

I would also express my sincere gratitude to my father Kang Zhang and my mother Juan Liu, for the financial support to make the education available for me.

I would like to say thanks to colleagues in the team of finite similitude researching and fracture mechanics analysis. Thanks to Dr Hamed Sadeghi and Dr Mahdi Ahmadi who gives me numbers of ideas and supports for the research.

And I want to send my regard to my friends and colleagues in Pariser Building, The University of Manchester, who helps me in my life of study.

Finally, I would like to acknowledge the staffs of School of Mechanical, Aerospace and Civil Engineering in The University of Manchester for their support in my Doctoral studies.

Dedication

I wish to dedicate this work to my parents, Kang Zhang, and Juan Liu, who support me to complete this honourable education, and also for their patient and encouragement through the whole process of the study.

Nomenclature

α_0^{Ψ}	Scalar for transport equation for field Ψ in 0^{th}-order theory
α_1^{Ψ}	Scalar for transport equation for field Ψ in 1^{st}-order theory
α_k^{Ψ}	Scalar for transport equation for field Ψ in k^{th}-order theory
$\alpha_0^{\Psi} T_0^{\Psi}$	Scaled transport equation for field Ψ in 0^{th}-order theory
$\alpha_1^{\Psi} T_1^{\Psi}$	Scaled transport equation for field Ψ in 1^{st}-order theory
$\alpha_k^{\Psi} T_k^{\Psi}$	Scaled transport equation for field Ψ in k^{th}-order theory
a	Crack length
a_0	Initial crack length
A	Static yield stress
A_0	Cross section area of rod
A_{pl}	Area under the load-displacement curve
β	Length scalar
b	Remain ligament length of model (Chapter 4)
b	Crack depth of semi-elliptical crack (Chapter 3)
b_0	Initial remain ligament length
$\boldsymbol{b}^{\Psi}$	Source term in transport equation for field Ψ
$\boldsymbol{b}_{ts}^{v}$	Source term in transport equation of momentum (body force) in trial space
$\boldsymbol{B}_{ps}(\boldsymbol{b}_1)$	Body force of physical space
B	Thickness of the ASTM specimen (Chapter 4)
B	Hardening coefficient (Chapter 5)
C	Strain rate coefficient
$D_1 - D_5$	Damage parameters of J-C damage model
$\boldsymbol{e}_i$	Direction vector of crack travel
E	Young's modulus
F	Coefficient of invariant
g	Time scalar
G_c	Fracture energy per unit area (critical energy for fracture)
$\boldsymbol{J}^{\Psi}$	Flux term in transport equation for field Ψ
J^*	Extended J-integral

J_c	Critical J-integral at failure
J_{el}	Elastic J-integral
J_{pl}	Plastic J-integral
J_{IC}	Fracture toughness in J-integral
K_I	Stress intensity factor (Mode I crack)
K_{IC}	Fracture toughness in stress intensity factor
ℓ	Length of the rod
m	Thermal softening coefficient
M	Mass of projectile
M_J	Slope of the construction line in J-R curve
n	Hardening exponent
$\mathbf{n}^*$	Outward pointing normal
$\boldsymbol{n}$	Unit normal vector
P	Load
P_Q	Critical load for stress intensity factor calculation.
Q	The near-tip stress triaxiality
R_1^{Ψ}	Differential scaling parameter in 1st order for field Ψ
S	Span of the TPB model (distance between the support pin)
t	Time
τ	Surface traction vector
$\boldsymbol{T}$	The *T*-stress in *J-T* theory
T	Thickness of the pressure vessel
T_{tr}	Transition temperature
T_m	Melting temperature
T_{ps}^{Ψ}	Transport equation of physical space for field Ψ
T_{k+1}^{Ψ}	Transport equation for field Ψ in $(k+1)^{th}$-order theory
$\boldsymbol{u}$	Displacement field
$\boldsymbol{u}_{\beta}$	Scaled displacement
u	Displacement
$\boldsymbol{U}_{ps}$	Displacement field of physical space
V	Volume
$\boldsymbol{v}^*$	Velocity field

$\boldsymbol{v}_{\beta_1}$	Reversed velocity from trial space to physical space (virtual data)
$\boldsymbol{V}_{ps}(\boldsymbol{v}_1)$	Velocity field of physical space
ν	Poisson's ratio
W	Width of the test specimen
$\boldsymbol{x}$	Function of coordinate points in affine map
$\boldsymbol{\chi}$	Coordinate point in reference control volume
$\bar{Y}^d$	Mean yield stress
ρ	Material density
σ_c	Maximum principal stress
σ_d	Dynamic yield stress
σ_Y	Yield stress
σ_{TS}	Tensile strength
$\boldsymbol{\sigma}$	Stress field
$\boldsymbol{\sigma}_\beta$	Scaled stress
σ^*	Stress triaxiality
$\bar{\Sigma}^d$	Mean dynamic yield stress
$\boldsymbol{\Sigma}_{ps}(\boldsymbol{\sigma}_1)$	Stress field of physical space
ε	Strain
ε_Y	Yield strain
ε_{UTS}	Strain at tensile strength
$\boldsymbol{\varepsilon}_\beta$	Scaled strain
ε^p	Plastic strain
$\dot{\varepsilon}$	Strain rate
$\dot{\varepsilon}^0$	Reference strain rate
$\dot{\boldsymbol{\varepsilon}}$	Equivalent strain rate
ε_f	Failure strain
$\bar{E}^f$	Mean failure strain
δ_j^j	Kronecker delta symbol
δ	Separation value in load-displacement curve of CZM
δ_c	Critical separation in load-displacement curve of CZM
$\boldsymbol{d\Gamma}$	Elemental surface-area vector

Γ^*	Orientable boundary
$\boldsymbol{\Psi}$	Physical field
ω	Strain-energy density
Ω^*	Control volume
$\aleph$	Algebra of parameters used in Table 1

Chapter 1 Introduction

1.1. Background of the research project

Large engineering structures, for example, aeroplanes, ships, trains, bridges, and buildings, are consistently among the essential parts of human life. These structures must be tested and simulated for the failure and damage criteria for the safety conditions. Considering the financial cost and detailly investigation of the test and simulation, scaling of models is always used for predicting the performance of large-scale industries, where scaling in physical engineering is carried out with two different-scale models that need to be studied.

Research of the scaling theory has a long history. It was firstly aware by Leonardo da Vinci in the 15th century [1], who discovered the mathematical relationships for the modes of behaviour between similar geometrical models. Leonardo da Vinci designed an experiment to find the load-bearing capacity of iron wires, from where it was declared that 'Among cords of equal thickness, the longest is the least strong', and the phenomenon is called 'scale effect'. In the 18th century, Galileo [2] then extended this study. It was founded and stated that the strength of the structure will not decrease with its size; however, if the dimension decrease, the 'strength' will increase. Then the first scientific work was presented by Rayleigh's paper [3] in 1915, followed by Goodier and Thomson's report [4], which discussed the applicability of similitude in structural systems [5]. The research applies dimension analysis to several structural problems, including complex and straightforward, buckling and plastic behaviour, and materials with no linear stress and strain relationship. After many works based on dimensional analysis were presented, approaching to recent time, Singer et al. (1997), Baker et al. (1991) and Sonin (2001) published books [6-8] mainly focusing on the application of dimensional analysis with different scaling models, and scaling methods. The approaches of scaling theory are most successful when applied;

however, due to some limitations and disadvantages, the scaling theory keeps studying and developed till today.

On the other hand, fatigue and fracture were founded on a phenomenon for over a century. Griffith [9] first found the failure load in brittle materials and then postulated that the high stress at the locality of defects can lead to failure, which initiates the crack propagation. It was also concluded that an invisible crack inside the structure appeared during the work, and damage occurred by the crack, which cannot be directly seen. After that, the concept of fracture mechanics is produced with the case of ductile material, where Irwin (1958) [10] and Miller (1968) [11] investigated the plastic behaviour around the crack. The linear-elastic fracture mechanics (LEFM) and elastic-plastic fracture mechanics (EPFM) are then concluded and distinguished by the plastic zone. Based on that, several physical quantities of fracture mechanics are created systematically, like stress intensity factor, and J-integral are proposed by Irwin [12] and Rice [13], which quantify the intensity of elastic and plastic crack-tip fields. Other quantities like crack-tip opening distance (CTOD) and crack-tip opening angle (CTOA) are proposed to describe crack propagation behaviour. These quantities are generally applied in laboratory tests and engineering design, which involves fracture mechanics; typically, they could be founded on the technical standard of ASTM international (American Society for Testing and Materials).

It is appreciated that the fracture properties are commonly affected by specimen size. This is due to the relative size of the fracture process zone compared to the size of the specimen. This also influences the application of LEFM and EPFM and indicates the importance of size-dependent fracture properties for structural design and analysis. The importance of scale related fracture phenomenon was studied by Bažant [14-15], involving dimensional analysis, fracture, and size effects. His size-effect studies started with notched concrete specimens to characterise the transition from failure to the LEFM criterion in all geometrical similar models. His proposed size-effect law modifies experimental parameters to fit results from scaled experiments to reveal the influence of physical size on those geometrical similar specimens.

Subsequently, further size effect models have been presented and include for example the multi-fractal size-effect law by Carpinteri and Chiaia [16-17], which accounts for size-effects related to crack length. All size-effect studies aim to investigate the material behaviour with changes in specimen size and describe how these size-dependence parameters work in scaling studies and typically involve dimensional analysis. In forming dimensionless groups in dimensional analysis any size-dependent parameters should be treated with caution since by default (under scaling) dimensional analysis cannot accommodate size effects. A size effect is a scale effect that occurs with a material and a scale effect exists when the governing dimensionless equations change with scale. Typical studies involving dimensional analysis and size-effect laws in fracture mechanics focus on the critical characteristics of specimens [14-17]. They focus in on properties that change with the size to substantiate that differences that appear with scaling are explainable but also to provide redress as necessary. It is appreciated however that size-effect laws do not constitute a scaling theory being developed to characterise scaled experiments. They are ad hoc and empirical in scope and consequently must be used with caution and in limited circumstances [18]. This is one of the main reasons for this research to provide an alternative scaling theory that can provide a robust and wide-ranging description for scale effects in fracture mechanics.

It is appreciated that a new scaling theory and deeper understanding of scale and size effects can provide significant benefits for the engineering community. Scaling and fracture mechanics could be considered as a twin track approach for the assessment of some industrial problem where both safety and financial considerations feature. A new scaling theory implemented through scaled experiments could become an essential approach in engineering. Over and above any financial savings, the new approach could facilitate the building and study of models at convenient scales to understand the response of hard-to-study problems possibly because of their size. Moreover, repeat trials can be performed relatively cheaply and alternative boundary conditions can be assessed and applied conveniently with more flexible arrangements. In

addition, the number of samples for tests, requiring specimens of appropriate sizes, can be built more easily. Presently, scaled experimentation is not the primary choice for simulation but it is recognised that this view is informed by the lack of a suitable scaling theory. The preferred choice at the present time is the adoption of constitutive laws informed by material tests for the use in advanced numerical tools. Numerical simulation does have limitations however particularly for complex processes involving uncertain boundary conditions and material properties.

This research proposes to make scaled experimentation more attractive with the development and application of a new scaling theory to fracture mechanics. It is shown in the work how one of the similitude rules from the theory called finite similitude can be applied to fracture mechanics. The first-order finite-similitude rule is explored and confirmed to be the correct rule for fracture characterisation. An extraordinary new feature is explored in the proposed work with the possibility of investigating problems with physical models. This aspect is unseen in fracture studies simply because dimensional analysis does not apply to problems where size effects feature. The work presented here aims to push forward both the finite similitude theory and the exploration of scaling in fracture mechanics.

1.2. Research Aim and Objectives

The research aims to investigate the efficacy of the finite similitude theory in fracture problems and show how the two-experiment theory can affect and improve the simulation based on the one-experiment theory. Therefore, the overall focus is on understanding the necessary physical quantities of crack propagation at scale, intending to relate the results from large-scale models to those obtained by small-scale models. Different types of cracked models are to be considered, including a variety of loading and boundary conditions, materials, and investigations, to demonstrate the practical value of the approach.

For these aims, the objectives of the study are listed below:

1. Employ analytical calculations for linear elastic fracture mechanics and evaluate how physical quantities can be connected across the scales through the finite similitude scaling theory equations.

2. Using numerical studies applying finite similitude theory in elastic plastic fracture mechanics, build ABAQUS models to form a full-scale virtual material model. The creation of a virtual model is to be achieved using the properties of small-scale models and the scaling theory. Comparing the results between zeroth-order theory (single scaled experiment) and first-order theory (two scaled experiments) with the prototype should assess the approach.

3. Test standard cracked specimens at different scales with identical materials to obtain and calculate different physical quantities salient to elastic-plastic fracture mechanics. The tests should lead to the precise quantification of size effects as revealed by the output of the ABAQUS models.

4. Associate the results at different scales with the first-order theory (two scaled experiments) to discover if scale effects present under a single scaled experiment are removed under two scaled experiments.

5. Build a dynamic impact fracture model for the Charpy impact test and apply the finite similitude theory to the output of different models to ascertain the optimum conditions for scaling (e.g., scaling factors and material selection).

6. Apply the conditions found in the Charpy impact test to other dynamic impact tests with damaged models to discover if good accuracy is returned.

In this way, materials and settings for physical models can be predetermined from standard tests, which is of practical importance.

1.3. Research Methodology

1.3.1. Fracture Mechanics Method

Fracture mechanics is based on the finding that structures contain an initial defect, where this defect will initial crack with critical load applied, and finally occur failure. The fracture mechanics method is proposed to estimate the relationship between the safety factor and the crack length and then identify the load criteria of material which will make the crack start propagating.

It was founded that the stress field becomes different around the crack tip of a structure, and regularly field equations of stress for complete structure cannot evaluate the stress around the crack. In this case, Irwin [12] introduced a new physical quantity stress intensity factor, which defines the intensity of elastic crack-tip based on the stress σ and the certain crack length a. It could be founded in Eq. (1.1)

$$K_I = \sigma\sqrt{\pi a} \tag{1.1}$$

Moreover, it is stated that when the value of stress intensity factor (K_I) reaches its critical value, fracture toughness (K_{IC}), the crack starts propagating. Therefore, the critical condition of stress could be determined by fracture toughness.

Furthermore, the initiation and behaviour of crack propagation could also be evaluated by the energy method, which was firstly introduced by Griffith's study [9]. In this study, linear elastic fracture of brittle material is considered in energy rather than stress only, released by a uniformly extended plate of unit thickness. When a $2a$ length of the crack is formed, and the displacement remains constant in an infinity plate, the elastic strain energy is shown as

$$W_e = \frac{\pi a^2 \sigma^2}{E} \tag{1.2}$$

After this, Rice [13] developed the concept of J-integral, which shows the release of total potential energy along the extension crack. J-integral is available for linear or no-linear elastic cases, and it is now an essential and widely used parameter in fracture mechanics studies. The J-integral can define both initiation and extension of crack by determining the critical value J_{IC} and evaluating the path integral surrounding the crack path.

1.3.2. Contour integral analysis

ABAQUS evaluates the parameters for fracture mechanics studies, for example, J-integral, stress intensity factor and T-stress, based on the J-integral application in the finite element method and the boundary element method which can express the behaviour of crack in different ways. These can be evaluated by contour integral evaluations, which could be the motion of blocks or elements around the crack tip (in 2D) or surrounding the node on the crack path (in 3D). These blocks are defined by contours, where the contour is a ring of elements surrounding the crack tip, which is then recursively surrounded by other contours. In the finite element analysis, the definition of crack can be founded on the element from rings from the region, and each contour evaluation the contour integral in this way.

1.3.3. Extend Finite Element Method

Belytschko and Black [19] firstly introduced the extended finite element method (XFEM). This method is based on the concept of partition of unity [20] and could be regarded as an extension or enrichment of the standard FE method, with benefit in modelling crack growth. The enrichment functions with an additional degree of freedom are added in the approximation of finite elements by the concept of partition of unity, which could handle the discontinuities, for example, cracks and interfaces.

For the fracture analysis with XFEM, the enrichment function includes the crack-tip asymptotic function and discontinuous function. One is for stress singularity around the crack tip, and the other is for displacement and jump along the crack surface. The

mathematic function to approximate the displacement of a gauss point [x] could be written as

$$u(x) = \sum_{j=1}^{n} N_j(x)u_j + \sum_{h=1}^{mh} N_h(x)(H(x) - H(x_h))\boldsymbol{a}_h + \sum_{k=1}^{mt} N_k(x)\left[\sum_{l=1}^{4}(F_l(x) - F_l(x_k))\boldsymbol{b}_k^l\right] \tag{1.3}$$

Here n is the number of standard finite element nodal, $N_i, N_j, N_k(x)$ are continuous shape functions, u_j is the freedom vector of standard finite element nodal, $H(x)$ is the Heaviside function of gauss point x and $H(x_h)$ is the Heaviside function of enrichment nodal h, $\boldsymbol{a}_h$ is the freedom vector of sides around the crack, mh and mt are nodal number of Heaviside enrichment and crack-tip enrichment respectively, $F_l(x)$ and $F_l(x_k)$ are the crack-tip enrichment function at gauss point x and enrichment nodal k, and $\boldsymbol{b}_k^l$ is the freedom vector of crack-tip enrichment nodal. The Heaviside function is jumped from 1 to -1 from one side to the other side, and the crack-tip asymptotic function could be written with

$$\{F_l(r,\theta)\}_{l=1}^{4} = \left\{\sqrt{r}\sin\frac{\theta}{2}, \sqrt{r}\cos\frac{\theta}{2}, \sqrt{r}\sin\theta\sin\frac{\theta}{2}, \sqrt{r}\sin\theta\cos\frac{\theta}{2}\right\} \tag{1.4}$$

where (r,θ) is the polar coordinate at point x, and $\theta = 0$ for the tangent direction of crack. Here for example a crack propagation with enrichment nodal could be shown in Fig. 1.1, where the nodes highlighted are enriched with the functions.

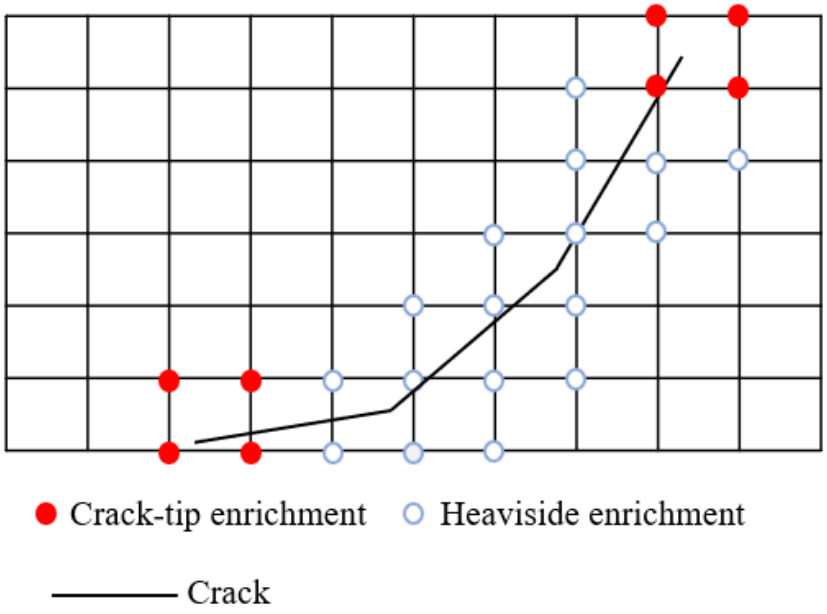

Figure 1.1 Enrichment nodes by XFEM functions.

In XFEM, the traction-separation cohesive behaviour is generally applied in Abaqus/Standard to simulate the crack initiation and propagation. In this case, the XFEM crack growth is based on the linear elastic traction-separation model, damage initiation criteria and damage evolution laws. Here the damage initiation criteria are applied with maximum principal stress [21], which could be the core property controlling the initiation and direction of crack propagation [22]. It follows the theory of maximum principal stress that material failure will occur when the maximum value of principal stress reaches the yield criterion. Damage evolution applies according to the descending linear part of the bilinear traction-separation law, representing the material softening behaviour and stiffness degradation; the input of damage evolution would be the failure displacement δ_c, which shows the displacement of nodes when the element fails.

1.3.4. Finite Similitude Theory

The scaling theory applied to fracture mechanics in this research is finite similitude theory, a new theory founded on the metaphysical concept of space scaling. The theory proposes that space can be expanded or contracted during the scaling experiment. It could be imagined that a large space is contracted to a small space

during the scaling experiment, and things in the large space are also contracted and located in the corresponding place in the small space. The movements of these things could be investigated by linking them as two points in the control volume, and the equations between points in different scales and the moving process can be set, which is then used to synchronize the scaling experiment. Though it is not valid for practical and individual scale experiments, it is possible to assess the physical impact or change of the metaphysical process on the underpinning physics dictating the behaviour of an experiment.

The basis of finite similitude consists of several theories. Where one is the space scaling theory, which considers the affine map related to the points between physical space (large scale) and trial space (small scale), and the selected points in their frame are assumed to be temporally invariant. Then it would be the control volume concept, which evaluates the effect of different physical values in the scaling experiment, which regards the scaling as a movement or deformation in the finite region, and then synchronizes the movement somehow. It proposes the projected transport equations based on the synchronization of movement in the control volume. The transport equation is built in the integral form by the material density and velocity field, based on the finite boundary and control volume, with the selected physical field and source. The relationship of the selected physical field between physical space and trial space can be relatively deduced from the transport equation. These theories around finite similitude will be introduced detailly in the main text.

Evaluating the efficacy of the theory can be done with a numerical test. A virtual material can be created with real physical and trial model materials. This virtual object can be tested numerically and compared with the numerical result of the real physical model. Then the application of finite similitude theory can be concluded with several steps. For the determined materials and scaled sizes, the trial model's scaling factors and boundary conditions can be calculated by the material properties and sizes; based on the result of the trial model (under the determined boundary conditions), the scaling factors can calculate the analytical result. According to this, it can find that the

theory aims to predict the result of large scale-model from the tests of small-scale models with the same or different materials.

1.4. Thesis outline

It has introduced the comprehensive information in this first Chapter about the historical background, research aim and methodology. Following this, the structure of the thesis will be shown below:

In **Chapter 2**, reviews of detailed knowledge and related work in the literature are listed to identify how this research works and what is the pros and cons of the existing research. Especially for how fracture mechanics is studied with scaling theory and what are the limitations that need or can be overcome by finite similitude.

Chapter 3, which corresponds to *paper 1*, introduces the basis of finite similitude theory and proves its efficacy in fracture mechanics in two ways. One is an analytical calculation of facture energy and J-integral in LEFM between different scales with different materials. And the other is considering no-linear evaluation, which generates numerical study for J-integral in EPFM.

Chapter 4 shows the research of *paper 2*, which proposed a new two-experiment theory for fracture mechanics based on scale invariance. It designs several scale experiments to express the size effect in identical material and vanish the error caused by the size effect with the scaling theory and scale invariance. The experiments are around the standard test of material in fracture mechanics, which designs the procedure of ASTM E399 in finite element method with the elastic-plastic behaviour.

The view moves from quasi-static loading to dynamic loading in **Chapter 5**, which concerns the dynamic fracture mechanics study with the Charpy impact test. The Charpy impact test determines the scaling parameters and conditions and applies to other dynamic impact studies with damaged models. It relates to the topic in *paper 3*, which shows the extended range of finite similitude application and investigates the different behaviour in another close engineering model.

It will finally end in **Chapter 6** with a summary and conclusion of the works, the improvement and jobs in the future will also be raised in this section.

Chapter 2 Literature Review

2.1. Introduction

As defined in the historical background, fracture mechanics and scaling theory play an essential role in human life. They are primarily founded in the works of large industries for safety and financial purpose. The evaluation of fracture mechanics around the crack propagation is mature and includes the criteria of fracture initiation and physical behaviour during the crack propagation. As for scaling theory, dimensional analysis can be regarded as the most well-known and widely used method in this field. There is some research around scaling fracture mechanics using dimensional analysis, and then some new dimensionless numbers are derived in this area. Furthermore, the size effect is presented during this period, which must be considered when generating scale experiments in fracture mechanics.

2.2. Fracture mechanics

Failure of a solid is displayed as a body separation. In an atomistic-scale view, the strength of the atomic bond can decide the failure strength of the 'perfect' material. For example, Figure 2.1 depicts two arrays of atoms located in a perfect crystal in static equilibrium, where the distance between arrays can increase when the stress σ increases. The breaking of the atomic bond will start when the stress reaches a critical value σ_c, resulting in the separation of the solid body.

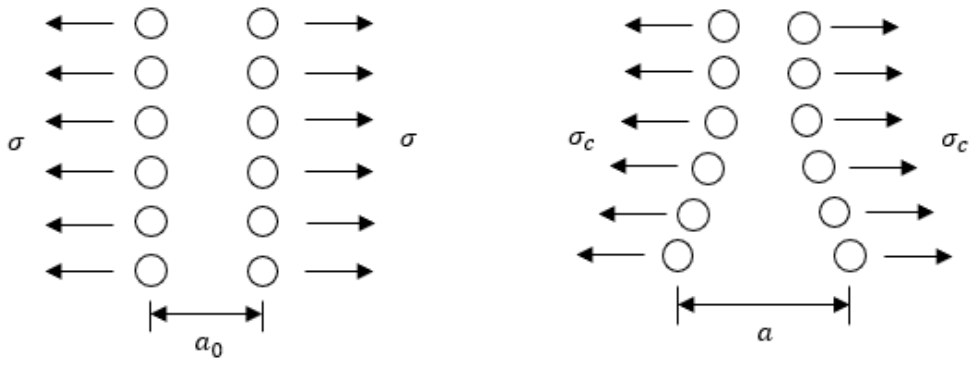

Figure 2.1 Atomic plane separation in a perfect crystal.

2.2.1. Linear Elastic Fracture Mechanics

Fracture mechanics is a critical theory for improving the performance of solid structures and components by describing the behaviour of materials theoretically. It is a part of mechanics that focuses on crack propagation in materials, which considers force and crack extension and uses the theory of solid mechanics to express fracture resistance. The fundamentals of fracture mechanics were developed by Irwin [12] when investigating the stress field around the crack tip. Irwin proposed two new physical quantities, stress intensity factor and fracture toughness for linear elastic fracture mechanics (LEFM), which describe a significantly small plastic zone surrounding the crack tip compared to crack length (small-scale yielding). The geometry of a solid body and the boundary conditions will affect the crack tip singular field through the stress intensity factor *K*. The initiation of crack growth occurs when the stress intensity factor reaches the value of fracture toughness K_{IC}. The fracture criterion function in Eq. (1.1) assumes linear elasticity with the existence of an inverse square root singular stress, which represents the near-tip stress field *K*-dominance zone. In this case, any complex nonlinear deformation around the crack tip can be ignored in principle. As shown in Fig. 2.2, the condition of the fracture criterion assumes that nonlinear deformation and the fracture process zone should be small and well contained inside the *K*-dominance zone around the crack tip.

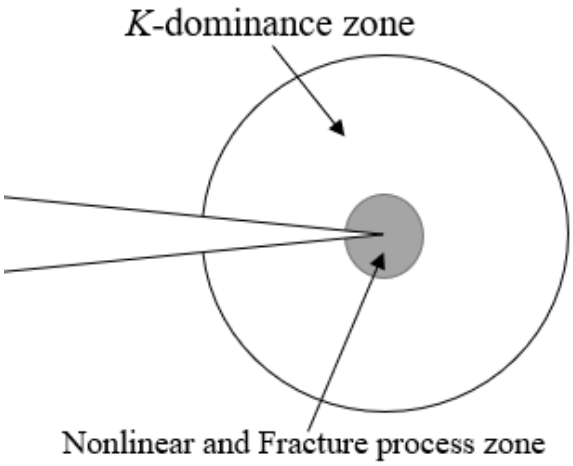

Figure 2.2 *K*-dominance zone and fracture process zone.

Moreover, a criterion of crack initiation is determined to be $K_I = K_{IC}$, where the

fracture toughness K_{IC} is hence determined to be a material property which defines the material's ability to resist failure. It is worth emphasising that this criterion is founded on linear elasticity, which assumes no limits to the strength of materials. Therefore, within the confines of the theory, the stress intensity factor is well defined.

Another approach for establishing a fracture criterion is based on a global energy balance during crack propagation. When the crack length of a two-dimension elastic body is a, then the total potential energy per unit thickness in the crack growth could be written to be $\Pi = \Pi(a)$, so that the energy release of the structure could be $d\Pi$ when there is a small crack extension (da). Thus, for the linear material under constant load, the energy release can be described by the proportion of the potential energy decrease per unit crack extension $G = -\frac{d\Pi}{da}$ proposed by Irwin's other work [23]. The found energy release per unit area confirms Griffith's study [9] but is not confined to brittle material behaviour. Irwin then created a similar process as fracture toughness that $G = G_C$, where G_C is the critical value of energy release, plays the same role as fracture toughness. The energy release rate refers to Griffith's energy law shown in Eq. (1.2), divided by two times the unit surface area along the crack path; hence it was written like $G = \frac{\pi a \sigma^2}{2E}$ (the equations are for plane stress). Stress intensity factor and energy release rate are two new concepts arising from fracture mechanics and distinguish fracture mechanics from classical failure criteria. For the method based on the stress intensity factor, the stress intensity factor needs to be calculated with the known applied load and crack geometry, and the fracture toughness should be measured as well. With these parameters, the maximum load or, for a given load, the maximum crack extension the structure can withstand without crack propagation can be calculated. Compared to the approach based on the stress intensity factor, the energy release rate is more readily extended to cases that involve nonlinear effects. This is because energy is universal and fundamental to all thermos-mechanics.

2.2.2. J-integral

The energy-based method, a path integral around the crack, J-integral, was first

proposed by Cherepanov [24] in 1967 and independently by Rice [13] in 1968. Rice's 1968 paper aimed to find a way to analyse the stress-concentration problem and deal with the mathematically challenging concentrated-strain field near a notch or a crack. The J-integral has the effect of transforming the stress concentration into a boundary-value problem. The J-integral is a path-independent line integral around the crack in a two-dimensional field, which applies to linear and nonlinear elastic materials. The integral can be applied to the contour around the crack tip, starting from the lower surface and ending at the upper surface of the crack. For the determined path Γ of the crack and the stress field that all stresses σ_{ij} depend only on two Cartesian coordinates, since the homogenous body of linear and nonlinear elastic material free of body force and subjected to a two-dimensional deformation field, the J-integral can be written like the energy dissipation as

$$J = \int_{\Gamma} (Wdy - T\frac{du}{dx}ds) \tag{2.1}$$

where W is the strain energy density that can be represented by

$$W = W(x, y) = W(\varepsilon) = \int_0^{\varepsilon} \sigma_{ij} d\epsilon_{ij} \tag{2.2}$$

And T is the traction vector defined by the outward normal, which could be expressed by $T_i = \sigma_{ij} n_i$, ds is an element of arc length along the path, u is displacement vector. Furthermore, Rice then proved the path independent of J-integral with the sum of two path integrals equal to zero. It could be imagined that two boundaries Γ_1 and Γ_2 from an enclosed ring with crack surfaces, the energy is dissipated clockwise through Γ_1 and then dissipated anticlockwise through Γ_2; for the enclosed ring there is

$$\begin{aligned}(anti)\int_{\Gamma_1} Wdy - T_i\frac{\partial u_i}{\partial x}ds \\ + (\text{clockwise})\int_{\Gamma_2} Wdy - T_i\frac{\partial u_i}{\partial x}ds = 0\end{aligned} \tag{2.3}$$

$$\int_{\Gamma_1} Wdy - T_i\frac{\partial u_i}{\partial x}ds = \int_{\Gamma_2} Wdy - T_i\frac{\partial u_i}{\partial x}ds$$

Furtherly, Rice developed the consideration of J-integral in a small-scale yielding model; with the boundary layer and polar coordinate introduced in Irwin's stress

intensity factor theory, it was founded that for small-scale yielding, J-integral is represented by stress intensity factor as the fracture energy, for example in Mode I crack under the plane strain,

$$J = \frac{1 - v^2}{E} K_I^2 \tag{2.4}$$

When J-integral was proposed in 1968, it was estimated to evaluate the stress and strain field around a crack tip of a non-linear elastic-plastic material with path independence by Rice, Rosengren [25] and Hutchinson [26], who considered plane stress and plane strain conditions. It is now known as the Hutchinson-Rice-Rosengren field, or HRR solution. It shows from their study about J-integral that the stress and strain distribution vary with the radius around the crack tip, and the HRR field presents for solving the stress and strain field, which develops that

$$\frac{\varepsilon}{\varepsilon_y} = \frac{\sigma}{\sigma_y} + \alpha \left(\frac{\sigma}{\sigma_y}\right)^n \tag{2.5}$$

$$\sigma_{ij} = \sigma_0 \left(\frac{J}{\alpha \sigma_0 \varepsilon_0 I_n r}\right)^{\frac{1}{n+1}} \tilde{\sigma}_{ij}(n, \theta) \tag{2.6}$$

$$\varepsilon_{ij} = \alpha \varepsilon_0 \left(\frac{J}{\alpha \sigma_0 \varepsilon_0 I_n r}\right)^{\frac{n}{n+1}} \tilde{\varepsilon}_{ij}(n, \theta) \tag{2.7}$$

where α is geometry parameter, physical (half) crack length, r, θ is radial coordinate and angular coordinate of polar field, I_n is a constant value of integral which relates to n, the strain hardening exponent; and $\tilde{\sigma}_{ij}, \tilde{\varepsilon}_{ij}$ are functions of polar coordinates. The J-integral can work for isotropic, perfectly-brittle, linear-elastic materials related to the fracture toughness, as shown in Eq. (2.4), with crack extending straightforward. In addition, the HRR field-based J-integral is used to describe the singularity intensity of the crack-tip stress-strain field for elastic-plastic materials and plays a similar role to stress intensity factor in a linear elastic stress field. According to Eq. (2.7) the stress field in terms of elastic-plastic crack-tip zone varies as $r^{-\frac{1}{n+1}}$ and consequently the HRR field dominates a small plastic zone around the crack tip. Note that when r is too small, the irrelevant finite geometry change at the crack-tip makes the HRR solution invalid [27]. The HRR solution is accurate in an annular contour within the

elastic-plastic deformation zone. It replicates the characteristic of HRR based J-integral, which develops a fundamental criterion of EPFM, and is not valid when the radius of FPZ is too small. Hence the HRR field J-integral should apply in EPFM theory for the elastic-plastic hardening materials. Rice also proposed that the path-independent J-integral is not valid for irregular Mode I and II loading for elastic-plastic material. So, except for some exceptional unloading cases, path-independent J-integral is only available with proportional load, and only contours close to the crack-tip give accurate energy release rate value.

Similar to the stress and strain function in linear elastic fracture mechanics with stress intensity factor, these equations evaluate the singular stress and strain field around the crack tip of elastic-plastic material. In addition, the value of path integral J would also be used to define fracture criteria, $J = J_C$; the J-integral represents the energy release rate along the given path. J has a similar meaning to G, and Rice proves that J and G could be the same because they have the same relation formula between stress intensity factors. Moreover, the critical J-integral value is a kind of material parameter. It could be measured on the crack initialization by testing several specimens with crack and applying the energy theory to it. Begley and Landes [28] did a successful measurement first in 1972. The critical J-integral was determined by the load-displacement graph of specimens with different crack lengths when the specimens fully absorbed energy, and the crack started growth. Kobayashi [29] first proposed investigating the link between finite element analysis and J-integral by simulating the centre-cracked steel plate with different load and heat conditions. After that, the critical J-integral can be measured as a material parameter, which makes J-integral a new important fracture criterion in fracture mechanics. Then it is developed to estimate the resistance of crack extension in nonlinearly elastic materials.

2.3. Fracture toughness testing

Fracture toughness evaluation is the crucial test to obtain the fracture toughness value of materials for LEFM and EPFM. These values include the K-based fracture

toughness (K_{IC}) and J-based fracture toughness (J_C) which are mentioned above, and the crack-tip opening displacement (CTOD) and crack-tip opening angle (CTOA). These parameters describe the metallic material in three main aspects: the fracture behaviour, strength and deformation during fracture, and the constraint effect of the geometry. Since the 1950s, when the concepts of fracture mechanics fracture toughness were proposed, analytical, numerical, and experimental tests of fracture toughness never stopped. Most of the experimental techniques and procedures were developed and maintained by ASTM.

The first fracture toughness standard test for plane strain fracture toughness (K_{IC}) is developed in ASTM E399 [30], which is concluded from Srawley and Brown's studies [31-32]. These establish the standard for fracture toughness testing, including the specimens' size, pre-cracking, specimen fixturing, loading applier, gage of crack opening, test procedure and data calculation. The recommended and frequently used specimens for K_{IC} testing are compact tension specimen (CT), three-point bending specimen (TPB or SE(B)), and disk-shape compact tension specimen (DCT). It needs a pre-crack from 0.45 to 0.55 length of specimen width. The load and crack mouth opening displacement are recorded in the test, and P_Q for calculating the fracture toughness is obtained in the load-displacement curve by the 5% secant method [33]. It calculates the conditional fracture toughness$K_Q$by

$$K_Q = \frac{P_Q}{\sqrt{WBB_N}} f(\frac{a}{W}) \tag{2.8}$$

where W is specimen width, B is thickness, $B_N = B$ for non-grove model and a is the distance from centre of loading to the end of pre-crack. $f(\frac{a}{W})$ is the geometry function which is different with test specimen, the conditional fracture toughness K_Q can be regarded as plane strain fracture toughness under the conditions

$$B, a \geq 2.5\left(\frac{K_Q}{\sigma_Y}\right)^2 \tag{2.9a}$$

$$P_{max} \leq 1.1P_Q \tag{2.9b}$$

$\sigma_Y$is yield stress and P_{max} is the maximum load in the load-displacement curve. The conditions are proposed by Brown and Srawley [32] and Srawley et al. [34]. It always

needs an extensive test program for the available criteria to ensure a consistent outcome of the test standard, and it was tested in CT specimen [35] and TPB specimen [36]. Wallin improved the test standard [37] and suggested determining the conditional fracture toughness K_Q, with a fixed amount of crack growth to eliminate the size effect. Furthermore, Eq. (2.9) is not necessary if the suggestion is available. Additionally, Joyce [38-39] also stated that applying the standard specimens of J-integral from ASTM 1820 [40] can evaluate the crack initiation of stress intensity factor (K_{IC}) in an accurate and size independent way, which will also improve solving the restriction of K_{IC} test.

For the J-based fracture toughness, after Rice proposed the similarity between *J* and *G*, where J-integral is more general for nonlinear elastic energy release rate, it was determined that $J_{el} = \frac{K_I^2}{E} = G$. It is then estimated that J can be the total energy absorbing over the surface area, which is

$$J = \frac{2A_{total}}{B\,b} \tag{2.10}$$

where A_{total} is the total area under the load-displacement curve, b is the remain ligament that $b = W - a$. It was tested in CT specimens by Merkle and Corten [41], who found that the elastic J-integral in this method is slightly smaller than the *G* value. Then, it was suggested to consider the tensile component of load on the specimen with an additional multiplier. The total displacement and J-integral are separated into two parts by elastic and plastic with

$$J = J_{el} + J_{pl} \tag{2.11}$$

The equation is defined by Sumpter and Tuner [42] in a general way with η-factor method

$$J = \frac{K_I^2}{E'} + \frac{\eta A_{pl}}{B\,b} \tag{2.12}$$

It was proved that J-based fracture toughness calculation could work with η-factor, and Clarke [43] obtained the approximate fitted function of η for CT specimen, which is

$$\eta = 2 + 0.522\,b\,/W \tag{2.13}$$

And for TPB or SE(B) specimen, $\eta = 2$ when $a/W > 0.282$. The uses of Eq. (2.12) simplified tasks of J-integral calculation for numerical and experimental evaluation of J-integral for specimens with the load-displacement record. It was then taken as the basic procedure of J_{IC} evaluation in ASTM 1820, which can be noticed as the maximum load-based J_{IC} evaluation.

2.4. Fracture constraint (*J*-*T* and *J*-*Q*) theories

As reviewed in previous sections, stress and strain fields are fundamental to fracture mechanics providing *K*-factors and J-integral for LEFM and EPFM, respectively, within the crack-tip field. According to the theories, both *K* and *J* are intensity parameters of the singular crack-tip stress fields. However, when a significant difference is made in the test conditions, for example, crack depth, crack geometry, loading mode and temperature, the non-singular terms will affect the result of adequate fracture toughness. A good example of the crack-tip constraint effect caused by specimen geometry and load mode is provided in the study by McClintock [44], who showed the effect of different stress and strain fields around the crack-tip for bending and centre-cracked tension specimens. Extensive research has been undertaken to define a second parameter related to the non-singular stress function and quantify the effect of constraint. The purpose of this research is the correction of *K* and *J* to account for crack-tip constraints in LEFM and EPFM.

Initial work in LFEM involved the inclusion of the second term in the *K*-based stress field function of Williams [45], which is

$$\sigma_{ij} = \frac{K_I}{\sqrt{2\pi r}} \bar{f}_{ij}(\theta) + T\delta_{1i}\delta_{ij} \tag{2.14}$$

where δ_{ij} is the Kronecker delta, T is the new parameter introduced in the T-stress theory, since T represents the tensile stress parallel to the crack surface.

It is shown to be significantly effective in the plastic zone under small-scale yielding and even permitted by ASTM limits for the fracture toughness of *K*. In dimensionless terms Eq. (.14) can be represented by

$$\sigma_{ij} = \sigma_Y \bar{f}_{ij}\left(\frac{r}{J/\sigma_0}, \theta; T/\sigma_Y\right) \tag{2.15}$$

where the biaxiality ratio T/σ_Y accounts for the specimen geometry effect of near-tip crack triaxialities.

In this case, the biaxiality ratio corresponds to the observed experimental trend [46]. For example, in ASTM for CT specimen there is a permitted range $0.45 \leq a/W \leq 0.7$, with biaxiality ratio $0.5 \leq T/\sigma_0 \leq 0.6$; in SE(B) specimen, the biaxiality ratio varies between -0.1 and 0.5 linearly with the range of a/W, even over the limitation of ASTM. It presents that the positive value of the biaxiality ratio represents a high level of constraint, and the negative value gives a low level.

As *T*-stress is a linear elastic parameter, it is less meaningful with the expansion of the plastic zone. To overcome the problem of plasticity, O'Dowd and Shih provided a new parameter *Q* by using the finite element model, the near-tip stress triaxiality. It was proposed for the elastic-plastic crack in both small-scale and large-scale yielding, which is known as *the J-Q* theory. Here O'Dowd and Shih [47] considered the difference between small-scaled yielding plane strain solution and HRR field solution and hence produced it to be

$$(\sigma_{ij})_{diff} = (\sigma_{ij})_{SSY} - (\sigma_{ij})_{HRR} \tag{2.16a}$$

$$(\sigma_{ij})_{diff} = Q\sigma_Y \hat{\sigma}_{ij}(\theta) \tag{2.16b}$$

The formulation based on J-Q theory could be founded with a modified boundary layer, which is similar to Eq. (2.15), i.e.,

$$\sigma_{ij} = \sigma_Y f_{ij}\left(\frac{r}{J/\sigma_0}, \theta; Q\right) \tag{2.17}$$

where Q is the near-tip stress triaxiality created in *J-Q* theory, used to represent the function of the difference stress.

Compared to the single parameter fracture criteria, which is applicable for small-scaled yielding, the *J-Q* theory, which adds a *Q*-family, can also consider the effect of geometry as an extra field. According to studies by O'Dowd and Shih [47], the *J-Q* solution is determined by a plane strain solution. The load-displacement curve of specimens evaluates *J*, and the corresponding *Q* would be taken by the figure in the

case of well-constrained yielding. An example of *J-Q* theory application by Sumpter and Forbes [48], took a test of -50 °C mild steel and the fracture occurs by cleavage with no prior stable crack growth. Figure 2.3, created by Krik [49], shows the dashed line that divides areas of fracture and safety using the *J-Q* theory. On the other hand, a study by Sumpter and Forbes [48] also shows that the result could not consist of a *J-T* toughness curve for a fully yielded centre-crack specimen, which means that the *J-T* theory is not valid for EPFM.

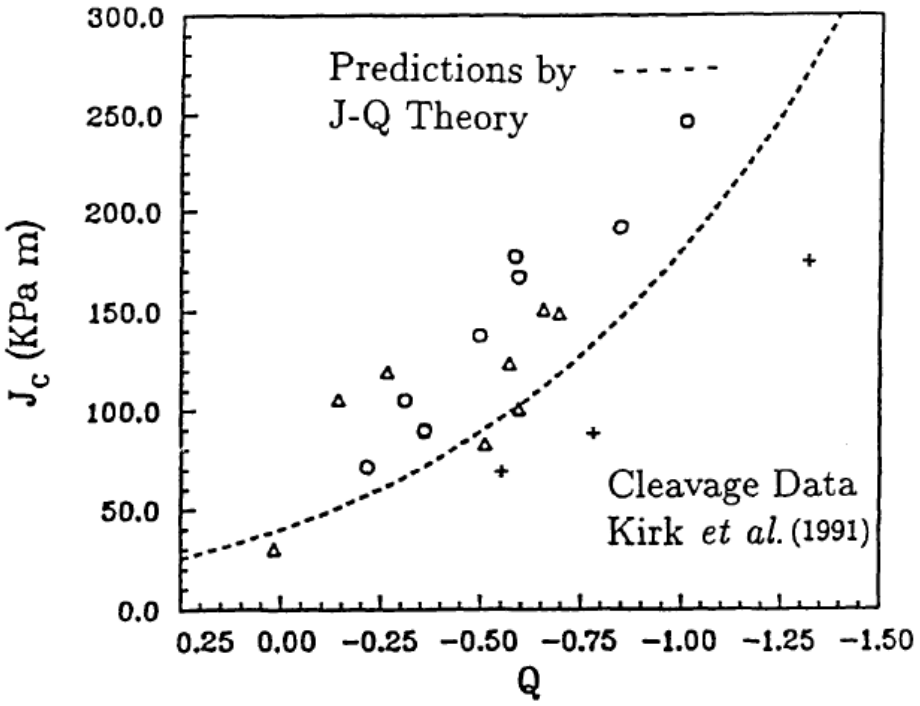

Figure 2.3 Cleavage data for edge crack bending bars in different thickness, the dashed line shows toughness data predicted by J-Q theory. [49]

2.5. Dimensional Analysis

Dimensional analysis is a method for changing a complex problem into the most straightforward form before obtaining a quantitative answer. [50] In physical terms, similarity refers to some equivalence between two things or different phenomena; for example, in a very particular situation, there is a direct relationship between the forces acting on a full-size aircraft and those on a small-scale model of it. To sort out this situation, the condition of this particular situation should be founded, and the relationship between forces also needs to be calculated. Mathematically, similarity

refers to a transformation of variables that reduces the number of independent variables that specify the problem. Here, the dimensional analysis addresses both these questions. Its primary utility derives from its ability to contract, or make more succinct, the functional form of physical relationships. A problem that at first looks formidable may sometimes be solved with little effort after dimensional analysis.

In applying dimensional analysis, Buckingham's pi theory is the most used method in recent years. The premise of dimensional analysis is that the form of any physically significant equation must be such that the relationship between the actual physical quantities remains valid, independent of the magnitudes of the base units. The dimensional analysis derives the logical consequences of this premise. Generally, it could be divided into eight steps:

- Step 1: List all the variables that are involved in the problem.
- Step 2: Express each variable in terms of the essential dimensions.
- Step 3: Determine the required number of pi terms by variables.
- Step 4: Select several repeating variables, where the number required is equal to the number of reference dimensions.
- Step 5: Form a pi term by multiplying one of the non-repeating variables by the product of the repeating variables, each raised to an exponent that will make the combination dimensionless.
- Step 6: Repeat Step 5 for each remaining non-repeating variable.
- Step 7: Check all the resulting pi terms to ensure they are dimensionless.
- Step 8: Express the final form as a relationship among the pi terms and think about the means.

Mathematically, it could be expressed in combinations between variables functions. It identifies a complete set of independent quantities, for example $Q_1, Q_2 \dots Q_n$ which will determine a target value like Q_0. And it could be written as the function like

$$Q_0 = f(Q_1, Q_2 \dots Q_n) \tag{2.18}$$

Here each independent quantity (Q)will not influence others, and the target value could only be adequate by those parameters. Moreover, the target value could be founded when the independent quantities change function. Refer to Norman [51], Buckingham's Pi- theorem is the most important and generally used theory in dimensional analysis. It said that when a complete relationship between dimensional physical quantities is expressed in dimensionless form, the number of independent quantities is reduced from the original *n* to *n-k*, where *k* is the maximum number of the original *n* that are dimensionally independent. For example, as the independent parameters in the previous function, are based on basic dimensions, it could be described to be

$$Q_i = L^{l_i} M^{m_i} F^{f_i} T^{t_i} \tag{2.19}$$

where L, M, F, T are basic parameters in physics, and here l_i, m_i, f_i and t_i are dimensionless numbers that follow from each quantity's definition. It now defines dimensionless forms of the $n-k$ remaining independent variables by dividing each one with the product of powers of $Q_1, Q_2 \ldots Q_k$which has the same dimension, and thus it will get

$$\Pi_i = \frac{Q_{k+i}}{Q_1^{N_{(k+i)1}} Q_2^{N_{(k+i)2}} \ldots Q_k^{N_{(k+i)k}}} \tag{2.20}$$

where $i = 1,2, \ldots, n-k$ and for the dependent variable

$$\Pi_0 = \frac{Q_0}{Q_1^{N_{01}} Q_2^{N_{02}} \ldots Q_k^{N_{0k}}} \tag{2.21}$$

All of the varieties are involved here, which makes the number of quantities lower, which could be written as

$$\Pi_0 = f(\Pi_1, \Pi_2 \ldots \Pi_{n-k}) \tag{2.22}$$

where Π includes different dimensionless varies. It would simplify the relationship and reduce the considered parameters by using Buckingham's Pi- Theorem.

2.6. Dimensional Analysis in Fracture Mechanics

Dimensional analysis is a wide-used theory of scaling, which is then frequently applied in fracture mechanics. According to Buckingham-Pi theory [50], it is crucial to obtain the dimensionless parameters in fracture. There are few parameters in the situation, so the dimensionless parameter should be able to reflect the fundamental effect directly. In previous studies, Cherepanov [52] defined the brittleness number as $\gamma = \frac{1}{2}\frac{K_{IC}^2}{\sigma_y^2 l}$ in plane stress, l is the characteristic dimension of model. It is known that the size of the plastic zone area would relate to $r \sim \frac{K_{IC}^2}{\sigma_y^2}$, so the brittleness number could be regarded as the order of the ratio of the plastic zone size to the cracked body size. Then Carpinteri's stress brittleness number [53] is defined by $s = \frac{K_{IC}}{\sigma_u \sqrt{l}}$, where σ_u means the ultimate stress of material. It can find that their brittleness numbers are similar, but Carpinteri's is the order of square root of the ratio between plastic zone size and model size. After that, Carpinteri [54] raised the energy brittleness number in the linear elastic material that is $s_E = \frac{G_{IC}}{\sigma_u l}$, where G_{IC} is energy release rate. Additionally, the energy brittleness number in the case of Ramberg-Osgood material could be written as $s_E^* = \frac{J}{\sigma_y l}$ where J here is J-integral. The J-integral could be considered as function of yield stress and crack-tip opening displacement ($J = \sigma_y \delta$), thus the s_E^* can be regarded as the order of ratio between CTOD and dimension of cracked model. The Irwin number is defined by Barenblatt [55, 56] that $Ir = \frac{\sigma_y \sqrt{l}}{K_{IC}}$, which has a same order as Carpinteri's stress brittleness number. It can find that there is some relationship between those dimensionless numbers, and they respectively represent to one order of the ratio between a distance and dimension of crack structure, it could be written like $\frac{l}{D} = f(\gamma(s, s_E, s_E^*, Ir), v)$,$v$ here is passion ratio. Zhao's study [57] proved that Irwin number can be used to predict ductile-brittle transition, which is achieved by dimensional analysis. From this Zhao also studied about other functions of the dimensionless numbers shown above [58] and suggested another dimensionless number [59] which is $Z = \frac{E\sqrt{l}}{K_{IC}}$, where l is the characteristic dimension of cracked body. With the dimensionless number and a given displacement boundary

condition, a general dimensional function relationship could be $\Delta = f(l, E, K_{IC}, v)$, where Δ is the given displacement boundary condition. According to Buckingham-Pi theory, the dimensionless function could be expressed by $\frac{\Delta}{l} = f(Z, v)$. Then Zhao [60] focus on the scaling law for fracture mechanics. Apart from these, the topic of scaling, similitude and dimensional analysis are extensively studied [61-64] and are also widely applied in fracture mechanics and related field [65-70].

2.7. Size effect of Fracture studies

Scaling is the leading theory in this project, which uses two different materials in different sizes. So that size effect is necessary to be considered when applying scaling theory. In solid mechanics, for example, elastic or plastic structures, nominal stress is always independent of the size of the material. However, the size effect would cause the difference in nominal stress between different sizes of structures.

2.7.1. Statistical size effect

The theory of the statistical size effect is based on random strength in material, which Weibull proposed in 1939 [71-73]. The theory is successfully applied in metal structure failure. According to Weibull's theory, the structure could be regarded as several small elements, and it will fail when the strength limit is reached in one element. It means a large structure has more probability of failure because it has more small elements that may cause failure. It relates the probability of elements failure to material failure, called the statistic size effect. Weibull then created the model consisting of many small elements, which fail when some of these elements fail. As shown in Fig. 2.4, the failure elements distribute on the crack. According to the concept shown in Fig. 2.4, the failure probability of material (P_f) can be represented by the probability of element failure (P_1) under the given stress, which is

$$1 - P_f = \prod_{k=1}^{N} [1 - P_1(\sigma_k)] \tag{2.22}$$

where N is the number of small elements which may cause the failure, which

increases with the FPZ.

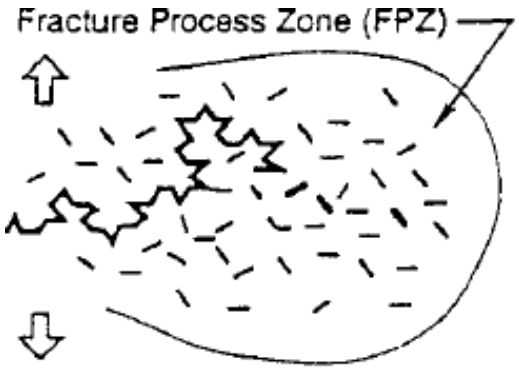

Figure 2.4 Fracture process zone with distributed small cracks. [71]

It is known that higher stress can cause higher probability of failure. With constant stress applied, the increasingly number of the elements will make the failure probability higher. Weibull also discovered a power law of the size effect that considers the relationship between nominal stress and structure size and volume. It is inferred from the probability integral, which further proves larger structure increases the probability of failure in stress field.

$$\sigma_N \propto k_0 V^{-1/m} = k_0 D^{-n/m} \tag{2.22}$$

where k_0 is the constant of characterising the structure shape, m is the shape parameter, and n is the number of spatial dimensions of the structure, V and D are structure volume and size, respectively.

However, it was then shown that the statistical size effect could not apply to quasi-brittle and concrete materials, which fail with larger cracks. Weibull's theory is a power law without characteristic material length. It is not available for a structure whose material is highly heterogeneous, with the material length which cannot be neglected. Bazant and Chen's study [74] declared that the statistical size effect is not valid when the structures are relatively large. It was pointed out that Weibull's theory is significantly dominated by the FPZ, which is a significant limitation. For example, when the FPZ is small and negligible compared to the structural size, it will keep constant with increasing structural size; in this case, the failure probability will not change with size.

2.7.2. Energetic size effect

Unlike the statistic size effect, Bazant [75] proposed the energetic size effect, which is a formula using deterministic energetic cause of size effect. In other words, it mainly considers the relationship between nominal stress and the characteristic size of the material. Bazant [76] introduced a scaling law and applied it in continuum mechanics, then focused on how the size will affect the fracture criterion in the different scaled models. For example, Bazant first proposed a formula of maximum stress at fatigue for a concrete beam, which is

$$f_r = \frac{6M_u}{bD^2} = \sigma_N \tag{2.23}$$

where f_r is the maximum stress which will cause failure, M_u is the maximum bending moment, b is the width of the beam and D is the characteristic size.

For a structure that fails at crack initiation, its fracture process zone, representing the boundary layer of distributed cracking, is not negligible. The thickness is determined to be l_f, and would be assumed to develop at the tensile face of the beam before the maximum stress is reached. Then Bažant [76] calculated the stress distribution in this assumption

$$f_r = f_t'(1 + \frac{2l_f}{d}) \tag{2.24a}$$

$$f_r = \frac{2d}{3L} f_t'(1 + \frac{rl_f}{d})^{1/r} \tag{2.24b}$$

where f_t' means standard direct tensile strength, d is the beam depth, L is the length of beam and r is an arbitrary positive constant, which has different value for different structure. Eqs. (2.24) can only work if the thickness of FPZ l_f is significantly smaller than the depth of beam d.

Bazant introduced a scaling law of size effect, which depends on the scaling ratio of models, and is independent of a specific length. Thus, the scaling law could be determined as a power law if and only if the characteristic dimension is absent, for example, plasticity, continuum damage mechanics and LEFM. In his study, when the fracture criterion is only stress or strain, or the fracture energy in LEFM, there is no

size effect between the small and large scaled model for the failure condition.

Furthermore, when the fracture criterion includes both stress (strain) and energy, the scaling law represents a gradual transition from strength theory for small size to LEFM for large size. Bazant gave a simple scaling law that tries to compare the failure condition between two different size models. However, the scaling law has several limitations. For example, to create a consistent power law between parameters, materials' properties are set to be equal (which means the two materials must be the same). In the theorem of scaling, it is supposed to have for a value Ω, there is $\Omega(x) = \mu\Omega(\beta x)$, and the solution which is a simple power law that $\Omega(x) = Cx^{\alpha}, \alpha = -\frac{log\mu}{log\beta}$. And the ration of scale-invariance Ω is $\Omega(\beta x)/\Omega(x) = \beta^{\alpha}$ which depends on the ratio between characteristic dimensions but not the size. This is proved to be a fundamental statute that associates power laws to scale invariance and self-similarity to criticality [77]. At the same time, for the cracked structure, Bazant [74,78] also applied the scaling law between the size effect and the nominal strength, which was gradually developed in LEFM like

$$\sigma_N = f_r = f_{r,\infty}\left(1 + \frac{rl_f}{d}\right)^{1/r} l_f/d \tag{2.25a}$$

$$f_{r,\infty} = \sqrt{\frac{EG_c}{a_{eff}g'(\frac{a_0}{d})}}, l_f = \left|-\frac{a_{eff}g''(\frac{a_0}{d})}{4g'(\frac{a_0}{d})}\right| \tag{2.25b}$$

where a_0 and a_{eff} are initial (half) crack length and effective (half) crack length respectively, $g'$and g'' are the function of $\frac{a_0}{d}$ and a_{eff}.

The equations above describe the relationship between failure stress, the crack length, the crack thickness, and the specimen thickness. It can investigate the size effect over the size or relative size like a_0 and d, l_f. The fundamental relation curves in LFEM can be plotted as Fig 2.5.

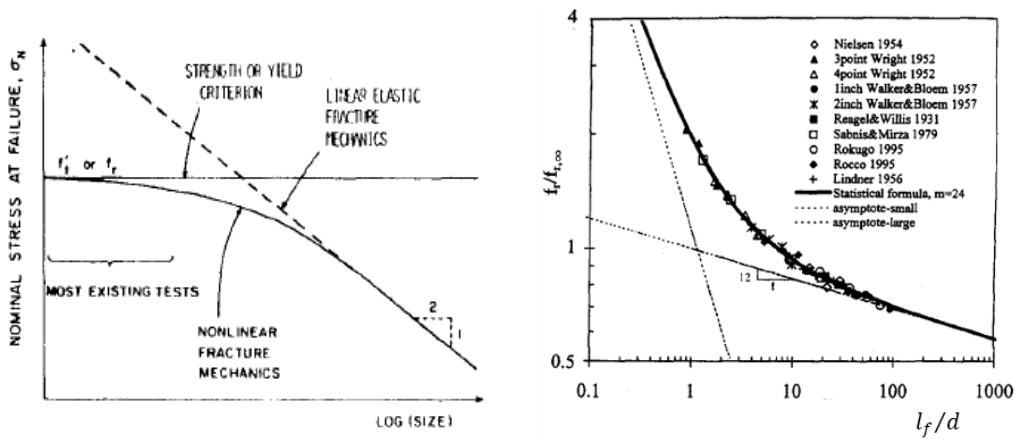

Figure 2.5 Relation curves between nominal stress and size, modulus of rupture $f_r/f_{r,\infty}$ versus relative size l_f/d.

However, in these studies, they focused on comparing different scaled models to show how the size affects the material behaviour. Then Bazant [75] applied different scaling laws in quasi-brittle structure failure in many different cases, where many kinds of relationship functions between nominal stresses are displayed, which are discovered from the fundamental scaling law (power law) in different situations. Moreover, the size effect is widely used to investigate fracture and continuum mechanics [79-82]. To conclude, Bazant's studies give good examples of scaling laws. It raises some functions between stress and energy release rate in different sizes; in the journal, most properties between different models are fixed to compare the parameters like nominal strength and energy, which means there is the same material in the comparison, which could view the size effect obviously.

2.8. Summary

From the parameters involved in these dimensionless numbers of fracture, it could find that they are mostly considered with LEFM or represent the plastic behaviour with linear elasticity, which limits the application in complex ductile metals. In addition, the dimensionless numbers are proposed with the point-to-point similarity, which intends to express the scaling of one critical point rather than the forming process. It can be founded that the number of studies of dimensional analysis with metal forming is limited [69-70]. However, fracture mechanics investigation is

supposed to be the forming process of materials, with both LEFM and EPFM involved.

On the other hand, the dimensionless numbers are all based on dimensional homogeneity, which can explain that the terms in a physical equation should be in the same dimension. Application of these dimensionless numbers represented by the dimensional parameters, for the full-scale and small-scale process, requires the scale invariance of the parameters, which causes the restriction due to the size effect of most factors in realistic.

Size effect causes the limitations of dimensional analysis in fracture mechanics, which cannot be ignored due to the scale invariance for dimensionless components. Studies around the size effect and dimensional analysis mainly focus on investigating the size effect and how to resolve that. The alternative scaling approach finite similitude is introduced here, which aims to describe the forming of ductile materials and deal with the feature of size effect in fracture mechanics.

Chapter 3 Finite Similitude in Fracture Mechanics

3.1 Introduction

Product and component testing is an important practice in many industries and is required to assure in-service reliability and performance. Scaled experimentation has an important role to play in many testing systems but care must be taken to ensure that any results from a scaled experiment are carefully scrutinised. The principal concern with scaling is scale effects where the scaled system behaves in a manner that can be markedly different from the full-size system. It might well be contended that if scale effects were not a feature of scaling, then scaled experimentation would play a far greater role than it presently does. The absence of scale effects would enable complex systems to be more readily analysed at a fraction of the cost of a full-scale trial. Observed phenomena at scale would then replicate that at full size and large-scale reductions would pose no concern; however, the reality is somewhat different.

Despite the presence of scale effects, scaled experiments are performed in industry. There are several reasons for this, but these are largely related to cost and/or the impracticability of full-scale trials. The ever-increasing accuracy and effectiveness of computational modelling has undoubtedly impacted on the type and nature of experiments performed. Scaling is widely applied in different areas of engineering, for example in structural failure and fracture [83], structural impact [84-87], explosion engineering [88-89] and thermofluids [90]. A reliable computational model can often replace experiments altogether but in addition it can supplement scaled experimentation. Numerical analysis at scale and at full size can be used to identify and gauge the importance of scale effects [74]. For more complex systems involving significant uncertainties, placing too much reliance on computation is not sensible and experimentation is therefore needed; for instance, the scaling of fluid mechanics [91] or simulation in complex conditions [92].

One of earliest works in structural mechanics on similitude followed some 30 years

after Rayleigh's 1915 paper [3] in a US aeronautical advisory committee report by Goodier and Thomson [4]. This was followed by Goodier's book in 1950 [5] covering the applicability of similitude to structural systems. Goodier and Thomson presented the first application of dimensional analysis to relatively simple and more complex structural problems. They examined aspects of large deformation, buckling and plastic behaviour covering aspects of materials with nonlinear stress-strain characteristics. A good review of the many works based on dimensional analysis up to 2000 is provided by Simitses et al. in reference [93].

Despite the wide application of dimensional analysis, it has been shown to suffer some limitations in many studies all stemming from scale effects. Particularly renown for such effects is indentation [94], which is of relevance to instrumentation for the measurement of hardness. Even in the early work of Brinell [95] it was observed that the hardness value is sensitive to ball diameter. In this case the difference can be predominantly attributed to size effects arising with the size of the deformation zone and the change in material response because of this. However other scale effects have been identified and these include surface contamination, energy, and roughness along with indenter tip rounding and friction [15].

The behaviour of concrete in fracture is a material that has notoriety for size effects; see for example the work of Bažant [15]. Since scale effects are characterized by the failure of dimensional analysis in the sense that the invariance of the dimensionless governing equations breaks down with scale, it is often used in investigations of scale effects. An example of this is a recent study concerned with scaling and its effects on fatigue and lifetime [78], where dimensional analysis is applied to qualify whether scale effects are present or not. Other studies concerned with fatigue, size effect and the application of dimensional analysis [96,97] again highlight the presence of scale effects through change to the dominant governing dimensionless equation with scale.

This paper is concerned with a new approach to scaled experimentation applied to fracture. The finite-similitude theory [98-100] is founded on the metaphysical concept of space scaling, where it is imagined that space is contracted and all things in

the space suffer scaling therefore. Although patently such scaling cannot be achieved practically, what is possible is an examination of the effect that this metaphysical process has on the governing equations constraining the behavior of the phenomena of study. The metaphysics of space scaling is introduced in Section 3.2 along with its effects on a moving control volume in the space being considered. The immediacy of the effect of space scaling on a control volume, which is simply a region of space, is one of the underlying reasons for describing the equations of interest is an integral transport form. A generic form of transport equation is therefore introduced in Section 3.3 and the effect space scaling has on it is examined. Critical to the finite similitude approach is the representation of trial-space physics on the full-scale space. It is through this representation that scale dependencies are revealed in either an explicit or implicit form. Moreover, the representation provides a mechanism for the contrasting of behaviors at different scales and in fact defines what is algebraically allowable. This aspect is examined in greater detail in Section 3.4 under the title of *projected continuum mechanics*, where trial-space conserved and non-conserved transport equations are examined in their projected form in the full-scale physical space. The proportional relationships typical to dimensional analysis are revealed in this section on application of the simple assumption that the projected transport equations do not change with scale. This is equivalent to the condition that the differentiation of the projected equations with respect to the length scalar (β in this chapter) is identically zero. The realization that this is just one possibility and other possibilities exist is examined in Section 3.5. Introduced is *high-order finite similitude* but focus of this paper is on first order only, where an identity involving two nested derivatives with respect to β is involved. Two derivatives signify two scaled experiments but more fundamentally, scale effects as previously defined using dimensional analysis can cease to be scale effects under the new definition. Analytical applications are examined in Section 3.6 for the J-integral and the cohesive zone model since both concepts play important roles in fracture mechanics. Numerical studies are presented in Sections 3.7, 3.8 and 3.9 to demonstrate the

practical benefit of the new scaling approach to fracture mechanics where scale effects (as previously defined) are prevalent. The chapter concludes with a list of conclusions in 3.8.

3.2 Background concepts

Finite similitude is a new scaling theory founded on the metaphysical concept of space scaling. The idea that space can be expanded or contracted for the purpose of scaled experimentation is evidently not feasible but what is possible is the ability to assess the impact of this metaphysical process on the underpinning physics dictating the behaviour of an experiment. In this way it is possible to assess what changes take place as space deforms and design experiments accordingly.

3.2.1. Space scaling

To enact the space-scaling concept consider the affine map $\boldsymbol{x}_{ps} \mapsto \boldsymbol{x}_{ts}$ which relates coordinate points in the inertial frame in the physical space (full size) to those in the trial space (scaled size). Points in each inertial frame are placed in one-to-one correspondence and the map is assumed to be affine and temporally invariant. In differential terms the map provides $\boldsymbol{dx}_{ts} = F\boldsymbol{dx}_{ps}$ where F is both spatially and temporally invariant and in coefficient form is $dx^i_{ts} = F^i{}_j dx^j_{ps}$, where $F^i{}_j = \partial x^i_{ts}/\partial x^j_{ps}$, where x^i_{ts} and x^i_{ps} are coordinate functions. The matrix F dictates the manner in which space distorts, where anisotropic scaling is possible but focus here is on isotropic scaling, where F takes on the relatively simple form $F = \beta I$ or $F^i{}_j = \beta\delta^j_j$, where δ^j_j is the well-known Kronecker delta symbol and takes the value of either zero or one. The scalar β is a positive real parameter that quantifies the extent of the scaling involved. For $0 < \beta < 1$ the space is contracted, for $\beta = 1$ no scaling takes place and for $\beta > 1$ the space is expanded. The space scaling concept is illustrated in in Fig. 3.1, where contraction and expansion are depicted.

With the assumed existence of the differential map $\boldsymbol{dx}_{ts} = \beta\boldsymbol{dx}_{ps}$ it is now possible

to relate differential volumes and areas in the two spaces. This is achieved readily by means of Nanson's identities, which take the form $dV_{ts} = \beta^3 dV_{ps}$ and $\boldsymbol{d\Gamma}_{ts} = \beta^2 \boldsymbol{d\Gamma}_{ps}$, where $\boldsymbol{d\Gamma}_{ts} = \boldsymbol{n}_{ts}\, d\Gamma_{ts}$, and $\boldsymbol{d\Gamma}_{ps} = \boldsymbol{n}_{ps}\, d\Gamma_{ps}$, and $\boldsymbol{n}_{ts}$ and $\boldsymbol{n}_{ps}$ are unit normal vectors in the respective spaces. The quantities dV_{ts} and dV_{ps} along with $d\Gamma_{ts}$ and $d\Gamma_{ps}$ are differential measures of volume and area respectively in the two spaces.

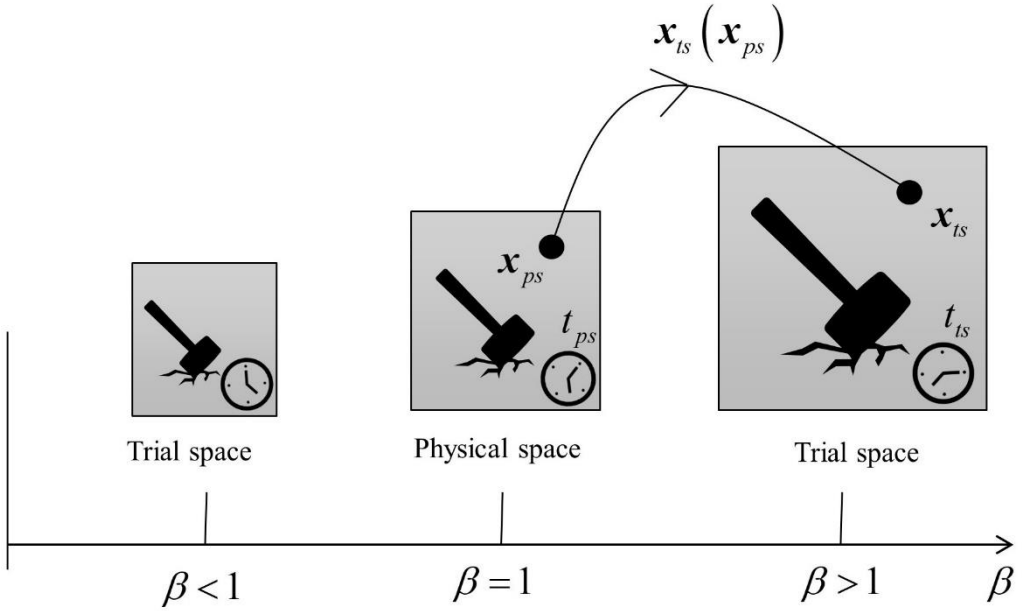

Figure 3.1 Depiction of space scaling and mapping between inertial physical and trial-space frames.

The adoption of a Newtonian framework means the assumed existence of absolute time, labelled t_{ts} and t_{ps} in the respective spaces. These are assumed to be related by the differential identity $dt_{ts} = g dt_{ps}$, where g is a positive scalar and measures the extent of the difference in rate at which processes proceed in the two spaces.

3.2.2. Control volume movement

With the establishment of space scaling, it expedient here to examine what affect this has on the behaviour of the underpinning pertinent physics in a continuum mechanics framework. The physical description adopted here is founded on the control-volume concept as this approach immediately brings into play the effects of the differential measures of volume, area and length arising from space scaling. A control volume is

a finite region of space and takes the form of a continuous open domain Ω_{ts}^{*} (in the trial space) whose closure contains the orientable boundary Γ_{ts}^{*} with outward pointing unit normal $\boldsymbol{n}_{ts}$. The exact same apparatus applies to the physical space, and it should be recognised that both Ω_{ps}^{*} and Ω_{ts}^{*} are free to deform and move but in the context of scaled experimentation it can be anticipated that their movement must be synchronised in some manner. The movement of Ω_{ts}^{*} can be related to the velocity field $\boldsymbol{v}_{ts}^{*}$ using the identity $\boldsymbol{v}_{ts}^{*} = D^{*}\boldsymbol{x}_{ts}^{*}/D^{*}t_{ts}^{*}$, where the temporal derivative $D^{*}/D^{*}t_{ts}^{*}$ is a partial derivative that holds constant points in a reference control volume Ω_{ts}^{*ref}, i.e. $D^{*}/D^{*}t_{ts}^{*} \equiv \partial/\partial t_{ts}^{*}|_{\boldsymbol{\chi}_{ts}}$, where $\boldsymbol{\chi}_{ts} \in \Omega_{ts}^{*ref}$. In this manner the movement of a coordinate point is precisely described by the solution of the differential equation $\boldsymbol{v}_{ts}^{*} = D^{*}\boldsymbol{x}_{ts}^{*}/D^{*}t_{ts}^{*}$ (with $\boldsymbol{v}_{ts}^{*}$ known) or the map $\Omega_{ts}^{*ref} \rightarrow \Omega_{ts}^{*}$ (i.e. $\boldsymbol{\chi}_{ts} \mapsto \boldsymbol{x}_{ts}^{*}$).

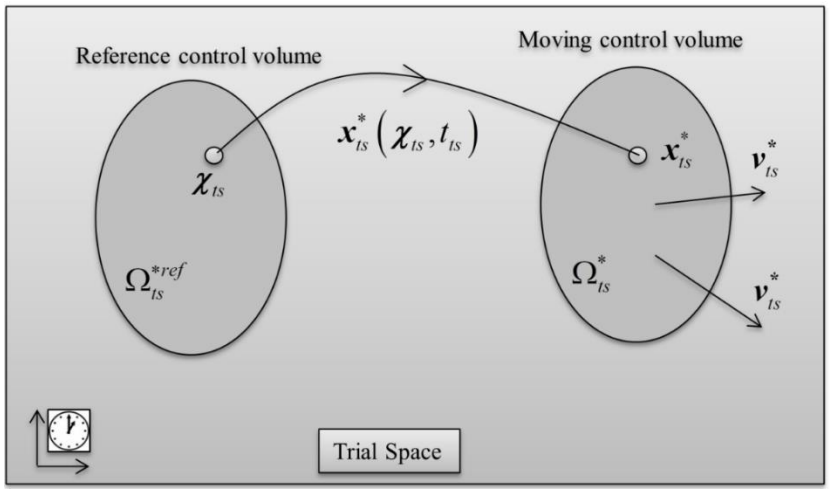

Figure 3.2 Moving control volume in the trial space and mapping from a reference control volume.

The concept is illustrated in Fig. 3.2, where a moving control volume of arbitrary shape facilitates the focus on a particular region of space, allowing for changing shape and movement, as necessary. Needless to say the exact same apparatus applies in the physical space with the identity $\boldsymbol{v}_{ps}^{*} = D^{*}\boldsymbol{x}_{ps}^{*}/D^{*}t_{ps}^{*}$. The assumed relationship between $\boldsymbol{x}_{ts}^{*}$ and $\boldsymbol{x}_{ps}^{*}$ suggests a map of the form $\boldsymbol{x}_{ps}^{*} \mapsto \boldsymbol{x}_{ts}^{*}$. This map transpires to be identical in form to the space-scaling map, i.e. $\boldsymbol{dx}_{ts}^{*} = \beta \boldsymbol{dx}_{ps}^{*}$, and in view of the

temporal relationship $dt_{ts} = g dt_{ps}$, the velocities $\boldsymbol{v}^*_{ts}$ and $\boldsymbol{v}^*_{ps}$ are related by $\boldsymbol{v}^*_{ts} = \beta g^{-1} \boldsymbol{v}^*_{ps}$ and further details on this can be found in reference [98]. The ability to relate control-volume movement without reference to the physical processes in the two spaces is important as it provides for a generic approach.

3.3 The projected transport equations

Due to the relative dominance of variational methods, control-volume approaches involving transport equations in their integral form for applications in solid mechanics are somewhat neglected (see Davey & Darvizeh [101]). In the field of fracture mechanics in particular the theory of configurational forces [102] does make reference to control-volume ideas although in a material-reference frame and also their use is required in shock physics [103] to capture discontinuous behaviour. The ability to capture all the physical laws relating to continuum physics using the control volume approach is its principal advantage in scaling theory. Moreover, it is made apparent here that all scale dependencies are revealed, and different forms of scale effects arise depending on the how similitude is defined. Transport equations in their most generic form in the physical space can be represented by [101]

$$\begin{aligned} \frac{D^*}{D^* t_{ps}} \int_{\Omega^*_{ps}} \rho_{ps} \boldsymbol{\Psi}_{ps} \, dV^*_{ps} + \int_{\Gamma^*_{ps}} \rho_{ps} \boldsymbol{\Psi}_{ps} (\boldsymbol{v}_{ps} - \boldsymbol{v}^*_{ps}) \cdot \boldsymbol{n}_{ps} \, d\Gamma^*_{ps} \\ = - \int_{\Gamma^*_{ps}} \boldsymbol{J}^{\Psi}_{ps} \cdot \boldsymbol{n}_{ps} d\Gamma^*_{ps} + \int_{\Omega^*_{ps}} \rho_{ps} \boldsymbol{b}^{\Psi}_{ps} dV^*_{ps} \end{aligned} \tag{3.1}$$

where ρ_{ps}, $\boldsymbol{\Psi}_{ps}$, $\boldsymbol{v}_{ps}$, $\boldsymbol{J}^{\Psi}_{ps}$, $\boldsymbol{b}^{\Psi}_{ps}$, $\boldsymbol{n}_{ps}$ signify material density, physical field, material velocity field, flux, source and unit normal to boundary $\Gamma^*_{\mathrm{ps}}$of the control volume Ω^*_{ps}.

Similarly, and somewhat more importantly the trial-space transport equations take the identical form

$$\begin{aligned} \frac{D^*}{D^* t_{ts}} \int_{\Omega^*_{ts}} \rho_{ts} \boldsymbol{\Psi}_{ts} \, dV^*_{ts} + \int_{\Gamma^*_{ps}} \rho_{ts} \boldsymbol{\Psi}_{pts} (\boldsymbol{v}_{ts} - \boldsymbol{v}^*_{ts}) \cdot \boldsymbol{n}_{ts} \, d\Gamma^*_{ts} \\ = - \int_{\Gamma^*_{ts}} \boldsymbol{J}^{\Psi}_{ts} \cdot \boldsymbol{n}_{ts} d\Gamma^*_{ts} + \int_{\Omega^*_{ts}} \rho_{ts} \boldsymbol{b}^{\Psi}_{ts} dV^*_{ts} \end{aligned} \tag{3.2}$$

where on substitution of the identities $dV_{ts}^* = \beta^3 dV_{ps}^*$, $\boldsymbol{d\Gamma}_{ts}^* = \beta^2 \boldsymbol{d\Gamma}_{ps}^*$, $dt_{ts} = g dt_{ps}$, and on multiplication throughout by g and a scalar α_0^{Ψ}, gives rise to the critically important equation

$$\begin{aligned}\alpha_0^{\Psi} T_0^{\Psi}(\beta) = \frac{D^*}{D^* t_{ps}} \int_{\Omega_{ps}^*} \alpha_0^{\Psi} \rho_{ts} \beta^3 \boldsymbol{\Psi}_{ts}\, dV_{ps}^* \\ + \int_{\Gamma_{ps}^*} \alpha_0^{\Psi} \rho_{ts} \beta^3 \boldsymbol{\Psi}_{ts} (\beta^{-1} g \boldsymbol{v}_{ts} - \beta^{-1} g \boldsymbol{v}_{ts}^*) \cdot \boldsymbol{n}_{ps}\, d\Gamma_{ps}^* \\ + \int_{\Gamma_{ps}^*} \alpha_0^{\Psi} \beta^2 g \boldsymbol{J}_{ts}^{\Psi} \cdot \boldsymbol{n}_{ps} d\Gamma_{ps}^* - \int_{\Omega_{ts}^*} \alpha_0^{\Psi} \rho_{ts} \beta^3 g \boldsymbol{b}_{ts}^{\Psi} dV_{ps}^* = 0\end{aligned} \tag{3.3}$$

which is essentially Eq. (3.2) but represented now on the physical space, where the scalar α_0^{Ψ} along with g are assumed to be functions of β.

The explanation to why Eq. (3.2) is critical to finite-similitude theory is that all scale dependencies are captured by it. A requirement of this equation is that for $\beta = 1$ it matches the exact same equation expected for the physical space, i.e., $\alpha_0^{\Psi} T_0^{\Psi}(1) = T_{ps}^{\Psi}$ and a direct consequence is $\alpha_0^{\Psi}(1) = 1$. In addition the following identities must apply: $\rho_{ts}(1) = \rho_{ps}$, $\boldsymbol{v}_{ts}(1) = \boldsymbol{v}_{ps}$, $\boldsymbol{\Psi}_{ts}(1) = \boldsymbol{\Psi}_{ps}$, $\boldsymbol{J}_{ts}(1) = \boldsymbol{J}_{ps}$, $\boldsymbol{b}_{ts}(1) = \boldsymbol{b}_{ps}$ and $g(1) = 1$. Note that all geometric dependencies are explicit (i.e., β^3 and β^2 terms) yet the fields $\rho_{ts}(\beta)$, $\boldsymbol{v}_{ts}(\beta)$, $\boldsymbol{\Psi}_{ts}(\beta)$, $\boldsymbol{J}_{ts}(\beta)$ and $\boldsymbol{b}_{ts}(\beta)$ are implicit. The significance of Eq. (3.2) (i.e., $\alpha_0^{\Psi} T_0^{\Psi}(\beta) = 0$) is that it provides an exact description of trial-space physics but projected onto the physical space. This projection reveals all $\beta -$ dependencies in either an explicit or implicit form and effectively transforms the scaling problem in one where the objective is to reveal the hidden dependencies. The advantage this approach has over dimensional analysis is that it is not restricted to a single invariance (i.e., dimensionless equations are invariant). It transpires and is revealed below for fracture mechanics that a particular invariance applies. Thus, by means of the generalisation of scaled experimentation a new theory for fracture mechanics is shown below to be possible.

3.4 Projected continuum mechanics

Fracture mechanics predominantly makes use of Newtonian mechanics (i.e. three equations) but in scaling theory eight transport equations are to be considered, i.e. two scalar equations for volume and mass conservation, and two vector equations momentum and movement. Although movement is a feature of fracture mechanics it is seldom considered in transport form and was first introduced by Davey and Darvizeh [101] in order to bring the displacement field $\boldsymbol{u}_{ps}$ into the family of transport equations for continuum mechanics. In summary the eight equations are:

$$\alpha_0^1 T_0^1(\beta) = \frac{D^*}{D^* t_{ps}} \int_{\Omega_{ps}^*} \alpha_0^1 \beta^3 \, dV_{ps}^* - \int_{\Gamma_{ps}^*} \alpha_0^1 \beta^3 \left(\beta^{-1} g \boldsymbol{v}_{ts}^* \cdot \boldsymbol{n}_{ps}\right) d\Gamma_{ps}^* = 0 \tag{3.4a}$$

$$\alpha_0^\rho T_0^\rho(\beta) = \frac{D^*}{D^* t_{ps}} \int_{\Omega_{ps}^*} \alpha_0^\rho \rho_{ts} \beta^3 \, dV_{ps}^* + \int_{\Gamma_{ps}^*} \alpha_0^\rho \rho_{ts} \beta^3 (\beta^{-1} g \boldsymbol{v}_{ts} - \beta^{-1} g \boldsymbol{v}_{ts}^*) \cdot \boldsymbol{n}_{ps} \, d\Gamma_{ps}^* = 0 \tag{3.4b}$$

$$\begin{aligned} \alpha_0^v T_0^v(\beta) = \frac{D^*}{D^* t_{ps}} & \int_{\Omega_{ps}^*} [\alpha_0^v g^{-1} \beta \rho_{ts} \beta^3] (\beta^{-1} g \boldsymbol{v}_{ts}) \, dV_{ps}^* \\ & + \int_{\Gamma_{ps}^*} [\alpha_0^v g^{-1} \beta \rho_{ts} \beta^3] (\beta^{-1} g \boldsymbol{v}_{ts}) (\beta^{-1} g \boldsymbol{v}_{ts} - \beta^{-1} g \boldsymbol{v}_{ts}^*) \cdot \boldsymbol{n}_{ps} \, d\Gamma_{ps}^* \\ & + \int_{\Gamma_{ps}^*} \alpha_0^v \beta^2 g \boldsymbol{\sigma}_{ts} \cdot \boldsymbol{n}_{ps} d\Gamma_{ps}^* - \int_{\Omega_{ts}^*} \alpha_0^v \rho_{ts} \beta^3 g \boldsymbol{b}_{ts}^v dV_{ps}^* = 0 \end{aligned} \tag{3.4c}$$

$$\alpha_0^u T_0^u(\beta) = \frac{D^*}{D^* t_{ps}} \int_{\Omega_{ps}^*} \alpha_0^u \beta \rho_{ts} \beta^3 (\beta^{-1} \boldsymbol{u}_{ts}) \, dV_{ps}^* + \int_{\Gamma_{ps}^*} \alpha_0^u \beta \rho_{ts} \beta^3 (\beta^{-1} \boldsymbol{u}_{ts}) (\beta^{-1} g \boldsymbol{v}_{ts} - \beta^{-1} g \boldsymbol{v}_{ts}^*) \cdot \boldsymbol{n}_{ps} \, d\Gamma_{ps}^* - \int_{\Omega_{ts}^*} \alpha_0^u \beta \rho_{ts} \beta^3 (\beta^{-1} g \boldsymbol{v}_{ts}) dV_{ps}^* = 0 \tag{3.4d}$$

where to satisfy the zeroth-order identity

$$\frac{d}{d\beta} (\alpha_0^\Psi T_0^\Psi) \equiv 0 \tag{3.5}$$

the necessary and sufficient identities arising from these equations are presented in Table 3.1.

Table 3.1 Necessary and sufficient zeroth-order scaling identities.

Eq. No.	Field	Scalars	Flux	Source	Duplicate
(3.4a)	$\boldsymbol{v}_{ts}^{*} = \beta g^{-1}\boldsymbol{v}_{ps}^{*}$	$\alpha_0^1 = \beta^{-3}$	-	-	-
(3.4b)	$\alpha_0^{\rho}\rho_{ts}\beta^3 = \rho_{ps}$	$\alpha_0^{\rho}(1) = 1$ $g(1) = 1$			$\boldsymbol{v}_{ts} = \beta g^{-1}\boldsymbol{v}_{ps}$ $\boldsymbol{v}_{ts}^{*} = \beta g^{-1}\boldsymbol{v}_{ps}^{*}$
(3.4c)	$\boldsymbol{v}_{ts} = \beta g^{-1}\boldsymbol{v}_{ps}$	$\alpha_0^{v} = \alpha_0^{\rho} g\beta^{-1}$	$\alpha_0^{v}\beta^2 g\boldsymbol{\sigma}_{ts}$ $= \boldsymbol{\sigma}_{ps}$	$\alpha_0^{v}\rho_{ts}\beta^3 g\boldsymbol{b}_{ts}^{v}$ $= \rho_{ts}\boldsymbol{b}_{ps}^{v}$	$\boldsymbol{v}_{ts}^{*} = \beta g^{-1}\boldsymbol{v}_{ps}^{*}$
(3.4d)	$\boldsymbol{u}_{ts} = \beta\boldsymbol{u}_{ps}$	$\alpha_0^{u} = \alpha_0^{\rho}\beta^{-1}$		$\boldsymbol{v}_{ts}$ $= \beta g^{-1}\boldsymbol{v}_{ps}$	$\boldsymbol{v}_{ts}^{*} = \beta g^{-1}\boldsymbol{v}_{ps}^{*}$

Table 3.1 presents those identities arising from Eqs. (3.4) because of Eq. (3.5), which is the situation where scale effects are absent. An additional "Duplicate" column is included in Table 3.1 to capture those field identities that appear in more than one equation. Observe that the role of Eq. (3.4a) is the determination of the identity $\boldsymbol{v}_{ts}^{*} = \beta g^{-1}\boldsymbol{v}_{ps}^{*}$, which is required so that control-volume movement in the trial space at any scale can be described in the physical space. In this sense the behaviour of the trial-space system is played out on the physical space enabling differences to be gauged. In order to satisfy Eq. (3.5) for Eq. (3.4b) it is necessary and sufficient to set $\alpha_0^{\rho}\rho_{ts}\beta^3 = \rho_{ps}$ and $\boldsymbol{v}_{ts} = \beta g^{-1}\boldsymbol{v}_{ps}$ (along with $\boldsymbol{v}_{ts}^{*} = \beta g^{-1}\boldsymbol{v}_{ps}^{*}$) with $\alpha_0^{\rho}(1) = 1$ and $\boldsymbol{v}_{ts}(1) = \boldsymbol{v}_{ps}$. Although continuity plays little part in fracture mechanics it is needed for similitude to establish a relationship for density with scale (i.e. $\alpha_0^{\rho}\rho_{ts}\beta^3 = \rho_{ps}$), which opens up the possibility of selecting alternative materials for a scaled experiment. The velocity relationship $\boldsymbol{v}_{ts} = \beta g^{-1}\boldsymbol{v}_{ps}$ is particularly constraining and it is effectively restricting all scaled experiments to the same pattern of deformation, which is unrealistic in practice. The momentum transport Eq. (3.4c) has a critical role

to place in fracture mechanics and to satisfy Eq. (3.5) with $\alpha_0^\rho \rho_{ts} \beta^3 = \rho_{ps}$ it is necessary and sufficient to set $\alpha_0^v = \alpha_0^\rho g \beta^{-1}$ (as above $\boldsymbol{v}_{ts} = \beta g^{-1} \boldsymbol{v}_{ps}$ and $\boldsymbol{v}_{ts}^* = \beta g^{-1} \boldsymbol{v}_{ps}^*$), $\alpha_0^v \beta^2 g \boldsymbol{\sigma}_{ts} = \boldsymbol{\sigma}_{ps}$ and $\alpha_0^v \rho_{ts} \beta^3 g \boldsymbol{b}_{ts}^v = \rho_{ts} \boldsymbol{b}_{ps}^v$; note that $\alpha_0^v(1) = 1$. Again in view of the relationship $\alpha_0^\rho \rho_{ts} \beta^3 = \rho_{ps}$ it is necessary and sufficient in the movement equation, Eq. (3.4d) to set $\alpha_0^u = \alpha_0^\rho \beta^{-1}$ (as above $\boldsymbol{v}_{ts} = \beta g^{-1} \boldsymbol{v}_{ps}$ and $\boldsymbol{v}_{ts}^* = \beta g^{-1} \boldsymbol{v}_{ps}^*$) and $\boldsymbol{u}_{ts} = \beta \boldsymbol{u}_{ps}$; note also that $\alpha_0^u(1) = 1$ and $\boldsymbol{u}_{ts}(1) = \boldsymbol{u}_{ps}$. The relationship for displacement is not too unexpected since differentiation of $\boldsymbol{u}_{ts} = \beta \boldsymbol{u}_{ps}$ with respect to time (given the identity $dt_{ts} = g dt_{ps}$) provides as required $\boldsymbol{v}_{ts} = \beta g^{-1} \boldsymbol{v}_{ps}$. Note also that the two identities $\boldsymbol{u}_{ts} = \beta \boldsymbol{u}_{ps}$ and $\boldsymbol{dx}_{ts} = \beta \boldsymbol{dx}_{ps}$ provide the small-strain tensor identity $\boldsymbol{\varepsilon}_{ts} = \boldsymbol{\varepsilon}_{ps}$, which immediately infers that the strain tensor $\boldsymbol{\varepsilon}_{ts}$ is independent of β.

Overall, it is fairly evident that identity Eq. (3.5) is very restrictive on the behaviour of the trial-space systems and unlikely to be satisfied for realistic problems. See previous studies on the practical application of zeroth-order finite similitude theory in references [104-106]. The reality in practice therefore is the inequality

$$\frac{d}{d\beta}(\alpha_0^\Psi T_0^\Psi) \not\equiv 0 \tag{3.6}$$

which of course provides scale effects, and these can be expected to change with scale, i.e. be dependent on β.

3.5 First-order finite similitude

Eq. (3.3) provides the framework for the analysis of scale dependence but contains hidden dependencies that require information on such things such as material behaviour (e.g. size dependence) and boundary conditions (e.g. surface conditions) to uncover them. However, an alternative (and the approach adopted here) is to simply enforce a global $\beta-$ invariant condition and apply this in the design of experiments. First-order finite similitude [107] examines an alternative to Eq. (3.5) that involves an additional scaled experiment to shed additional light on changes that are taking place

and to add extra flexibility. Consider then the following definition:

3.5.1. Definition (High-order finite similitude)

The concept of k[th]-order finite similitude is identified by the lowest derivative that satisfies

$$T_{k+1}^{\Psi} = \frac{d}{d\beta}(\alpha_k^{\Psi} T_k^{\Psi}) \equiv 0 \tag{3.7}$$

$\forall \beta > 0$, with $\alpha_0^{\Psi} T_0^{\Psi}$ defined by Eq. (3.3) and non-zero scalars α_k^{Ψ} are functions of β with $\alpha_k^{\Psi}(1) = 1$, where the sign "≡" means identically zero in Eq. (3.7).

The corresponding scaling theory is termed k[th]-order finite similitude but the focus in this paper is on first-order finite similitude only, i.e.

$$T_2^{\Psi} = \frac{d}{d\beta}(\alpha_1^{\Psi} T_1^{\Psi}) = \frac{d}{d\beta}\left(\alpha_1^{\Psi} \frac{d}{d\beta}(\alpha_0^{\Psi} T_0^{\Psi})\right) \equiv 0 \tag{3.8}$$

where α_1^{Ψ} is required to play a role similar to that of α_0^{Ψ} in the annihilation of β terms to facilitate the satisfaction of this identity.

To apply this identity to Eqs. (3.4) it is convenient first to insert the established zeroth-order conditions to give

$$\alpha_0^{\rho} T_0^{\rho}(\beta) = \frac{D^*}{D^* t_{ps}} \int_{\Omega_{ps}^*} \rho_{ps}\, dV_{ps}^* + \int_{\Gamma_{ps}^*} \rho_{ps}(\boldsymbol{V}_{ps} - \boldsymbol{v}_{ps}^*) \cdot \boldsymbol{n}_{ps}\, d\Gamma_{ps}^* = 0 \tag{3.9a}$$

$$\alpha_0^{v} T_0^{v}(\beta) = \frac{D^*}{D^* t_{ps}} \int_{\Omega_{ps}^*} \rho_{ps} \boldsymbol{V}_{ps}\, dV_{ps}^* + \int_{\Gamma_{ps}^*} \rho_{ps} \boldsymbol{V}_{ps}(\boldsymbol{v}_{ps} - \boldsymbol{v}_{ps}^*) \cdot \boldsymbol{n}_{ps}\, d\Gamma_{ps}^* + \int_{\Gamma_{ps}^*} \boldsymbol{\Sigma}_{ps} \cdot \boldsymbol{n}_{ps} d\Gamma_{ps}^* - \int_{\Omega_{ps}^*} \boldsymbol{B}_{ps} dV_{ps}^* = 0 \tag{3.9b}$$

$$\alpha_0^{u} T_0^{u}(\beta) = \frac{D^*}{D^* t_{ps}} \int_{\Omega_{ps}^*} \rho_{ps} \boldsymbol{U}_{ps}\, dV_{ps}^* + \int_{\Gamma_{ps}^*} \rho_{ps} \boldsymbol{U}_{ps}(\boldsymbol{v}_{ps} - \boldsymbol{v}_{ps}^*) \cdot \boldsymbol{n}_{ps}\, d\Gamma_{ps}^* - \int_{\Omega_{ps}^*} \rho_{ps} \boldsymbol{V}_{ps} dV_{ps}^* = 0 \tag{3.9c}$$

where $\boldsymbol{V}_{ps} = \beta^{-1} g \boldsymbol{v}_{ts}, \boldsymbol{\Sigma}_{ps} = \alpha_0^{v} \beta^2 g \boldsymbol{\sigma}_{ts}, \boldsymbol{B}_{ps} = \alpha_0^{v} \rho_{ts} \beta^3 g \boldsymbol{b}_{ts}^{v}, \boldsymbol{U}_{ps} = \beta^{-1} \boldsymbol{u}_{ts}$ and Eq. (3.4a) is not included here since it satisfies the zeroth-order condition Eq. (3.5) and evidently automatically satisfies Eq. (3.8).

Note also that the terms $\boldsymbol{V}_{ps}\left(\boldsymbol{V}_{ps}-\boldsymbol{v}_{ps}^{*}\right)$ and $\boldsymbol{U}_{ps}(\boldsymbol{V}_{ps}-\boldsymbol{v}_{ps}^{*})$ have been approximated by $\boldsymbol{V}_{ps}\left(\boldsymbol{v}_{ps}-\boldsymbol{v}_{ps}^{*}\right)$ and $\boldsymbol{U}_{ps}(\boldsymbol{v}_{ps}-\boldsymbol{v}_{ps}^{*})$ in Eqs. (3.9b) and (3.9c) in recognition that convective terms are negligible in fracture mechanics but also to avoid the need for higher order similitude terms. In first-order finite similitude the transport equations of interest are obtained on differentiation of Eqs. (3.9) with respect to β and on multiplication by α_1^{ψ} to give

$$\alpha_1^{\rho}T_1^{\rho}(\beta)=\int_{\Gamma_{ps}^{*}}\alpha_1^{\rho}\rho_{ps}\boldsymbol{V}_{ps}'\cdot\boldsymbol{n}_{ps}\,d\Gamma_{ps}^{*}=0 \tag{3.10a}$$

$$\alpha_1^{v}T_1^{v}(\beta)=\frac{D^{*}}{D^{*}t_{ps}}\int_{\Omega_{ps}^{*}}\alpha_1^{v}\rho_{ps}\boldsymbol{V}_{ps}'\,dV_{ps}^{*}+\int_{\Gamma_{ps}^{*}}\alpha_1^{v}\rho_{ps}\boldsymbol{V}_{ps}'\left(\boldsymbol{v}_{ps}-\boldsymbol{v}_{ps}^{*}\right)\cdot\boldsymbol{n}_{ps}\,d\Gamma_{ps}^{*} \tag{3.10b}$$

$$+\int_{\Gamma_{ps}^{*}}\alpha_1^{v}\boldsymbol{\Sigma}_{ps}'\cdot\boldsymbol{n}_{ps}d\Gamma_{ps}^{*}-\int_{\Omega_{ps}^{*}}\alpha_1^{v}\boldsymbol{B}_{ps}'dV_{ps}^{*}=0$$

$$\alpha_1^{u}T_1^{u}(\beta)=\frac{D^{*}}{D^{*}t_{ps}}\int_{\Omega_{ps}^{*}}\alpha_1^{u}\rho_{ps}\boldsymbol{U}_{ps}'\,dV_{ps}^{*}+\int_{\Gamma_{ps}^{*}}\alpha_1^{u}\rho_{ps}\boldsymbol{U}_{ps}'(\boldsymbol{v}_{ps}-\boldsymbol{v}_{ps}^{*})\cdot\boldsymbol{n}_{ps}\,d\Gamma_{ps}^{*} \tag{3.10c}$$

$$-\int_{\Omega_{ps}^{*}}\alpha_1^{u}\rho_{ps}\boldsymbol{V}_{ps}'dV_{ps}^{*}=0$$

where the dash " $'$ " signifies derivative with respect to β and note that these equations have a similar appearance to their corresponding counterparts in Eqs. (3.9).

Zeroth-order finite similitude requires that the integrands in Eqs. (3.9) do not vary with β and similarly for first order the integrands in Eqs. (3.10) are required to be invariant of β. An alternative but equivalent approach is the direct integration of identity Eq. (3.8).

Under the new definition zeroth-order finite similitude as discussed in Section 3.4 is identified by the identity $T_1^{\Psi}\equiv 0$. Recognising the reality of practical testing is scale effects and the inequality $T_1^{\Psi}\not\equiv 0$ and recognising the dependence $T_1^{\Psi}(\beta)$ motivates the need for something more suitable. Definition is designed to provide a pragmatic way forward in a situation where specific information on scale effects is absent. Since it is necessary to integrate the similitude identity to link experiments the

definition involving nested derivatives is particularly convenient. A desirable feature of the definition is the nesting of similitude orders, so if zeroth-order finite similitude ($T_1^{\Psi} \equiv 0$) applies, then first order ($T_2^{\Psi} \equiv 0$) immediately follows from Eq. (3.8). Yet another feature is apparent on examination of Eq. (3.8) arising from its foundation on transport equations in the trial space in the form $\alpha_0^{\Psi} T_0^{\Psi} = 0$, which immediately infers that $\alpha_1^{\Psi} T_1^{\Psi} = 0$ and consequently a different set of transport equations arise. The fields associated with this new set of transport equations are the derivatives of the fields in $\alpha_0^{\Psi} T_0^{\Psi} = 0$ with respect to β. This aspect is not pursued here as integration of Eq. (3.8) is ultimately required to relate experiments at different scales. The overall idea for three scales β_2, β_1 and $\beta_0 = 1$ is depicted in Fig. 3.3., where trial space behaviour is played out on the physical space at each scale. In the following section it is shown how projected equations are combined to provide a virtual replica of the full-scale process.

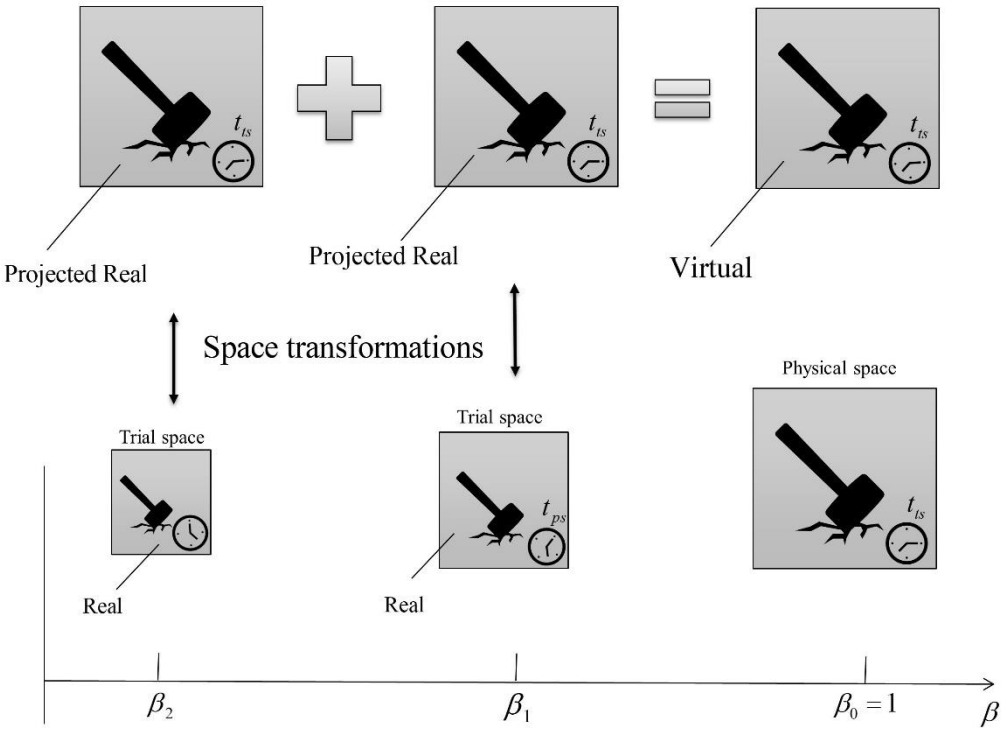

Figure 3.3. Projected trial-space behaviour described on a control volume at scale β_i by transport equations $\alpha_0^{\Psi} T_0^{\Psi}(\beta_i) = 0$ and combined to provide a full-scale virtual model.

3.5.2. Integrated similitude conditions

The reality of fracture-mechanics experimentation is discrete experiments at different scales, which invariably means that derivatives with respect to β are required to be evaluated by means of finite differences. There exist many forms finite differences can take but for down scaling with $0 < \beta \leq 1$ and considering that predicting the behaviour of systems at $\beta = 1$ is of prime importance, backward difference formulations naturally emerge. *First-order finite similitude* involves three scales β_2, β_1 and $\beta_0 = 1$, and the identity $T_2^{\Psi} = d\,(\alpha_1^{\Psi} T_1^{\Psi})/d\beta \equiv 0$. In order to evaluate this expression consider then the divided-difference table for $\alpha_0^{\Psi} T_0^{\Psi}$ with three data points $\{\beta_2, \beta_1, \beta_0\}$, where the first-divided difference and important mean-value identities (mean-value theorem for derivatives) are:

$$\alpha_1^{\Psi}|_{\widehat{\beta}_2^1} \frac{\alpha_0^{\Psi} T_0^{\Psi}(\beta_1) - \alpha_0^{\Psi} T_0^{\Psi}(\beta_2)}{\beta_1 - \beta_2} = \alpha_1^{\Psi}|_{\widehat{\beta}_2^1} T_1^{\Psi}\left(\hat{\beta}_2^1\right) \tag{3.11a}$$

$$\alpha_1^{\Psi}|_{\widehat{\beta}_1^o} \frac{\alpha_0^{\Psi} T_0^{\Psi}(\beta_0) - \alpha_0^{\Psi} T_0^{\Psi}(\beta_1)}{\beta_0 - \beta_1} = \alpha_1^{\Psi}|_{\widehat{\beta}_1^o} T_1^{\Psi}\left(\hat{\beta}_1^o\right) \tag{3.11b}$$

where $\beta_i \leq \hat{\beta}_i^{i-1} \leq \beta_{i-1}$ and bearing in mind that the next divided difference is

$$\frac{\alpha_1^{\Psi}|_{\widehat{\beta}_1^o} T_1^{\Psi}\left(\hat{\beta}_1^o\right) - \alpha_1^{\Psi}|_{\widehat{\beta}_2^1} T_1^{\Psi}\left(\hat{\beta}_2^1\right)}{\hat{\beta}_1^o - \hat{\beta}_2^1} \equiv 0 \tag{3.12}$$

which for first-order finite similitude is identically zero and on substitution of Eqs. (3.9) provides

$$\alpha_0^{\Psi} T_0^{\Psi}(\beta_0) \equiv \alpha_0^{\Psi} T_0^{\Psi}(\beta_1) + R_1^{\Psi}\left(\alpha_0^{\Psi} T_0^{\Psi}(\beta_1) - \alpha_0^{\Psi} T_0^{\Psi}(\beta_2)\right) \tag{3.13}$$

where the scaling parameter R_1^{Ψ} in this equation is

$$R_1^{\Psi} = \left(\frac{\alpha_1^{\Psi}|_{\widehat{\beta}_2^1}}{\alpha_1^{\Psi}|_{\widehat{\beta}_1^o}}\right)\left(\frac{\beta_0 - \beta_1}{\beta_1 - \beta_2}\right) \tag{3.14}$$

Examination of Eq. (3.13) reveals several important aspects. First, first-order finite similitude is about proportional relationships between the differences in the transport equations at different scales. Second, since $\alpha_0^{\Psi} T_0^{\Psi}(\beta_1) = 0$ and $\alpha_0^{\Psi} T_0^{\Psi}(\beta_2) = 0$ it immediately follows from Eq. (3.13) that $\alpha_0^{\Psi} T_0^{\Psi}(\beta_0) = 0$, i.e. a set of transport equations for the physical space is obtained. Note additionally if zeroth-order similitude applies, then Eq. (3.13) reduces to

$$\alpha_0^{\Psi} T_0^{\Psi}(\beta_0) \equiv \alpha_0^{\Psi} T_0^{\Psi}(\beta_1) \tag{3.15}$$

which is the expected form being the integrated form of Eq. (3.5).

3.5.3. First-order identities

Eq. (3.13) gives rise to a set of first order identities on application to Eqs. (3.4a) to (3.4c), which are:

$$\boldsymbol{v}_{ps} = \beta_1^{-1} g_1 \boldsymbol{v}_{ts1} + R_1^{\rho}(\beta_1^{-1} g_1 \boldsymbol{v}_{ts1} - \beta_2^{-1} g_2 \boldsymbol{v}_{ts2}) \tag{3.16a}$$

$$\boldsymbol{v}_{ps} = \beta_1^{-1} g_1 \boldsymbol{v}_{ts1} + R_1^{v}(\beta_1^{-1} g_1 \boldsymbol{v}_{ts1} - \beta_2^{-1} g_2 \boldsymbol{v}_{ts2}) \tag{3.16b}$$

$$\boldsymbol{\sigma}_{ps} = \alpha_{01}^{v} g_1 \beta_1^2 \boldsymbol{\sigma}_{ts1} + R_1^{v}\left(\alpha_{01}^{v} g_1 \beta_1^2 \boldsymbol{\sigma}_{ts1} - \alpha_{02}^{v} g_2 \beta_2^2 \boldsymbol{\sigma}_{ts2}\right) \tag{3.16c}$$

$$\boldsymbol{b}_{ps}^{v} = g_1^2 \beta_1^{-1} \boldsymbol{b}_{ts1}^{v} + R_1^{v}(g_1^2 \beta_1^{-1} \boldsymbol{b}_{ts1}^{v} - g_2^2 \beta_2^{-1} \boldsymbol{b}_{ts2}^{v}) \tag{3.16d}$$

$$\boldsymbol{u}_{ps} = \beta_1^{-1} \boldsymbol{u}_{ts1} + R_1^{u}(\beta_1^{-1} \boldsymbol{u}_{ts1} - \beta_2^{-1} \boldsymbol{u}_{ts2}) \tag{3.16e}$$

$$\boldsymbol{v}_{ps} = \beta_1^{-1} g_1 \boldsymbol{v}_{ts1} + R_1^{u}(\beta_1^{-1} g_1 \boldsymbol{v}_{ts1} - \beta_2^{-1} g_2 \boldsymbol{v}_{ts2}) \tag{3.16f}$$

and where $\boldsymbol{\sigma}_{ts1} = \boldsymbol{\sigma}_{ts}(\beta_1)$, $\boldsymbol{v}_{ts2} = \boldsymbol{v}_{ts}(\beta_2)$ etc. and a consistent velocity field requires $R_1^u = R_1^v = R_1^\rho$ and set to be R_1 henceforth.

Note that Eq. (3.16e) along with the identities $\boldsymbol{dx}_{ts1} = \beta_1 \boldsymbol{dx}_{ps}$ and $\boldsymbol{dx}_{ts2} = \beta_2 \boldsymbol{dx}_{ps}$ yield the small strain relationship

$$\boldsymbol{\varepsilon}_{ps} = \boldsymbol{\varepsilon}_{ts1} + R_1^{u}(\boldsymbol{\varepsilon}_{ts1} - \boldsymbol{\varepsilon}_{ts2}) \tag{3.17}$$

which confirms that to a limited degree, strain is permitted to be unequal in the trial and physical spaces, which is the reality in most physical experiments.

The identities pertaining to first-order finite similitude theory are summarised in Table 3.2 and revealed is that despite the initial complexity of the theory, relatively straightforward relationships are its product.

Table 3.2 Necessary and sufficient first-order scaling identities.

Eq. No.	Field	Scalars	Flux	Source
(3.4a)	$\boldsymbol{v}_{ts}^{*} = \beta g^{-1} \boldsymbol{v}_{ps}^{*}$	$\alpha_0^1 = \beta^{-3}$	-	-
(3.4b)	$\alpha_0^{\rho} \rho_{ts} \beta^3 = \rho_{ps}$	$\alpha_0^{\rho}(1) = 1$ $g(1) = 1$		
(3.4c)	$\boldsymbol{v}_{ps}$ $= \beta_1^{-1} g_1 \boldsymbol{v}_{ts1}$ $+ R_1 \left(\beta_1^{-1} g_1 \boldsymbol{v}_{ts1}$ $- \beta_2^{-1} g_2 \boldsymbol{v}_{ts2}\right)$	$\alpha_0^{v} = \alpha_0^{\rho} g \beta^{-1}$	$\boldsymbol{\sigma}_{ps}$ $= \alpha_{01}^{v} g_1 \beta_1^2 \boldsymbol{\sigma}_{ts1}$ $+ R_1 \left(\alpha_{01}^{v} g_1 \beta_1^2 \boldsymbol{\sigma}_{ts1}\right.$ $\left. - \alpha_{02}^{v} g_2 \beta_2^2 \boldsymbol{\sigma}_{ts2}\right)$	$\boldsymbol{b}_{ps}^{v}$ $= g_1^2 \beta_1^{-1} \boldsymbol{b}_{ts1}^{v}$ $+ R_1 \left(g_1^2 \beta_1^{-1} \boldsymbol{b}_{ts}^{v}\right.$ $\left. - g_2^2 \beta_2^{-1} \boldsymbol{b}_{ts2}^{v}\right)$
(3.4d)	$\boldsymbol{u}_{ps}$ $= \beta_1^{-1} \boldsymbol{u}_{ts1}$ $+ R_1 \left(\beta_1^{-1} \boldsymbol{u}_{ts1}\right.$ $\left. - \beta_2^{-1} \boldsymbol{u}_{ts2}\right)$	$\alpha_0^{u} = \alpha_0^{\rho} \beta^{-1}$		$\boldsymbol{v}_{ps}$ $= \beta_1^{-1} g_1 \boldsymbol{v}_{ts1}$ $+ R_1 \left(\beta_1^{-1} g_1 \boldsymbol{v}_{ts1}\right.$ $\left. - \beta_2^{-1} g_2 \boldsymbol{v}_{ts2}\right)$

3.6 Analytical fracture studies

This section is concerned with applying the new scaling concepts to two critical methods in fracture mechanics, i.e., the J-integral and the cohesive zone model. Depicted in Fig. 3.4 is the compact tension (CT) test, one of the most commonly used specimens in J-integral fracture mechanics, and forms the main focus of this section.

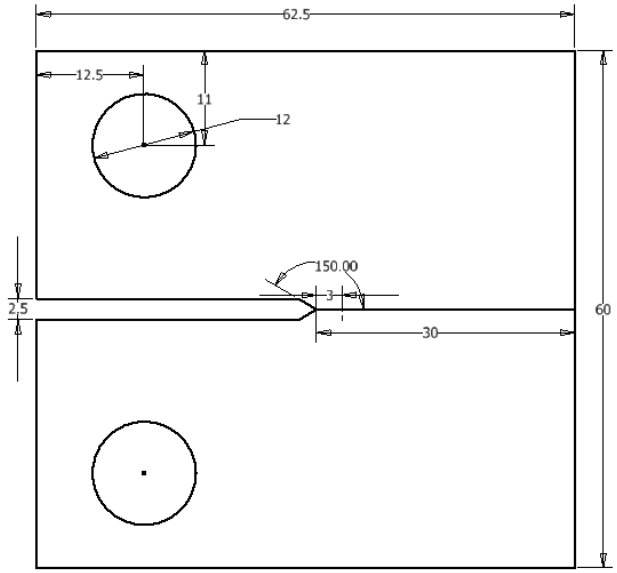

Figure 3.4. Typical testing arrangement for a compact tesion (CT) specimen.

3.6.1. The J-Integral

The J-integral on a moving control volume traversing a loaded body in equilibrium (in a trial space) with velocity $\boldsymbol{v}_{ts}^{*}$ is provided by Davey and Darvizeh in reference [101] in an extended form

$$J_{ts}^{*} = \int_{\Gamma_{ts}^{*}} \omega_{ts} \boldsymbol{v}_{ts}^{*} \cdot \boldsymbol{n}_{ts}\, d\Gamma_{ps}^{*} - \int_{\Gamma_{ts}^{*}} (\boldsymbol{v}_{ts}^{*} \cdot \nabla_{ts} \boldsymbol{u}_{ts}) \cdot \boldsymbol{\tau}_{ts}\, d\Gamma_{ts}^{*} \tag{3.18}$$

where ω_{ts} is strain-energy density and $\boldsymbol{\tau}_{ts}$ is traction (i.e. $\boldsymbol{\tau}_{ts} = \boldsymbol{\sigma}_{ts} \cdot \boldsymbol{n}_{ts}$), which yields the standard J-integral form [13] on setting $\boldsymbol{v}_{ts}^{*} = v_{ts}^{*} \boldsymbol{e}_i$ with $\boldsymbol{e}_i$ indicating the direction of crack travel and v_{ts}^{*} is a uniformly invariant speed.

Substitution of the identities $dV_{ts}^{*} = \beta^2 dV_{ps}^{*}$ and $\boldsymbol{d\Gamma}_{ts}^{*} = \beta \boldsymbol{d\Gamma}_{ps}^{*}$ (note 2-D here) and on multiplication throughout by g, β^{-1} and a scalar α_0^{ω}, gives rise to

$$\begin{aligned} \alpha_0^{\omega} g\beta^{-1} J_{ts}^{*} = & \int_{\Gamma_{ps}^{*}} \alpha_0^{\omega} \omega_{ts} \beta (g\beta^{-1} \boldsymbol{v}_{ts}^{*}) \cdot \boldsymbol{n}_{ps}\, d\Gamma_{ps}^{*} \\ & - \int_{\Gamma_{ps}^{*}} \alpha_0^{\omega} (\alpha_0^{v})^{-1} g^{-1} \beta^{-1} \left((g\beta^{-1} \boldsymbol{v}_{ts}^{*}) \cdot \nabla_{ps} \beta^{-1} \boldsymbol{u}_{ts} \right) \\ & \cdot \left(\alpha_0^{v} \beta^2 g \boldsymbol{\sigma}_{ts} \cdot \boldsymbol{n}_{ps} \right) d\Gamma_{ps}^{*} \end{aligned} \tag{3.19}$$

from which is can be deduced that $\alpha_0^{\omega} = \alpha_0^{v} g\beta = \alpha_0^{\rho} g^2$ and consequently invariance

of $\alpha_0^{\omega} g\beta^{-1} J_{ts}^*$ with respect to β (i.e. i.e. $\alpha_0^{\omega} g\beta^{-1} J_{ts}^* = J_{ps}^*$) requires $\alpha_0^{\omega}\beta\omega_{ts} = \alpha_0^{v} g\beta^2\omega_{ts} = \omega_{ps}$.

The standard J-integral J_{ts} satisfies the relationship $J_{ts}^* = v_{ts}^* J_{ts}$ and if invariant with respect to β, then $\alpha_0^{\omega} J_{ts} = J_{ps}$ with $\alpha_0^{\omega} = \alpha_0^{v} g\beta$. It is of interest to examine a relatively simple analytical example at this stage to demonstrate the scaling concepts on familiar material. Consider then a crack of length $2a_{ts}$ in an infinite plate, where in this case the J-integral in the absence of plasticity has a simple analytical solution, which is

$$J_{ts} = \frac{K_{I\,ts}^2}{E'_{ts}} = \pi a_{ts} \frac{\sigma_{ts}^2}{E'_{ts}} \tag{3.20}$$

where stress intensity $K_{I\,ts} = \sigma_{ts}\sqrt{\pi a_{ts}}$ and E'_{ts} represent Young's modulus E_{ts} or $E_{ts}/(1-\nu_{ts}^2)$, and where ν_{ts} is Poisson's ratio.

Consider then $\alpha_0^{\omega} J_{ts}$, which provides

$$\alpha_0^{\omega} J_{ts} = \alpha_0^{v} g\beta J_{ts} = \pi(\beta^{-1} a_{ts}) \frac{\left(\alpha_0^{v}\beta^2 g\sigma_{ts}\right)^2}{\alpha_0^{v}\beta^2 g E'_{ts}} \tag{3.21}$$

where for zeroth-order conditions (e.g. $\alpha_0^{v}\beta^2 g E'_{ts} = E'_{ps}$) it is evident that $\alpha_{01}^{\omega} J_{ts}(\beta_1) = J_{ps}$ and consequently a single trial-space experiment is sufficient.

However, observe that $\alpha_0^{\omega}\sqrt{\beta} K_{I\,ts} = \left(\alpha_0^{v}\beta^2 g\sigma_{ts}\right)\sqrt{\pi\beta^{-1} a_{ts}}$ and should zeroth-order apply, then $\alpha_0^{\omega}\sqrt{\beta} K_{I\,ts} = K_{I\,ps}$ but it is relatively easy to break zeroth-order conditions. Using the same material for a single-scaled experiment would be suffice since α_0^{v} is insufficient for the matching of the three material properties, i.e. $K_{Ic\,ts} = K_{Ic\,ps}$ (fracture toughness), $E_{ts} = E_{ps}$ and $\nu_{ts} = \nu_{ps}$ (and additionally yield stress if plasticity is involved). Additional flexibility is required, and first-order finite similitude provides greater scope for capturing the full-scale physical behaviour.

3.6.2. Analytical calculation of J

It is of interest to examine the situation of two scale experiments where the objective is the prediction of the onset of crack propagation in an infinite full-scale plate. The situation is depicted in Fig. 3.5 where the possibility of using three different materials is considered for the scale choices of $\beta_1 = \frac{1}{2}$ and $\beta_2 = \frac{1}{4}$, and the full-scale plate. The general concept presented in Fig. 3.3 is recreated in Fig. 3.5 for the specific case of a single crack subjected to a uniform stress field, where it is assumed here that the analytical result in Eq. (3.20) applies to the real scaled experiments. The test for success is how close the virtual model matches the full-scale real result, which again is assumed to comply with Eq. (3.20). Observe from Eq. (3.16c) and Fig. 3.5 that the products $\alpha_{01}^v g_1$ and $\alpha_{02}^v g_2$ appear, which confirms that g_1 and g_2 have no part to play in what is after all a quasi-static analysis. Changing g_2 (say) can be negated by changing α_{02}^v so that the product $\alpha_{02}^v g_2$ remains unchanged. As far as the selection of α_{01}^v and α_{02}^v is concerned, these are set to satisfy zeroth-order conditions for fracture toughness being zeroth-order scalars and consequently satisfy

$$\boldsymbol{\sigma}_{ps}^{crit} = \frac{K_{Ic\,ps}}{\sqrt{\pi a_{ps}}} = \alpha_{01}^v g_1 \beta_1^2 \boldsymbol{\sigma}_{ts}^{crit}(\beta_1) = \alpha_{01}^v g_1 \beta_1^2 \frac{K_{Ic\,ts}(\beta_1)}{\sqrt{\pi a_{ts1}}}$$

$$= \alpha_{02}^v g_2 \beta_2^2 \boldsymbol{\sigma}_{ts}^{crit}(\beta_2) = \alpha_{02}^v g_2 \beta_2^2 \frac{K_{Ic\,ts}(\beta_2)}{\sqrt{\pi a_{ts2}}} \tag{3.22}$$

with $a_{ts1} = a_{ts}(\beta_1) = \beta_1 a_{ps}$ and $a_{ts2} = a_{ts}(\beta_2) = \beta_2 a_{ps}$ and consequently

$$\alpha_{01}^v g_1 = \frac{\sqrt{\beta_1}}{\beta_1^2} \frac{K_{Ic\,ps}}{K_{Ic\,ts}(\beta_1)} \tag{3.23a}$$

$$\alpha_{02}^v g_2 = \frac{\sqrt{\beta_2}}{\beta_2^2} \frac{K_{Ic\,ps}}{K_{Ic\,ts}(\beta_2)} \tag{3.23b}$$

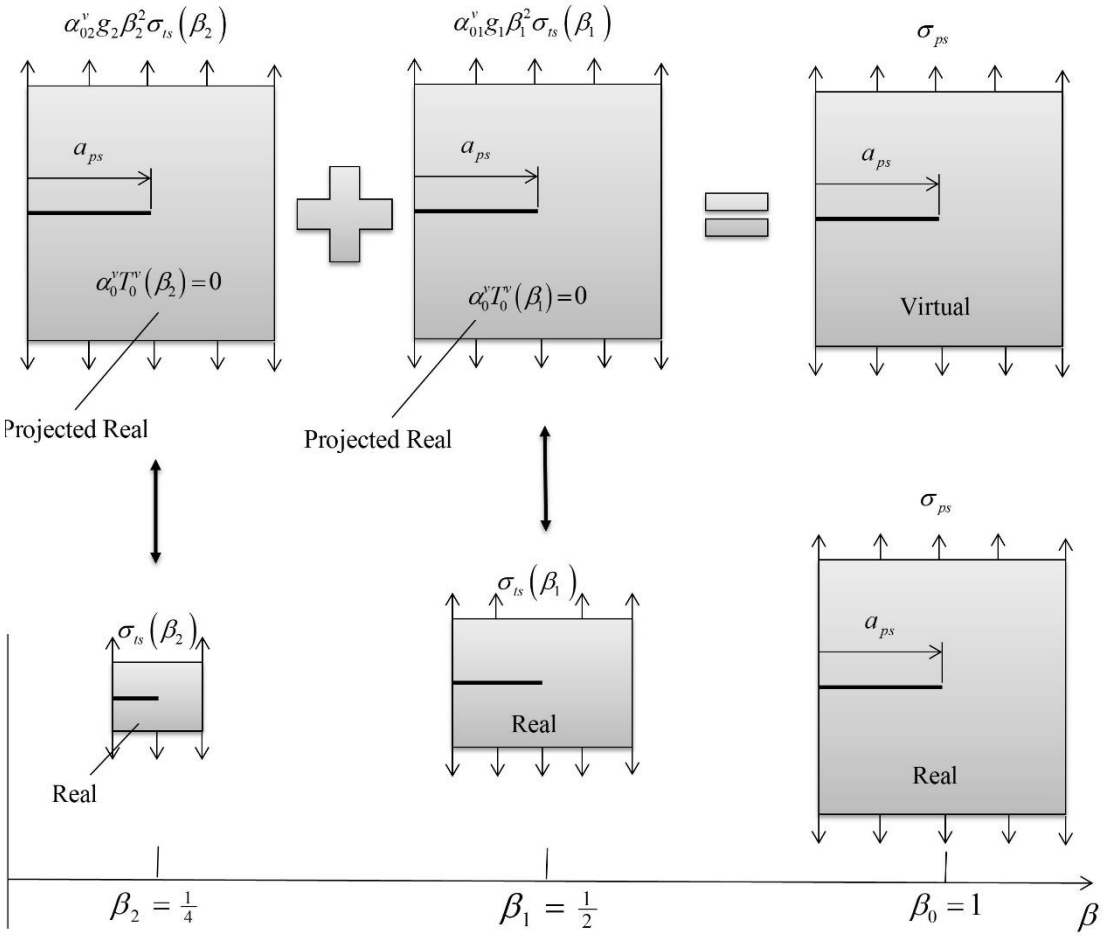

Figure 3.5. Portrayal of a side crack in an infinite plate subjected to a uniform stress field.

Note here that the zeroth-order conditions $\alpha_{01}^{\rho}\rho_{ts1}\beta_1^3 = \rho_{ps}$ and $\alpha_{02}^{\rho}\rho_{ts2}\beta_2^3 = \rho_{ps}$ along with $\alpha_{01}^{v} = \alpha_{01}^{\rho} g_1 \beta_1^{-1}$ and $\alpha_{02}^{v} = \alpha_{02}^{\rho} g_2 \beta_2^{-1}$ in Table 3.1 are not applied since density is not a feature of this simple problem. However, their inclusion has the not too unexpected consequence that time plays a part in the analysis. This follows because their incorporation constrains the values of α_{01}^{v} and α_{02}^{v} but Eq. (3.23) can still be satisfied provided g_1 and g_2 are free to be set. Observe that $\alpha_{01}^{v} g_1 = \alpha_{01}^{\rho} g_1^2 \beta_1^{-1}$ and $\alpha_{02}^{v} g_1 = \alpha_{02}^{\rho} g_2^2 \beta_2^{-1}$ and consequently on setting g_1 and g_2 equal to

$$g_1 = \sqrt{\frac{\beta_1^2\sqrt{\beta_1}}{\alpha_{01}^{\rho}\beta_1^3}\frac{K_{Ic\,ps}}{K_{Ic\,ts1}}} = \beta_1\sqrt{\sqrt{\beta_1}\frac{\rho_{ts1}}{\rho_{ps}}\frac{K_{Ic\,ps}}{K_{Ic\,ts1}}} \tag{3.24a}$$

$$g_2 = \sqrt{\frac{\beta_2^2\sqrt{\beta_2}}{\alpha_{02}^{v}\beta_2^3}\frac{K_{Ic\,ps}}{K_{Ic\,ts2}}} = \beta_2\sqrt{\sqrt{\beta_2}\frac{\rho_{ts2}}{\rho_{ps}}\frac{K_{Ic\,ps}}{K_{Ic\,ts2}}} \tag{3.24b}$$

ensures that Eqs. (3.23) are satisfied.

It is understood that although time is not a feature of quasi-static processes, it is of course a feature of real experiments. Here g_1 and g_2 informs on how the information from the two experiments are combined. Although inertia is not a feature of the quasi-static process and consequently material density is not involved necessarily it can still be incorporated on imagining the loading process to occur over a specified period. This period can be different at the two scales as indicated by $g_1 \neq g_2$.

It is evident from Eq. (3.20) that in order to be able to predict the J-integral at full scale by means of scaled experimentation it is necessary to say something about deformation and strain energy, reflected by the presence of Young's modulus in this equation. One approach is depicted in Fig. 3.6, which is essentially the situation in Fig. 3.5, with the cracks removed and the scales β_1 and β_2 assumed free.

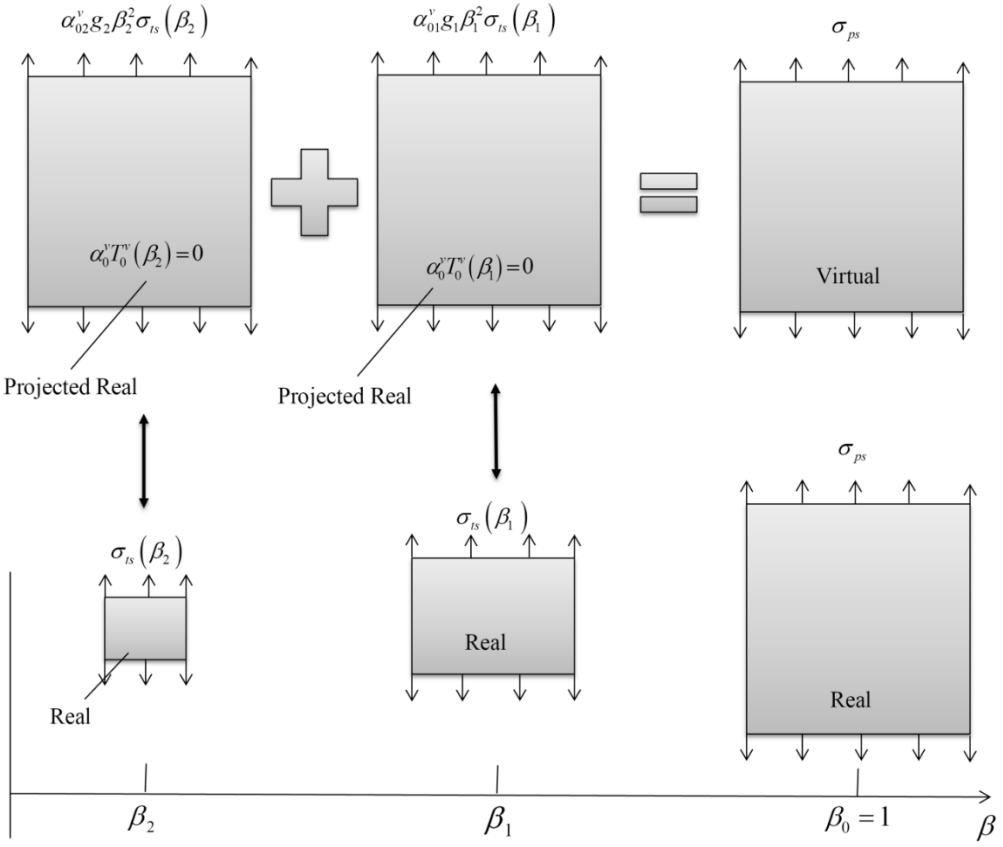

Figure 3.6 Imagined stress loading in the absence of a crack.

In this case at $\boldsymbol{\sigma}_{ps} = \boldsymbol{\sigma}_{ps}^{crit}$ the following zeroth-order conditions are assumed to apply

$$\boldsymbol{\sigma}_{ps}^{crit} = E'_{ps}\varepsilon_{ps}^{crit} = \alpha_{01}^{v} g_1 \beta_1^2 \boldsymbol{\sigma}_{ts1}^{crit} = \alpha_{01}^{v} g_1 \beta_1^2 E'_{ts1}\varepsilon_{ts1}^{crit} = \alpha_{02}^{v} g_2 \beta_2^2 \boldsymbol{\sigma}_{ts2}^{crit} = \alpha_{02}^{v} g_2 \beta_2^2 E'_{ps2}\varepsilon_{ts2}^{crit} \tag{3.25}$$

where it is assumed further that $\varepsilon_{ps}^{crit} = \varepsilon_{ts1}^{crit} = \varepsilon_{ts2}^{crit}$ and given that the conditions in Eqs. (3.23) apply it follows that

$$\alpha_{01}^{v} g_1 = \frac{\sqrt{\beta_1}}{\beta_1^2}\frac{K_{Ic\,ps}}{K_{Ic\,ts1}} = \frac{1}{\beta_1^2}\frac{E'_{ps}}{E'_{ts1}} \tag{3.26a}$$

$$\alpha_{02}^{v} g_2 = \frac{\sqrt{\beta_2}}{\beta_2^2}\frac{K_{Ic\,ps}}{K_{Ic\,ts1}} = \frac{1}{\beta_2^2}\frac{E'_{ps}}{E'_{ts2}} \tag{3.26b}$$

which leads to specific values of β_1 and β_2 depending on the material chosen, i.e. it provides

$$\beta_1 = \left(\frac{K_{Ic\,ts1}}{K_{Ic\,ps}}\frac{E'_{ps}}{E'_{ts1}}\right)^2 \tag{3.27a}$$

$$\beta_2 = \left(\frac{K_{Ic\,ts2}}{K_{Ic\,ps}}\frac{E'_{ps}}{E'_{ts2}}\right)^2 \tag{3.27b}$$

and since $\beta_2 \leq \beta_1$ these relationships require materials that satisfy $\frac{K_{Ic\,ts1}}{E'_{ts1}} \leq \frac{K_{Ic\,ts2}}{E'_{ts2}}$.

Thus, with the extra flexibility afforded the approach by allowing β_1 and β_2 to vary, zeroth-order matching is possible. Therefore, it is of interest to test a simple example consisting of three materials to represent the two trial and full-scale experiments.

The material properties for all the materials applied in this paper are tabulated in Table 3. Specifically, the materials considered are titanium (Ti6Al4V) [108-110], stainless steel (AISI 201), tungsten [111], steel (EN3B), copper (C101) and aluminium (6082). The material selection includes some generally used materials, rare and expensive materials, and strong and weak materials. This provided an opportunity for unusual comparisons as well as highlighting the practical value of the approach through the comparison of cheap and expensive materials.

The three materials selected here are given in Table 4 and consist of titanium, stainless and tungsten for physical and trial space at scales at β_1 and β_2, respectively. These three materials are stronger than the other three, which is supposed to have a better result in zeroth-order theory in the beginning. To identify the materials in the virtual

models the notation Ti-Ti, Ti-SS, Ti-Tung and Ti-SS-Tung is employed to signify that the full-scale material is titanium and the scaled materials are titanium, stainless or tungsten with Ti-SS-Tung signifying that first-order theory is employed with two trial-space experiments. Eq. (3.20) is applied to determine the J-integral for the virtual model, with length scales set by Eqs. (3.27) and $\alpha_{01}^{v} g_1$ and $\alpha_{02}^{v} g_2$ are calculated using Eqs. (3.26). As alluded to above however, this arrangement ensures that zeroth-order theory is sufficient and consequently $J_{ps} = \alpha_{01}^{v} g_1 \beta_1 \, J_{ts1}$ and $\alpha_{01}^{v} g_1 \beta_1 \, J_{ts1} = \alpha_{02}^{v} g_2 \beta_2 \, J_{ts2}$. The objective here is to predict the J-integral (at its critical value) at full scale which is known to satisfy Eq. (3.20). Examination of Table 4 confirms that the three combinations Ti-Ti, Ti-SS, Ti-Tung gives as expected the exact prediction for both E_{ps} and $J_{c\,ps}$, i.e. 120 GPa and 100.8 kJ/m^2, respectively, as tabulated for titanium in the first row of Table 3.3.

Table 3.3 Materials properties used in the paper.

Material	E (GPa)	σ_Y (MPa)	σ_{TS} (MPa)	K_{IC} (GPa m$^{\frac{1}{2}}$)	G_c (kJ/m^2)	v (Poisson ratio)
Titanium	120	812	1077	110	100.8	0.36
Stainless	200	881	1206	100	50.0	0.30
Steel	190	324	491	50	13.2	0.29
Tungsten	410	1123	1255	150	54.9	0.28
Copper	130	92	243	30	11.7	0.34
Aluminium	70	98	370	30	12.9	0.35

Table 3.4 Virtual material properties for three material combination.

i	Material	β_i	$J_c = \frac{K_{Ic}^2}{E}$ (kJ/m^2)	$\alpha_{0i}^{v} g_i$	Virtual Properties		
					E_{ps} (GPa)	$J_{c\,ps}$ (kJ/m^2)	Mat. type
0	Titanium (ps)	1	100.8	1	120	100.8	Ti-Ti
1	Stainless (ts)	0.2975	50.0	6.78	120	100.8	Ti-SS
2	Tungsten	0.1593	54.9	11.53	120	100.8	Ti-Tung

	(ts)						

As a further check on the analytical study each of the three CT specimens at the length scales and materials specified in Table. 3.2 are re-evaluated numerically with the commercial code Abaqus. This involved meshing three CT specimens that are scaled versions of the model depicted in Fig. 3.4. The top circle depicted in Fig. 3.4 is displacement by 0.25 mm in the physical space (to ensure elasticity) with the bottom circle is fixed in all directions. The J-integrals in this instance were determined using the facility within Abaqus and the results are provided in Table 3.5.

Table 3.5 Numerical J-integral comparison between the virtual and numerical models.

i	Material	β_i	$J_{ts}(\beta_i)$ $(\mathrm{kJ/m^2})$	$\alpha_{0i}^{v} g_i$	Virtual		
					E_{ps} (GPa)	J_{ps} $(\mathrm{kJ/m^2})$	Mat. type
0	Titanium (ps)	1	13.1	1	120	13.1	Ti-Ti
1	Stainless (ts)	0.2975	6.2	6.78	120	13.1	Ti-SS
2	Tungsten (ts)	0.1593	6.2	11.53	120	13.1	Ti-Tung

The results confirm the veracity of the theory for predicting J-integrals with scaled tests for the CT specimens, although the analysis is limited here to linear elastic fracture mechanics. Further details on the numerical simulation are provided in subsequent sections, where elastic-plastic fracture mechanics is considered.

3.6.3. Cohesive zone model

The cohesive zone model represents damage that results in fracture by means of a single failure usually along a predefined path or along element edges in any finite element analysis. The most rudimentary cohesive model is identified by a traction-separation curve consisting of three properties, which are critical stress σ_c, critical separation δ_c and the area under the curve G_c, which is the cohesive fracture energy. In the simplest linear case $G_c = 0.5\sigma_c\delta_c$ and it is evident that the three properties are related. The J-integral property $J_c = G_c$ suggests that $\alpha_0^{\omega} G_{ts}$ should be considered for the purpose of scaling. Note that

$$\alpha_0^{\omega} G_{c\,ts} = \alpha_0^{v} g \beta G_{c\,ts} = \frac{1}{2}\left(\alpha_0^{v} \beta^2 g \sigma_{c\,ts}\right)\left(\beta^{-1} \delta_{c\,ts}\right) \tag{3.28}$$

where it is apparent that for zeroth-order scaling to apply, critical material properties must be changed.

However, theoretically the critical separation δ_c would be affected by β, and ultimately stress σ_c will not changed with β for the same material, which makes G_c affected by β but it should not be. This provides a conflict in zeroth-order theory and leads to the need of high-order theories.

In order to gain some insight into the response of a cohesive element under scaling it is of interest to consider 1-D rod (see ref. [112]) represented by a linear spring and linear cohesive model as depicted in Fig. 3.7.

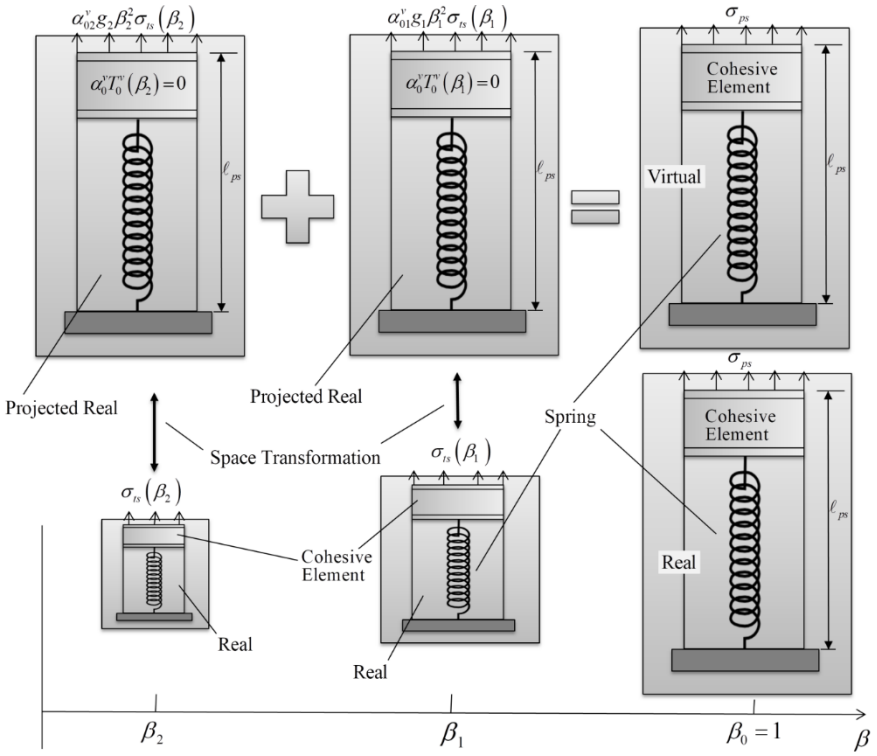

Figure 3.7 Scaling of rod presented by a spring and cohesive element.

Consider then a rod of length ℓ_0 and area A_0 that is subjected a displacement δ at the free end with its lower end fixed. The behaviour of all the real experiments in Fig. 3.7 is linear extension followed by linear unloading once the critical stress σ_c is attained. The total extension of the rod is $\delta = \delta^{el} + \delta^{coh}$ with uniaxial applied stress $\sigma =$

$\sigma^{el} = \sigma^{coh}$, with $\delta^{el} = \frac{\sigma^{el}\ell_0}{E}$ and when meaningful $\sigma^{coh} = \sigma_c \left(1 - \frac{\delta^{coh}}{\delta_c}\right)$, where E is Young's modulus, δ^{el} and δ^{coh} are the extensions arising from the spring and cohesive element, respectively. Note that the equilibrium condition $\sigma^{el} = \sigma^{coh}$ provides the expression:

$$\frac{\sigma}{\sigma_c} = \begin{cases} \dfrac{\delta}{\delta_c^{el}} & \text{if} \quad 0 \le \delta \le \delta_c^{el} \\ \left(1 - \dfrac{\delta_c^{el}}{\delta_c}\right)^{-1}\left(1 - \dfrac{\delta}{\delta_c}\right) & \text{if} \quad \delta_c^{el} < \delta \le \delta_c \end{cases} \tag{3.29}$$

where $\delta_c^{el} = \frac{\sigma_c \ell_0}{E}$ and it is assumed that this equation applies to each of the real experiments in Fig. 3.7; in particular ℓ_0 takes up the values ℓ_{ps}, $\beta_1\ell_{ps}$, and $\beta_2\ell_{ps}$ for each of the lengths of the rods.

The focus of interest is the behaviour of the full-scale virtual model depicted in Fig. 8. The scaling theory does not provide explicit function relationships of the type in Eq. (3.29) as it supplies both the stress σ_{ps} and the displacement $u_{ps} = \delta_{ps}$ by means of Eqs. (3.16c) and (3.16e), respectively. The issue alluded to above with regards to G_c being dependent on β is made explicit here since with σ_c and E fixed for the same material, then $\delta_c^{el} = \frac{\sigma_c}{E}\ell_0$ will scale with the specimen size and consequently, so must δ and δ_c for Eq. (3.29) to remain unchanged. Unfortunately, this provides a contradiction since $G_c = 0.5\sigma_c\delta_c$, which means G_c scales with length also. As this is not the case σ_c and δ_c must be allowed to vary (for zeroth-order finite similitude) and this aspect in many respects highlights the problem faced in the literature with setting σ_c (or δ_c) with these types of element. Thus for zeroth-order scaling with $\sigma_{ps} = \alpha_{01}^{v} g_1 \beta_1^2 \sigma_{ts1}$ and $u_{ps} = \beta_1^{-1} u_{ts1}$ it is clear that with all displacement and stress terms in Eq. (3.29) behaving like $\delta_{ps} = \beta_1^{-1}\delta_{ts1}$ and $\sigma_{ps} = \beta_1\ \sigma_{ts1}$ (i.e. $\alpha_{01}^{v} g_1 = \beta_1^{-1}$), then $G_{c\,ts} = G_{c\,ps}$ and successful zeroth-order scaling is possible.

It is interest to examine two different materials for trial space models and two cases

are considered (i) $G_{c\,ts1} = G_{c\,ts2}$, $\beta_1\ E_{c\,ts1} = \beta_2\ E_{c\,ts2}$ and (ii) $\beta_1^{-1} G_{c\,ts1} = \beta_2^{-1} G_{c\,ts2}$, $E_{c\,ts1} = E_{c\,ts2}$; in both cases it is assumed $\beta_1 = \frac{1}{2}$ and $\beta_2 = \frac{1}{4}$. The zeroth-order condition $\alpha_{01}^{v} g_1 \beta_1^2 E_{ts1} = \alpha_{02}^{v} g_2 \beta_2^2 E_{ts2}$ is satisfied in (i) with $\alpha_{01}^{v} g_1 = \beta_1^{-1}$ and $\alpha_{02}^{v} g_2 = \beta_2^{-1}$ and (ii) with $\alpha_{01}^{v} g_1 = \beta_1^{-2}$ and $\alpha_{02}^{v} g_2 = \beta_2^{-2}$. The parameters for the two cases are tabulated in Table 6 in dimensionless form and the arrangements are depicted in Fig. 3.8. Examination of the figure reveals how the real behaviours are projected and then combined to form virtual models. In this case, to keep things reasonably simple, the arrangement is confined to zeroth-order constructs with more complex problems (involving plasticity) being presented in the following section.

Table 3.6 Test parameters for scaled cohesive elements

Test Case	$\frac{G_{c\,ts1}}{G_{c\,ts2}}$	$\frac{E_{ts1}}{E_{ts2}}$	$\frac{\sigma_{c\,ts1}}{\sigma_{c\,ts2}}$	$\frac{\delta_{c\,ts1}}{\delta_{c\,ts2}}$	$\frac{\ell_{ts1}}{\ell_{ts2}}$	$\frac{\delta_{c\,ts1}^{el}}{\delta_{c\,ts2}^{el}}$
(i)	1	0.5	0.5	2	2	2
(ii)	2	1	1	2	2	2

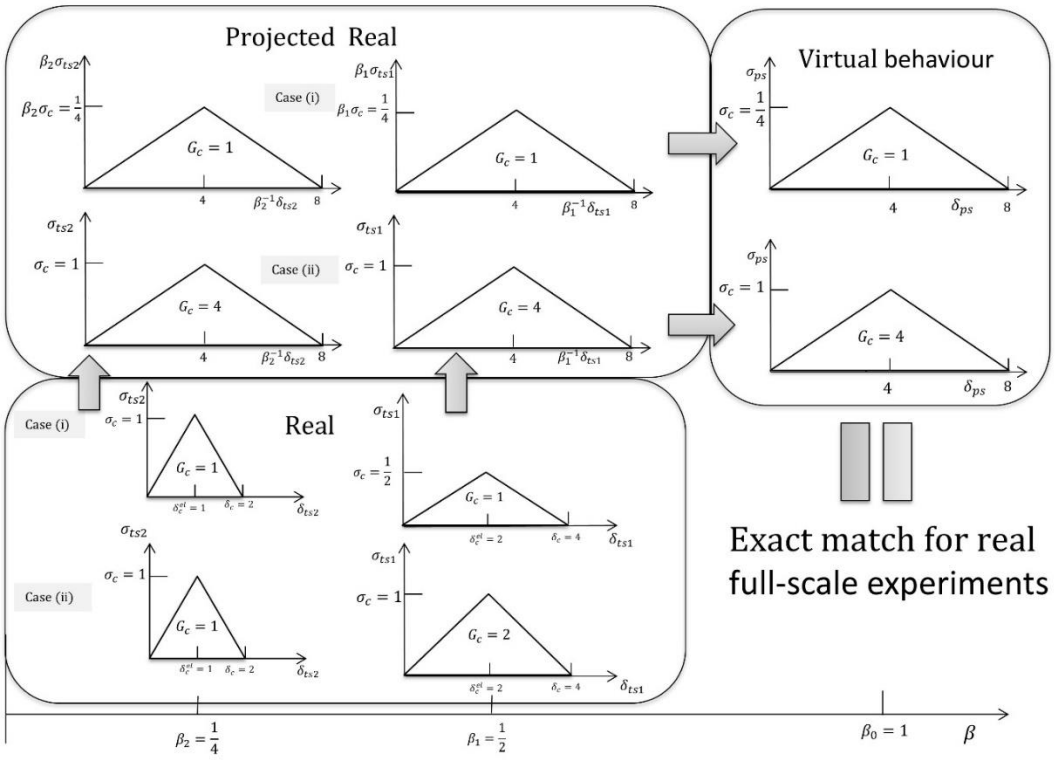

Figure 3.8 The construction of virtual cohesive models for two test-case materials

3.7 Non-linear material selection

All the examples considered above are for linear materials and it is of interest to involve plasticity for physical modelling and examine how scaling parameters are set. Stress and strain are the principal focus here and the solution of

$$\boldsymbol{\sigma}_{ps} = \alpha_{01}^{v} g_1 \beta_1^2 \boldsymbol{\sigma}_{ts1} + R_1 \left(\alpha_{01}^{v} g_1 \beta_1^2 \boldsymbol{\sigma}_{ts1} - \alpha_{02}^{v} g_2 \beta_2^2 \boldsymbol{\sigma}_{ts2} \right) \tag{3.30a}$$

$$\boldsymbol{\varepsilon}_{ps} = \boldsymbol{\varepsilon}_{ts1} + R_1 \left(\boldsymbol{\varepsilon}_{ts1} - \boldsymbol{\varepsilon}_{ts2} \right) \tag{3.30b}$$

which are Eqs. (3.14c) and (3.15) reproduced here for readability sake.

The scaling parameters α_{01}^{v} and α_{02}^{v} are set here based on zeroth-order conditions followed subsequently with the setting of R_1 . The way this is achieved is to target critical material properties in the physical space and consider a scenario where Eqs. (3.30) can be set. To aid in this analysis it is useful first to reduce Eqs. (3.30), which are tensorial relationships, into scalar equations. This is achieved here with a proportional-fields concept, where the following relationships are assumed:

$$\boldsymbol{\sigma}_{ts1} = \hat{a}_1 \boldsymbol{\sigma}_{ps} \tag{3.31a}$$

$$\boldsymbol{\sigma}_{ts2} = \hat{a}_2 \boldsymbol{\sigma}_{ps} \tag{3.31b}$$

$$\boldsymbol{\varepsilon}_{ts1} = \hat{b}_1 \boldsymbol{\varepsilon}_{ps} \tag{3.31c}$$

$$\boldsymbol{\varepsilon}_{ts2} = \hat{b}_2 \boldsymbol{\varepsilon}_{ps} \tag{3.31d}$$

which on substitution into Eqs. (3.30) provide

$$1 = \alpha_{01}^{v} g_1 \beta_1^2 \hat{a}_1 + R_1 \left(\alpha_{01}^{v} g_1 \beta_1^2 \hat{a}_1 - \alpha_{02}^{v} g_2 \beta_2^2 \hat{a}_2 \right) \tag{3.32a}$$

$$1 = \hat{b}_1 + R_1 \left(\hat{b}_1 - \hat{b}_2 \right) \tag{3.32b}$$

which are the sought scalar equations, where $\hat{a}_1$, $\hat{a}_2$, $\hat{b}_1$ and $\hat{b}_2$ are dimensionless parameters.

It is important to appreciate here that the assumed proportional form of Eqs. (3.31) does not constrain the governing fields to be proportional since the purpose of Eqs.

(3.32) is limited to the determination of scaling parameters. The determination of these dimensional parameters transpires to be relatively straightforward. In the case of zeroth-order theory with one trial experiment a simple process would be to consider synchronised uniaxial tests in both the trial space and physical space. At the point when both bars reach yield stresses Y_{ts1}, Y_{ps} and yield strains $\varepsilon_{ts1}^{Y} = \frac{Y_{ts1}}{E_{ts1}}$, $\varepsilon_{ps}^{Y} = \frac{Y_{ps}}{E_{ps}}$, then Eqs. (3.32) reduce to $1 = \alpha_{01}^{v} g_1 \beta_1^2 \hat{a}_1$ and $1 = \hat{b}_1$ with $\hat{a}_1 = \frac{Y_{ts1}}{Y_{ps}}$ and $\hat{b}_1 = \frac{\varepsilon_{ts1}^{Y}}{\varepsilon_{ps}^{Y}}$, which provides the means to set $\alpha_{01}^{v} g_1$, ie $\alpha_{01}^{v} g_1 \beta_1^2 = \frac{1}{\hat{a}_1} = \frac{Y_{ps}}{Y_{ts1}}$. Strains match, for zeroth-order finite similitude, which is precisely what is inferred by the equation $\hat{b}_1 = 1$ or equivalently $\varepsilon_{ts1}^{Y} = \varepsilon_{ps}^{Y}$, which gives $\frac{Y_{ts1}}{E_{ts1}} = \frac{Y_{ps}}{E_{ps}}$ or $E_{ps} = E_{ts1}\frac{Y_{ps}}{Y_{ts1}}$. As regards first order, the zeroth-order conditions $\hat{a}_1 = \frac{Y_{ts1}}{Y_{ps}}$, $\hat{a}_2 = \frac{Y_{ts2}}{Y_{ps}}$, $1 = \alpha_{01}^{v} g_1 \beta_1^2 \hat{a}_1$ and $1 = \alpha_{02}^{v} g_2 \beta_2^2 \hat{a}_2$ are assumed to apply making $\alpha_{02}^{v} g_2 \beta_2^2$ and $\alpha_{01}^{v} g_1 \beta_1^2$ known. To determine R_1, Eq. (3.32a) is reused, where in this case mean values for stress are utilised. This approach enables the effect of material work hardening to be accommodated and the method was first introduced in reference [106] although limited to zeroth-order problems in that case. The mean-value is defined to be

$$\bar{\sigma} = \frac{1}{\varepsilon^{max}} \int_0^{\varepsilon^{max}} \sigma d\varepsilon \tag{3.33}$$

where ε^{max} is taken from the material stress-strain curves used in the experiments; these are depicted in Fig. 3.9 with is ε^{max} indicated for the materials introduced in Table 3.3. Note from the figure that ε^{max} is limited to 0.1 for materials with strain ranges greater than that for titanium.

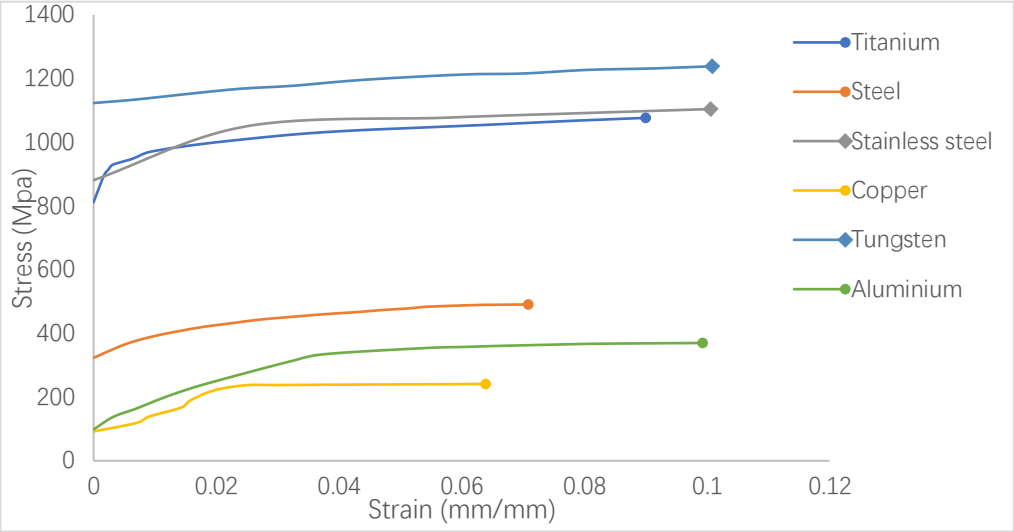

Figure 3.9 Strain-hardening curves for materials listed in Table 1.

With the application of Eq. (3.33) it follows that Eq. (3.32a) can be rearranged to give

$$R_1 = \frac{1 - \alpha_{01}^{v} g_1 \beta_1^2 \hat{a}_1}{\alpha_{01}^{v} g_1 \beta_1^2 \hat{a}_1 - \alpha_{02}^{v} g_2 \beta_2^2 \hat{a}_2} \tag{3.34}$$

where in this case $\hat{a}_1 = \frac{\bar{\sigma}_{ts1}}{\bar{\sigma}_{ps}}$, $\hat{a}_2 = \frac{\bar{\sigma}_{ts2}}{\bar{\sigma}_{ps}}$, and where it is appreciated that this approach for the determination of the scaling parameters is one of many possibilities; no attempt is made here to determine the length scales β_1 and β_2, which are set here to be $\beta_1 = \frac{1}{2}$ and $\beta_2 = \frac{1}{4}$.

3.7.1. Zeroth-order material selection

The materials presented in Table 3 are utilised as trial materials with titanium being the material chosen for the physical model. The objective here is to examine how well material choices for the trial space capture the uniaxial behaviour of titanium.

Table 3.7 Zeroth-order virtual material properties with yield-stress targeting and $\beta_1 = \frac{1}{2}$.

Material	Yield stress (MPa)	$\alpha_{01}^{v} g_1$	Virtual Material	Virtual material properties	
				Yield stress (MPa)	Young's Modulus E (GPa)

Titanium (PS)	812	4	Ti-Ti	812	120
Stainless steel (TS)	881	3.69	Ti-SS	812	120
Steel (TS)	324	10.04	Ti-S	812	120
Tungsten (TS)	1123	2.89	Ti-Tung	812	120
Copper (TS)	92	35.25	Ti-C	812	120
Aluminium (TS)	98	30.03	Ti-Al	812	120

Recall that a virtual-material model is produced by targeting selected materials properties (e.g. yield stress) of titanium where in the case stainless steel as the trial material it is noted as Ti-SS. The scaling parameters $\alpha_{01}^{v} g_1$ for each of the material combinations are presented in Table 3.7, where it is apparent that the virtual materials match both the yield stress and Young's modulus of titanium. As the objective is J-integral simulation, when the LEFM parts are matched after material synchronization, the main factor that affects the elastic-plastic J-integral should be the strain-hardening curves between physical and virtual materials. The non-linear J-integral cannot be directly synchronized in the output. For this reason, materials properties are first synchronized, which aims to produce virtual materials with a close strain-energy density to the physical material (the area under the strain-hardening curves).

The stress strain curves for titanium and the virtual material can be found in Fig. 3.10, where large deviations are apparent for some combinations. The virtual material model Ti-SS gives the closest match with Ti-Al providing the worst. The issue here is that although yield stress and Young's modulus match, there is mismatch in strain hardening and with zeroth-order theory there is no practical solution to this dilemma.

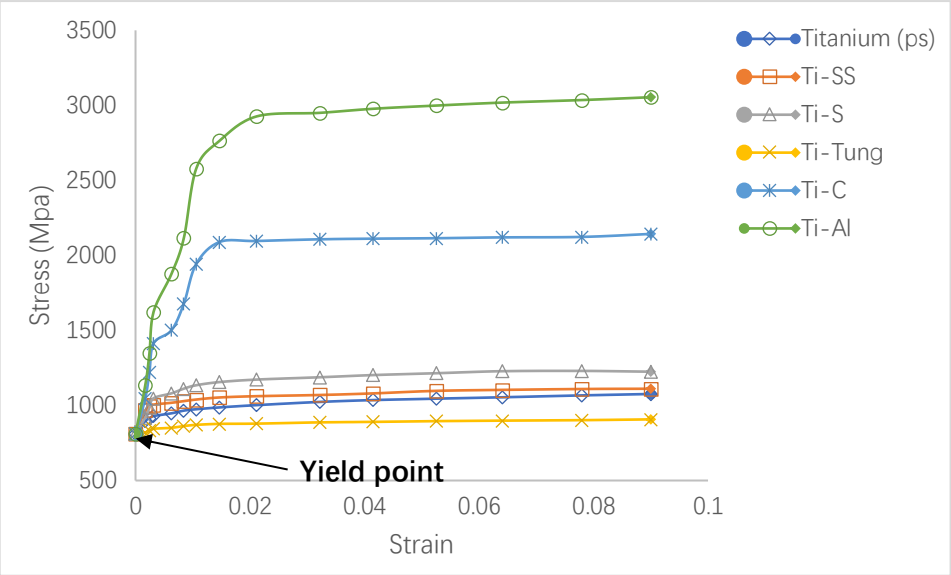

Figure 3.10 Stress-hardening curves for virtual models targeting titanium yield stress.

Table 3.8 First-order virtual material properties with $\beta_1 = \frac{1}{2}$. and $\beta_2 = \frac{1}{4}$.

Material	ε_{max}	Mean stress (MPa)	$\alpha_{01}^{v} g_1$ ($\beta_1 = \frac{1}{2}$)	$\alpha_{02}^{v} g_2$ ($\beta_2 = \frac{1}{4}$)	Virtual Material	R_1	Virtual properties	
							Mean stress (MPa)	Yield stress (MPa)
Titanium (PS)	0.09	1026	4	16	Ti-SS-S	-0.386	1022	812
Stainless steel (TS)	0.10	1051	3.69	14.76	Ti-SS-C	-0.647	1013	812
Steel (TS)	0.07	445	10.04	40.16	Ti-SS-Tung	0.539	1023	812
Tungsten (TS)	0.10	1194	2.89	11.56	Ti-S-C	0.124	1039	812
Copper (TS)	0.06	210	35.25	141.0	Ti-C-Tung	-0.835	1010	812
Aluminium (TS)	0.10	312	30.03	120.12	Ti-SS-Al	-0.035	1014	812

Considering the results presented in Fig. 3.10 it is of interest to examine what improvement can be made on the application of first-order theory to the materials in Table 3.8.

3.7.2. First-order material selection

Following the procedure outlined above, both $\alpha_{01}^{v} g_1$ and $\alpha_{02}^{v} g_2$ are determined on targeting the yield stress and are tabulated in Table 3.8. Additionally, R_1 is evaluated based on Eq. (3.34) with the objective of matching the mean stress for titanium. The properties of real and virtual materials are provided in Table 6 and stress-strain curves over the strain range for titanium are depicted in Fig. 3.11. On contrasting Figs. (3.10) and (3.11) it is apparent just how marked the improvements are with significantly reduced disparity between the titanium and all other curves. A perfect match is not revealed but the improvement brought about by an additional trial experiment is demonstrable.

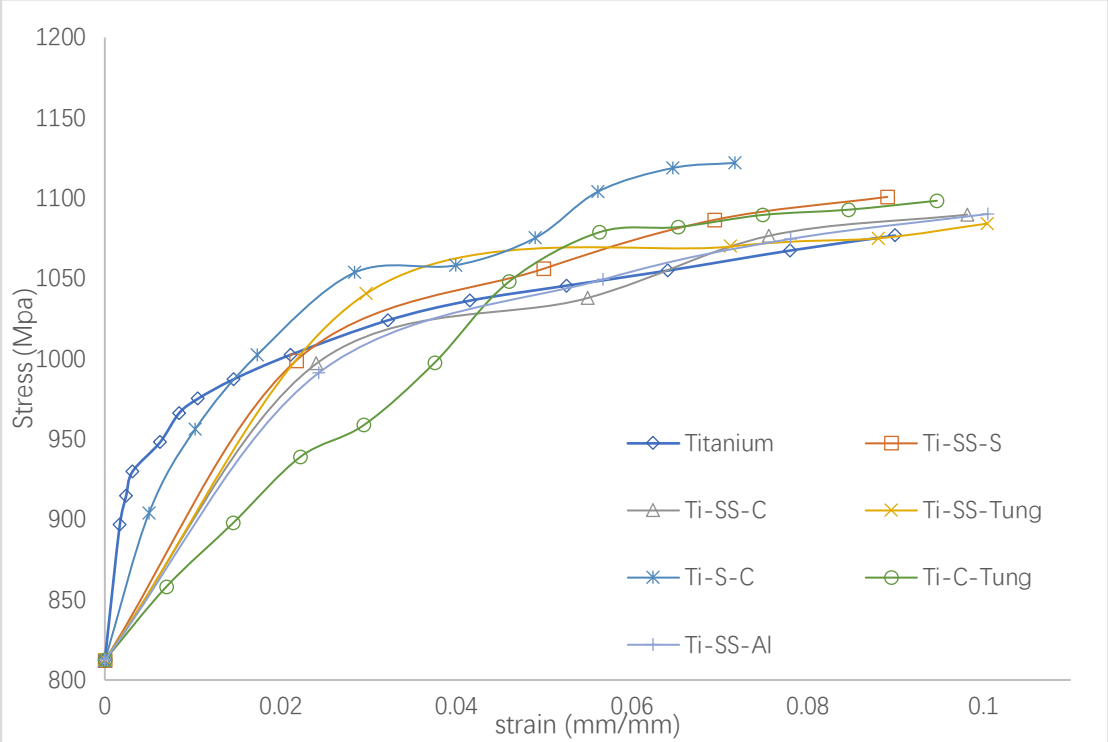

Figure 3.11 Strain-hardening curves for virtual materials over the strain range for titanium.

3.8 Test specimen analysis (numerical)

The virtual materials of Section 3.7 are tested numerically using the commercial finite element package Abaqus. The context of the study is physical modelling with a view of examining how one (zeroth order) or two (first order) modelling materials can be

used to predict the behaviour of a full-scale model. Practical experimental trials would replace the numerical models, but the focus here is on confirming the validity of the finite similitude approach, and numerical simulation is sufficient for that purpose. For this purpose, the virtual materials are applied to finite element models with contour integral, where the J-integral value can be directly read. As the outputs of the models can represent the material behaviour, the comparison in J-integral production between physical and virtual models can prove the applicability of the finite similitude process. Two relatively simple classical elastic-plastic fracture mechanics problems are considered; these are the quasi-statically loaded 2D compact-tension (CT) specimen along with the 3D three-point bending (TPB) problem. The evaluation of the J-integral is the focus using the inbuilt facility within the Abaqus software and the evaluation of the zeroth and first-order theories.

3.8.1. Compact tension and bending models

The compact tension specimen depicted in Fig. 3.4 is meshed and loaded in the manner depicted in Fig. 3.12, where a displacement of 2mm is applied to initiate plastic behaviour. The mesh consists of 4-noded continuum plane-stress elements (CPS4R).

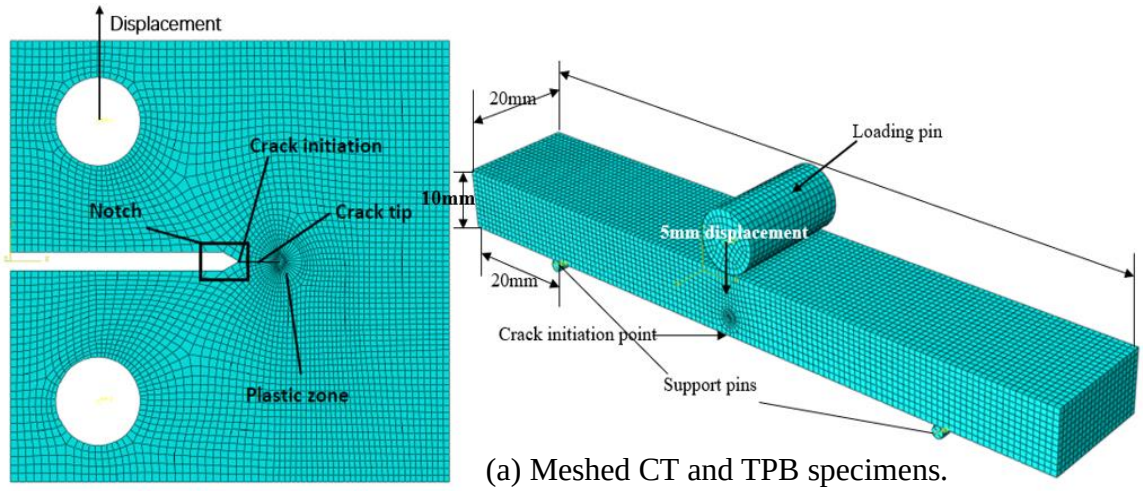

(a) Meshed CT and TPB specimens.

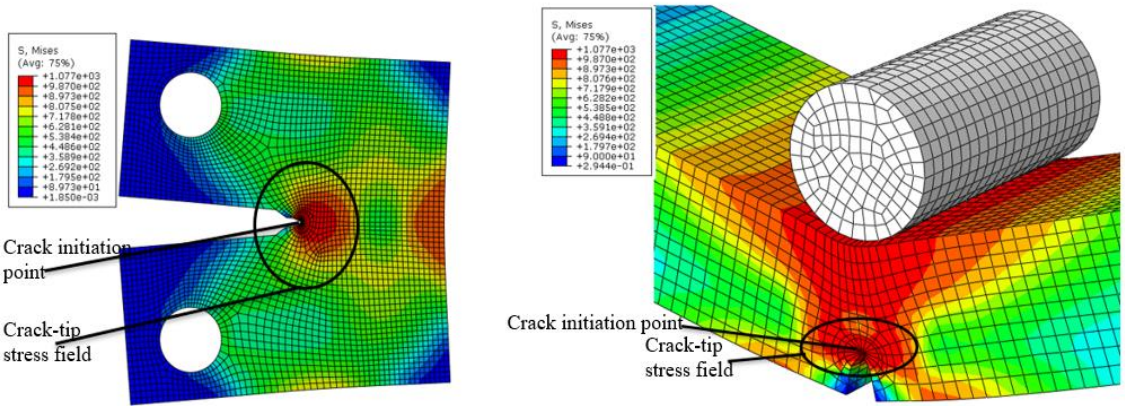

(b) Stress levels for deformed CT and TPB full-scale titanium models.

Figure 3.12 CT and TPB specimens used in finite similitude analysis.

Similarly, a three-point bending model specimen consisting of a beam with dimensions 10mm height, 120mm length (between loading points) and 20mm depth is depicted in Fig. 3.12(a) along with the Abaqus model highlighting the mesh used in the analysis. In this case the loading pin is displaced 5mm to induce plastic behaviour, and 8-noded continuum 3D stress elements (C3D8R) form the mesh. The results of the Abaqus simulation for the CT and TPB specimens for titanium are depicted in Fig. 3.12(b), where not unexpectedly high stress levels are apparent at the crack tip.

3.8.2. Virtual material models

The finite similitude theory does not require the formulation of constitutive models as the stress and strain fields are directly provided by Eqs. (3.28). It is of interest

nonetheless in view of the uniaxial data in Fig. 3.11 and the ease at which Abaqus accepts discrete data to form a multi-axial constitutive law based on equivalent stress and strain. Incorporation of the data in Fig. 3.11 and the running of Abaqus readily facilitates the determination of J-integrals. In the case of the CT and TPB specimens depicted in Fig. 3.12, fifteen contours are located around each of the plastic zones and the results on the averaging fourteen of these are provided in Table 3.9 for both zeroth and first-order material models. Each model is aiming to capture the full-scale J-integral values for titanium (i.e. CT (570.4 kJ/m^2), TPB (746.9 kJ/m^2)) and as revealed in the table the virtual material Ti-S-C provides the closest result.

The first purpose of the numerical tests is to show the validity of finite similitude theory by exploring the prediction of outputs with synchronised inputs. When input synchronisation is available, it can also work for outputs. The criterion for validation of the scaling experiments is determined, by the average error between different materials in elastic-plastic stress. Results are deemed acceptable if the output errors are lower than 5%. Under this condition, the first-order results are all acceptable, showing the scaling theory's efficacy. It is evident on examination of Table 3.9 that first-order provides a significant improvement on the zeroth-order predictions. For zeroth-order, most results are not acceptable, especially copper and aluminium. It can be explained that these two materials are significantly weaker than others, as also shown in Fig.3.10 with the curves of Ti-C and Ti-Al. Considering the results of stainless steel, which is closest to titanium from the beginning, the scaling experiment between different materials should have two materials with relative strength. Furthermore, comparing the curves and data in Figs. 3.10 and 3.11 and Table 3.9 can find an expected behaviour between inputs and outputs, which shows the rationality of the test.

Table 3.9 Results of numerical simulations of J-integral.

	Material	J-integral for CT (kJ/m^2)	Error in CT test	J-integral for TPB (kJ/m^2)	Error in TPB test
Physical (real)	Titanium	570.4	-	746.9	-

Zeroth order (virtual)	Ti-SS	584.4	2.5%	824.2	10.3%
	Ti-S	606.2	6.3%	780.8	4.5%
	Ti-C	714.4	25.2%	952.8	27.6%
	Ti-Tung	533.3	6.5%	693.8	7.1%
	Ti-Al	758.1	32.9%	994.3	33.1%
First order (virtual)	Ti-SS-S	547.0	4.1%	712.8	4.2%
	Ti-SS-C	548.7	3.8%	713.2	4.1%
	Ti-SS-Tung	548.0	3.9%	710.4	4.5%
	Ti-S-C	574.4	0.7%	734.6	1.6%
	Ti-C-Tung	556.2	2.5%	707.7	4.9%
	Ti-SS-Al	549.0	3.8%	713.3	4.1%

Overall, the results of the study have confirmed the improvement that can be achieved by the adding of an additional trial-space experiment. It should note that the criterion of validation of the scaling experiment needs to consider numerical and practical results, where the criterion can be an error between them in the physical model [107]. As for the entire numerical simulation, the criterion should be lower since only acceptable errors like different plastic behaviour are considered.

3.9 A practical demonstration in Ansys

To demonstrate that the approach presented has practicality and additionally is not reliant on a particular package a semi-elliptical crack located on the outer wall of a cylindrical pressure vessel is examined in this section using the commercial software package ANSYS [113]. The problem is slightly more nuanced than those described above being truly 3D in nature with focus on calculating stress intensity factors (SIFs) and J-integrals. The details of the crack and the pressure vessel are presented in Fig.3.13 along with the finite element mesh employed. The pressure vessel is pressurised internally but constrained laterally to impose plane strain conditions on the crack. The cross-section view of the crack presented Fig. 3.13 (b) shows crack depth (minor radius) *b*, half crack length (major radius) *a*, and thickness *T* of the cylindrical pressure vessel. The pressure vessel dimensions are outer radius $R_o = 1.5$ m, inner radius $R_i = 1.4$ m, length $L = 8$ m and the following ratios apply: $\frac{R_i}{T} = 14, \frac{b}{T} = \frac{b}{a} = 0.5$.

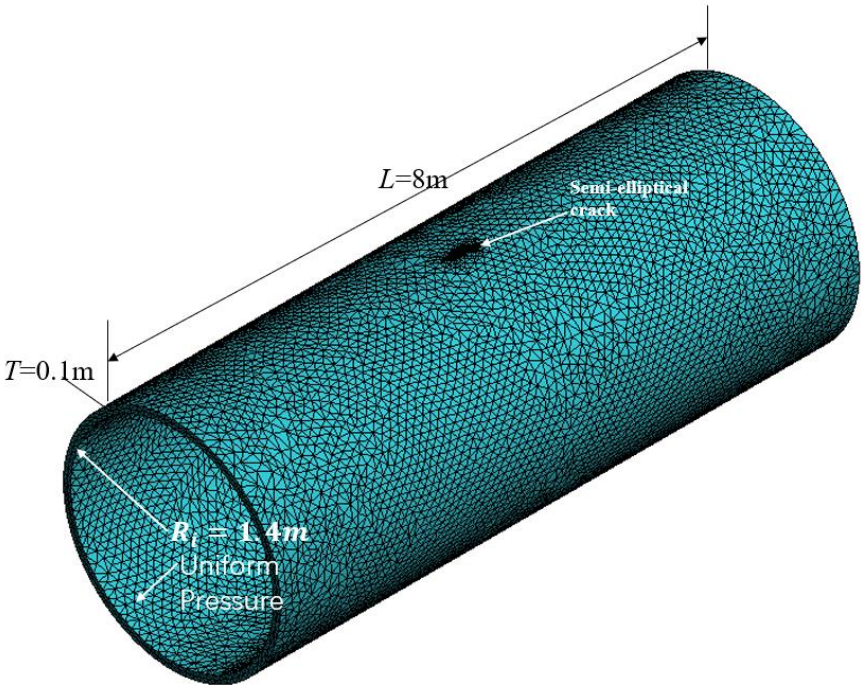

(a) Mesh and overall dimensions

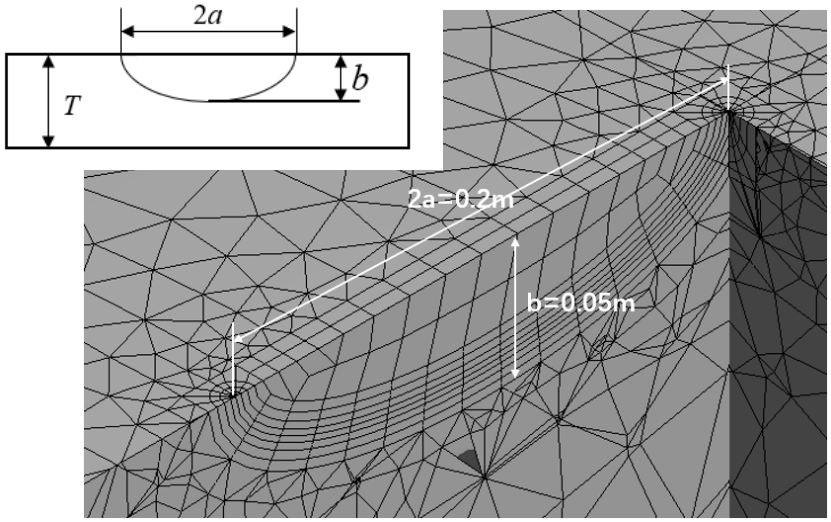

(b) Cross section of the semi-elliptical crack

Figure 3.13 Mesh and crack details for an internally pressurized pressure vessel

The FE mesh for the pressure vessel depicted in Fig. 3.13(a) is made up of 52283 solid tetrahedron elements (element size ~ 0.1m) and a total of 100234 nodes. The overall dimensions of the semi-elliptical (SE) crack are provided in Fig. 3.13(b) and conform to the relationship $\frac{b}{a} = 0.5$. The ANSYS software evaluates SIFs using a contour integration procedure with the facility to set the number contours. In this study the number of contours around the crack tip is set equal to be 3 with the largest

contour radius equalling 0.05m. Unlike the case studies above, here, the SIF value is the target for comparison, which can be directly synchronised between different materials. It makes the process possible to apply in practical cases, that the outputs of trial specimens can predict the output of physical specimens.

3.9.1. Linear elastic analysis

Zeroth-order theory is sufficient for a linear-elastic analysis and since the SIF $K \propto \sigma\sqrt{\pi a}$ and $J = \frac{K^2}{E'}$ the analysis in Section 3.6.1 applies, which for an identical material (i.e. titanium) at full size and scale, Eq. (3.26) provides $\alpha_{01}^{v} g_1 = \frac{1}{\beta_1^2}\frac{E'_{ps}}{E'_{ts1}} = \frac{1}{\beta_1^2}$. The precise relationship for the SIF for the SE crack is

$$K = \sigma\sqrt{\pi a} \cdot f(a') \tag{3.35}$$

where $f(a')$ is a shape function and takes the form,

$$f(a') = \sqrt{1 + 0.52a + 1.29a^2 - 0.07a^3} \tag{3.36}$$

and where $a' = \frac{a}{\sqrt{R_i T}}$, which is a dimensionless parameter unaffected by scale and consequently $a'_{ps} = a'_{ts}$.

It follows therefore that $\boldsymbol{\sigma}_{ps} = \alpha_{01}^{v} g_1 \beta_1^2 \boldsymbol{\sigma}_{ts1} = \boldsymbol{\sigma}_{ts1}$, $K_{ps} = \alpha_{01}^{v} g_1 \beta_1^{3/2} K_{ts1} = \beta_1^{-1/2} K_{ts1}$ and $J_{ps} = \alpha_{01}^{v} g_1 \beta_1 J_{ts1} = \beta_1^{-1} J_{ts1}$, which are relationships that are confirmed on comparison of virtual and real results presented Fig. 3.17 (i.e. Ti-Ti and Ti curves), with 5MPa internal uniform pressure and $\beta_1 = \frac{1}{2}$ and $\frac{1}{4}$. Note that the measure used along the abscissas in Fig. 3.14(b) and (c) is the length along the middle contour (of the 3 contours) starting from point 1 in Fig 3.14(a) and ending at point 2. In the situation where a different material is used at scale, then Eq. (3.26) provides $\alpha_{01}^{v} g_1 = \frac{1}{\beta_1^2}\frac{E'_{ps}}{E'_{ts1}}$ and consequently $\boldsymbol{\sigma}_{ps} = \alpha_{01}^{v} g_1 \beta_1^2 \boldsymbol{\sigma}_{ts1} = \frac{E'_{ps}}{E'_{ts1}}\boldsymbol{\sigma}_{ts1}$, which means the pressure in the scaled model must change as shown in Table. 3.10 for a selection of materials. Note also in this case $K_{ps} = \alpha_{01}^{v} g_1 \beta_1^{3/2} K_{ts1} = \frac{E'_{ps}}{E'_{ts1}}\beta_1^{-1/2} K_{ts1}$ and $J_{ps} = \alpha_{01}^{v} g_1 \beta_1 J_{ts1} = \frac{E'_{ps}}{E'_{ts1}}\beta_1^{-1} J_{ts1}$, which are confirmed to reasonable accuracy by the results

presented in Fig. 3.14.

Table 3.10 Applied pressure for scaled material models

Materials	Titanium	Stainless steel	Steel	Copper	Aluminium
Young's modulus (GPa)	120	200	190	130	70
Pressure (MPa)	5	8.3333	7.9167	5.4167	2.9167

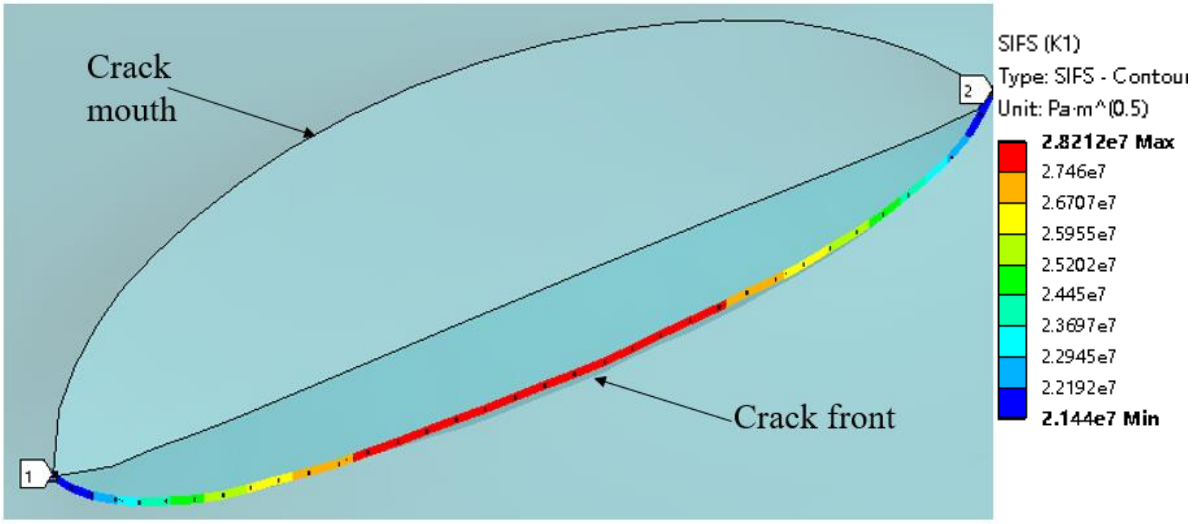

(a) Contour at crack front used by ANSYS

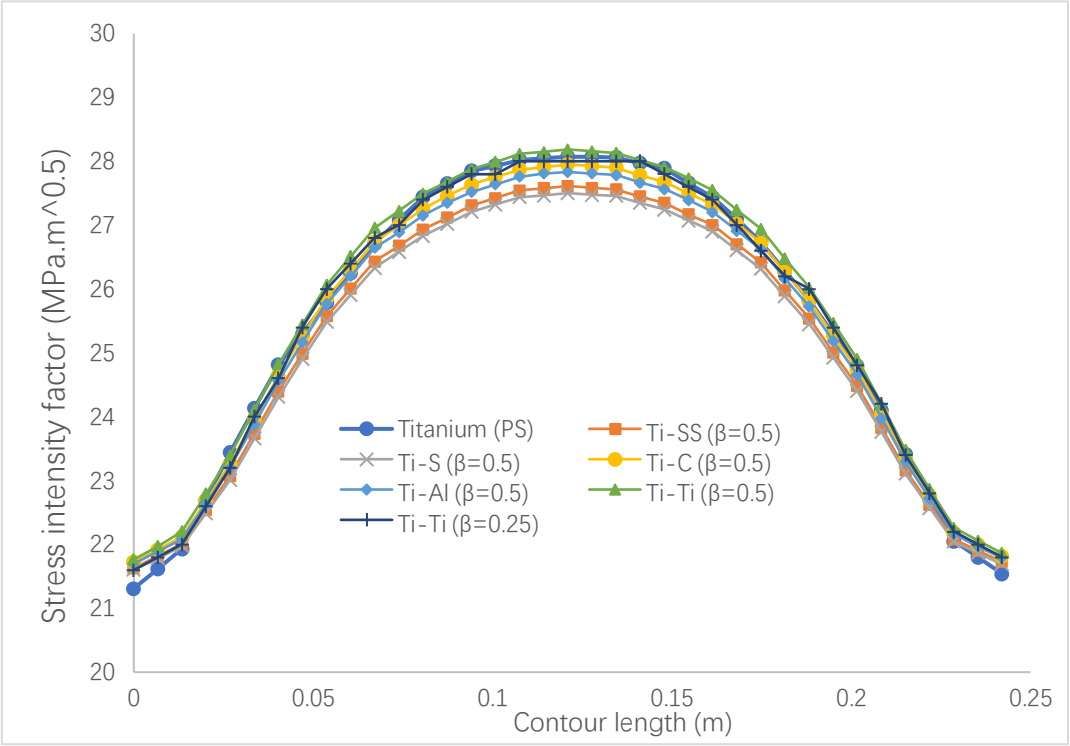

(b) SIFs along contour

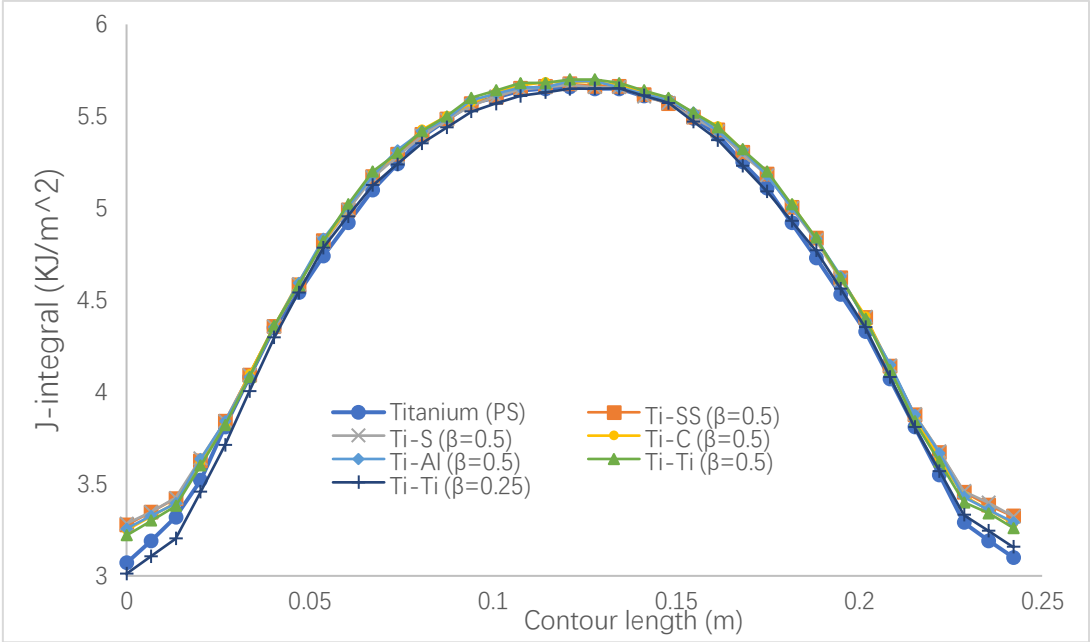

(c) J-integral along contour

Figure 3.14 J-integrals and SIFs along contour shown in (a)

3.9.2. Plastic analysis

Things are slightly more involved in the situation where the pressure loading is sufficient to initiate plastic behaviour. The approach outlined in Section 3.7 is applied here with the targeting of yield stress for zeroth order and both yield and mean stress (i.e. Eq. (3.33)) first order. The SIF in this situation can again be estimated using Eq. (3.35) but requires a plastic correction, according to Marie and Nédélec [114], which for a pressure vessel takes the form

$$K_{pl} = K_{el}\left[1 + \frac{1}{2(1-\nu^2)}\sqrt{1-\left(\frac{1}{1+2\frac{r_y}{a}}\right)^2}\right]\sqrt{\frac{\frac{a}{2}+r_y}{\frac{a}{2}}} \tag{3.37}$$

where r_y is a measure of the extent of the plastic zone at the crack tip, and one possible estimate is Irwin's formula $r_y = \frac{1}{6\pi}\left(\frac{K_{el}}{Y}\right)^2$ with yield stress Y.

The presence of K_{el} in r_y means that K_{pl} is nonlinearly related to K_{el} and hence to the shape function and the ratio between applied stress and yield stress (see Shlyannikov [115]). The applied stress between physical and trial space still obeys $\boldsymbol{\sigma}_{ps} = \alpha_{01}^{v} g_1 \beta_1^2 \boldsymbol{\sigma}_{ts}$, thus, in order to negate differences in plastic correction at scale it is

necessary to set $\alpha_{01}^{v} g_1 \beta_1^2 = \frac{Y_{ps}}{Y_{ts1}}$. This again provides different pressures at scale for different materials as tabulated in Table 3.11.

Table 3.11 Applied pressure for each material in plastic model

Materials	Titanium	Stainless steel	Steel	Copper	Aluminium
Yield stress (MPa)	812	881	323.5	92.2	98.4
Pressure (MPa)	50	54.25	19.99	5.68	6.06

Note that the relationship between stress intensity factors for first-order theory is

$$K_{ps} = \alpha_{01}^{v} g_1 \beta_1^{3/2} K_{ts1} + R_1 \left(\alpha_{01}^{v} g_1 \beta_1^{\frac{3}{2}} K_{ts1} - \alpha_{02}^{v} g_2 \beta_2^{\frac{3}{2}} K_{ts2} \right) \tag{3.38}$$

with zeroth order returned on setting $R_1 = 0$.

The results of the trial are provided in Fig. 3.15 with reasonable accuracy returned for both zeroth and first order except for Ti-Al. The errors are listed after the material-combination, which is calculated by the average value of the corresponding points. Finally, Fig. 3.16 highlights the vast improvement possible for J-integrals using the first order theory with the J-integrals determined using the in-built facility in ANSYS. The accuracies visible in the figures reflect to a large extent the closeness of the curves to titanium in Figs. 3.10 and 3.11.

(a)

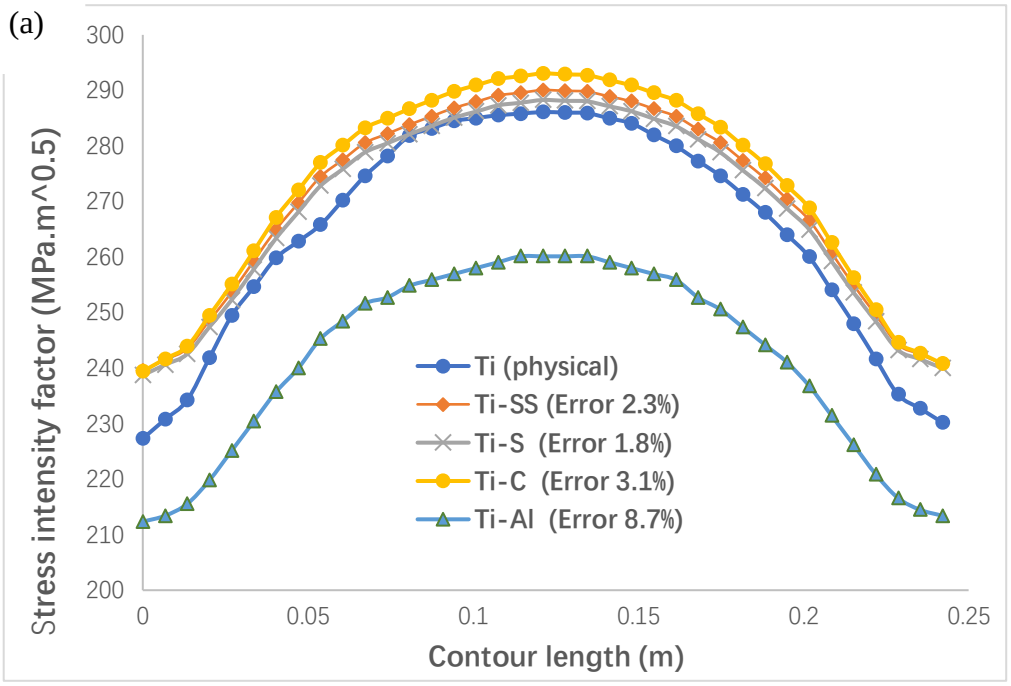

(b)

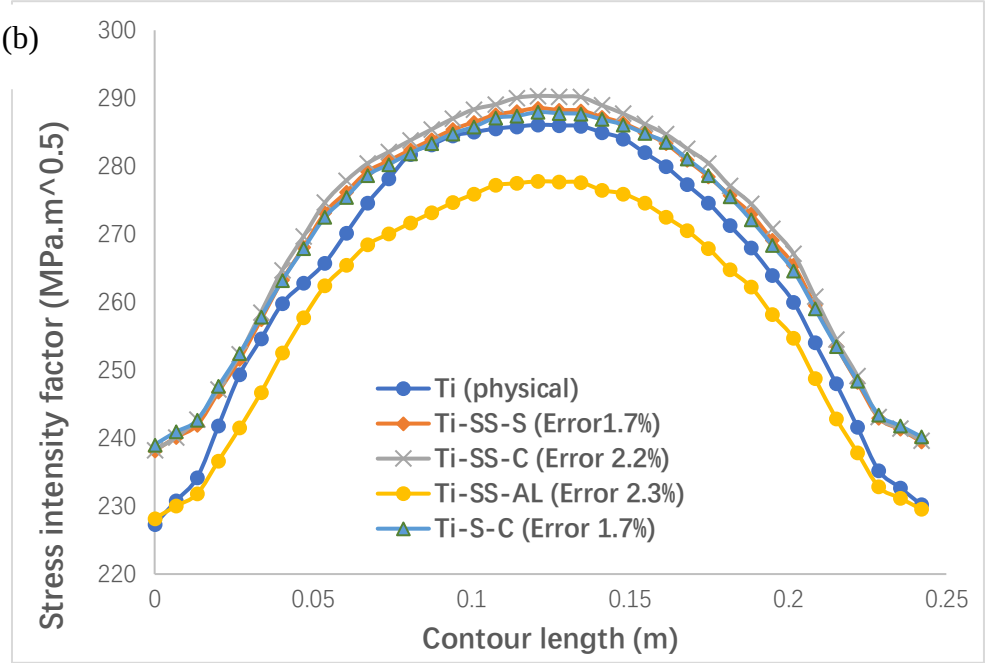

Figure 3.15 SIF predictions with (a) zeroth-order and (b) first-order using the in-built facility in ANSYS and Eq. (36).

(a)

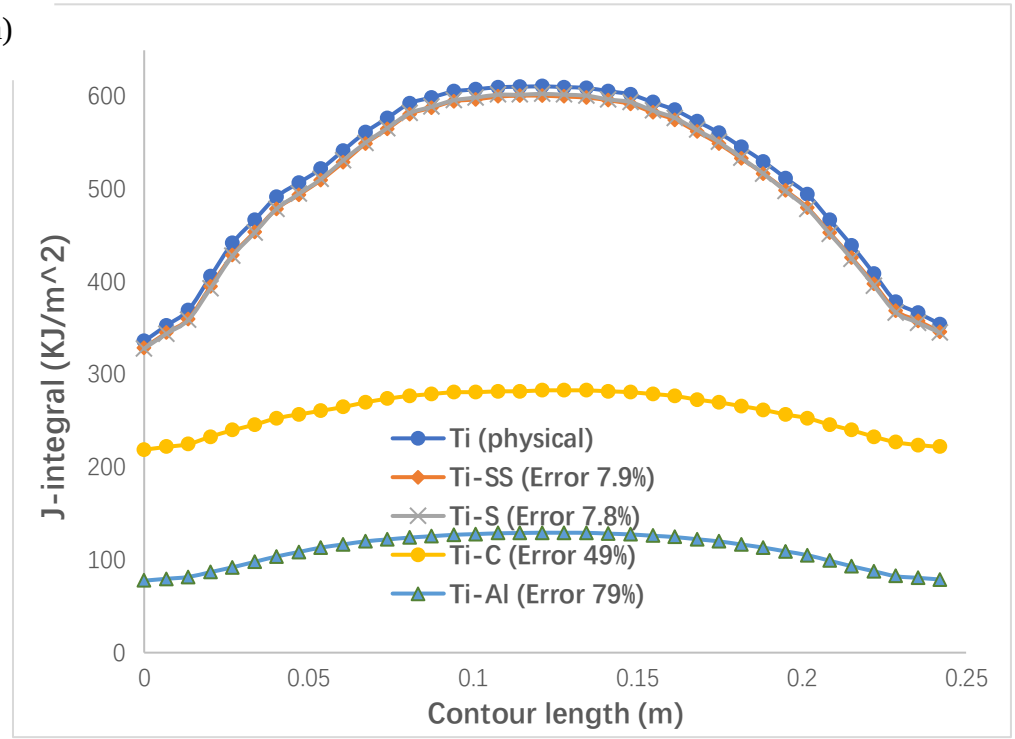

(b)

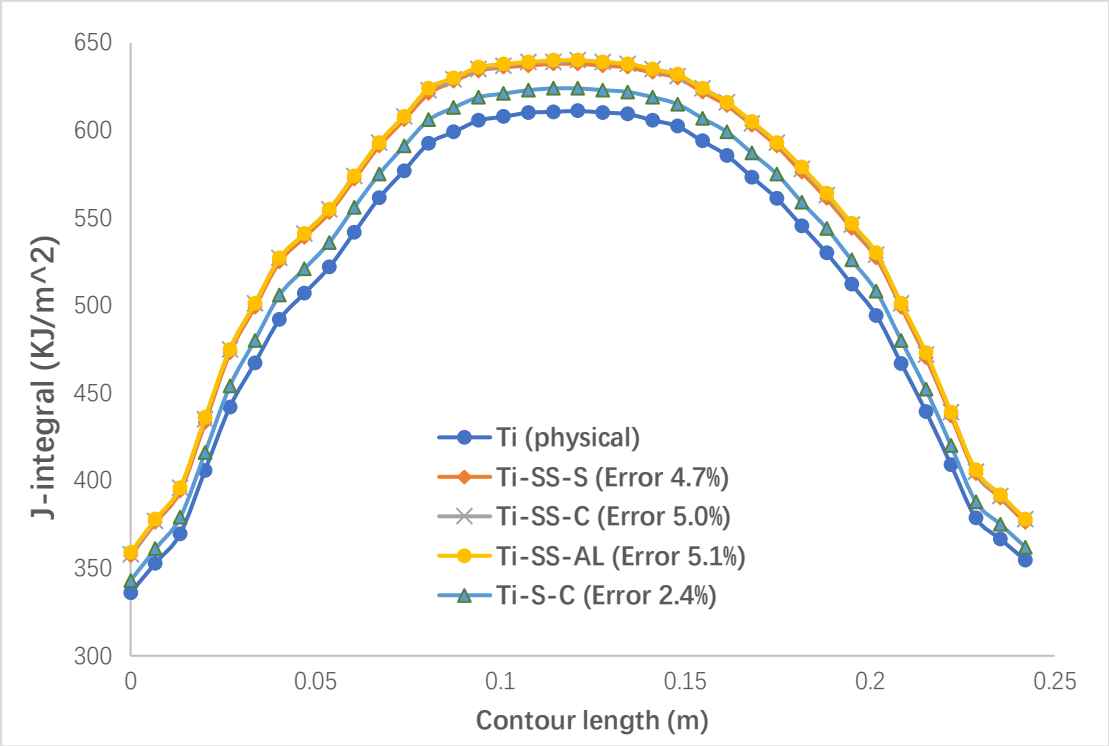

Figure 3.16 J-integral predictions for (a) zeroth-order and (b) first-order using the in-built facility within ANSYS.

It can find that both the zeroth-order and first-order theories can produce acceptable (lower than 5%) results in the SIF simulation, except for aluminium. Because of SIF's linearity, even the model becomes plastic in the process, and errors are further reduced by first-order theory. As for the J-integral comparison, the errors are higher, especially for copper and aluminium, which have the same performance as contour integral models. Though the J-integral is still investigated in virtual models, it proves the first-order theory's efficacy by comparing the curves in Fig. 3.16.

3.10 Conclusion

The chapter examines a new scaling theory for the creation of physical models for the representation of full-scale cracked specimens. A particularly novel feature is the employment of two scaled fracture-mechanics experiments at distinct scales and the application of a theory founded on the metaphysical concept of space scaling. The following conclusions can be drawn from the investigation outlined in the chapter:

1. The finite similitude theory has been further developed so that it captures all scale dependencies that arise in the fields describing fracture mechanics.
2. A new differential form of similarity has been established, which when integrated links information across two scaled-fracture experiments to the full-scale behaviour.
3. The new theory has been shown to be equally applicable to analytical and numerical fracture models and provides improvements in accuracy, which on occasions can be markedly superior to those obtained from a single-scale trial experiment.
4. Scale effects as previously defined by dimensional analysis can up to a limited extent be accommodated and cease to be scale effects in the new theory (e.g. proportional field differences are now possible).
5. The efficient determination of scaling parameters has been shown possible by the application of a proportional-fields assumption.

More specifically for the trial experiments performed it has been shown that:

1. Linear elastic fracture mechanics was captured exactly for the CT specimen by allowing the length scale for the trial experiments to be determined as part of the analysis. A pure-mathematical analytical simulation is first produced in Section 3.6.2. It shows the most straightforward situation and approach to applying finite similitude theory in LEFM, which is successful as the foundation of the theory. It is not complex since all the transported processes are linear, making the results match perfectly.
2. Zeroth-order theory involving one single trial experiment proved to be insufficient for elastoplastic fracture mechanics, but significant improvement was shown possible with two trial scale experiments. The elastic-plastic J-integral tests in Sections 3.7 to 3.8 shows the efficacy of finite similitude theory in fracture mechanics. It offers a standard of material selection that materials with different strengths will occur significant errors. Then it produces results with errors lower than 5% with first-order theory, which uses

an inexact similitude (mean value) when the properties are non-linear. It provides the direction for applying the scaling theory, though the test is not applicable in practice.

3. Section 3.9 applies the theory in the cracked-cylindrical tube with internal pressure. It directly calculates the SIF results by trial models and compares them to the physical model, providing practical application evidence. However, the J-integral simulations in this Chapter are in the virtual models, which cannot apply in reality. This is because of the higher order and non-linearity of J-integral. Hence, the next step aims to transfer the J-integral to other outputs, which can be directly calculated in the scaling process, and then return them to the value of J for comparison.

Chapter 4 Two-experiment Method for Standard Tests

4.1 Introduction

Fracture mechanics is a field of solid mechanics concerned with the propagation of cracks through materials. It is founded on the twin pillars of analytical mechanics for the quantification of crack-driving forces and experimental mechanics to characterise the resistance offered to crack propagation by the material. In essence, fracture mechanics is a methodology for the prediction of failure for loaded parts housing existing flaws and provides the correct description for categorising cracks into those that grow and those that do not. However, the dependence on defect size, orientation and location has profound influence on both analytical and experimental approaches. It in effect necessitates bespoke methodologies to be applied for the consideration, analysis, and assessment of the vast array of possible flawed structural configurations. The now seminal work of Griffith in 1921 [9] postulated that it was the presence of defects in solids that gave rise to unexpectedly lower failure loads in brittle materials (e.g., glass and ceramics). He postulated that the mechanism leading to failure under loading is the generation of high stresses at the locality of defects, which have the potential to initiate crack propagation. In the case of ductile parts, loading leads to plastic behaviour in the vicinity of the crack (Irwin, 1958 [10] and Miller,1968 [11]) and the size of the plastic zone at the tip of a crack can dictate the fracture-mechanics theory most suited to its analysis. In the case of a diminishingly small plastic zone, linear-elastic fracture mechanics (LEFM) is applicable and for larger zones elastic-plastic fracture mechanics (EPFM) may be required.

There are several physical quantities important to fracture mechanics and one is the stress intensity factor K proposed by Irwin in 1957 [12], which characterizes the intensity of elastic crack-tip fields. Likewise, the J-integral proposed by Rice in 1968 [13] quantifies the intensity of elastic-plastic crack-tip fields. Other commonly used fracture measures are the crack-tip opening distance (CTOD) and crack-tip opening

angle (CTOA), to describe the crack extension behaviour. These quantities along with others underpin fracture mechanics, which has grown into a robust combination of analytical and experimental approaches for the analysis of practical crack-related problems [116-118]. Many of testing procedures and terminology can be found in the technical standards of ASTM International (formerly the American Society for Testing and Materials). Important examples are, technical standards ASTM E399 and E1823 [30,119] for fracture toughness K_{IC} and energy release rate at crack initiation G_C along with ASTM E561 [120] for *K*-*R* curves, where the *R*-curve is a crack-extension, resistance-curve for macro-ductile tearing. The standard ASTM E1820 [40] describes the measurement of elastic-plastic initiation point J_{IC} and its related fields and ASTM E1290 and E2472 [121-122] are concerned with CTOD and CTOA testing, respectively. New and old methods and concepts are under continuous review and development [123-127] and typically ASTM standards are reappraised every five years. This basic infrastructure provides a means to ensure common standards along with the continued development of fracture properties for the application of fracture mechanics from laboratory testing to engineering design.

The focus in this paper is on scaling for the purpose of mechanical testing which is a feature not covered by the ASTM standards relating to fracture mechanics. The objective here is to gauge the response of a specimen at any scale from the results obtained from two scaled experiments at selected scales. It is well appreciated that scaling is widely used in continuum mechanics (e.g., structural failure [83,128] and impact [86-87], and thermal-fluids [90]) and underpinned by dimensional analysis. Dimensional analysis is presently the only ubiquitous scaling method that could in principle be applied in fracture mechanics [94-97] but the presence of size effects means it has limited applicability. It offers no solution to scale effects, which are invariably present in all non-trivial processes. The works of Bažant [74-76] for example sheds light on the problem, where size effects in materials effectively negates the efficacy of dimensional analysis in fracture mechanics.

A new scaling theory [107] has recently appeared in the open literature, where

dimensional analysis corresponds to just one similitude identity out of a countable infinite number of alternative possibilities realised by the new scaling theory. The new theory describes all scale dependencies for all physical systems and involves no approximation in doing so. Many of the dependencies are hidden yet can be revealed by the application of a similitude identity. Depending on the identity chosen more than one scaled experiment may be required yet the theory provides the means to communicate across the scales to make sense of the information recorded. The application of what is termed *first-order finite similitude*, which is a particular invariance involving two experiments (which is particularly pertinent in this paper) has just appeared the open literature [107]. The foundation of the scaling theory is somewhat surprising as it brings together two seemingly disparate concepts of *scaled experimentation* and *space scaling*. It is recognised of course that experimental research lies at the very heart of the scientific method and has an established history and underpins current practice and technological development (Popper. K, 1977) [129]. An altogether newer concept however is the premise that *space scaling* [104,130] can provide the means to examine the behaviour of physical phenomena, where a laboratory, a piece of equipment, a process or a prototype can be scaled by means of space expansion or contraction. This somewhat surprising view of things transpires to be the correct approach and leads to *the theory of scaling* [104]. The approach is being rolled out in the open literature being applied to different fields including: cohesive zone models [112], structural impact [129-130], metal forming [104] and biomechanics tests [105,131].

Although fairly evident how a scaling theory might help in the creation of scaled models for processes and structures, its role in mechanical testing in fracture mechanics requires some explanation. It is shown in the paper how the similitude condition termed *first-order finite similitude* provides a new way of thinking about fracture mechanics. The condition provides additional fields over and above those provided by Newtonian mechanics and constitutive laws, which are in fact derivatives with respect to length scaling of those fields. Field derivatives quantify how things

change with scale and for fracture mechanics with size effects present these changes can be stipulated. This provides a definitive theory for fracture mechanics, which happens to coincide with that provided by the first-order finite similitude identity; this is the principal hypothesis of the work presented here.

The developed two-experiment theory will be introduced in Section 4.2, which uses the scale invariance of identical material during the scaling process. In Section 4.3 a new definitive method for fracture mechanics is introduced founded on the first-order finite similitude identity. It is shown how under quasistatic loading the first-order similitude rule can be identically satisfied leading to a two-experiment theory for fracture mechanics. The theory is applied to relatively simple well-known analytical examples in Section 4.4, where it is revealed how exact matches are possible with two scaled models. The theory is also applied to standard tests in Section 4.5, for K_{IC} and J_C in accordance with ASTM E399 and E1820. This confirms how scaled experiments can be related to standard tests performed under conditions pertaining to LEFM and EPFM. All the tests are analysed numerically using the FE method (see references [132-135] for precedents) and with the use of extended finite elements (i.e., XFEM). The tests provide good supporting evidence for the new theory revealing high levels of conformity for a wide range of specimen sizes. The chapter finishes with a set of conclusions.

4.2 Two experiment theory for fracture mechanics

To establish a definitive theory for fracture mechanics it is necessary to confirm that Eqs. (3.16) can be solved under conditions that are germane to quasistatic fracture. Prior to examining the solution of these equations in detail however it is revealing to examine the integrated equations (i.e., Eqs. (3.16)) first to observe the impact of two important scale invariances in fracture mechanics.

4.2.1. Scale invariance in fracture mechanics

The first consideration is the stress field under scaling and the contention that local to

a crack tip near-identical stress fields can be anticipated in each of the scaled fracture specimens. This requirement leads to the scale invariance $\boldsymbol{\sigma}_{ps} = \boldsymbol{\sigma}_{ts1} = \boldsymbol{\sigma}_{ts2}$ should be captured by the theory and consequently Eq. (3.16c) reduces to

$$1 = \alpha_{01}^{v} g_1 \beta_1^2 + R_1 \left(\alpha_{01}^{v} g_1 \beta_1^2 - \alpha_{02}^{v} g_2 \beta_2^2\right) \tag{4.1a}$$

or equivalently in differential terms $\alpha_1^v\left(\alpha_0^v g \ \ \beta^2\right)'$=const., which is a condition that arises from Eq. (3.10b) and condition Eq. (3.8), where "const" here means independent of β.

The idea that stress fields are nearly identical (under scaling) local to a crack tip can be readily accepted on consideration of the yield zones and the expectation that these will take on a similar form in any scaled specimen. There exists an additional desirable scale invariance that at first sight might appear somewhat unexpected but nonetheless happens to be a feature of cohesive elements, which is the fixing of displacement (separation in cohesive elements), i.e., $\mathbf{u}_{ps} = \boldsymbol{u}_{ts1} = \boldsymbol{u}_{ts2}$, which on application to Eq. (3.16e) provides,

$$1 = \beta_1^{-1} + R_1 \left(\beta_1^{-1} - \beta_2^{-1}\right) \tag{4.1b}$$

or equivalently in differential terms $\alpha_1^u\left(\beta^{-1}\right)'$=const., which is a condition that arises from Eq. (3.10c) and condition Eq. (3.8); note that it can be deduced that $\alpha_1^v = \alpha_1^u = \beta^2$ (recall the requirement $\alpha_1^v(1) = \alpha_1^u(1) = 1$) and R_1 is obtained from Eq. (4.1b) once the scales β_1 and β_2 are set.

An argument for a displacement-scale invariance arises on consideration of the cohesive element, where separation can be defined to be $\delta = [\![\boldsymbol{u} \cdot \boldsymbol{n}]\!]$, where the notation $[\![\ \ ]\!]$ signifies a jump, and $\boldsymbol{n}$ identifies the outward pointing unit normal at either side of the jump. A lot more about this can be found in reference [101], where Davey & Darvizeh examine the application of transport equations to fracture. It is sufficient to observe here however that separation scales in the same manner as displacement but peculiarly in cohesive elements there exists a critical value of separation δ_c that does not scale. The contention here is that if cohesive elements

provide a good model for fracture, then it is necessary to have displacement as a scale invariance in any two-experiment theory on fracture.

Another point of consideration is strain, in small deflection theory of the type considered here. Note that the similitude theory does not produce a constitutive equation in the physical space as is evident from the existence of Eqs. (3.16c) and (3.17); in essence any constitutive rule is implicit. However, elastic behaviour is very much anticipated to be accurately described by identical constitutive rules in all spaces. Consider then the substitution of a constitutive law of the type $\boldsymbol{\sigma} = \boldsymbol{C\varepsilon}$ into Eq. (3.16c) to provide the identity,

$$\boldsymbol{\varepsilon}_{ps} = \alpha_{01}^{v} g_1 \beta_1^2 \boldsymbol{\varepsilon}_{ts1} + R_1 \left(\alpha_{01}^{v} g_1 \beta_1^2 \boldsymbol{\varepsilon}_{ts1} - \alpha_{02}^{v} g_2 \beta_2^2 \boldsymbol{\varepsilon}_{ts2}\right) \tag{4.1c}$$

which can be contrasted with Eq. (3.17).

This provides the requirement that $\alpha_{01}^{v} g_1 \beta_1^2 = \alpha_{02}^{v} g_2 \beta_2^2 = 1$ or $\alpha_{01}^{v} g_1 = \beta_1^{-2}$ and $\alpha_{02}^{v} g_2 = \beta_2^{-2}$; note that g_1 and g_2 have no role to play in a quasistatic analysis. Observe that Eq. (4.1a) is not too unexpectedly satisfied by this selection for $\alpha_{01}^{v} g_1$ and $\alpha_{02}^{v} g_2$ and what has emerged is a definitive two-experiment theory for fracture mechanics with freedoms limited only to the selection of the scales β_1 and β_2. Note the condition $\alpha_1^{v}\left(\alpha_0^{v} g \ \ \beta^2\right)'$=const. with $\alpha_1^{v} = \beta^2$ is satisfied by the two possibilities $\alpha_0^{v} g \ \ = \beta^{-3}$ and $\alpha_0^{v} g \ \ = \beta^{-2}$, with the latter condition providing "const" identically equal to zero; more on this in the next section.

It is worth noting in passing that the zeroth-order conditions $\rho_{ps} = \alpha_0^{\rho} \rho_{ts} \beta^3$, $\alpha_0^{v} g^{-1} \beta = \alpha_0^{\rho}$ and $\alpha_0^{u} \beta = \alpha_0^{\rho}$ (or $\alpha_0^{u} = \alpha_0^{v} g^{-1}$) provide $\alpha_0^{\rho} = \beta^{-3}$ and $\alpha_0^{u} = \alpha_0^{v} g^{-1} = \beta^{-4}$. This can be reconciled with the condition $\alpha_0^{v} g \ \ = \beta^{-2}$ (and $\alpha_0^{v} g \ \ = \beta^{-3}$) by matching $\alpha_0^{v} = g^{-1}\beta^{-2} = g\beta^{-4}$ (and $\alpha_0^{v} = g^{-1}\beta^{-3} = g\beta^{-4}$), which provides $g = \beta$ (and $g = \beta^{\frac{1}{2}}$). It is important to recognise that the inclusion of the condition $\rho_{ps} = \alpha_0^{\rho} \rho_{ts} \beta^3$ provides a signal to the theory that inertia is involved and consequently time is a feature leading to the explicit specification of g. Although the focus here is quasistatic testing it is reassuring nonetheless to note that dynamics can

(at least in principle) feature as required.

4.2.2. A new differential theory for fracture mechanics

To confirm that the application of the scale invariances $\boldsymbol{\sigma}'_{ts} \equiv 0$ and $\boldsymbol{u}'_{ts} \equiv 0$ provide a new description for fracture mechanics under quasistatic loading and under first-order similitude it is required to show that Eqs. (3.9) and (3.10) are satisfied. Eqs. (3.9) are effectively the governing transport equations on the trial space and simplify considerably for quasistatic conditions. It is of interest however to keep things general at this stage and bring these simplifications in at the point of necessity as this approach reveals the scope and limitations of the new approach. Consider first the impact of the displacement invariance $\boldsymbol{u}'_{ts} \equiv 0$ and note that $\boldsymbol{U}'_{ps} = (\beta^{-1}\boldsymbol{u}_{ts})' = (\beta^{-1})'\boldsymbol{u}_{ts} = (\beta^{-1})'\beta\boldsymbol{U}_{ps}$. In view of the relationship between velocity and displacement it can be anticipated that this result must impact on $\boldsymbol{V}'_{ps} = (\beta^{-1}g\boldsymbol{v}_{ts})'$. The outcome is revealed by the following equation:

$$\begin{aligned}\boldsymbol{V}'_{ps} = (\beta^{-1}g\boldsymbol{v}_{ts})' = \left(\beta^{-1}g\frac{d\boldsymbol{u}_{ts}}{dt_{ts}}\right)' = \left(\beta^{-1}\frac{d\boldsymbol{u}_{ts}}{dt_{ps}}\right)' = \frac{d}{dt_{ps}}(\beta^{-1}\boldsymbol{u}_{ts})' \\ = (\beta^{-1})'\frac{d\boldsymbol{u}_{ts}}{dt_{ps}} = (\beta^{-1})'g\boldsymbol{v}_{ts} = (\beta^{-1})'\beta\boldsymbol{V}_{ps}\end{aligned} \tag{4.2}$$

which is a result that relies on the ability to interchange the temporal derivative $\frac{d}{dt_{ps}}$ (being independent of β) and the scale derivative $\frac{d}{d\beta}$.

Substitution of Eq. (4.2) and $\boldsymbol{U}'_{ps} = (\beta^{-1})'\beta\boldsymbol{U}_{ps}$ into Eq. (3.10c) provides,

$$\begin{aligned}\alpha_1^u T_1^u(\beta) = \frac{D^*}{D^* t_{ps}}\int_{\Omega^*_{ps}} \beta^2\rho_{ps}(\beta^{-1})'\beta\boldsymbol{U}_{ps}\, dV^*_{ps} \\ + \int_{\Gamma^*_{ps}} \beta^2\rho_{ps}(\beta^{-1})'\beta\boldsymbol{U}_{ps}(\boldsymbol{v}_{ps} - \boldsymbol{v}^*_{ps})\cdot\boldsymbol{n}_{ps}\, d\Gamma^*_{ps} \\ - \int_{\Omega^*_{ps}} \beta^2\rho_{ps}(\beta^{-1})'\beta\boldsymbol{V}_{ps} dV^*_{ps} = 0\end{aligned} \tag{4.3}$$

where $\alpha_1^u = \beta^2$, which ensures that this equation is invariant of β but observe also that this equation is no more than $\beta^2(\beta^{-1})'\beta$ times Eq. (4.8c).

Thus, the identity $\boldsymbol{u}'_{ts} \equiv 0$ provides the relationship $\alpha_1^u T_1^u(\beta) = \beta^2(\beta^{-1})'\beta\alpha_0^u T_0^u(\beta) = 0$, which confirms that Eq. (3.10c) is satisfied and equally important satisfies the similitude identity Eq. (3.8). Turning attention now to Eq. (3.10a), which on substitution of $\boldsymbol{V}'_{ps} = (\beta^{-1})'\beta\boldsymbol{V}_{ps}$ and on setting $\alpha_1^\rho = \beta^2$ provides

$$\alpha_1^\rho T_1^\rho(\beta) = \int_{\Gamma^*_{ps}} \beta^2 \rho_{ps}(\beta^{-1})'\beta\boldsymbol{V}_{ps} \cdot \boldsymbol{n}_{ps}\, d\Gamma^*_{ps} = 0 \tag{4.4}$$

which is proportional to Eq. (3.9a) under the restriction that material density does not change.

It is seldom common practice to include the continuity equation for fracture mechanics since density is set to a constant for the material under consideration. Setting ρ_{ps} to a constant in Eq. (3.9a) simplifies it so that the identity $\alpha_1^\rho T_1^\rho(\beta) = \beta^2(\beta^{-1})'\beta\alpha_0^\rho T_0^\rho(\beta) = 0$ applies confirming that Eq. (3.10a) is satisfied along with the first-order similitude identity Eq. (3.8). The final consideration is Eq. (3.10b) under the invariance $\boldsymbol{\sigma}'_{ts} \equiv 0$ and note that $\boldsymbol{\Sigma}'_{ps} = \left(\alpha_0^v \beta^2 g \boldsymbol{\sigma}_{ts}\right)' = (\alpha_0^v \beta^2 g)'\boldsymbol{\sigma}_{ts}$ and the requirement to satisfy Eq. (3.8) raises two possibilities brought about by the invariance of $\beta^2(\alpha_0^v\beta^2 g)'$, which as mentioned above raises two possibilities, i.e. $\alpha_0^v g = \beta^{-3}$ and $\alpha_0^v g = \beta^{-2}$. With the objective in mind of relating Eq. (3.9b) to (3.9b) the former of these conditions appears the most likely and substitution of $\boldsymbol{\Sigma}'_{ps} = (\beta^{-1})'\beta\boldsymbol{\Sigma}_{ps}$ in Eq. (3.10b) along with $\boldsymbol{V}'_{ps} = (\beta^{-1})'\beta\boldsymbol{V}_{ps}$ provides

$$\begin{aligned} \alpha_1^v T_1^v(\beta) = \frac{D^*}{D^* t_{ps}} &\int_{\Omega^*_{ps}} \beta^2 \rho_{ps}(\beta^{-1})'\beta\boldsymbol{V}_{ps}\, dV^*_{ps} \\ &+ \int_{\Gamma^*_{ps}} \beta^2 \rho_{ps}(\beta^{-1})'\beta\boldsymbol{V}_{ps}\left(\boldsymbol{v}_{ps} - \boldsymbol{v}^*_{ps}\right) \cdot \boldsymbol{n}_{ps}\, d\Gamma^*_{ps} \\ &+ \int_{\Gamma^*_{ps}} \beta^2(\beta^{-1})'\beta\boldsymbol{\Sigma}_{ps} \cdot \boldsymbol{n}_{ps} d\Gamma^*_{ps} - \int_{\Omega^*_{ps}} \beta^2 \boldsymbol{B}'_{ts} dV^*_{ps} = 0 \end{aligned} \tag{4.5}$$

where $\alpha_1^v = \beta^2$ and observe that requirement for body force, i.e. $\mathbf{B}'_{ps} = (\beta^{-1})'\beta\mathbf{B}_{ps}$

with scale invariance of $\beta\mathbf{B}_{ps}$ and note for this case that $\boldsymbol{B}_{ps} = \alpha_0^v \rho_{ts} \beta^3 g \boldsymbol{b}_{ts}^v = \rho_{ts} \boldsymbol{b}_{ts}^v$.

Thus, the conditions $\boldsymbol{\sigma}'_{ts} \equiv 0$ and $\boldsymbol{u}'_{ts} \equiv 0$ and the choice $\alpha_0^v g = \beta^{-3}$ leads to the relationship $\alpha_1^v T_1^v(\beta) = \beta^2(\beta^{-1})'\beta\alpha_0^v T_0^v(\beta) = 0$ confirming the solution of Eq. (3.10b) as required. In quite general terms therefore it has been established that Eqs. (3.9) and (3.10) are solvable and at this stage quasistatic conditions have not been imposed. A problem remains however arising from the critical importance of elasticity in fracture mechanics and strain relationships Eqs. (3.17) and (4.1a). Finite similitude is not concerned with constitutive relationships and consequently in satisfying Eqs. (3.9) and (3.10) no recourse to them is required. The alternative way to satisfy Eq. (3.10b) is to simply set all the terms to zero and this can be achieved for quasistatic loading as velocity terms disappear and on setting $\alpha_0^v g = \beta^{-2}$ the stress term disappears but also on setting $\mathbf{B}'_{ps} \equiv 0$ to remove the body force.

4.2.3. The constraining effect of constitutive laws

The theory presented thus far does not take into consideration constitutive behaviour and as such the assumed desirable behaviour of stress and displacement are decoupled at this stage but are constricted in practice. However, the theory caters for other behaviours and an important feature arises from the zeroth-order condition. In particular, and critical to elasticity, is the zeroth-order displacement condition $\boldsymbol{u}_{ts} = \beta\boldsymbol{u}_{ps}$, which provides $\boldsymbol{U}'_{ps} \equiv \mathbf{0}$ and for quasistatic conditions Eqs. (4.3) to (4.5) are again satisfied. The satisfaction of these equations is no coincidence and is a feature of the nesting of similitude rules with lower-order rules contained within higher-order ones. Thus, a zeroth-order relationship will automatically satisfy the first-order similitude rule and in particular $\boldsymbol{u}_{ts} = \beta\boldsymbol{u}_{ps}$ satisfies Eq. (3.16c).

In conclusion a definitive theory for fracture mechanics has emerged from the first-order finite-similitude identity Eq. (3.8) being described in transport form by six equations (effectively fourteen equations since two are vector equations), which are

Eqs. (3.9) and (3.10). Shown here are how the equations are satisfied exactly under the invariances $\boldsymbol{\sigma}'_{ts} \equiv 0$ and $\boldsymbol{u}'_{ts} \equiv \mathbf{0}$, and additionally $\boldsymbol{u}'_{ts} \equiv \boldsymbol{u}_{ps}$, but note that no recourse is made to plasticity. Considered in the sections that follow are various test cases of increasing complexity that confirm the viability of the new theory even in the presence of plasticity.

4.3 Analytical fracture mechanics

To illustrate the new theory, it is of interest to consider a couple of well-known analytical examples where the bulk material response is assumed elastic.

4.3.1. J-Integral example

Consider then the classic problem of a crack of length $2a_{ts}$ in an infinite plate, where in the absence of plasticity, the J-integral has the simple analytical solution,

$$J_{ts} = \frac{K_{I\,ts}^2}{E'_{ts}} = \pi a_{ts} \frac{\sigma_{ts}^2}{E'_{ts}} \tag{4.6}$$

with stress intensity defined by $K_{I\,ts} = \sigma_{ts}\sqrt{\pi a_{ts}}$, where E'_{ts} is either Young's modulus E_{ts} (for plane stress) or $E_{ts}/(1-\nu_{ts}^2)$ (for plane strain), and where ν_{ts} is Poisson's ratio.

The objective here is to confirm how J_{ts1} and J_{ts2}, which are the J-integrals at β_1 and β_2, respectively can return J_{ps} the J-integral at $\beta_0 = 1$ by means of Eqs. (3.16). It should be appreciated that first-order finite similitude does not provide an identity (of the form Eqs. (3.16)) for J-integrals. The quadratic form of the J-integral excludes such a possibility, but the alternative route is Eqs. (3.16c) and (3.16e) provide

$$\sigma_{ps} = \sigma_{ts1} + R_1 \left(\sigma_{ts1} - \sigma_{ts2}\right) \tag{4.7a}$$

$$\boldsymbol{u}_{ps} = \beta_1^{-1}\,\boldsymbol{u}_{ts1} + R_1\,(\beta_1^{-1}\,\boldsymbol{u}_{ts1} - \beta_2^{-1}\,\boldsymbol{u}_{ts2}) \tag{4.7b}$$

with crack lengths $a_{ts1} = \beta_1 a_{ps}$ and $a_{ts2} = \beta_2 a_{ps}$, and $R_1 = (1-\beta_1^{-1})(\beta_1^{-1} - \beta_2^{-1})^{-1}$.

It is readily evident for this relatively simply example that by design $\sigma_{ts1} = \sigma_{ts2}$ and consequently from Eq. (4.7a) it follows that $\sigma_{ps} = \sigma_{ts1} = \sigma_{ts2}$. Since Eq. (4.6) does not require knowledge of deformation, it immediately follows that J_{ts} is determinable from σ_{ps} alone with $E'_{ps} = E'_{ts1} = E'_{ts1}$ assumed. A depiction of the scaled experiments and the use of space scaling to produce a full-scale virtual model is depicted in Fig. 4.1. The two-experiment theory provides the means for combining results from each of the two scaled experiments.

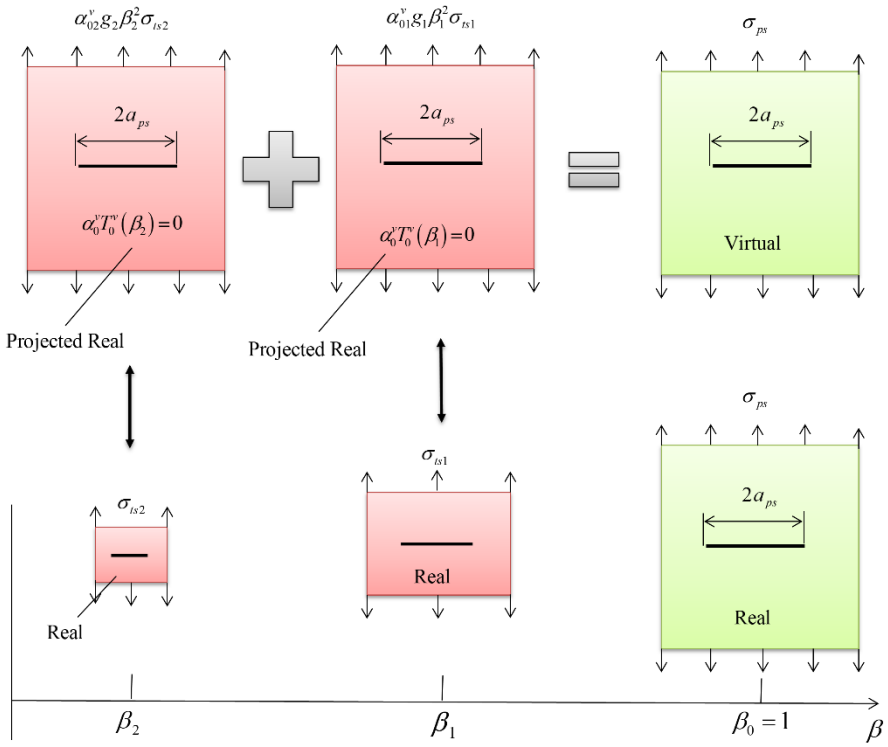

Figure 4.1 Depiction of how space scaling provides the means to predict full-scale behaviour in fracture mechanics.

4.3.2. One-dimensional cohesive element example

A cohesive zone model provides an attractive approach for the analysis of ductile tearing since it combines the many mechanisms involved in fracture into the single mechanism of material separation. A cohesive model in its simplest form involves a traction-separation curve featuring only three material properties, which are: critical stress σ_c, critical separation δ_c, and the area under the curve known as cohesive

fracture energy G_c. The most rudimentary cohesive zone model (termed here linear cohesive zone model (LCZM)) satisfies the relationship $G_c = 0.5\sigma_c\delta_c$ confirming the dependence of G_c on σ_c and δ_c. Note the identity,

$$\frac{1}{2}\Sigma_{c\,ts}\Delta_{c\,ts} = \frac{1}{2}\left(\alpha_0^v\beta^2 g\sigma_{c\,ts}\right)\left(\beta^{-1}\delta_{c\,ts}\right) = \frac{1}{2}\alpha_0^v g\beta G_{c\,ts} \tag{4.8}$$

where $\Delta_{c\,ts} = \beta^{-1}\delta_{c\,ts}$, confirms that zeroth-order scaling does not apply, since it is impossible to fix the three critical material properties under a scaling transformation.

To illustrate the application of the two-experiment theory it is convenient to consider here a one-dimensional model consisting of an elastic prismatic rod of length ℓ_0 and cross-sectional area A_0 with linear cohesive zone model (LCZM) embedded within it as depicted in Fig. 4.2.

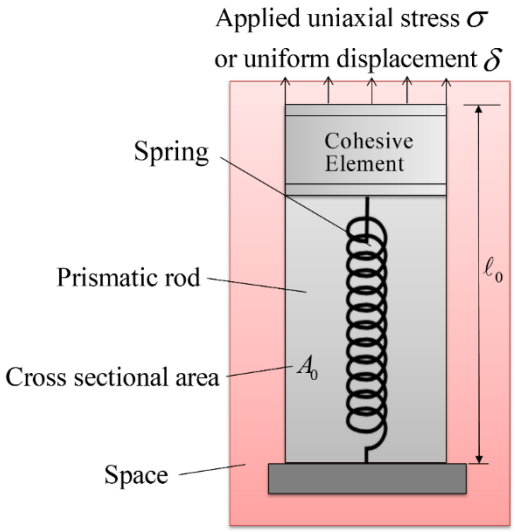

Figure 4.2 Elastic prismatic rod subjected to a uniform stress or displacement.

Subjecting the prismatic rod in Fig. 4.2 to a displacement δ at its free end (with its lower end fixed) raises the possibility that the stress level in the rod reaches the critical stress σ_c. The failure behaviour of the of the rod is modelled with a linear cohesive zone model (LCZM). The total extension therefore consists of two parts, i.e. $\delta = \delta^{el} + \delta^{coh}$ with stress $\sigma = \sigma^{el} = \sigma^{coh}$, where $\sigma^{el} = \frac{E\delta^{el}}{\ell_0}$ and $\sigma^{coh} = \sigma_c\left(1 - \frac{\delta^{coh}}{\delta_c}\right)$. Here E is Young's modulus of the bulk rod material, and δ^{el} and δ^{coh} are spring and cohesive extensions, respectively. The equilibrium condition $\sigma^{el} =$

σ^{coh} provides the displacement-loading response,

$$\frac{\sigma}{\sigma_c} = \begin{cases} \dfrac{\delta}{\delta_c^{el}} & \text{if} \quad 0 \le \delta \le \delta_c^{el} \\ \left(1 - \dfrac{\delta_c^{el}}{\delta_c}\right)^{-1} \left(1 - \dfrac{\delta}{\delta_c}\right) & \text{if} \quad \delta_c^{el} < \delta \le \delta_c \end{cases} \tag{4.9}$$

which describes a bilinear behaviour with $\delta_c^{el} = \frac{\sigma_c \, \ell_0}{E}$.

Shown in Fig. 4.3 is the application of the two-experiment theory to the prismatic rod with ℓ_0 taking on lengths ℓ_{ps}, $\beta_1 \ell_{ps}$, and $\beta_2 \ell_{ps}$. Note how the two scaled experiments are projected to the size of the full-scale system and observe the effect of this on length and stress.

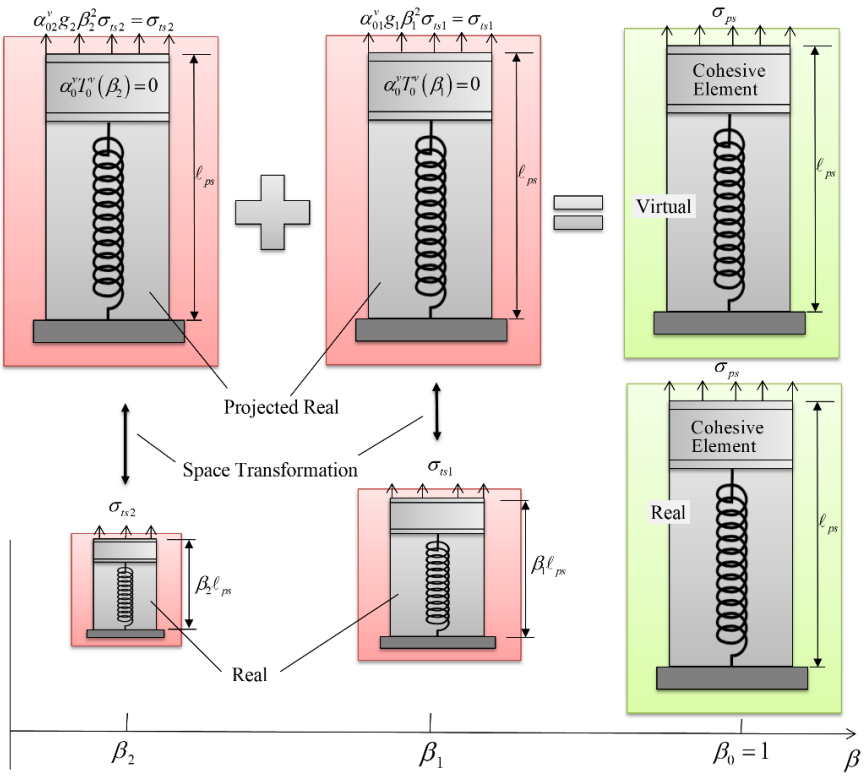

Figure 4.3 Uniaxial loading of prismatic rod with cracking captured by an embedded cohesive element.

Eqs. (4.7) also apply in this case, where it can be deduced that the fixed-point identity $\sigma_c = \sigma_{c\,ps} = \sigma_{c\,ts1} = \sigma_{c\,ts2}$ (satisfied by Eq. (4.3a)) applies and

$$\delta_{ps} = \beta_1^{-1} \, \delta_{ts1} + R_1 \, (\beta_1^{-1} \, \delta_{ts1} - \beta_2^{-1} \, \delta_{ts2}) \tag{4.10}$$

arising from Eq. (4.7b) for which the fixed point $\delta_c = \delta_{c\,ps} = \delta_{c\,ts1} = \delta_{c\,ts2}$ applies with $R_1 = (1-\beta_1^{-1})(\beta_1^{-1}-\beta_2^{-1})^{-1}$.

It is a simple matter to confirm that the theory provides a virtual model in Fig. 4.3 that is an exact replica of the real full-scale model as described by Eq. (4.9). For example, under assumption that both scaled models (at β_1 and β_2) are displaced by $\delta_{ts1} = \delta_{c\,ts1}^{el} = \beta_1 \frac{\sigma_c\,\ell_{ps}}{E}$ and $\delta_{ts2} = \delta_{c\,ts2}^{el} = \beta_2 \frac{\sigma_c\,\ell_{ps}}{E}$, respectively, then substitution into Eq. (4.10) provides $\delta_{c\,ps}^{el} = \delta_{ps} = \frac{\sigma_c\,\ell_{ps}}{E}$ as required. In addition, stress is provided by Eq. (4.7a), which confirms the expected result that $\sigma_c = \sigma_{c\,ps} = \sigma_{c\,ts1} = \sigma_{c\,ts2}$. Likewise, under the assumption that $\delta_{ts1} = \delta_{ts2} = \delta_c$, then $\delta_{ps} = \delta_c$ (from Eq. (4.10)) and stress is $0 = \sigma_{ps} = \sigma_{ts1} = \sigma_{ts2}$ (from Eq. (4.7a)) as required. The overall behaviour of the real projected real and the virtual models are depicted in Fig. 4.4, where it is confirmed how expected behaviour is returned from the results of two scaled experiments.

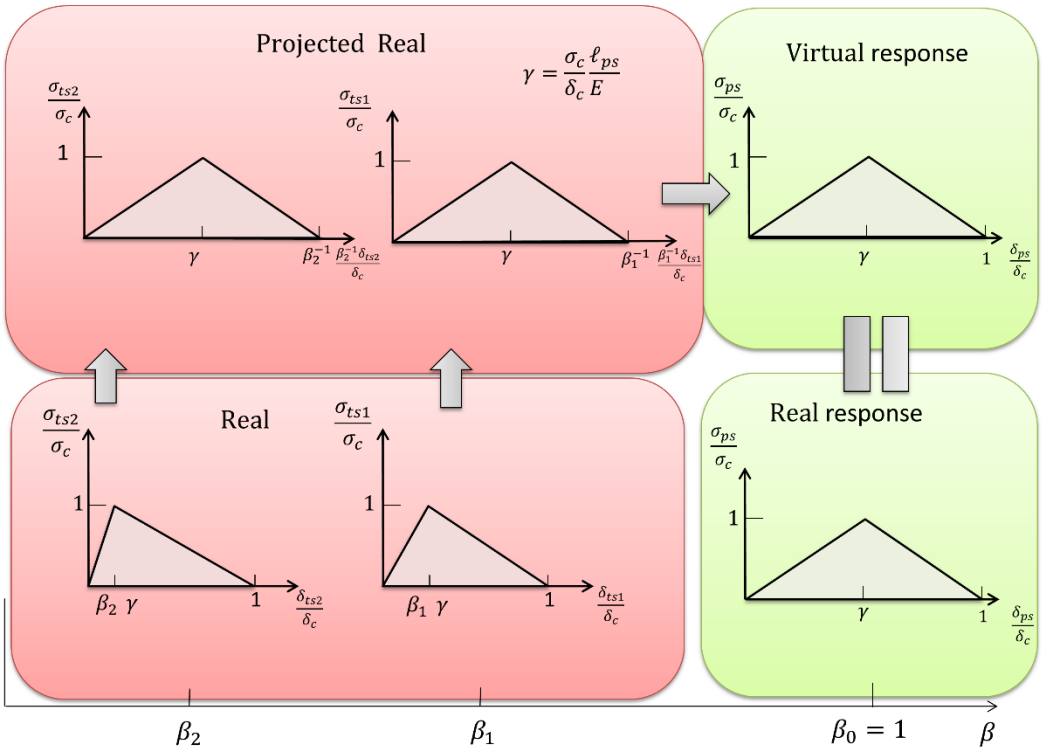

Figure 4.4 Depiction of the combined behaviour of a uniaxially-loaded rod with failure described by a linear cohesive zone model.

4.4 Application of the two-experiment theory

The two-experiment theory introduced in Section 4.3 is tested on classical problems in fracture mechanics to showcase its potential. Although the analysis is performed by means of the finite element method the aim here is to show that scaled testing has the advantage of providing results absent of size effects. This is achieved by combining information from two scaled tests of any size to reconstruct the behaviour of a test of fixed size. The theory provides the rules by which results from the scaled experiments should be interpreted. The finite element method in these studies simply serves to replace results that under normal circumstance would be returned by experiments. This does mean that certain types of behaviour are not fully representable as revealed in the open literature for similar tests comparing simulation with the experimental response [135]. In particular, the pre-crack tends to open earlier in Abaqus models compared to experiment, which means slight differences in deformational response. Despite this difference, peak loads tend to have good agreement [133, 135], which legitimises to some degree fracture toughness investigations with FE methods.

The case studies considered here examine the behaviour of specimens that would normally be used in the evaluation of toughness values K_{IC} and J_C based on procedures from ASTM E399 [25] and E1820 [40], respectively, where J_C is the critical J value at the failure point. The tests considered are compact tension (CT), three-point bending (TPB) and disk-shape compact tension (DCT), which are analysed by means of XFEM. The extended finite element method (XFEM) [136] has the facility for a crack to traverse elements facilitated by the partition of unity concept [137] along with the application of enrichment functions with additional degrees of freedom. The tests involved consider both stationary and propagating cracks with the use of scaled models, and consequently produce behaviours that do and do not change with scale. In particular, the procedure for estimating fracture toughness for a stationary crack readily scales yet propagating cracks can suffer changes with scale. In this way the tests assess the ability of the new theory to capture the different types of behaviours

under a single unified approach. The analysis approaches presented in this study replicate similar studies in the open literature; see for example, CT tests in references [135] and [138], TPB tests in references [132] and [135], and DCT tests in reference [133]. All the analysis presented below is quasistatic and all models are created in the commercial finite element software ABAQUS, the models are applied for an identical material, aluminium with material properties listed in Table 4.1. The displacement of failure of traction and separation law is fixed to be 0.2mm for all specimens, which should generally vary between 0.12mm to 0.3mm according to the structure size. It is set to be a fixed median value here for the scale invariance of the scaling theory. In a general scaling experiment with the same material, numerical simulation cannot detect the size effect, where the geometry and boundary conditions are restricted by size, and the input material properties are identical. So, the fixed failure displacement also aims to simulate the size effect in the numerical tests, which is the other primary purpose of the test. The value can make the model easier to fail on a large scale (failure displacement from 0.3mm to 0.2mm), and the opposite in a small-scale model (failure displacement from 0.12mm to 0.2mm). This operation cannot be regarded as the actual size effect, but it will display the material behaviour in different sizes close to the size effect. Obviously, the errors will appear in the simulation, which is even more significant than the real size effect. As it uses identical material numerically, the first-order theory is supposed to vanish the error caused by the 'size effect', that the criterion of the simulation should be Error $< 1\%$. (It leaves some space for non-linearity and element distribution difference in scaled models)

Table 4.1 Material properties of Aluminum used in the tests

Material properties	

Young's Modulus, E (MPa)	70000
Poisson's ratio, ν	0.33
Maximum Principal stress, σ_c (MPa)	310
Displacement at failure, δ_c (mm)	0.2
Yield stress, σ_Y (MPa)	276
Plastic strain (yield stress), ε_Y	0
Tensile strength σ_{TS} (MPa)	310
Plastic strain (tensile strength), ε_{TS}	0.06

Note that the maximum principal tensile stress σ_c [139] in Table 4.1 is utilized by the XFEM feature within Abaqus to control the initiation and direction of crack propagation [140]. It is founded on the assumption that material failure results when the maximum value of principle tensile stress reaches σ_c, which in this study is set to the tensile strength σ_{TS} in accordance with previous studies [141, 142]. The test specimens employed conform to ASTM code recommendations for geometric constraints, e.g., $0.45 < \frac{a}{W} < 0.55$, $2 \leq \frac{W}{B} \leq 4$, the size of the notch $\leq \frac{W}{10}$, pre-crack length $> 0.025W$, along with other constraints, where the initial crack length is a, the specimen width is W and the specimen thickness is B.

4.4.1. Compact tension specimen

Although, as mentioned above, one objective is the evaluation of toughness values K_{IC} and J_{IC} following the procedures set out in ASTM E399 and E1820, all specimens are loaded well beyond critical loads. Loading of the specimens in this way ensures that more challenging behaviours emerge with crack propagation. All simulation is performed using the commercial finite element software package Abaqus. The compact tension model analysed is presented in Fig. 4.5, detailing mesh and the pre-crack plane inserted along the notch. All dimensions are in accordance with ASTM E399 and input properties for the model are provided in Table 4.1. The element type is C3D8R and to ensure representative fracture toughness testing the specimen is divided into three meshed partitions around the crack. The element size in the crack-

tip, crack and global partitions is 0.5, 1 and 2mm, respectively.

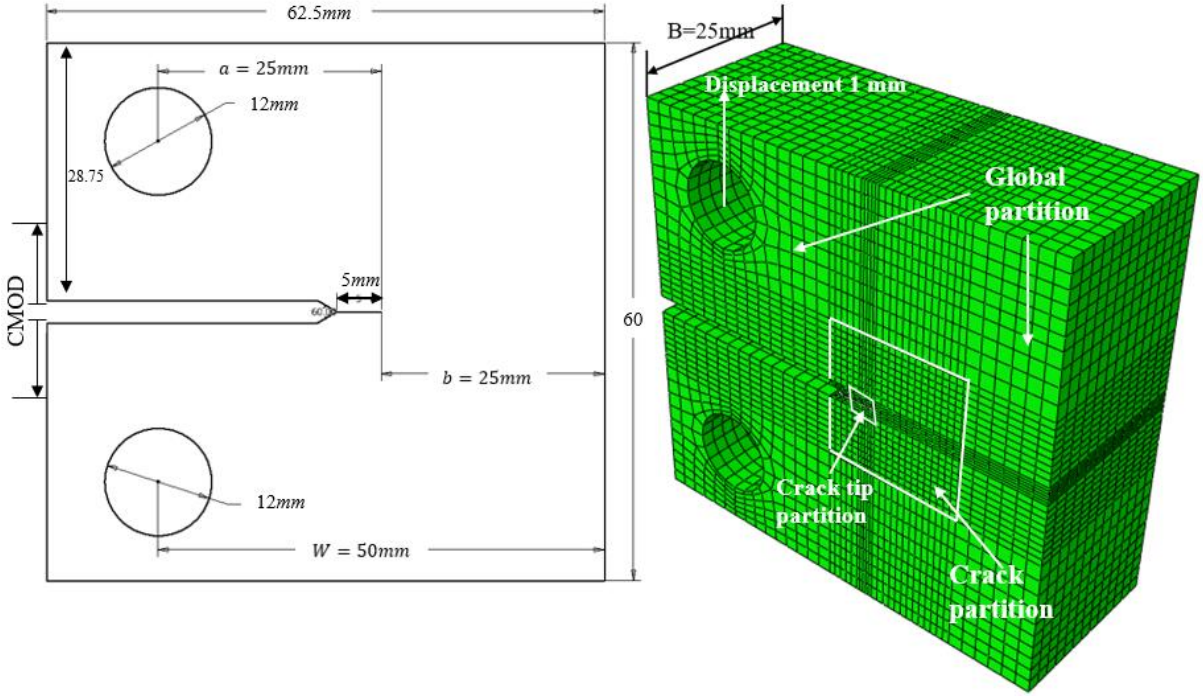

Figure 4.5 Overall dimensions and mesh for the compact tension model.

Depicted in Fig. 4.6 is the von Mises stress field at three instances during loading with the right-hand figure corresponding to a 1mm displacement of the loading point. This loading ensures that the crack has propagated beyond peak loading and the crack has advanced a good distance along the specimen. Note that in addition to plastic dissipation in the bulk material, localised energy dissipation through tearing at the crack tip is accommodated indirectly in XFEM by the absorption of cohesive energy as the crack propagates.

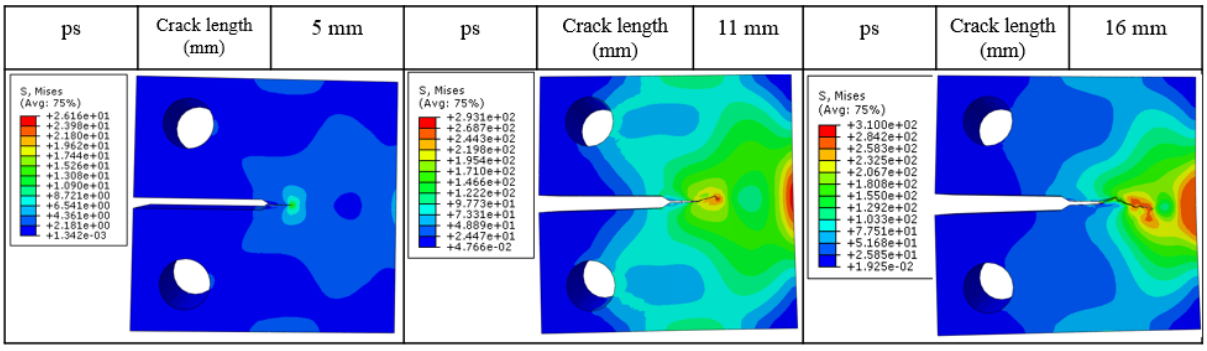

Figure 4.6 Von-Mises stresses for the deformed full-size CT specimen at three crack lengths.

The maximum principal stresses for all the scales considered at peak loading are shown in Fig. 4.7. It is of interest to observe that the cracks follow different paths in

the scaled specimens, which is something expected in real tests and influenced here by differences in the stress fields. Also shown are the stress levels for the virtual model on combination of the results from two scales, which provides a good match with the physical-space model. The stress allocation in the virtual model in Fig. 4.7 is governed by the relationship

$$\boldsymbol{\sigma}_{ps} = \alpha_{01}^{v} g_1 \beta_1^2 \boldsymbol{\sigma}_{ts1} + R_1 \left(\alpha_{01}^{v} g_1 \beta_1^2 \boldsymbol{\sigma}_{ts1} - \alpha_{02}^{v} g_2 \beta_2^2 \boldsymbol{\sigma}_{ts2}\right) \tag{4.11}$$

for the situation where $\beta_1 = 0.7$ and $\beta_2 = 0.2$ and is identified under the contour scale headed "analytical", with the numerical scale provided by Abaqus.

Under quasistatic loading the combination of results from scaled experiments suffers some flexibility since time does not feature. However, for consistency, an artificial time scale is applied to all experiments varying from zero to one with data recorded at every 0.04 units of time.

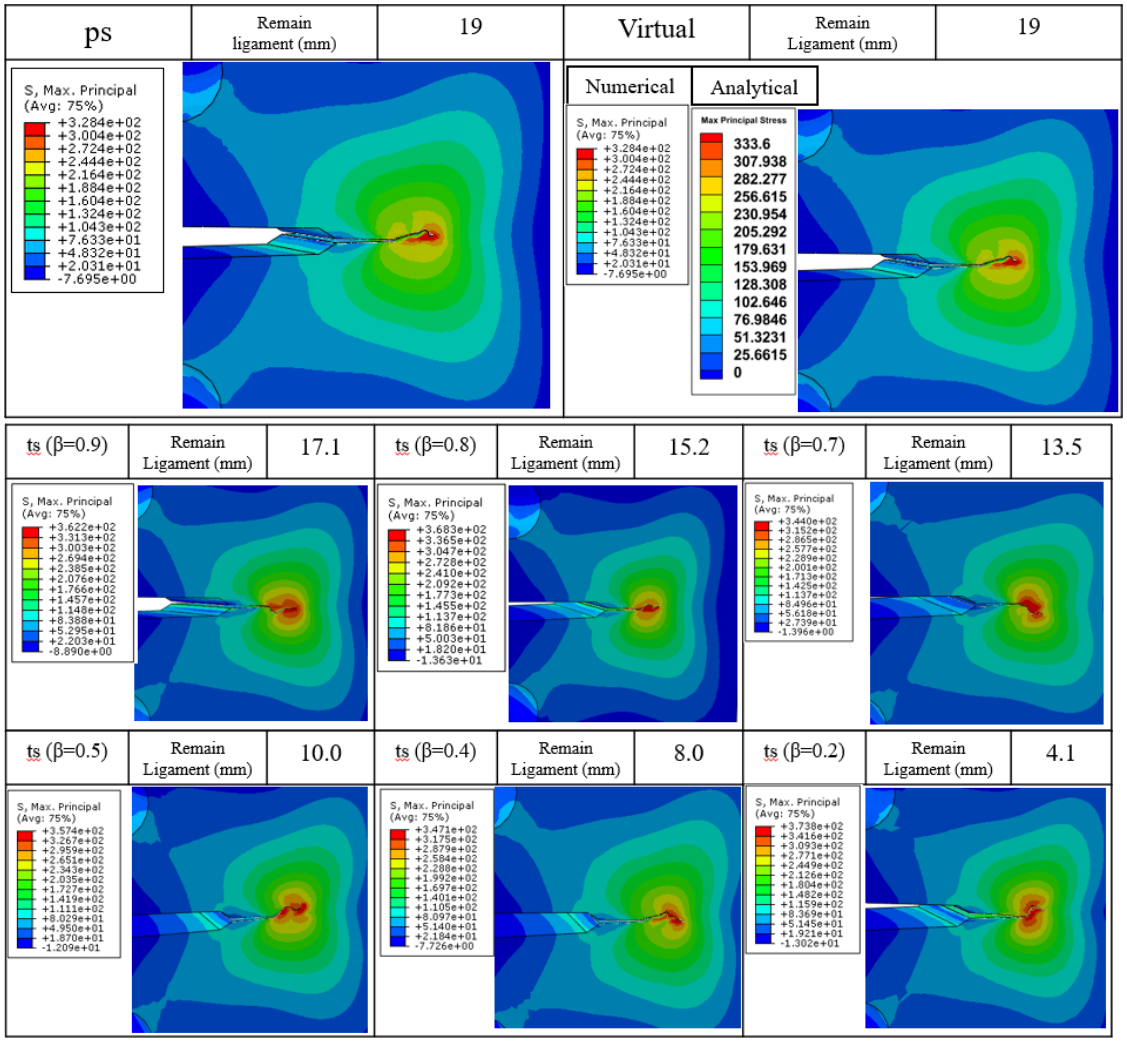

Figure 4.7 The deformed compact tension model in different scales.

- Determination of toughness value K_{IC}

According to the procedure outlined in ASTM E399, the toughness value K_{IC} can be calculated from the load-crack mouth opening displacement curve (CMOD). The CMOD is shown in Fig. 4.5 and is directly determinable through the vertical displacement of a point on the crack mouth in this Mode I fracture test. The properties and dimensions pertaining to the physical-space (full-size) and trial-space (scaled) specimens are listed in Table 4.2. The load-displacement data for all the specimens is obtained on noting the reaction force and applied displacement at the loading point; the data retrieved from the finite element models is presented in Fig. 4.8.

Table 4.2 Specimen dimensions for CT models at different scale.

	β	Initial crack size a (mm)	Specimen width W (mm)	Specimen thickness B (mm)	Ligament length $b = W - a$ (mm)	Specimen height (mm)	Pre-crack length (mm)	Critical displacement at peak load (mm)
Physical	1.0	25.0	50	25.0	25.0	60	5.0	0.60
Trial	0.9	22.5	45	22.5	22.5	54	4.5	0.552
	0.8	20.0	40	20.0	20.0	48	4.0	0.504
	0.7	17.5	35	17.5	17.5	42	3.5	0.456
	0.5	12.5	25	12.5	12.5	30	2.5	0.36
	0.4	10.0	20	10.0	10.0	24	2.0	0.312
	0.2	5.0	10	5.0	5.0	12	1.0	0.216

As the failure displacement of the element is fixed, the load-displacement curves display different shapes between different scales. Same appearance is shown in Fig. 4.7 and Table 4.2, the remain ligament length and critical displacement are not proportional with size. It becomes hard to fail when β decreases, and the individual experiment method (zeroth order) cannot return the scaled results to physical result accurately. The load-displacement curves show linearity at the beginning, where the crack does not start to propagate, as the first step in Fig. 4.6 showed. Then it displays yielding and blunting and drops with crack growth.

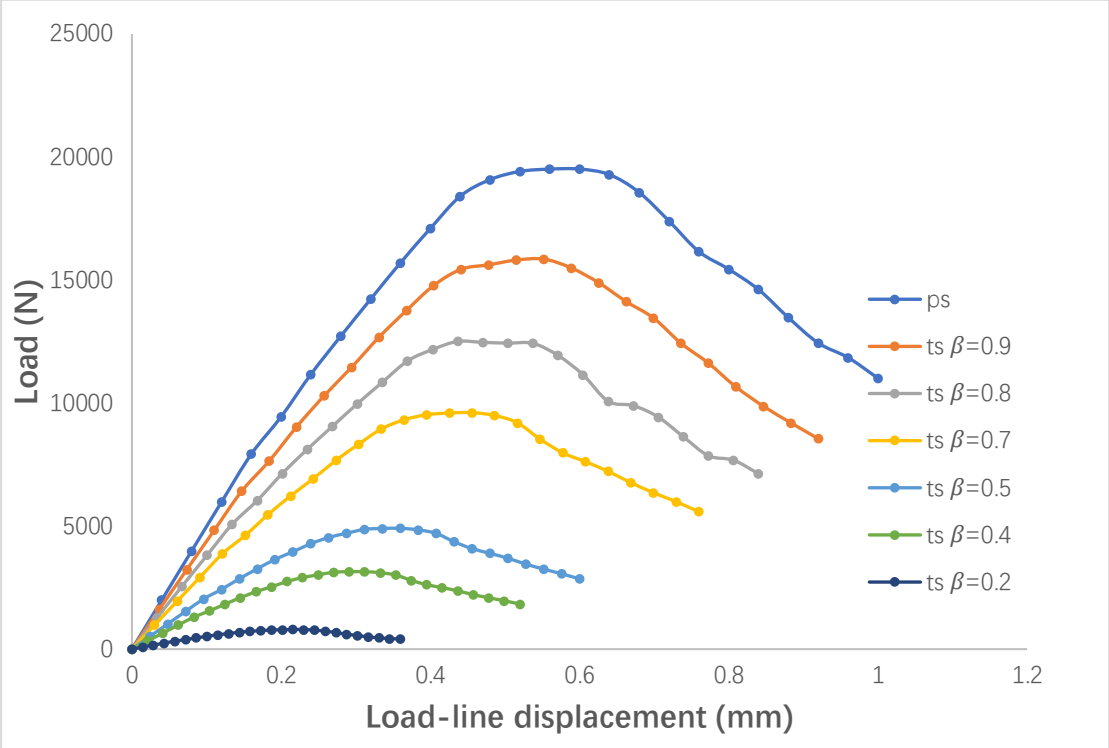

Figure 4.8 Load-displacement results for the CT specimens returned from Abaqus finite element models.

The calculation of the K_{IC} is predominantly related to the force P_Q identified by the curves presented in Fig. 4.9 [30]. The 95% secant line is the line that passes through the zero and has a gradient equal to 95% of the tangent line for the load-CMOD curve. The tangent line is determined automatically in this study on recording the deviation of the gradient of the load-CMOD curve as depicted in Fig. 4.9(b). As indicated in the figure, P_Q is the point located on load-CMOD curve and the 95% secant line but satisfying the condition that $P_{max}/P_Q \leq 1.1$. The toughness value K_{IC} is calculated from the simple relationship,

$$K_{IC} = \frac{P_Q}{\sqrt{WBB_N}} f\left(\frac{a}{W}\right) \tag{4.12a}$$

where $B_N = B$ for the non-groove models and the shape function f for the CT model depicted in Fig. 4.5 is given by

$$f\left(\frac{a}{W}\right) = \frac{(2+\frac{a}{W})\left[0.886+4.64\frac{a}{W}-13.32\left(\frac{a}{W}\right)^2+14.72\left(\frac{a}{W}\right)^3-5.6\left(\frac{a}{W}\right)^4\right]}{\left(1-\frac{a}{W}\right)^{3/2}} \quad (4.12b)$$

and where for $\frac{a}{W}=\frac{1}{2}$ the shape function equates to $f\left(\frac{a}{W}\right)=9.66$.

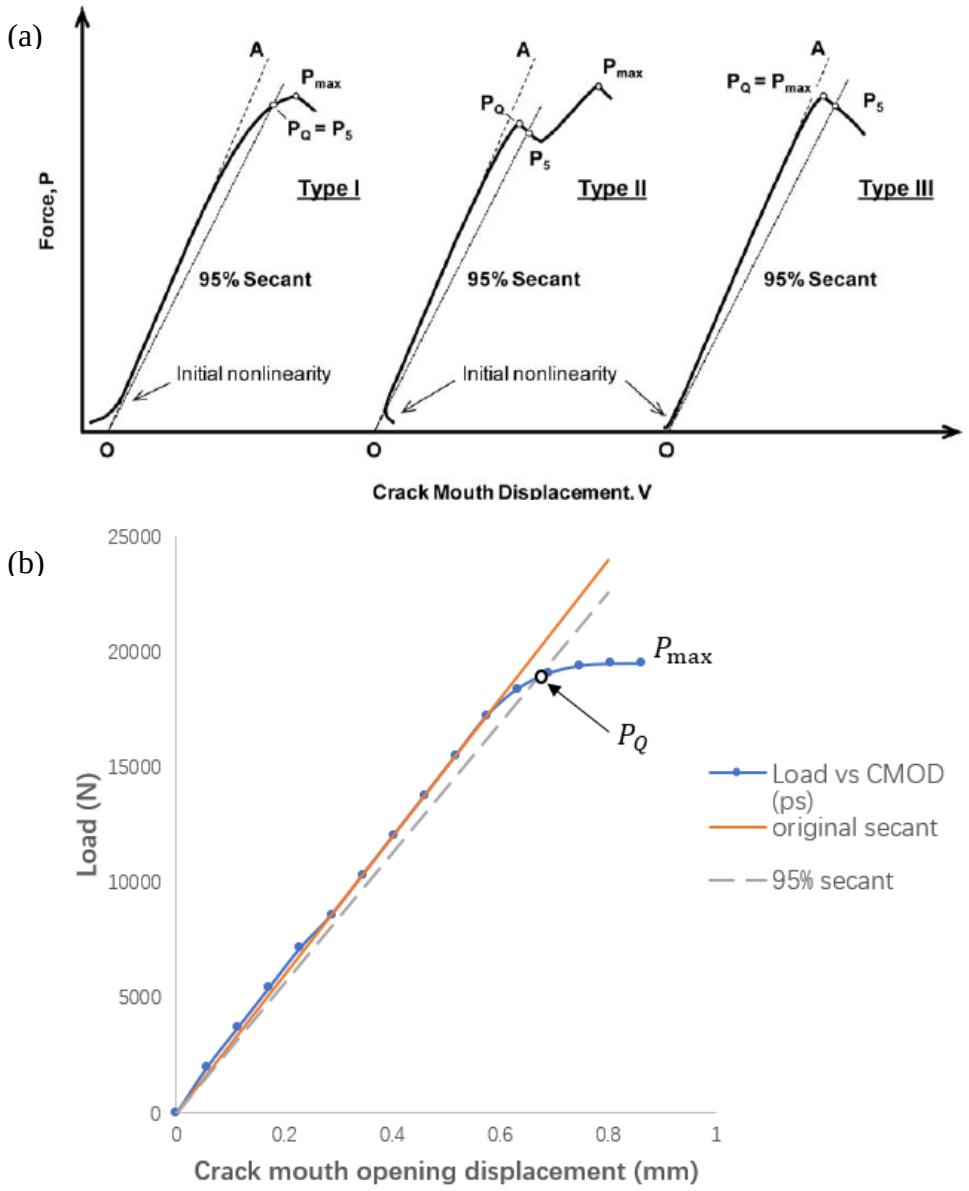

Figure 4.9 Principal types of load-CMOD records [30].

Note that although Eq. (4.12) can be applied at any scale, possessing a feature that does not change with scale (i.e., the function f) and one that is easily predicted (i.e., $\sqrt{WBB_N}$), it does however feature a term that possesses some degree of uncertainly

(i.e., P_Q) and hence the need for experimentation (or modelling). Although the value of P_Q can reasonably be expected to scale the two-experiment scaling theory is nevertheless applied here to accommodate P_Q on setting the scaling factor $\alpha_0^v g$ to β^{-2} as discussed in Sec. 4.3, with R_1 obtained from Eq. (4.1b). The values of $\alpha_0^v g$ and R_1 for the selected values of β_1 and β_2 used for the scaled models are recorded in Table 4.3.

Table 4.3 Scaling factors $\alpha_0^v g$ and R_1 for different combinations of β_i.

Case	β_1	β_2	$\alpha_{01}^v g_1$	$\alpha_{02}^v g_2$	R_1
Case1	0.9	0.5	1.234568	4.00	0.125000
Case2	0.9	0.4	1.234568	6.25	0.080000
Case3	0.9	0.2	1.234568	25.00	0.028571
Case4	0.8	0.5	1.562500	4.00	0.333333
Case5	0.8	0.4	1.562500	6.25	0.200000
Case6	0.8	0.2	1.562500	25.00	0.066667
Case7	0.7	0.5	2.040816	4.00	0.750000
Case8	0.7	0.4	2.040816	6.25	0.400000
Case9	0.7	0.2	2.040816	25.00	0.120000

With loads suitably synchronised the appropriate relationship connecting P_Q values across the scales is

$$P_{Qps} = \alpha_{01}^v g_1 P_{Qts1} + R_1 \left(\alpha_{01}^v g_1 P_{Qts1} - \alpha_{02}^v g_2 P_{Qts2}\right) \tag{4.13}$$

where P_{Qps} corresponds to the full-scale virtual model and consequently can be contrasted with results obtained directly at full scale.

There are two methods for obtaining P_Q, one is with Eq. (4.13), and the other is directly by applying the method in Fig. 9 to the virtual curve formed using the relationships

$$P_{ps} = \alpha_{01}^v g_1 P_{ts1} + R_1(\alpha_{01}^v g_1 P_{ts1} - \alpha_{02}^v g_2 P_{ts2}) \tag{4.14a}$$

$$u_{ps} = \beta_1^{-1} u_{ts1} + R_1(\beta_1^{-1} u_{ts1} - \beta_2^{-1} u_{ts2}) \tag{4.14b}$$

which combines the trial-space results according to the new theory.

Results from both approaches are tabulated in Table 4.4, where not too unexpectedly, obtaining values from the virtual curve provides the greatest accuracy as this matches the procedure in the physical space.

Table 4.4 P_Q and K_{IC} values for different cases for the CT specimen.

Case	P_Q in trial spaces		P_Q Eq. (28) (N)	Error %	P_Q (Virtual curve) (N)	Error %	K_{IC} $(MPa\ m^{\frac{1}{2}})$ Eq. (27)
	P_{Qts1} (N)	P_{Qts2} (N)					
ps			19000.00		19000.00		32.83
Case 1	15400	4800	18988.89	-0.06	19000.00	0.00	32.83
Case 2	15400	3100	18983.33	-0.09	19000.00	0.00	32.83
Case 3	15400	775	19001.98	0.01	19000.00	0.00	32.83
Case 4	12200	4800	19016.67	0.09	19000.00	0.00	32.83
Case 5	12200	3100	19000.00	0.00	19000.00	0.00	32.83
Case 6	12200	775	19041.67	0.22	19000.00	0.00	32.83
Case 7	9400	4800	19171.43	0.90	19000.00	0.00	32.83
Case 8	9400	3100	19107.14	0.56	19000.00	0.00	32.83
Case 9	9400	775	19160.71	0.85	19000.00	0.00	32.83

The value of toughness K_{IC} listed in Table 4 is determined using Eq. (4.15) with the virtual P_Q value (i.e., $19kN$) but equally Eq. (4.13) can be used, but additionally the following relationship also applies

$$K_{ICps} = \alpha_{01}^{v} g_1 \beta_1^{3/2} K_{ICts1} + R_1 \left(\alpha_{01}^{v} g_1 \beta_1^{\frac{3}{2}} K_{ICts1} - \alpha_{02}^{v} g_2 \beta_2^{\frac{3}{2}} K_{ICts2} \right) \tag{4.15}$$

which provides an alternative (to Eq. (4.28)) but identical means to determine the virtual K_{IC} values.

- Determination of the critical value J_C

According to the procedure outlined in ASTM E1820 [40], J can be assumed to consist of an elastic and plastic component and takes the form $J = J_{el} + J_{pl}$. The

elastic component J_{el} can be determined directly from the K_I value and is related through the identity

$$J_{el} = \frac{K_I^2(1-v^2)}{E} \tag{4.16a}$$

where E is Young's modulus and v is Poisson ratio, and similarly J_{pl} is obtained from

$$J_{pl} = \frac{\eta A_{pl}}{B_N b_0} \tag{4.16b}$$

where for the CT specimen $\eta = 2 + 0.522\, b_0/W$ and b_0 is the ligament length, $B_N = B$ and A_{pl} is the enclosed area shown in Fig. 9; J_C is returned on setting $K_I = K_{IC}$ and for A_{pl} taking the value for $P = P_{max}$ as depicted in the figure.

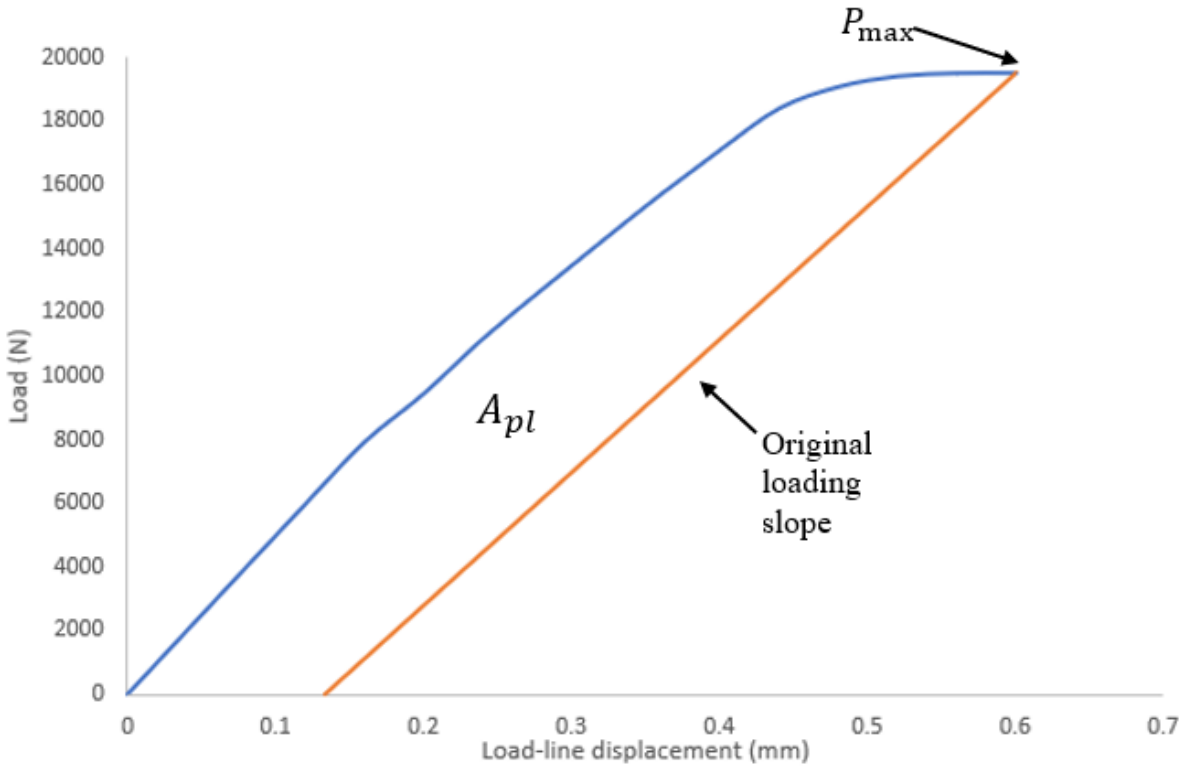

Figure 4.10 Definition of area A_{pl} for J_{IC} determination.

The load-displacement data presented in Fig. 4.8 is combined using Eqs. (4.14) to provide the full-scale (virtual) load-displacement curve depicted in Fig. 4.11. The data presented in Fig. 4.11 is for scales $\beta_1 = 0.8$ and $\beta_2 = 0.5$ with the displacements synchronised by means of identical time intervals (as mentioned above) applied over the displacement range of interest. The load-displacement curves for virtual models are provided in Fig. 4.12 for the scaled model combinations presented in Table 4.4.

These load curves provide the means for the determination of J_C with Eq. (4.16) and the results are presented in Table 4.5.

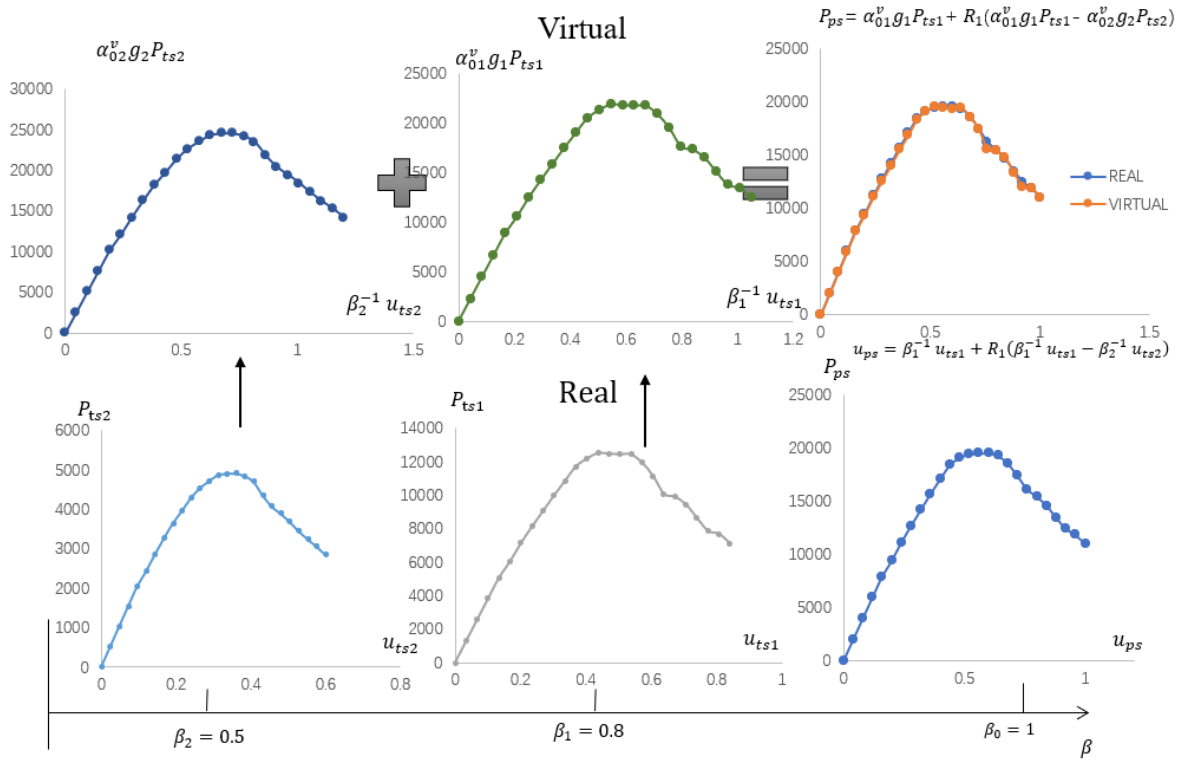

Figure 4.11 Procedure for combination of trial models to form a virtual model.

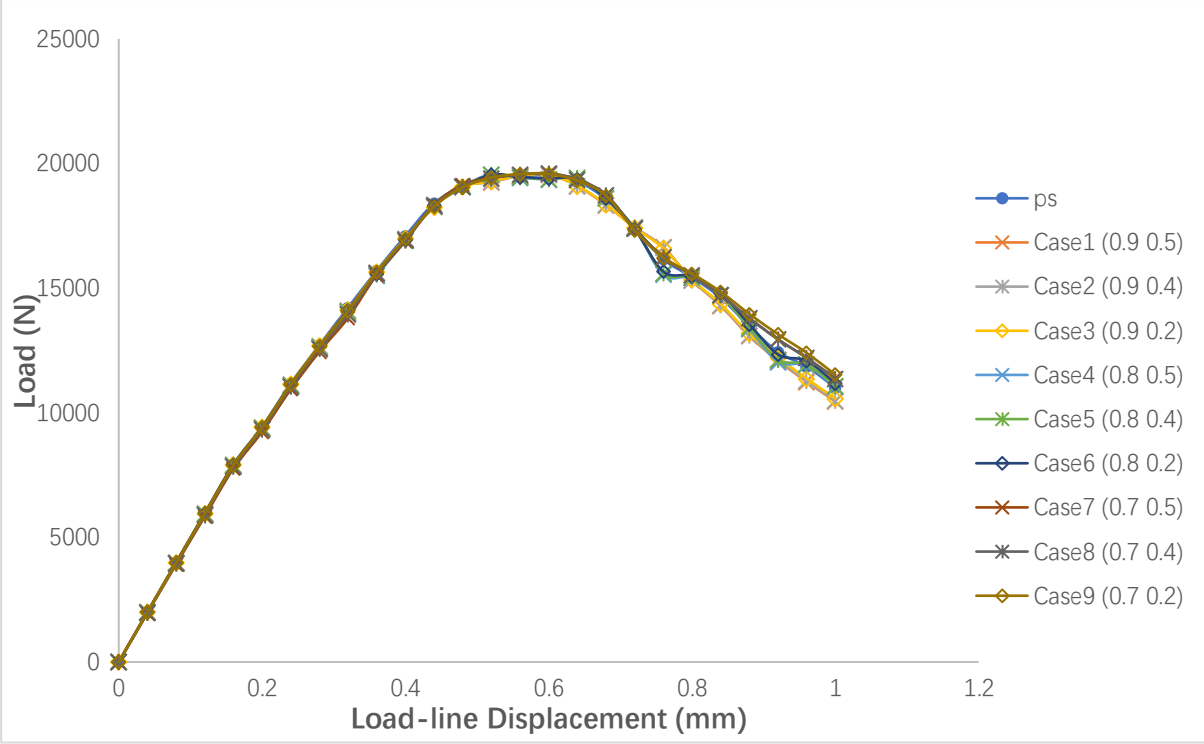

Figure 4.12 Load-displacement curve for the physical and virtual models.

Table 4.5 J_{IC} values for different virtual models for the CT test.

Case	β_1	β_2	J_{el} (kJ/m^2)	J_{pl} (kJ/m^2)	$J_c = J_{el} + J_{pl}$ (kJ/m^2)	Error %
ps			13.62	16.16	29.78	
Case 1	0.9	0.5	13.62	16.03	29.65	-0.42
Case 2	0.9	0.4	13.62	16.05	29.67	-0.38
Case 3	0.9	0.2	13.62	16.07	29.69	-0.31
Case 4	0.8	0.5	13.62	15.99	29.61	-0.58
Case 5	0.8	0.4	13.62	16.03	29.65	-0.45
Case 6	0.8	0.2	13.62	16.07	29.69	-0.30
Case 7	0.7	0.5	13.62	15.91	29.53	-0.83
Case 8	0.7	0.4	13.62	16.00	29.62	-0.52
Case 9	0.7	0.2	13.62	16.09	29.71	-0.23

It is evident on examination of Fig. 4.12 that good replication is returned in the linear and early non-linear parts of the load-displacement curves with deviation appearing during tearing as cracks take slightly different paths in the scaled specimens. Note that an accurate prediction of J_C is associated with the accurate determination of the peak loads and P_Q as noted above. It is possible and of interest to examine the change in value of the J with crack extension. This can be investigated using the ABAQUS output (for crack length) rather than the procedure stated in ASTM E399 since for quasistatic loading J can again be evaluated using Eqs. (4.16) for different values of crack extension, which is measured from the instance that material tearing initiates. The results of this study are presented in Fig. 4.13(a), showing the change in J over the full loading range up to 1mm load-displacement. As anticipated the J-value grows rapidly to the critical value J_{Ic} followed by a decreasing then constant rate of growth. The toughness value J_{Ic} can be defined by a 0.2mm offset construction line and the J-R curve, as shown in Fig. 4.13(b). This is a typical procedure to evaluate J_{Ic} according

to ASTM1820. A blunting construction line is first developed by the function $J = M_J \sigma_Y \Delta a$, where $M_J = 2$ is generally applied here. Then draw a line parallel to the construction line at an offset value of 0.2mm, and the J-value at the intersection point is J_Q. It is normally regarded as J_{Ic} when the qualification of criteria is met [40]. In this case study, the comparison is between J_C at failure rather than J_{Ic} since the former can be calculated with load-displacement data and the equations of J, which has a precise calculation procedure during scaling and simulation with finite similitude. The curves and value of J_C and J_{Ic}all follow a similar trend and provide good supporting evidence for the insensitivity of scale in the prediction.

(a)

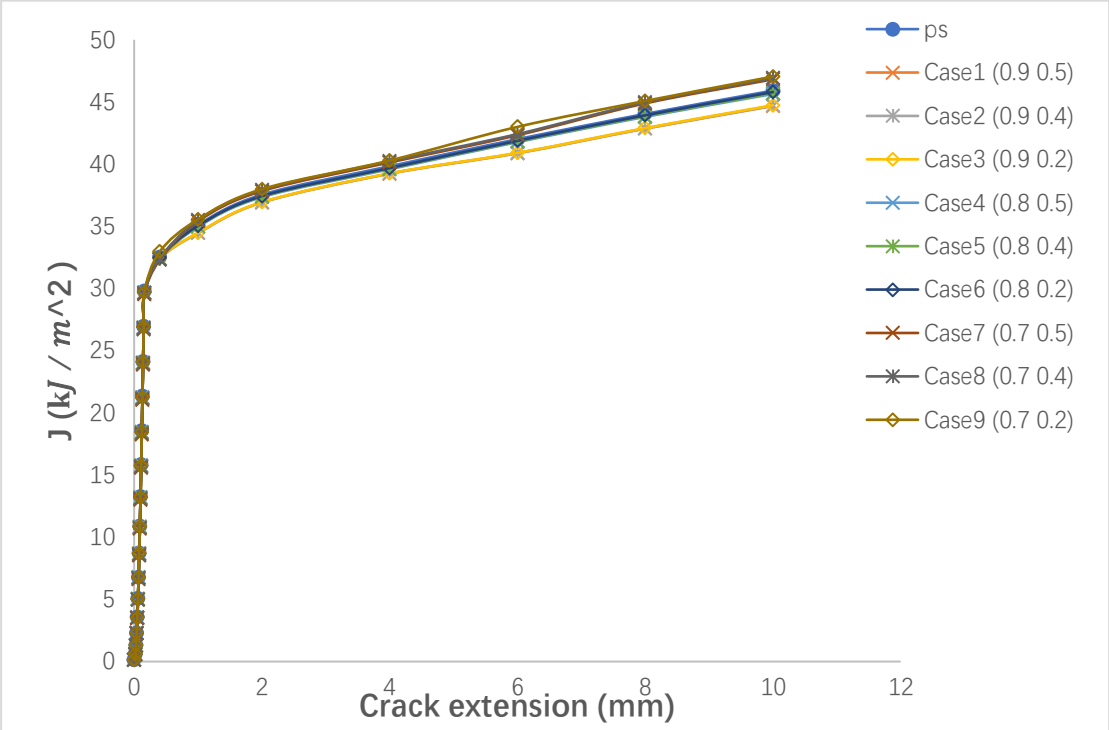

(b)

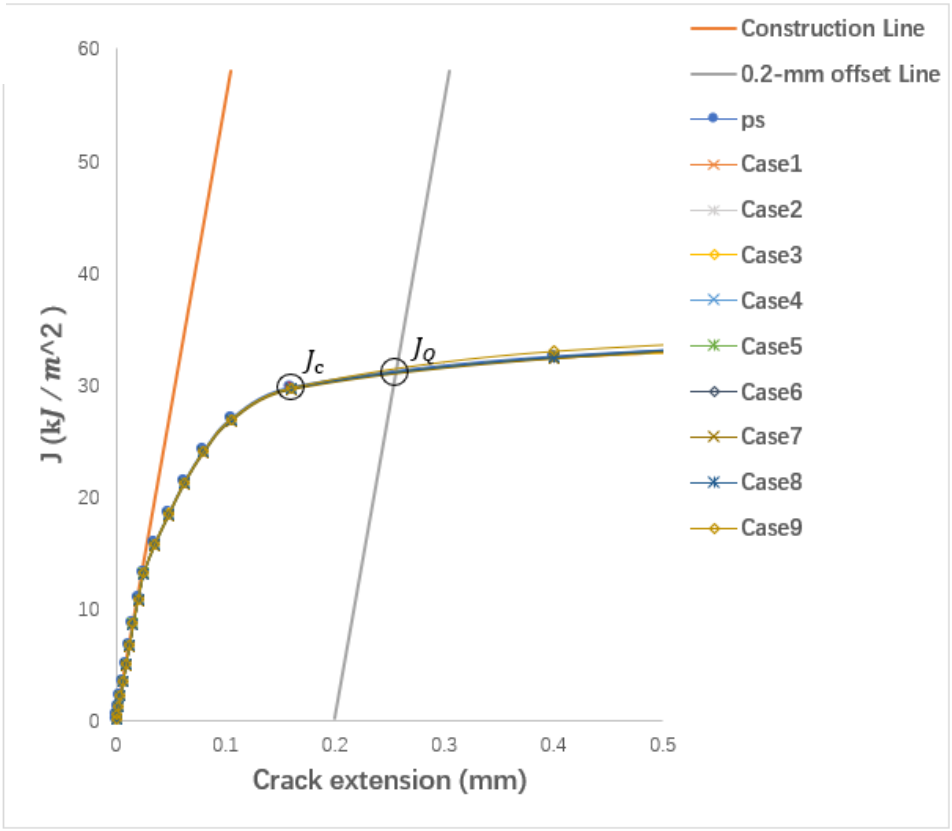

Figure 4.13 (a) J -values with crack length for different combinations of scaled CT models. (b) J_{Ic} evaluation and comparison with J_C

4.4.2. Three-point bending specimen

The testing of the three-point bending (TPB) specimen follows the exact same procedure applied to the CT specimen. The main differences all stem from the geometry of the TPB model, changing the form of some of the equations applied. Outline model details and meshes used for the physical specimen are presented in Fig. 4.14 with further details tabulated in Table 4.6. The mesh-partitioning approach adopted for the TPB model is slightly different to that applied to the CT specimen. A mesh sensitivity investigation for the physical model revealed that a converged mesh consisting of elements of $0.4 \times 0.5mm$ along the notch and crack propagation path, and 2mm lengths as depicted in Fig. 4.5. The deformed physical model for selected load displacements is shown in Fig. 4.15, where the last subfigure corresponds to a maximum load displacement of 2mm. The deformed scaled specimens at maximum load are presented in Fig 4.16, where stress levels and ligament lengths are shown.

The load-deflection data for the physical and trial TPB specimens returned by the Abaqus models is presented in Fig. 4.17.

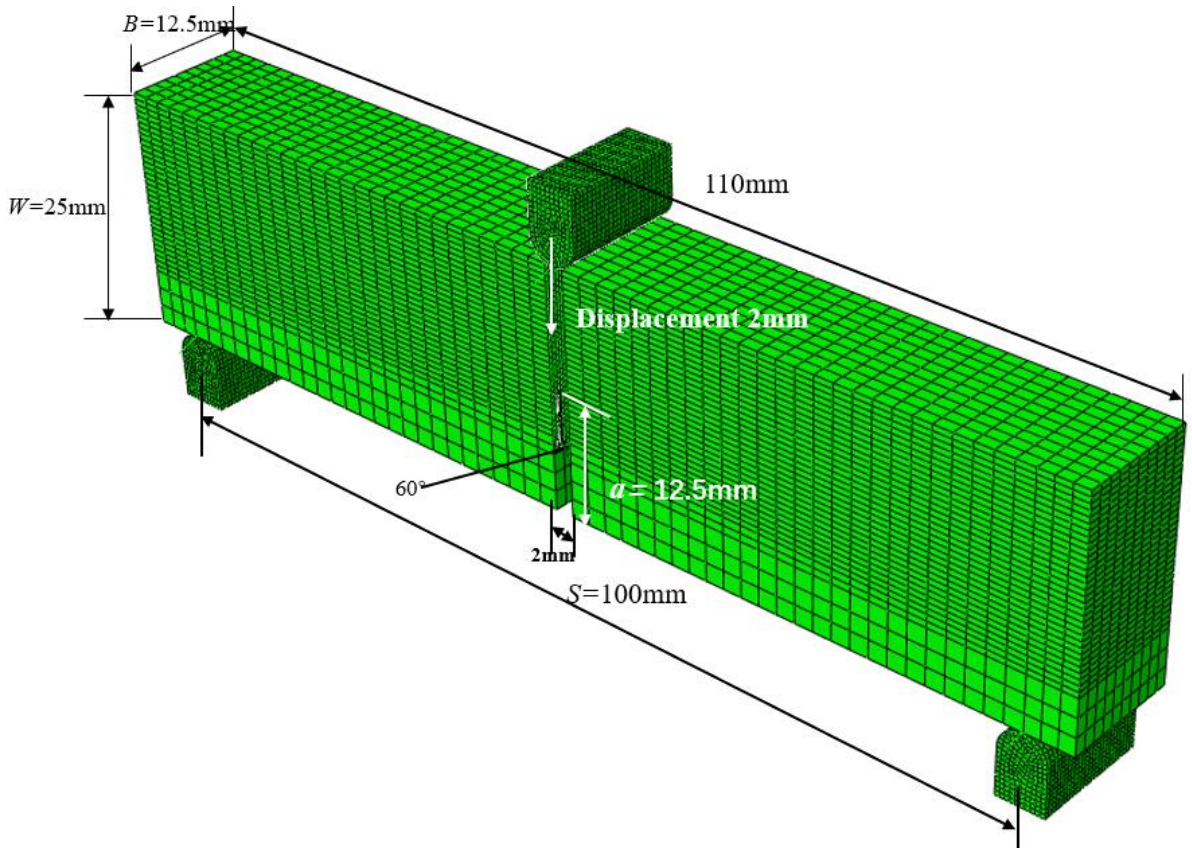

Figure 4.14 Overall dimensions and mesh for the three-point bending model.

Table 4.6 Specimen dimensions for TPB models at different scale.

	β	Initial crack size a (mm)	Specimen width W (mm)	Specimen thickness B (mm)	Ligament length $b = W - a$ (mm)	Specimen Length (mm)	Span of the model S (mm)	Pre-crack length (mm)	Critical displacement at peak load (mm)
Physical	1.0	12.50	25.0	12.50	12.5	110.0	100.0	5.0	0.56
Trial	0.9	11.25	22.5	11.25	11.25	99.0	90.0	4.5	0.51
	0.8	10.00	20.0	10.00	10.00	88.0	80.0	4.0	0.56
	0.7	8.75	17.5	8.75	8.75	77.0	70.0	3.5	0.41

	0.5	6.25	12.5	6.25	6.25	55.0	50.0	2.5	0.31
	0.4	5.00	10.0	5.00	5.00	44.0	40.0	2.0	0.26
	0.2	2.50	5.0	2.50	2.50	22.0	20.0	1.0	0.17

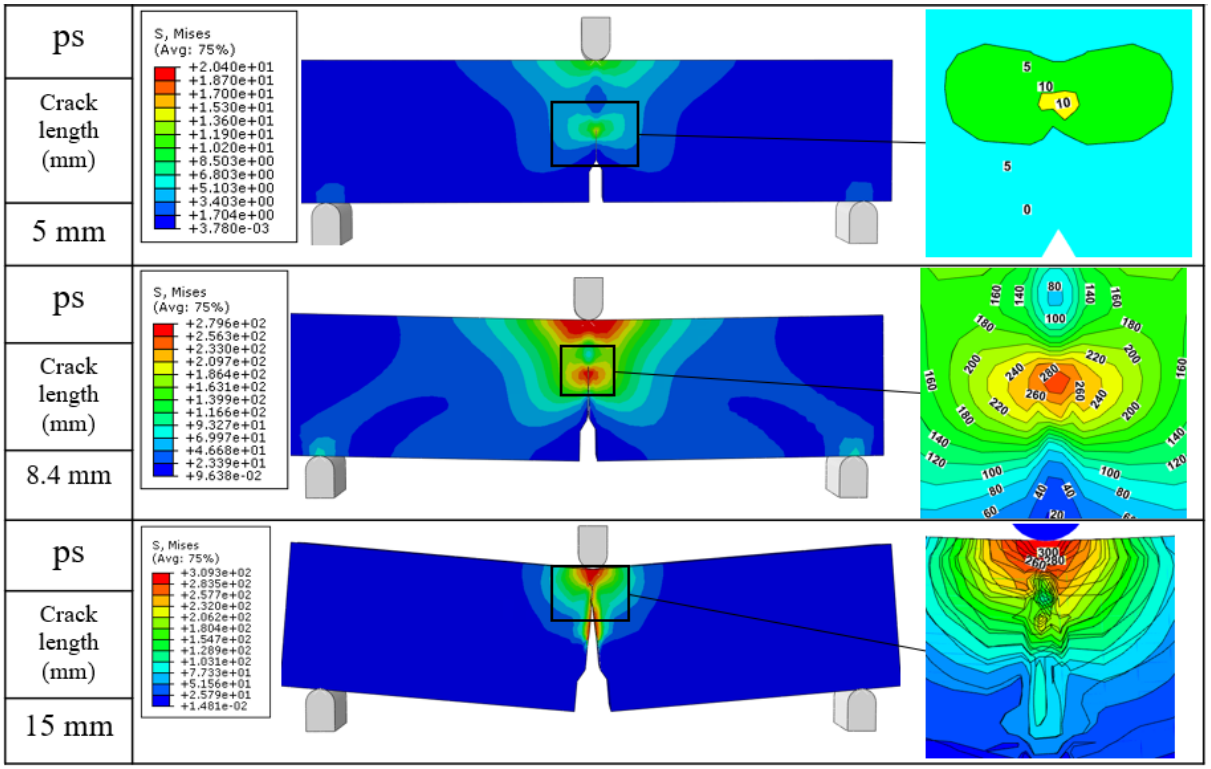

Figure 4.15 Von Mises stress levels for the loaded physical TPB model at different crack lengths.

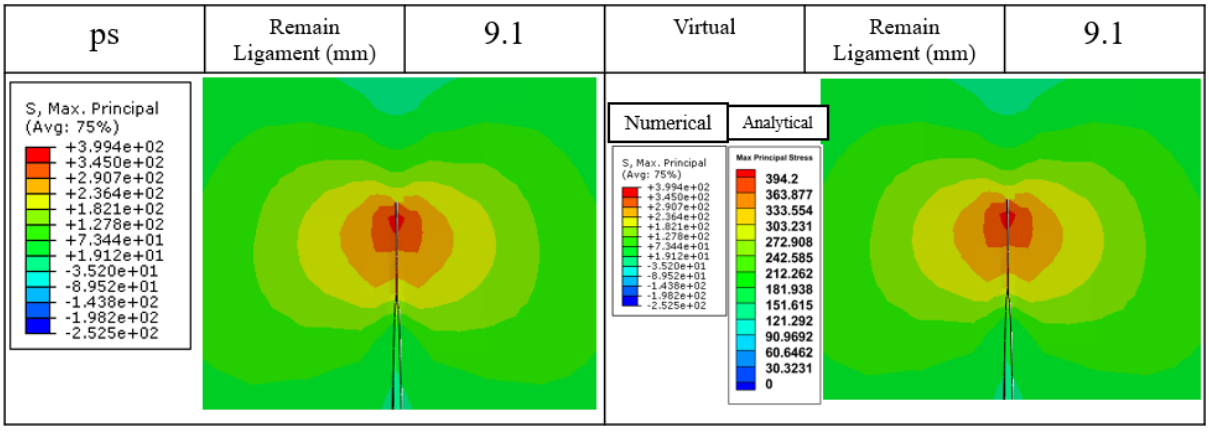

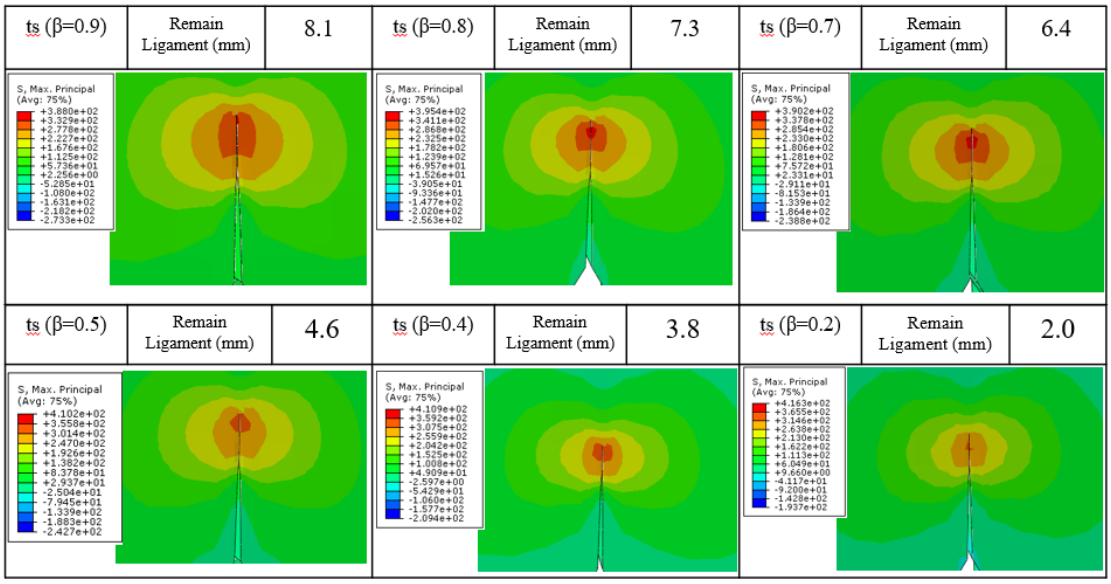

Figure 4.16 Principal stress levels in the loaded TPB models at the crack tip at different scales.

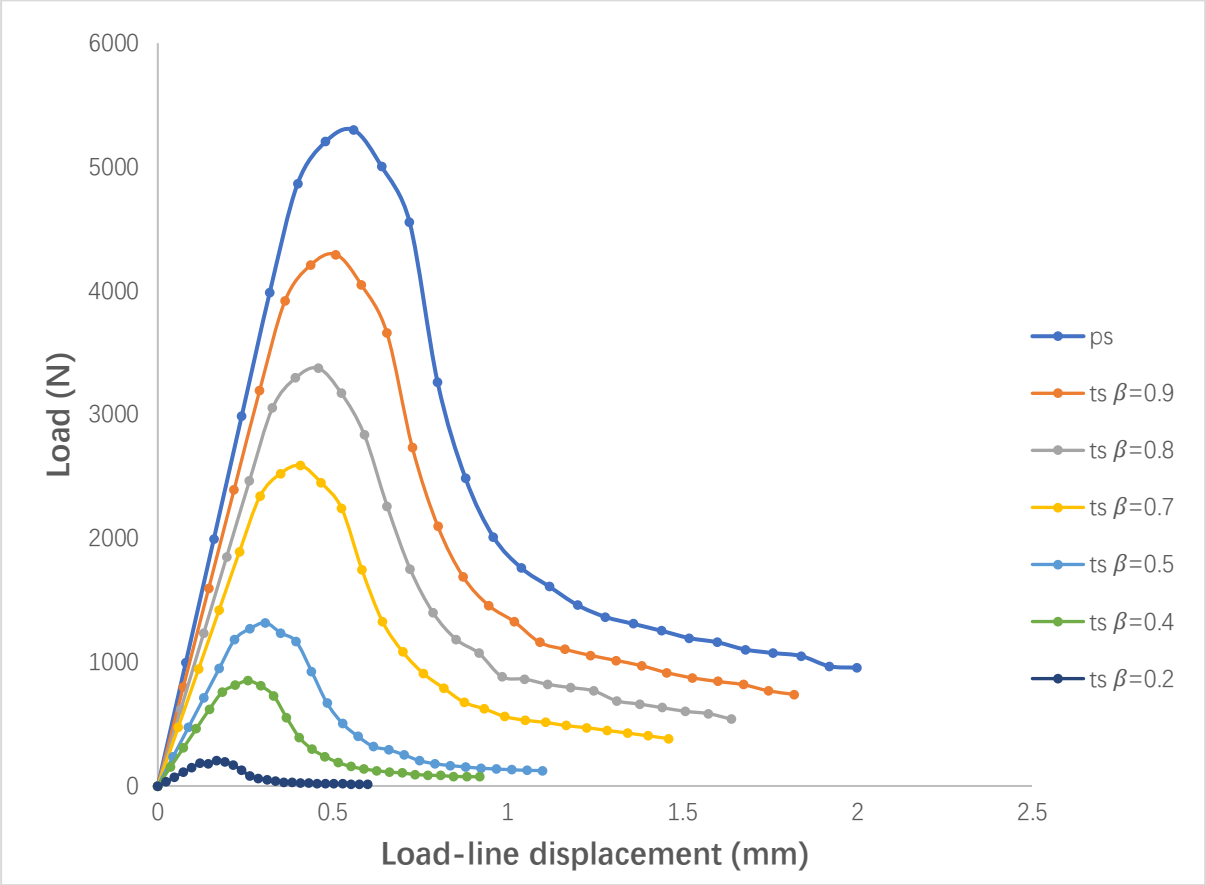

Figure 4.17 Load-displacement results for the TPB specimens returned from Abaqus finite element models.

- Determination of toughness value K_{IC}

For the TPB model the toughness value K_{IC} is determined using the relationships

$$K_{IC} = \frac{P_Q S}{B W^{3/2}} f(\frac{a}{W}) \tag{4.17a}$$

$$f\left(\frac{a}{W}\right) = \frac{3\sqrt{\frac{a}{W}}\left[1.99 - \frac{a}{W}(1-\frac{a}{W})\left[2.15 - 3.93\frac{a}{W} + 2.7\left(\frac{a}{W}\right)^2\right]\right]}{2\left(1+2\frac{a}{W}\right)\left(1-\frac{a}{W}\right)^{3/2}} \tag{4.17b}$$

where S is span (see Fig. 4.14) and $f\left(\frac{a}{W}\right) = 2.66$ for $\frac{a}{W} = 0.5$, and the obtained values of P_Q and K_{IC} are listed in Table 7 for various values of β.

Presented in Table 4.7 are the P_Q and K_{IC} values for the virtual models with values obtained using Eqs. (4.13) and (4.17), and from Fig. 4.18, where the values for $\alpha_0^v g$ and R_1 are precisely those presented in Table 4.2 for the CT specimen.

Table 4.7 K_{IC} and P_Q values for TPB specimens in physical and virtual models.

Case	P_Q in the trial space		P_Q Eq. (28) (N)	Error %	P_Q (Virtual curve) (N)	Error %	K_{IC} $(MPa\, m^{\frac{1}{2}})$
	$P_{Qts1}(N)$	$P_{Qts2}(N)$					
ps			5200.00		5200		27.99
Case1	4200	1250	5208.33	0.16	5200	0.00	27.99
Case2	4200	800	5200.00	0.00	5200	0.00	27.99
Case3	4200	200	5190.48	-0.18	5200	0.00	27.99
Case4	3300	1250	5208.33	0.16	5200	0.00	27.99
Case5	3300	800	5187.50	-0.24	5200	0.00	27.99
Case6	3300	200	5166.67	-0.64	5200	0.00	27.99
Case7	2500	1250	5178.57	-0.41	5200	0.00	27.99
Case8	2500	800	5142.86	-1.10	5200	0.00	27.99
Case9	2500	200	5114.29	-1.65	5200	0.00	27.99

- Determination of toughness value J_{IC}

As above, the toughness value J_{IC} is determined using the relationship $J = J_{el} + J_{pl}$

but here $\eta = 1.9$. The value of A_{pl} is calculated in the exact same manner as depicted in Fig. 10. Similarly, the virtual load-displacement curves are presented following the same procedure depicted in Fig. 4.11, with applied scaling factors listed in Table 4.3. The J_C values corresponding to the peak load of the curves shown Fig. 18, are tabulated in Table 4.8. The curves in Fig. 4.18 all follow a similar trend with earlier parts of the curves well matched and greatest deviation in the latter parts associated with crack propagation and with cracks taking different paths in the scaled specimens. The corresponding J values with crack extension are presented in Fig. 4.19, which like the CT specimen are absent of significant scale effects despite some apparent deviations in the latter parts of the curves.

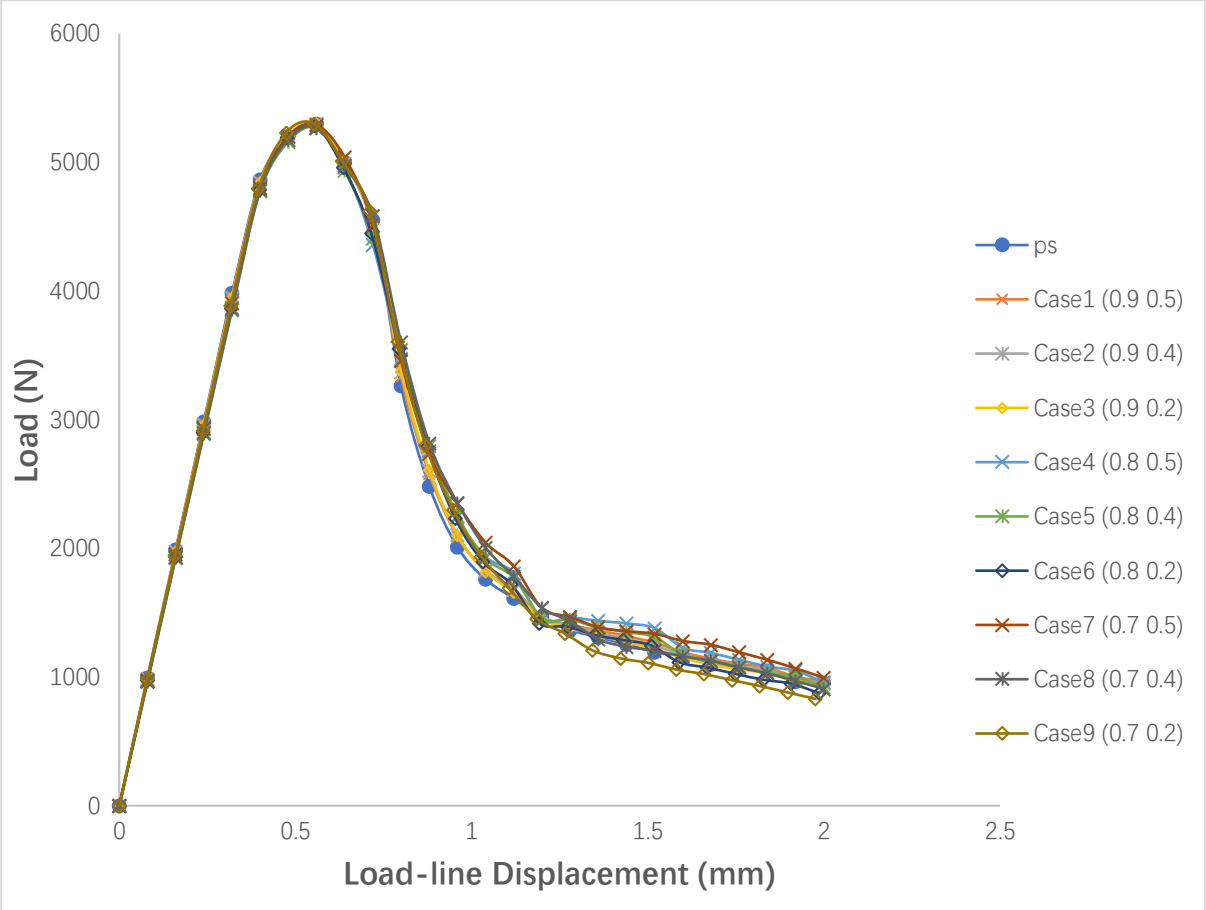

Figure 4.18 Load-displacement curves for physical and virtual models.

Table 4.8 J_C values for different virtual models in TPB test.

Case	β_1	β_2	J_{el} (kJ/m^2)	J_{pl} (kJ/m^2)	$J_c = J_{el} + J_{pl}$ (kJ/m^2)	Error %

PS			10.19	21.83	32.01	
Case1	0.9	0.5	10.19	21.74	31.93	-0.26
Case2	0.9	0.4	10.19	21.71	31.90	-0.37
Case3	0.9	0.2	10.19	21.74	31.93	-0.25
Case4	0.8	0.5	10.19	21.30	31.49	-1.64
Case5	0.8	0.4	10.19	21.26	31.45	-1.77
Case6	0.8	0.2	10.19	21.19	31.38	-1.99
Case7	0.7	0.5	10.19	21.55	31.74	-0.87
Case8	0.7	0.4	10.19	21.41	31.60	-1.28
Case9	0.7	0.2	10.19	21.25	31.44	-1.78

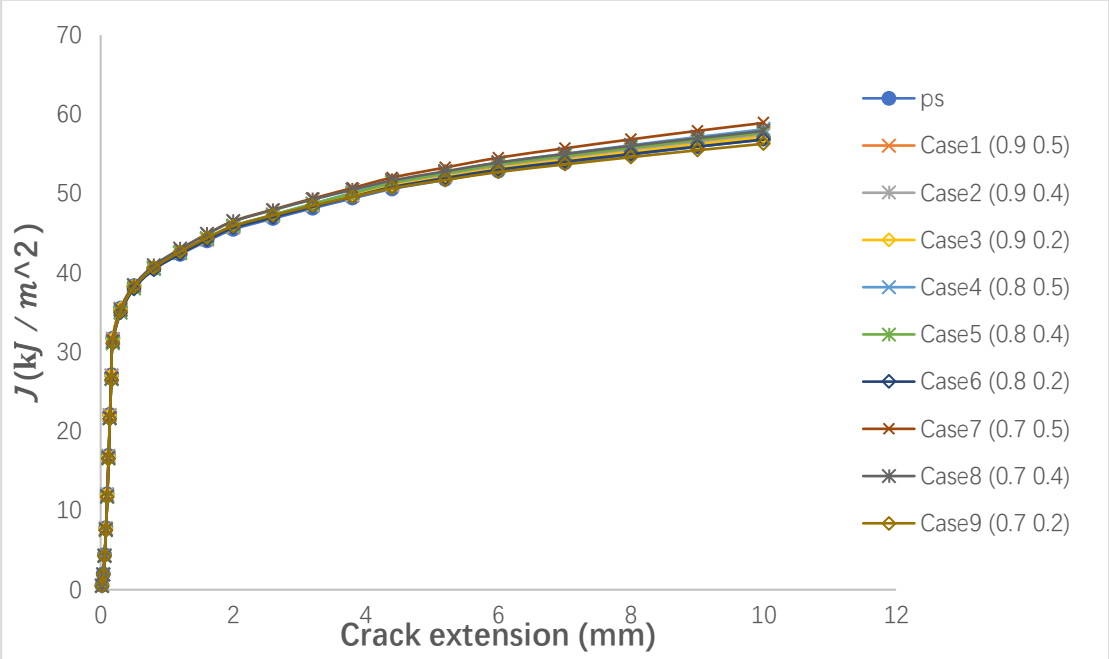

Figure 4.19 J -values for different values of crack length for the physical and virtual TPB models.

4.4.3. Disk-shape compact tension specimen

The disc shape CT (DCT) specimen provides another test described in ASTM E399 and E1820. The geometry of the DCT specimen is similar to the CT specimen with overall dimensions and mesh shown in Fig. 4.20. The dimensions of the scaled trial models are listed in Table 4.9 for convenience. The response of the physical-space specimen under loading is presented in Fig. 4.21, where crack propagation and von Mises stress levels are shown, and where the most deformed state corresponds to a

loading point displacement of 1mm. Similarly at peak load, stress levels for the scaled specimens are shown in Fig. 4.22 along with results for the virtual model formed by means of Eq. (4.26) from the scaled models at $\beta_1 = 0.7$ and $\beta_2 = 0.2$ for the case depicted. Also note in Fig. 4.22 are ligament lengths, which follow similar trends to those observed in the CT and TPB specimens. Similarly, the load-deflection data for the physical and trial DCT specimens retuned by the Abaqus models is presented in Fig. 4.23.

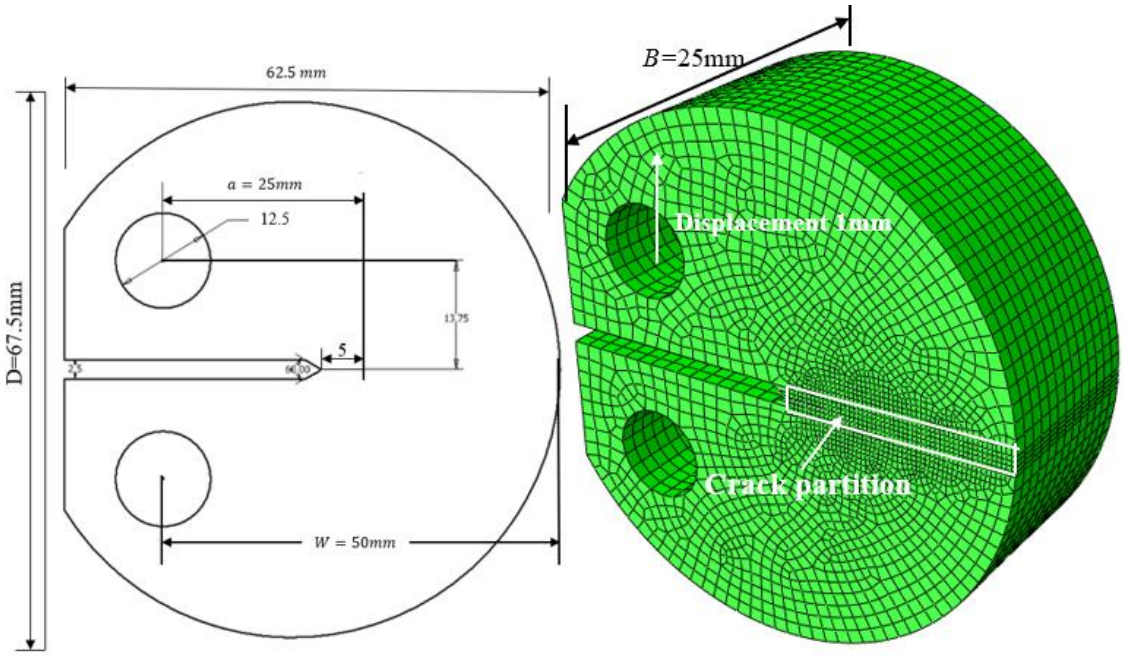

Figure 4.20 Overall dimensions and mesh details for the DCT model.

Table 4.9 Specimen dimensions for TPB models at different scales.

	β	Initial crack size a (mm)	Specimen width W (mm)	Specimen thickness B (mm)	Ligament length $b = W - a$ (mm)	Specimen height (mm)	Critical displacement at peak load (mm)
Physical	1	25.0	50	25.0	25.0	67.5	0.48
Trial	0.9	22.5	45	22.5	22.5	60.75	0.44
	0.8	20.0	40	20.0	20.0	54.00	0.40
	0.7	17.5	35	17.5	17.5	47.25	0.36
	0.5	12.5	25	12.5	12.5	3.75	0.29
	0.4	10.0	20	10.0	10.0	27.00	0.25
	0.2	5.0	10	5.0	5.0	13.50	0.17

The mesh used in the analysis, arrived at following a sensitivity study, is similar to that used for the CT specimen with a fine mesh along the crack propagation path (the crack partition). The global mesh size is set to be 2mm and the crack partition consisted of $0.5\text{mm} \times 0.5\text{mm}$ elements. The properties of the model are listed in Table 4.1, which apply to all the trial models, since identical materials are used throughout.

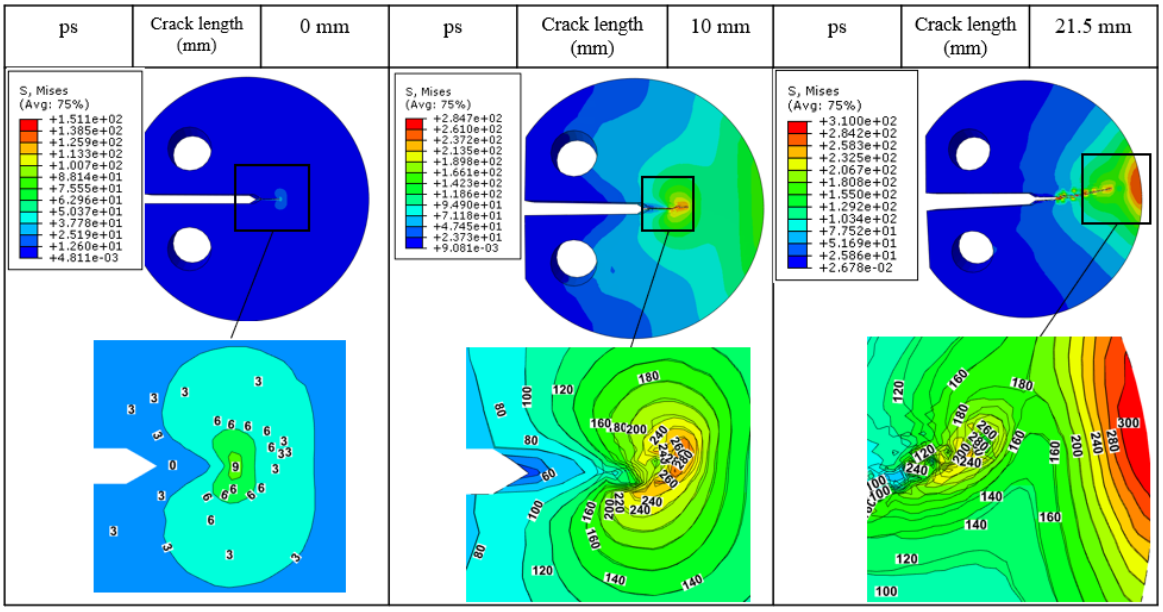

Figure 4.21 Von Mises stress levels for the physical DCT model at various loading stages.

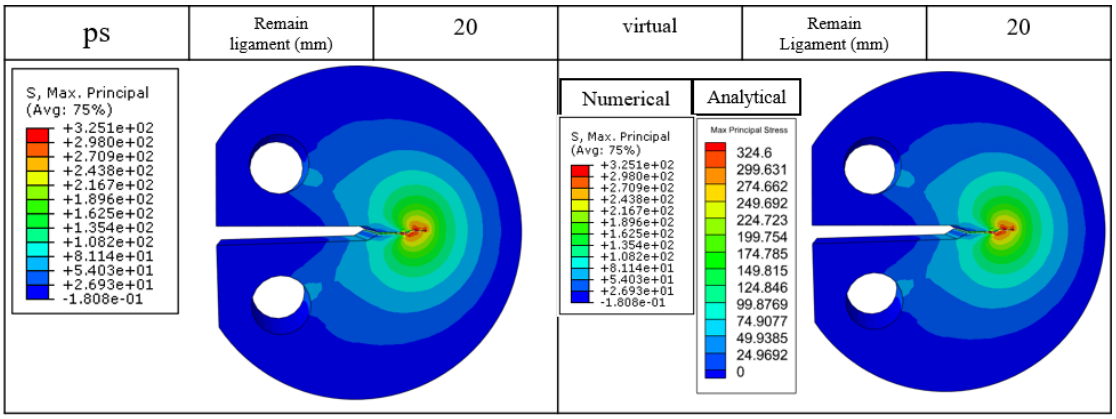

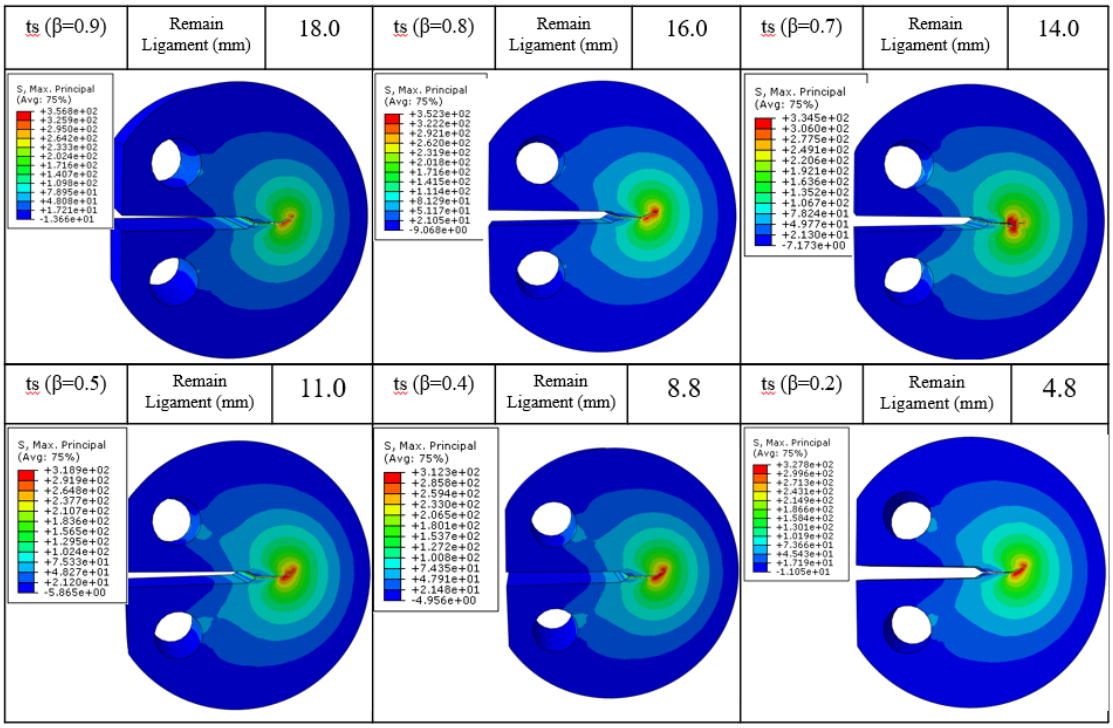

Figure 4.22 Principal stress levels for the DCT model at different scales.

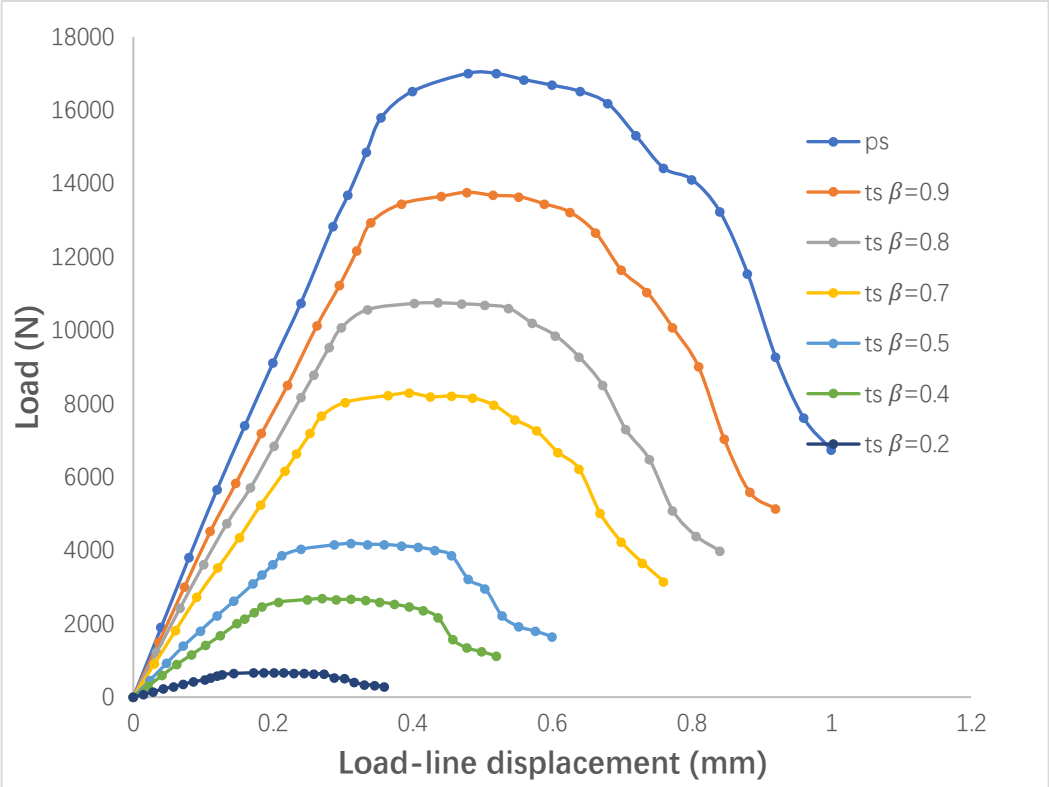

Figure 4.23 Load-displacement results for the DCT specimens returned from the Abaqus finite element models.

- Determination of toughness value K_{IC}

The determination of K_{IC} for DCT specimen is identical to the CT specimen involving Eq. (4.12) but the shape factor

$$f\left(\frac{a}{W}\right) = \frac{(2+\frac{a}{W})\left[0.76+4.8\frac{a}{W}-11.58\left(\frac{a}{W}\right)^2+11.43\left(\frac{a}{W}\right)^3-4.08\left(\frac{a}{W}\right)^4\right]}{\left(1-\frac{a}{W}\right)^{3/2}} \quad (4.18)$$

where $f\left(\frac{a}{W}\right) = 10.17$ with $\frac{a}{W} = \frac{1}{2}$, and presented in Table 4.10 are the corresponding critical loads P_Q and stress intensity factors K_{IC} for the different models.

Note that $\alpha_0^v g = \beta^{-2}$ applies and consequently scaling factors presented in Table 4.3 are pertinent here also. The values returned for P_Q in Table 4.3 are returned with high accuracy with highest accuracy attributable to readings obtained from the virtual curves recovered via Eqs. (4.14).

Table 4.10 K_{IC} and P_Q values for DCT specimens.

Case	P_Q in the trial space		P_Q Eq. (27a) (N)	Error %	P_Q (Virtual curve) (N)	Error %	K_{IC} $(MPa\, m^{\frac{1}{2}})$
	P_{Qts1} (N)	P_{Qts2} (N)					
ps			16000.00		16000		29.11
Case 1	13000	4000	16055.56	0.35	16050	0.32	29.20
Case 2	13000	2600	16033.33	0.21	16050	0.32	29.20
Case 3	13000	640	16050.79	0.32	16050	0.32	29.20
Case 4	10250	4000	16020.83	0.13	16000	0	29.11
Case 5	10250	2600	15968.75	-0.20	16000	0	29.11
Case 6	10250	640	16016.67	0.10	16000	0	29.11
Case 7	7850	4000	16035.71	0.22	16000	0	29.11
Case 8	7850	2600	15928.57	-0.45	16000	0	29.11
Case 9	7850	640	16022.86	0.14	16000	0	29.11

- Determination of toughness value J_C

The determination of J_C is identical to that presented for the CT specimen involving

Eqs. (4.16). The virtual load-displacement curves determined with Eqs. (4.14) and data from Fig. (4.23) (as shown in Fig. 4.11), are presented in Fig. 4.24. The corresponding J_C values for the physical and virtual models are tabulated in Table 4.11, where values are returned with good accuracy. In addition, J values with crack extension are provided in Fig. 4.25, and overall, the results follow a similar trend to those presented with other specimens. Although some deviation is apparent in the latter parts of the curves, arising primarily from deviations in crack paths in the scaled specimens, scale effects are essentially absent.

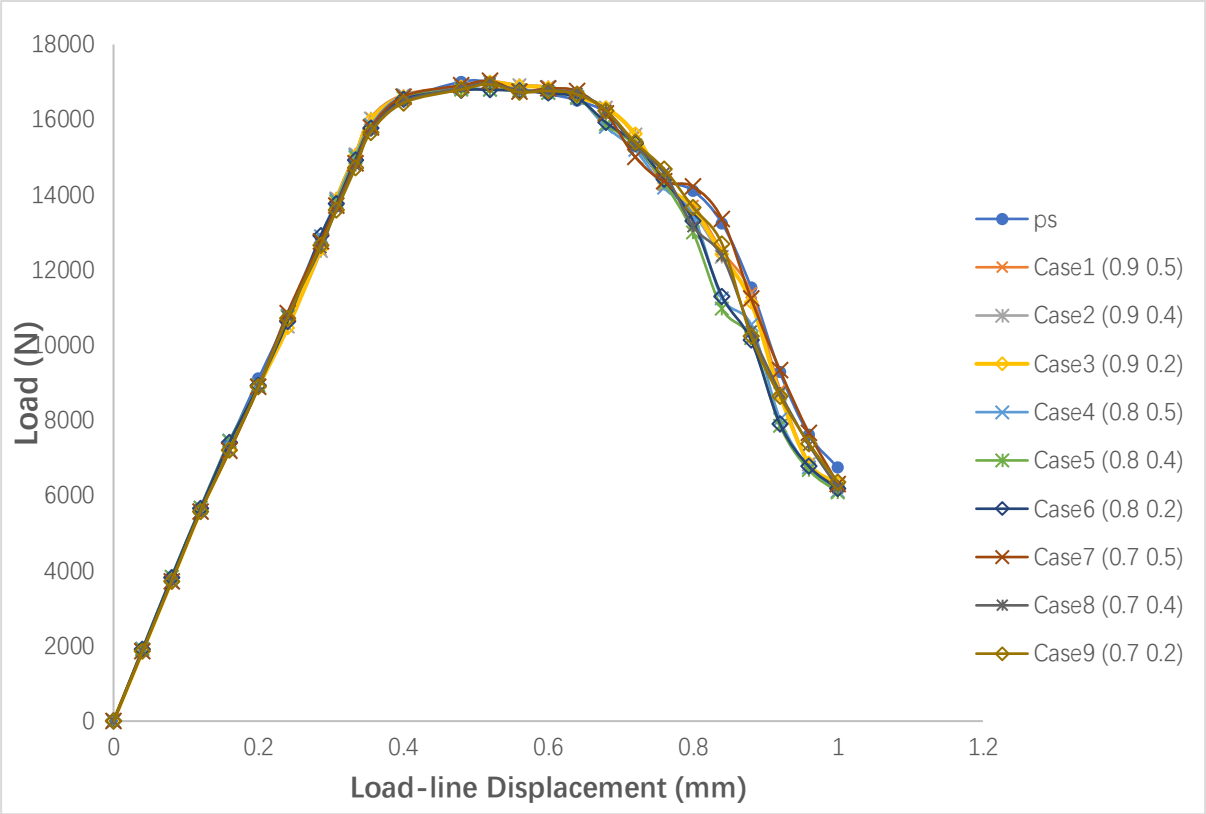

Figure 4.24 Load-displacement curves for physical and virtual models.

Table 4.11 J_C values for different virtual models in the DCT test.

Case	β_1	β_2	J_{el} (kJ/m^2)	J_{pl} (kJ/m^2)	$J_C = J_{el} + J_{pl}$ (kJ/m^2)	Error %
ps			11.01	20.00	31.01	
Case 1	0.9	0.5	11.08	19.82	30.90	-0.37
Case 2	0.9	0.4	11.08	19.79	30.87	-0.46
Case 3	0.9	0.2	11.08	19.77	30.85	-0.53

Case 4	0.8	0.5	11.01	19.89	30.90	-0.35
Case 5	0.8	0.4	11.01	19.74	30.75	-0.83
Case 6	0.8	0.2	11.01	19.68	30.69	-1.02
Case 7	0.7	0.5	11.01	19.89	30.90	-0.35
Case 8	0.7	0.4	11.01	19.74	30.75	-0.83
Case 9	0.7	0.2	11.01	19.68	30.69	-1.02

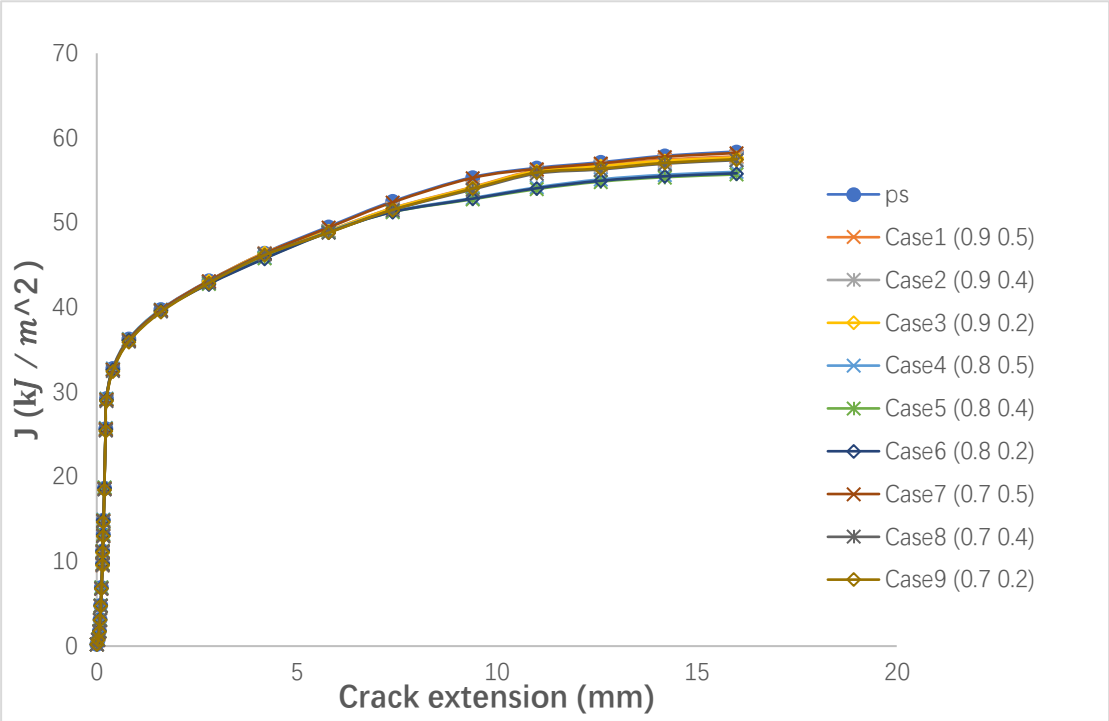

Figure 4.25 *J* -values for different values of crack lengths for physical and virtual DCT models.

4.5 Conclusions

The chapter examines a new description for fracture mechanics founded on the first-order finite similitude rule arising out of the recently discovered finite similitude theory. The new two-experiment description hypothesises how stress, displacement and strain fields change with scale. A feature of the theory is use of two scaled fracture-mechanics experiments at distinct scales to account for the size effect typical to fracture mechanics. The following conclusions can be drawn from the investigation outlined in the chapter:

- The first-order finite similitude rule has been confirmed to be satisfied for quasistatic loading under the assumption that stress field is scale independent and displacement field is either scale independent or linearly dependent.
- New differential governing equations for fracture mechanics have been established which can be integrated to link information across two scaled-fracture experiments.
- Analytical studies confirm that exact replication is possible with results from two scaled experiments, which when combined provide a perfect match with those obtained at full scale.
- Numerical studies provided results which are supportive of the new theory although small errors (typically less than 1%) were returned for propagating cracks arising principally from deviations in crack paths in the scaled experiments.
- The theory introduced in the work although at an early stage of development provides an alternative view of fracture mechanics with the inclusion of field differences and gradients with respect to scale. The direct analysis of fracture mechanics using Eq. (4.9) and Eq. (4.10) provides a new and interesting area for possible future research.

More specifically, from the trial experiments performed, the following statements can be made:

- Both LEFM and EPFM was shown to be reasonably well represented by the theory by means of numerical tests on CT, TPB and DCT specimens. A range or errors were returned although typically less than 1% and associated with crack propagation.
- The main hypothesis that the first-order theory effectively counters size effects in fracture mechanics is starkly revealed on comparison of the raw data presented in Figs. (4.8), (4.17) and (4.23) with the virtual curves presented in Figs. (4.12), (4.18) and (4.24), respectively. Despite the presence of small

errors, the virtual curves provide strong supporting evidence for the general contention.

- The two-experiment approach provides good outcomes for standard ASTM tests, but such tests are not necessarily optimum for the two-experiment approach. The investigation, design and recommendation of new two-experiment tests is an interesting area of possible future study.
- It shows high-accuracy results in Figs. (4.12), (4.13), (4.18), (4.19), (4.24) and (4.25), which are highly matched in LEFM and gradually occur larger errors with crack extension. Target results of toughness and critical values are matched (<1% error) since they are most related to the LEFM part. At the end of these curves, the increasing error shows the in-stability of material behaviour when specimen occurs significant damage, which makes the outputs vary with size.

Chapter 5 Finite similitude to damage and failure under high-rate loading

5.1 Introduction

Performing a full-scale experiment is possibly the surest way to accurately capture and assess the behaviour of a system or prototype. However, practical considerations including prohibitive costs, lack of available facilities and equipment can make this approach unfeasible. For this and other reasons alternative approaches are often pursued instead, which can include numerical simulation with the aid of advanced analysis software and/or testing with the aid of geometrical similar small-scale replicas. The use of scaled models falls under the theory of similitude, which is concerned with those conditions necessary and sufficient to achieve similarity required for good replication. Artefacts of interest and of particular focus in this paper are pressure vessels which are produced in a vast array of configurations and sizes but have the sole principal function to hold fluids at pressure. The range of sizes available makes them attractive for scaled experimentation and in view of the high pressures involved, pressure vessels must comply with stringent regulations and survive accidental occurrences.

Such incidents can be at high rate as with impact or blast loading, which itself is an area of study that makes good use of scaled experimentation [51]. Scaled high-loading rate studies are themselves not without difficulties as similarity can be lost arising from the non-scalability of strain rate effects and fracture toughness [51,143-145]. To resolve these difficulties, researchers have proposed tests designed with alternative dimensionless numbers formed from the dimensioned-physical quantities of impact velocity, impact mass and dynamic yield stress [85,146-148]. In refs [85,146] for example correction factors for impact velocity and impact mass are shown to provide good agreement with results from scaled experiments. A particular

drawback however is that the strain rate is required to be known *a priori* to determine the correction factors, which somewhat limits the general applicability of the approach. In a similar fashion, by means of the correct determination of the initial impact velocity, for a perfectly plastic, cylindrical shell, subjected to axial impact, it has been shown that a scaled experiment is able to predict reasonably accurately full-scale behaviour [147]. Unfortunately, this method works with the mean value of strain rate for the correction factor, which is not available in more complex scenarios. Success has been reported with the Norton-Hoff constitutive law [148] with its exponent featuring in the impact velocity correction factor. An exact match is recorded for rigid viscoplastic case studies but generalising the result to more complex situations is not obvious.

Replica scaling features in all the papers mentioned above (i.e., refs. [143-148]) with scaling restricted to space and time only with matching materials employed in the full and small-scale experiments. This restriction has a limiting effect on the types of response that can be captured since physical modelling involving different materials provides for additional flexibility. This flexibility is not only limited to the extended range of material behaviours possible, but also features in practical considerations including the cost and feasibility of an experiment given the apparatus available [149]. The examination and analysis of physical models in impact studies has appeared in the open literature [86,149-152]. These studies like those above involve the adjustment of conditions for mass and impact velocity but in this case contingent on the materials used. It should be mentioned however that these studies involve only moderate strain-hardening and strain-rate effects. Additionally, the overall constraint imposed by dimensional analysis remains limiting despite physical models being used.

It is evident and recognised that even with physical modelling that replication of behaviours by a scaled model is heavily constricted by the material properties available in standard materials. The correct combination of properties is invariably difficult to arrange; however, an alternative approach has recently appeared in the open literature [98]. The arrival of new similitude rules now makes it possible to

consider new forms of physical modelling but now involving more than one scaled model at distinct scales. The open question being answered in this paper is whether two scaled models with materials different from each other, and that at full scale, provides the flexibility needed to accurately capture the response of a pressure vessel when subject to localised impact and global blast loading conditions. The new scaling theory [98] has been applied to the high-rate loading tests [99,107,130] but the advantages of physical modelling have yet to be fully realised. To assess the efficacy of the new approach case studies are chosen involving the Charpy impact test, projectiles, and penetration to examine localised stress distributions around the damaged area. In addition, blast loading is applied using a Conwep model in finite element analysis, where reactive loads and displacements of the pressure vessel are the focus with the objective being to reproduce behaviours using a two-experiment physical model.

A feature of the new finite similitude theory is that it is based on the metaphysical concept of space scaling where “metaphysical” in this context means that although space scaling is not physically realizable it can be imagined and mathematically defined. The scaling theory does not involve constitutive laws but nevertheless these are very much needed and are introduced in Section 5.2. The focus is on the Johnson-cook constitutive and damage laws to capture the high-strain rate material response and any damage as it manifests. The effect of settings and different material choices is assessed in this section for the well-known test procedure the Charpy impact test. In Section 5.3 the theory is applied to a penetration test to assess the impact of projectiles on the pressure vessel model, where it is shown how a two-experiment physical model can reproduce the full-scale response to high accuracy. Attention turns next to the internal blast loading of the pressure vessel simulated by the Conwep model and again the flexibility provided by the two-experiment approach is showcased. The case studies considered in the paper are based on previously validated Abaqus studies for the Charpy impact test [153-155], the pressure vessel penetration test [156-158], and the pressure vessel under internal blast loading [159-

160]. The chapter ends with a set of conclusions.

5.2 Finite similitude for physical modelling

For the problem under scrutiny, the finite similitude theory requires the inclusion of those transport equations that contain the fields involved. For impact mechanics, transport equations for volume, mass, momentum, and movement are of interest. The equation for volume brings into play the velocity field $\boldsymbol{v}_{ts}^{*}$ dictating control volume movement, the continuity equation introduces density ρ_{ts} and material velocity $\boldsymbol{v}_{ts}$, momentum contributes the tensor field $\boldsymbol{\sigma}_{ts}$ and specific body force $\boldsymbol{b}_{ts}^{v}$, and lastly movement introduces displacement field $\boldsymbol{u}_{ts}$. The additional first-order identities returned by this procedure are tabulated in Table 5.1 in compact and expanded formats.

Table 5.1 First-order finite similitude identities

Fields	Compact representation	Expanded representation
Displacement	$\boldsymbol{u}_1 = \boldsymbol{u}_{\beta_1} + R_1\left(\boldsymbol{u}_{\beta_1} - \boldsymbol{u}_{\beta_2}\right)$	$\boldsymbol{u}_1 = \beta_1^{-1}\boldsymbol{u}_{ts1} + R_1\left(\beta_1^{-1}\boldsymbol{u}_{ts1} - \beta_2^{-1}\boldsymbol{u}_{ts2}\right)$
Velocity	$\boldsymbol{v}_1 = \boldsymbol{v}_{\beta_1} + R_1\left(\boldsymbol{v}_{\beta_1} - \boldsymbol{v}_{\beta_2}\right)$	$\boldsymbol{v}_1 = g_1\beta_1^{-1}\boldsymbol{v}_{ts1} + R_1\left(g_1\beta_1^{-1}\boldsymbol{v}_{ts1} - g_2\beta_2^{-1}\boldsymbol{v}_{ts2}\right)$
Acceleration	$\boldsymbol{a}_1 = \boldsymbol{a}_{\beta_1} + R_1\left(\boldsymbol{a}_{\beta_1} - \boldsymbol{a}_{\beta_2}\right)$	$\boldsymbol{a}_1 = g_1^2\beta_1^{-1}\boldsymbol{a}_{ts1} + R_1\left(g_1^2\beta_1^{-1}\boldsymbol{a}_{ts2} - g_1^2\beta_1^{-1}\boldsymbol{a}_{ts2}\right)$
Body force	$\boldsymbol{b}_1 = \boldsymbol{b}_{\beta_1} + R_1\left(\boldsymbol{b}_{\beta_1} - \boldsymbol{b}_{\beta_2}\right)$	$\rho_1\boldsymbol{b}_1^{v} = \alpha_{01}^{v}\rho_{ts1}g_1\,\beta_1^{3}\boldsymbol{b}_{ts1}^{v} + R_1\left(\alpha_{01}^{v}\rho_{ts1}g_1\,\beta_1^{3}\boldsymbol{b}_{ts1}^{v} - \alpha_{02}^{v}\rho_{ts2}g_2\,\beta_2^{3}\boldsymbol{b}_{ts2}^{v}\right)$
Stress	$\boldsymbol{\sigma}_1 = \boldsymbol{\sigma}_{\beta_1} + R_1\left(\boldsymbol{\sigma}_{\beta_1} - \boldsymbol{\sigma}_{\beta_2}\right)$	$\boldsymbol{\sigma}_1 = \alpha_{01}^{v}g_1\beta_1^{2}\boldsymbol{\sigma}_{ts1} + R_1\left(\alpha_{01}^{v}g_1\beta_1^{2}\boldsymbol{\sigma}_{ts1} - \alpha_{02}^{v}g_2\beta_2^{2}\boldsymbol{\sigma}_{ts2}\right)$
Strain	$\boldsymbol{\varepsilon}_1 = \boldsymbol{\varepsilon}_{\beta_1} + R_1\left(\boldsymbol{\varepsilon}_{\beta_1} - \boldsymbol{\varepsilon}_{\beta_2}\right)$	$\boldsymbol{\varepsilon}_1 = \boldsymbol{\varepsilon}_{ts1} + R_1\left(\boldsymbol{\varepsilon}_{ts1} - \boldsymbol{\varepsilon}_{ts2}\right)$

Strain rate	$\dot{\boldsymbol{\varepsilon}}_1 = \dot{\boldsymbol{\varepsilon}}_{\beta_1} + R_1\left(\dot{\boldsymbol{\varepsilon}}_{\beta_1} - \dot{\boldsymbol{\varepsilon}}_{\beta_2}\right)$	$\dot{\boldsymbol{\varepsilon}}_1 = g_1\dot{\boldsymbol{\varepsilon}}_{ts1} + R_1\left(g_1\dot{\boldsymbol{\varepsilon}}_{ts1} - g_2\dot{\boldsymbol{\varepsilon}}_{ts2}\right)$

Note that additional fields have been inserted into Table 5.1 over and above those obtained directly from transport equations defined in Chapter 3. This is a feature of the finite similitude theory and although constitutive equations are absent from the theory all fields needed are readily derived. For example, for strain (small deflection theory) application of the identities $\boldsymbol{dx}_{ts1} = \beta_1\boldsymbol{dx}_{ps}$ and $\boldsymbol{dx}_{ts2} = \beta_2\boldsymbol{dx}_{ps}$ to the identity for displacement provides the strain identity in Table 5.1 and similarly for strain rate and acceleration.

5.2.1. First-order physical models for impact

Although constitutive equations do not arise out of the fundamentals of the finite-similitude approach they are needed nonetheless in physical modelling as they bring into play important material properties. To capture the response of full-scale behaviours in impact mechanics, two principal aspects are critical, which are inertia and material response. Four fields are central to a good representation, and these are mass density $\rho_\beta = \alpha_0^\rho\rho_{ts}\beta^3$, stress $\boldsymbol{\sigma}_\beta = \alpha_0^v\beta^2 g\boldsymbol{\sigma}_{ts}$, strain rate $\dot{\boldsymbol{\varepsilon}}_\beta^p = g\dot{\boldsymbol{\varepsilon}}_{ts}^p$ and effective strain $\varepsilon_\beta^p = \varepsilon_{ts}^p$, with this latter quantity related to effective strain rate via the identity $d\varepsilon_\beta^p = \dot{\varepsilon}_\beta^p dt_\beta$, where $dt_\beta = g^{-1}dt_{ts}$. Although density is restricted to be a zeroth-order relationship here this is not of major obstacle since the expression $\rho_1 = \rho_\beta$ is generally satisfiable at arbitrary β. Since $\rho_\beta = \alpha_0^\rho\rho_{ts}\beta^3$ and under the assumption that ρ_{ps}, ρ_{ts1}, and ρ_{ts2} are known material densities (since density in solids is usually fixed), then setting the function α_0^ρ to equal $\alpha_0^\rho(\beta) = \beta^{-3}\frac{\rho_{ps}}{\rho_{ts}}$ ensures that $\rho_{ps} = \rho_{\beta_1} = \rho_{\beta_2}$ as required. Things are a little more involved when it comes to material response as there is invariably insufficient scope for similitude rules to match all the material properties involved despite first-order finite similitude having the advantage of two scaled material models. To examine this aspect for impact mechanics it is beneficial to examine a commonly used constitutive law and the focus

here is on the Johnson-Cook (J-C) viscoplastic law, which represents the dynamic-yield stress as a function of strain hardening and strain rate [161], and takes the form

$$\sigma^d = (A + B(\varepsilon^p)^n)\left(1 + C\ln\left(\frac{\dot{\varepsilon}^p}{\dot{\varepsilon}^0}\right)\right) \tag{5.1}$$

where σ^d is the dynamic yield stress, A is static yield stress, B is a hardening coefficient, ε^p is plastic strain, n is a hardening exponent, C is a strain rate coefficient and $\dot{\varepsilon}^p$, $\dot{\varepsilon}^0$ are strain rate and reference strain rate, respectively.

Similarly, a J-C law exists for damage, which assumes failure strain [161] is a function of stress triaxiality, strain rate and takes the form

$$\varepsilon^f = [D_1 + D_2\exp(D_3\sigma^*)]\left(1 + D_4\ln\left(\frac{\dot{\varepsilon}^p}{\dot{\varepsilon}^0}\right)\right) \tag{5.2}$$

where ε^f is the failure strain and should plastic strain ε^p reach this value, then damage is initiated, σ^* is stress triaxiality, and D_1 to D_4 are damage parameters, which are experimentally determined.

Eq. (5.1) and (5.2) are also assumed to apply in the physical space, and in the trial spaces at scales β_1 and β_2, where the freedom to select the materials involved exists. It should be appreciated that there exists only a limited number of freedoms with the similitude theory, which are the functions α_0^ρ and g, and parameters β and R_1. Once the scales β_1 and β_2 are decided upon, and since α_0^ρ is effectively dictated my material density, this leaves only the time scalars g_1 and g_2, and the parameter R_1. In view of the numbers of material properties involved in the J-C constitutive laws it is pretty evident that perfect replication of full-scale behaviours is difficult to achieve in practice. In this situation rather than target specific material properties it is best to target aspects that are important to the physics of the process under scrutiny. An approach that was applied in ref. [99] is to form weaker relationships from the constitutive laws, achieved through integration. Important measures are identified that are relatable across the scales using the similitude rules. Note that the form of the compact identities (in Table 5.1) is identical because each satisfies the exact same

second-order differential equation, i.e., $\frac{d}{d\beta}\left(\alpha_1 \frac{d\aleph_\beta}{d\beta}\right) = 0$, where $\aleph_\beta$ is any of the fields in Table 5.1. Ideally therefore any identified measure should also be a solution to this differential equation so that the difference identities in Table 1 apply. The first issue to address is functional dependence, as apparent in Eq. (5.1) and Eq. (5.2), which are functions of the form $\sigma_d\left(\varepsilon^p, \dot{\varepsilon}^p\right)$ and $\varepsilon_f(\sigma^*, \dot{\varepsilon}^p)$, respectively. This dependence is weakened by means of integration and on definition of the measures

$$\bar{\Sigma}^d = \frac{1}{\bar{E}^f \dot{\varepsilon}^{max}} \int_0^{\bar{E}^f} \int_0^{\dot{\varepsilon}^{max}} \sigma^d(\varepsilon^p, \dot{\varepsilon}^p) d\dot{\varepsilon}^p d\varepsilon^p \tag{5.3a}$$

$$\bar{E}^f = \frac{1}{\left(\sigma^{*max} - \sigma^{*min}\right)\dot{\varepsilon}^{max}} \int_{\sigma^{*min}}^{\sigma^{*max}} \int_0^{\dot{\varepsilon}^{max}} \varepsilon^f(\sigma^*, \dot{\varepsilon}^p) d\dot{\varepsilon}^p d\sigma^* \tag{5.3b}$$

which are assumed to apply in the trial and physical spaces, and where σ^{*max} and σ^{*min} are maximum and minimum stress triaxiality, $\dot{\varepsilon}^{max}$ is the maximum strain rate and note that $\bar{E}^f$ appears in the limits of Eq. (5.3a).

To keep things reasonably simple the integration limits in the physical space are set in accordance with ref. [99] to be $\sigma^{*min} = -2$, $\sigma^{*max} = 2$, $\dot{\varepsilon}^{max} = 10/ms$, which are values that can be improved upon as necessary through simulations with ABAQUS models, and $\bar{E}^{fmax} = 1$. Additionally, for integration purposes only, the following proportional measure relationships are assumed to apply

$$d\sigma^*_{ps} = \frac{\sigma^{*\max}_{ps} - \sigma^{*\min}_{ps}}{\sigma^{*\max}_{ts1} - \sigma^{*\min}_{ts1}} d\sigma^*_{ts1} \tag{5.4a}$$

$$d\sigma^*_{ps} = \frac{\sigma^{*\max}_{ps} - \sigma^{*\min}_{ps}}{\sigma^{*\max}_{ts2} - \sigma^{*\min}_{ts2}} d\sigma^*_{ts2} \tag{5.4a}$$

$$d\varepsilon^p_{ps} = \frac{\bar{E}^f_{ps}}{\bar{E}^f_{ts1}} d\varepsilon^p_{ts1} \tag{5.4c}$$

$$d\varepsilon^p_{ps} = \frac{\bar{E}^f_{ps}}{\bar{E}^f_{ts2}} d\varepsilon^p_{ts2} \tag{5.4d}$$

$$d\dot{\varepsilon}_{ps}^{p} = \frac{\dot{\varepsilon}_{ps}^{\max}}{\dot{\varepsilon}_{ts1}^{\max}} d\dot{\varepsilon}_{ts1}^{p} \tag{5.4e}$$

$$d\dot{\varepsilon}_{ps}^{p} = \frac{\dot{\varepsilon}_{ps}^{\max}}{\dot{\varepsilon}_{ts2}^{\max}} d\dot{\varepsilon}_{ts2}^{p} \tag{5.4f}$$

and with the help of Table 5.1 provides the measure relationships

$$\sigma_{ps}^{d} d\dot{\varepsilon}_{ps} d\varepsilon_{ps}^{p} = \alpha_{01}^{v} g_1 \beta_1^2 \frac{\bar{E}_{ps}^{f}}{\bar{E}_{ts1}^{f}} \frac{\dot{\varepsilon}_{ps}^{\max}}{\dot{\varepsilon}_{ts1}^{\max}} \sigma_{ts1}^{d} d\dot{\varepsilon}_{ts1} d\varepsilon_{ts1}^{p} + R_1 \left(\alpha_{01}^{v} g_1 \beta_1^2 \frac{\bar{E}_{ps}^{f}}{\bar{E}_{ts1}^{f}} \frac{\dot{\varepsilon}_{ps}^{\max}}{\dot{\varepsilon}_{ts1}^{\max}} \sigma_{ts1}^{d} d\dot{\varepsilon}_{ts1} d\varepsilon_{ts1}^{p} - \alpha_{02}^{v} g_2 \beta_2^2 \frac{\bar{E}_{ps}^{f}}{\bar{E}_{ts2}^{f}} \frac{\dot{\varepsilon}_{ps}^{\max}}{\dot{\varepsilon}_{ts2}^{\max}} \sigma_{ts2}^{d} d\dot{\varepsilon}_{ts2} d\varepsilon_{ts2}^{p} \right) \tag{5.5a}$$

$$\varepsilon_{ps}^{f} d\sigma_{ps}^{*} d\dot{\varepsilon}_{ps}^{p} = \frac{\sigma_{ps}^{*\max} - \sigma_{ps}^{*\min}}{\sigma_{ts1}^{*\max} - \sigma_{ts1}^{*\min}} \frac{\dot{\varepsilon}_{ps}^{\max}}{\dot{\varepsilon}_{ts1}^{\max}} \varepsilon_{ts1}^{f} d\sigma_{ts1}^{*} d\dot{\varepsilon}_{ts1}^{p} + R_1 \left(\frac{\sigma_{ps}^{*\max} - \sigma_{ps}^{*\min}}{\sigma_{ts1}^{*\max} - \sigma_{ts1}^{*\min}} \frac{\dot{\varepsilon}_{ps}^{\max}}{\dot{\varepsilon}_{ts1}^{\max}} \varepsilon_{ts1}^{f} d\sigma_{ts1}^{*} d\dot{\varepsilon}_{ts1}^{p} - \frac{\sigma_{ps}^{*\max} - \sigma_{ps}^{*\min}}{\sigma_{ts2}^{*\max} - \sigma_{ts2}^{*\min}} \frac{\dot{\varepsilon}_{ps}^{\max}}{\dot{\varepsilon}_{ts2}^{\max}} \varepsilon_{ts2}^{f} d\sigma_{ts2}^{*} d\dot{\varepsilon}_{ts2}^{p} \right) \tag{5.5b}$$

where integration of these expressions provides very convenient first-order relationships of the form

$$\bar{\Sigma}_{ps}^{d} = \alpha_{01}^{v} g_1 \beta_1^2 \bar{\Sigma}_{ts1}^{d} + R_1 \left(\alpha_{01}^{v} g_1 \beta_1^2 \bar{\Sigma}_{ts1}^{d} - \alpha_{02}^{v} g_2 \beta_2^2 \bar{\Sigma}_{ts2}^{d} \right) \tag{5.6a}$$

$$\bar{E}_{ps}^{f} = \bar{E}_{ts1}^{f} + R_1 \left(\bar{E}_{ts1}^{f} - \bar{E}_{ts2}^{f} \right) \tag{5.6b}$$

which connect mean values of dynamic stress and failure strain across the scales, where it is recognised that a mix of zeroth and first-order relationships have been utilised to arrive at these expressions.

Note that Eqs. (5.6) provided the identities $\bar{\Sigma}_{\beta}^{d} = \alpha_0^{v} \beta^2 g \bar{\Sigma}_{ts}^{d}$ and $\bar{E}_{\beta}^{f} = \bar{E}_{ts}^{f}$, which can be contrasted with the identities $\boldsymbol{\sigma}_{\beta} = \alpha_0^{v} \beta^2 g \boldsymbol{\sigma}_{ts}$ and $\bar{\boldsymbol{\varepsilon}}_{\beta} = \bar{\boldsymbol{\varepsilon}}_{ts}$, and consequently satisfy the differential equation $\frac{d}{d\beta}\left(\alpha_1 \ \frac{d\aleph_{\beta}}{d\beta} \right) = 0$ as required. Note additionally that Eqs (5.6) can be compactly represented by $\bar{\Sigma}_1 = \bar{\Sigma}_{\beta_1}^{d} + R_1 \left(\bar{\Sigma}_{\beta_1}^{d} - \bar{\Sigma}_{\beta_2}^{d} \right)$ and $\bar{E}_1^{f} = \bar{\mathrm{E}}_{\beta_1}^{f} + R_1 \left(\bar{\mathrm{E}}_{\beta_1}^{f} - \bar{\mathrm{E}}_{\beta_2}^{f} \right)$. There are three unknows (g_1, g_2 and R_1) in these two equations which suggests that either another equation or assumption is required. The simplest solution to Eq. (5.6) is to use zeroth order to set g_1 and g_2, which requires

substitution of $\alpha_0^v = g\beta^{-1}\alpha_0^\rho$ into Eq. (5.6a) give

$$\bar{\Sigma}_{ps}^d = \alpha_{01}^\rho \beta_1 g_1^2 \bar{\Sigma}_{ts1}^d + R_1 \left(\alpha_{01}^\rho \beta_1 g_1^2 \bar{\Sigma}_{ts1}^d - \alpha_{02}^\rho \beta_2 g_2^2 \bar{\Sigma}_{ts2}^d \right) \tag{5.7}$$

which is solved on setting $\bar{\Sigma}_{ps}^d = \alpha_{01}^\rho \beta_1 g_1^2 \bar{\Sigma}_{ts1}^d = \alpha_{02}^\rho \beta_2 g_2^2 \bar{\Sigma}_{ts2}^d$ and yields

$$g_1 = \sqrt{\frac{1}{\alpha_{01}^\rho \beta_1} \frac{\bar{\Sigma}_{ps}^d}{\bar{\Sigma}_{ts1}^d}} = \sqrt{\frac{\rho_{ts1}}{\rho_{ps}} \frac{\bar{\Sigma}_{ps}^d}{\bar{\Sigma}_{ts1}^d}} \beta_1 \tag{5.8a}$$

$$g_2 = \sqrt{\frac{1}{\alpha_{02}^\rho \beta_2} \frac{\bar{\Sigma}_{ps}^d}{\bar{\Sigma}_{ts2}^d}} = \sqrt{\frac{\rho_{ts2}}{\rho_{ps}} \frac{\bar{\Sigma}_{ps}^d}{\bar{\Sigma}_{ts2}^d}} \beta_2 \tag{5.8b}$$

on substitution of $\alpha_0^\rho(\beta) = \beta^{-3\frac{\rho_{ps}}{\rho_{ts}}}$, which transpires to give to give pretty good answers (see next section) with R_1 determined using Eq. (5.6b), i.e.,

$$R_1 = \frac{\bar{E}_{ps}^f - \bar{E}_{ts1}^f}{\bar{E}_{ts1}^f - \bar{E}_{ts2}^f} \tag{5.9}$$

An alternative approach is to target another feature of the constitutive law and one possibility is the mean yield stress defined by

$$\bar{Y}^d = \frac{1}{\dot{\varepsilon}^{max}} \int_0^{\dot{\varepsilon}^{max}} \sigma^d(0, \dot{\varepsilon}^p) d\dot{\varepsilon}^p \tag{5.10a}$$

which on following the approach above, yields the equation

$$\bar{Y}_{ps}^d = \alpha_{01}^v g_1 \beta_1^2 \bar{Y}_{ts1}^d + R_1 \left(\alpha_{01}^v g_1 \beta_1^2 \bar{Y}_{ts1}^d - \alpha_{02}^v g_2 \beta_2^2 \bar{Y}_{ts2}^d \right) \tag{5.11}$$

and consequently, provides a third equation if required.

5.2.2. Physical modelling test case

Prior to examining practical case studies, it is instructive at this point to explore how the different choices for the determination of g_1, g_2 and R_1 influence the outcomes for a standard test (e.g., the Charpy test). Such an investigation involving a selection of readily accessible materials for scaled models is shown to provide evidence for the likely success of a particular two-experiment physical modelling approach.

- Charpy impact test

The Charpy impact test [162] is designed to investigate the fracture toughness of materials through the absorbed energy following the impact of a specimen with a

striker. The test is performed under controlled laboratory conditions for specimens at temperature subjected to a striker mass at velocity, and equates the energy absorbed to the fracture toughness for the material. The Charpy V-notch dynamic impact test was investigated in ref [163], where changes in material strength and strain rate were shown to be the main factors influencing the energy absorbed. Simulation of the V-notch test [155] in Abaqus with application of the Johnson-Cook (J-C) damage model, for various striker impact velocities, confirmed that an increase in striker velocity produces lower absorbed energy. Also reaffirmed in ref. [155] is the suitability of the J-C constitute model in determining strain rate sensitivity of metallic materials, and its application to sudden impact [164-166].

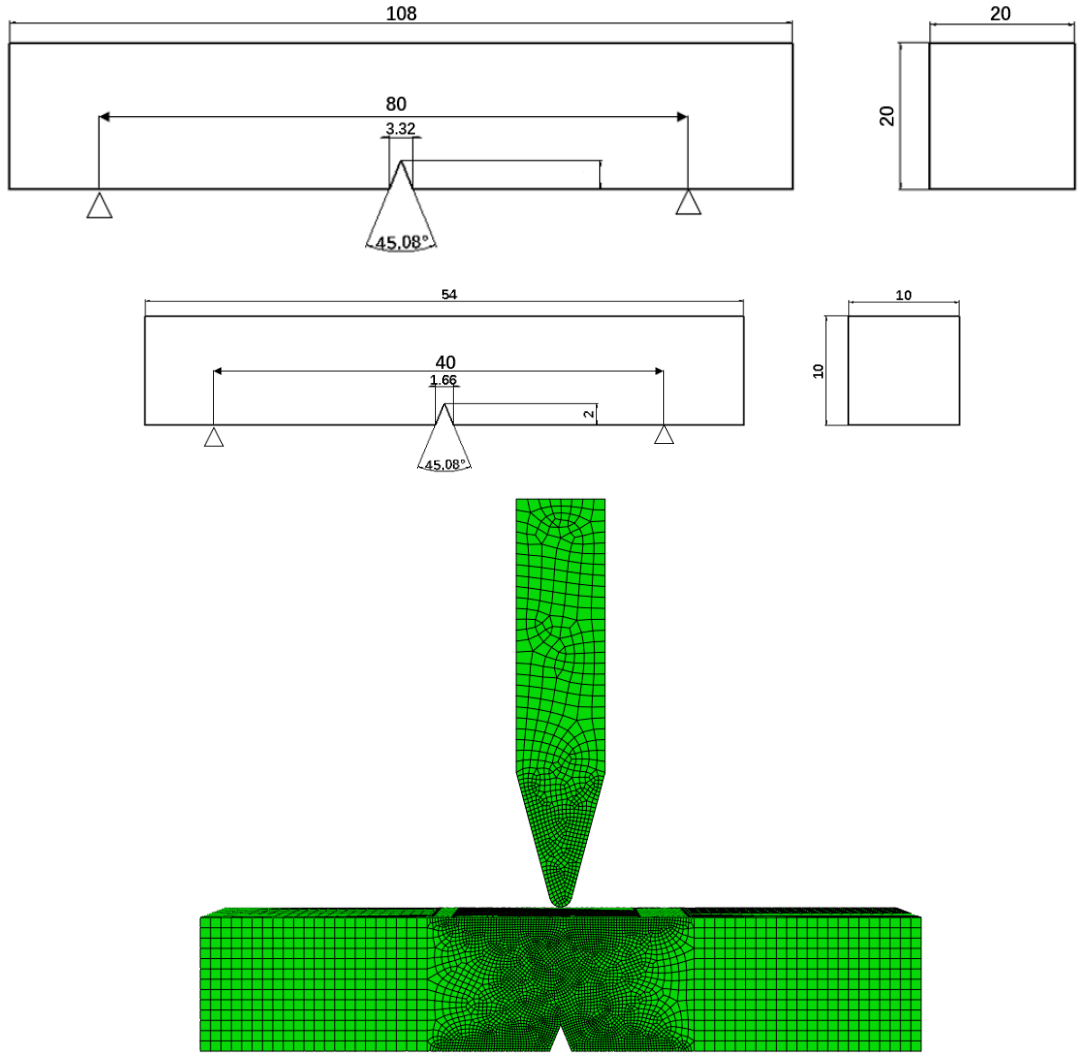

Figure 5.1 Dimensions of the Charpy impact test specimens and the meshed model in finite element analysis.

The specimens examined here in the physical ($\beta_0 = 1$) and trial ($\beta_1 = 0.5$) spaces are shown in Fig 5.1, which are modelled by Abaqus Explicit software. The J-C constitutive model described in Section 5.2.1 is applied to capture the constitutive response of the specimens, and the striker is modelled as a discrete rigid body. The elements selected (see Fig. 5.1) for the 3D analysis are available in Abaqus are C3D8R explicit with enhanced hourglass control. For the physical model, a finer mesh is applied in the middle region (80 mm around the centre line) of the specimen with the mesh size set to 0.4 mm; a global mesh size of 1.6 mm is applied to other parts providing a total of 205050 elements. The striker is furnished with a fine mesh in the triangular region (around its tip) with 0.6 mm mesh size, and 1.6 mm global size elsewhere; and is positioned 2 mm distance above the notched specimen in the physical space. Note that all these sizes are scaled by β for the trial models. The span length of the model in the physical space is 80 mm (see Fig. 5.1), where the fixed supports (nodes on the line) are not allowed to move in y-direction; the striker is constrained to move in y-direction. Material selection is based on the physical material Steel300. According to the finding in Chapter 3, it is recommended to apply a group of materials whose properties do not have large deviation with physical material. The material properties in J-C model are listed in Table 5.2.

Table 5.2 Properties of the materials involved.

	Steel 300 [155]	Ti6Al4V [167]	Aluminium Alloy 6061-T6 [168]	Aluminium Alloy 7075-T6 [169]	304L Stainless steel [170]	Steel Armox 500T [171]
Density $(kg/mm^3) \times 10^{-6}$	7.99	4.43	2.7	2.7	7.8	7.99
Elastic Modulus (GPa)	192	110	69	70	164.5	207
Poisson ratio	0.283	0.33	0.3	0.3	0.3	0.33
$A\ (GPa)$	0.758	1.098	0.324	0.546	0.345	1
$B\ (GPa)$	0.172	1.092	0.114	0.678	0.31	0.461
C	0.0522	0.014	0.002	0.024	0.24	0.02
n	0.2258	0.93	0.42	0.71	0.3	0.45

m	0.7799	1.10	1.34	0.81	1.03	2.31
$T_{tr}\ (K)$	293	298	298	293	294	293
$T_m\ (K)$	1685	1903	928	893	1693	1800
D_1	-0.09	-0.09	-0.77	-0.068	0.1	0.1055
D_2	0.27	0.25	1.45	0.451	0.76	2.7824
D_3	0.48	0.5	0.47	0.952	1.57	3.3863
D_4	0.014	0.014	0	0.036	0.005	-0.0509
D_5	3.87	0.0387	1.6	0.697	-0.84	0
$\dot{\varepsilon}^0(ms^{-1})$	0.001	0.001	0.001	5×10^{-7}	0.001	0.001

The length scaling factors for the two trial models are selected to be $\beta_1 = 0.5$ and $\beta_2 = 0.25$, respectively with different materials applied. The time scalars g_1 and g_2 are determined using Eqs. (5.8a) and (5.8b), so are affected by the range of stress triaxiality, strain rate and failure strain. For ductile metals the range of stress triaxiality is reasonably set to be from -2 to 2. Similarly, the maximum strain rate and failure strain is set at 10/*ms* and 1, respectively for the high-rate impact test in accordance with ref. [99]. Setting g_1 and g_2 to satisfy Eq. (5.8) provides two approaches for the determination of R_1 , i.e., either using the mean failure strain, Eq. (5.9), or the mean yield stress, Eq. (5.11). Presented in Table 5.3 are the material combinations considered along with determined scaling parameters. It transpires that in all cases apart from one, determination of R_1 using Eq. (5.11) provides better outcomes than Eq. (5.9). The R_1 values listed in Table 5.1 pertain to Eq. (5.11) with the exception being Case 1.7, which pertains to Eq. (5.9). Note that $R_1 = 0$ and $R_1 = -1$ return zeroth order results, which is a feature of Cases 1.1, 1.2 and 1.3 when the steel used in the full-scale model is involved in the trial models. Additional parameters are listed in Table 5.4, where striker mass and initial velocity for the trial models are calculated with zeroth-order relationships $M_{ts} = M_{ps}/\alpha^{\rho}$ and $v_{ts} = (\beta/g)v_{ps}$, respectively.

Table 5.3 Scaling parameters for trial models.

Case	Trial material 1 ($\beta_1 = 0.5$)	Trial material 2 ($\beta_2 = 0.25$)	g_1	g_2	α_1^{ρ}	α_2^{ρ}	R_1

1.1	Steel300	Steel300	0.4937	0.2438	8	64	-
1.2	Steel300	304LSS	0.4937	0.2	8	65.56	0.0008
1.3	Al7075	Steel300	0.2857	0.2438	23.67	64	-1.005
1.4	Steel500T	304LSS	0.4542	0.2	8	65.56	0.4
1.5	Ti6Al4V	AL6061	0.3074	0.2562	14.43	188.69	-1.3
1.6	Ti6Al4V	304LSS	0.3074	0.2	14.43	65.56	0.55
1.7	Al7075	304LSS	0.2857	0.2	23.67	65.56	0.53
1.8	Al7075	AL6061	0.2857	0.2562	23.67	188.69	-1.17

Table 5.4 Input conditions for the physical and trial models in Charpy impact test.

Scale	Material	Mass of striker $M\ (kg)$	Initial velocity of striker $v_i\ (m/s)$	Period of the impact process $(10^{-3}s)$
Physical	Steel300	80	5	2
Trial 1 $(\beta_1 = 0.5)$	Steel300	10	5.06	0.9874
	Ti6Al4V	5.544	8.133	0.6148
	Al7075	3.38	8.7513	0.5714
	Steel500T	10	5.504	0.9084
Trial 2 $(\beta_2 = 0.25)$	Steel300	1.25	5.127	0.4876
	Al6061	0.424	4.878	0.5124
	304LSS	1.22	6.25	0.4

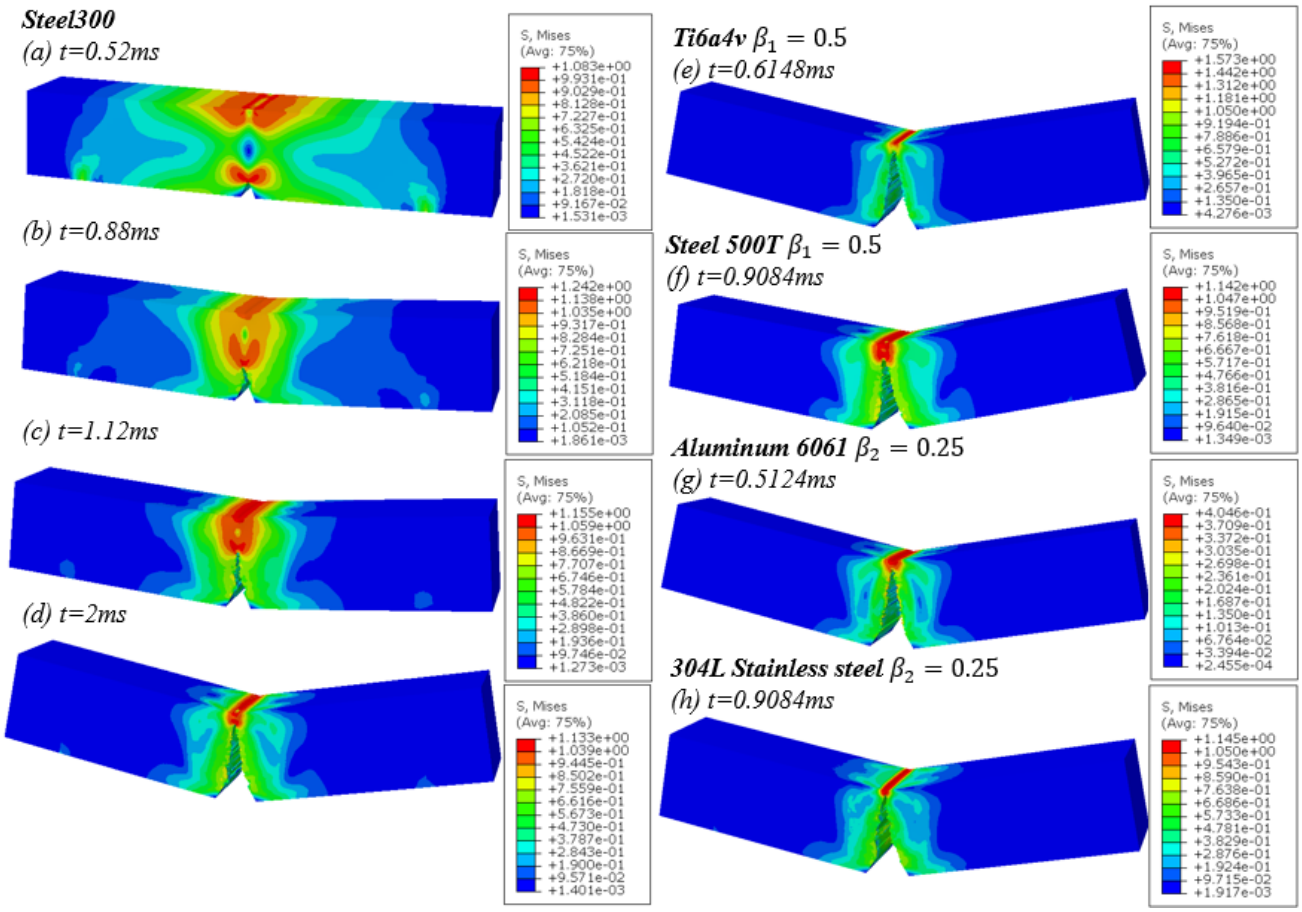

Figure 5.2 Charpy impact deformation for the physical model (a-d) along with a selection of trial models (e-h) displaying von-mises stress contours.

- Preliminary findings

Simulation results returned by Abaqus for the physical and a selection of trial models are presented in Fig. 5.2. The propagation of the crack through the specimen is shown in this figure for the physical model with trial models limited to an instant prior to specimen separation. A feature of the Charpy test is that its relative simplicity means that zeroth-order model with the same material provides good representative behaviour. Note that for zeroth order the first-order relationships in Table 1 for displacement, stress and strain rate (for example) simplify to $\boldsymbol{u}_1 = \beta_1^{-1}\boldsymbol{u}_{ts1}$, $\boldsymbol{\sigma}_1 = \alpha_{01}^{v} g_1 \beta_1^2 \boldsymbol{\sigma}_{ts1}$, and $\dot{\boldsymbol{\varepsilon}}_1 = g_1 \dot{\boldsymbol{\varepsilon}}_{ts1}$ (or $\boldsymbol{u}_1 = \beta_2^{-1}\boldsymbol{u}_{ts2}$, $\boldsymbol{\sigma}_1 = \alpha_{02}^{v} g_2 \beta_2^2 \boldsymbol{\sigma}_{ts2}$, and $\dot{\boldsymbol{\varepsilon}}_1 = g_2 \dot{\boldsymbol{\varepsilon}}_{ts2}$) which provides the means to relate quantities in the physical and trial spaces. Results as viewed in the physical space with identical materials throughout are provided in Fig. 5.3, which show a high level of conformity.

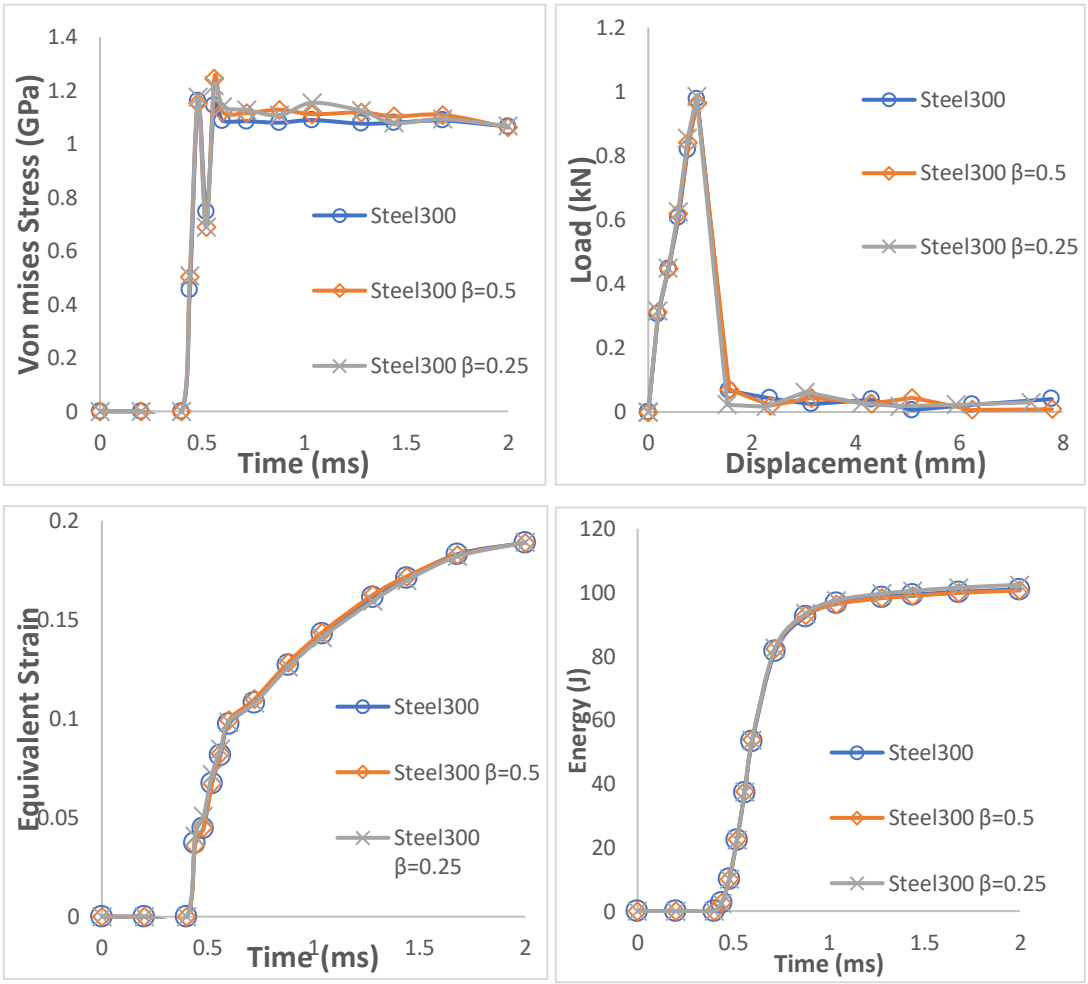

Figure 5.3 Trial and physical space results are viewed in the physical space with Steel300 used in all models.

The results of Fig. 5.3 confirm that there is little need to involve first-order theory for this case when identical materials are involved. However, the purpose of the study here is to examine whether different trial materials can be used to achieve similar outcomes as this is of practical importance. Referred to the references of the Charpy Impact test [153-155], the Charpy impact test evaluations should be representative of the material's behaviour. It needs to consider the unit of outputs, ensuring outputs with totally different units are tested in finite similitude theory. Hence, one is selected to be the load that the bending model affords versus the displacement of the impactor. Then there is the stress behaviour of an element during the deformed process. Finally, the energy dissipation over the process is the primary data to evaluate in the Charpy impact test. It investigates the EPFM issue between different materials, so the accuracy of the simulation is supposed to be close to the studies in Chapter 3, which is

'error < 5%'. Errors of outputs will be calculated with their maximum values, representing the strength of materials. The x-axis values like time and displacement are identical since the scaling theory controls the initial velocity and time. The results returned under zeroth-order theory involving different material are presented in Fig. 5.4, where large deviations are apparent. Also depicted is the element selected for detailed comparison between the physical model and the similitude method. However, the question of concern is whether it possible by means of the first-order theory to reduce some of the errors involved.

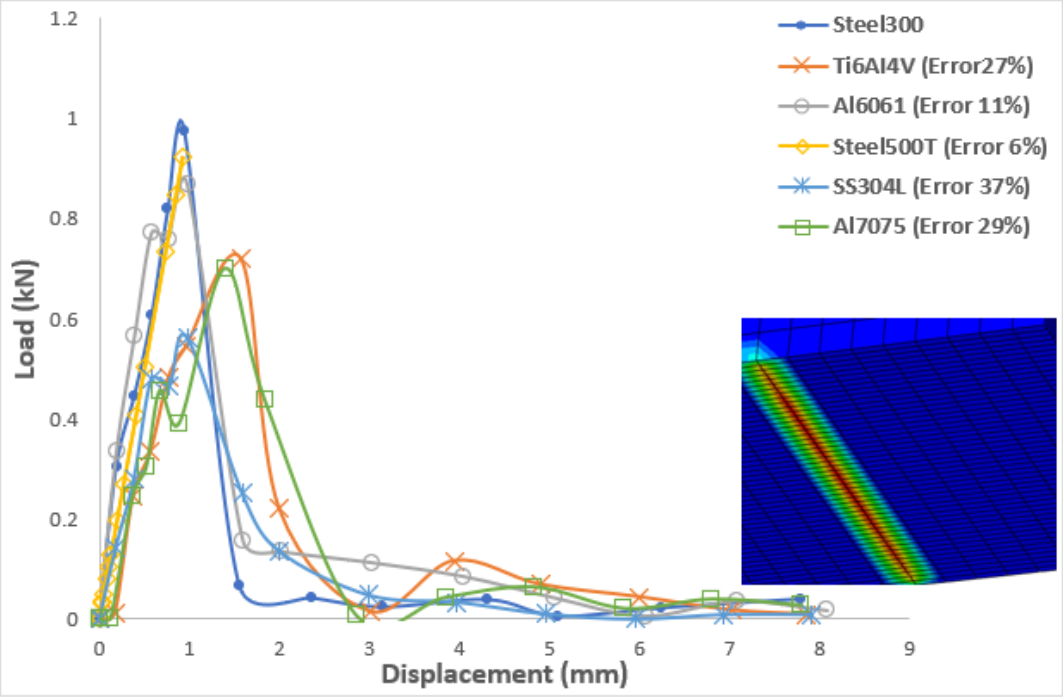

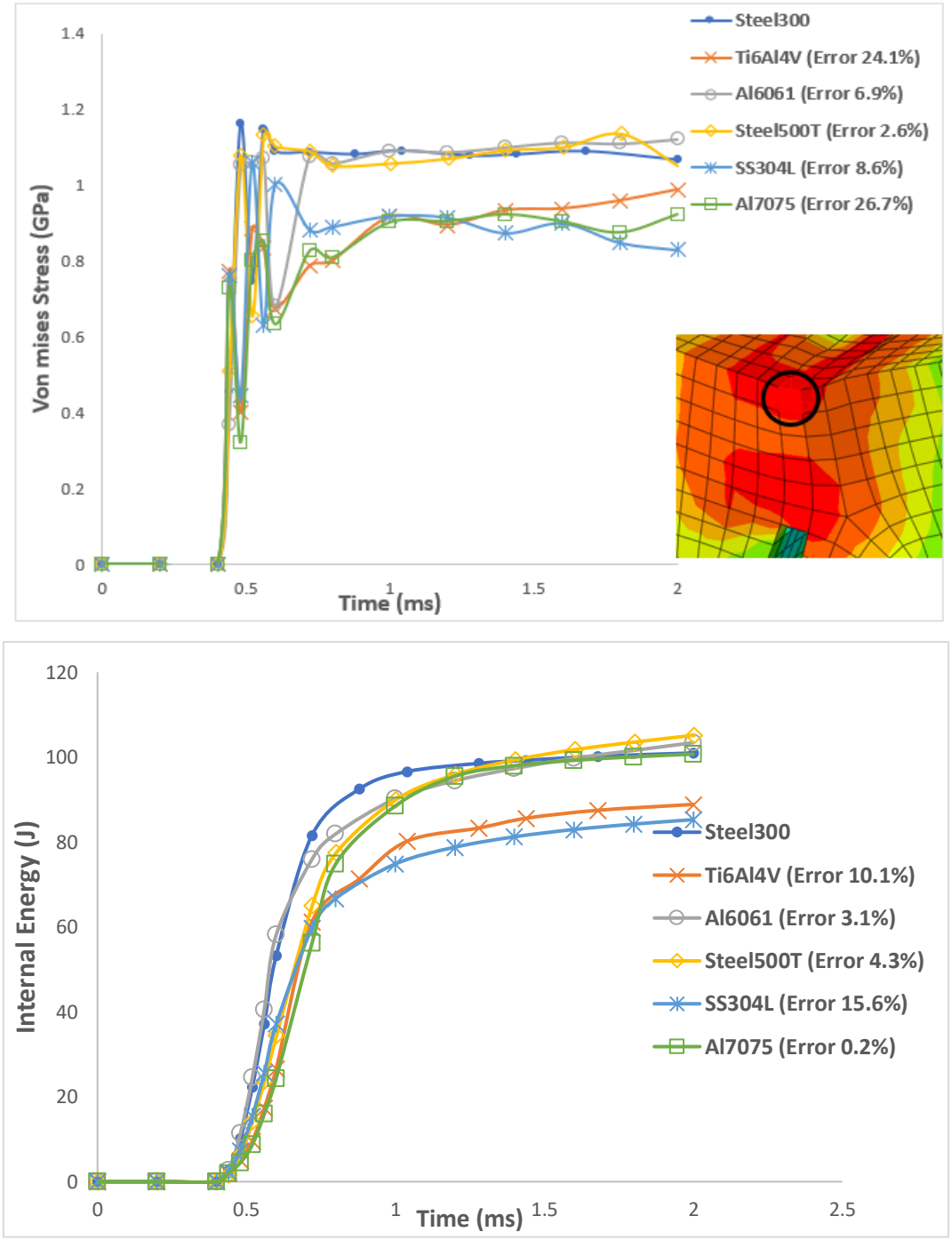

Figure 5.4 Trial and physical space results are viewed in the physical space for a selection of trial materials.

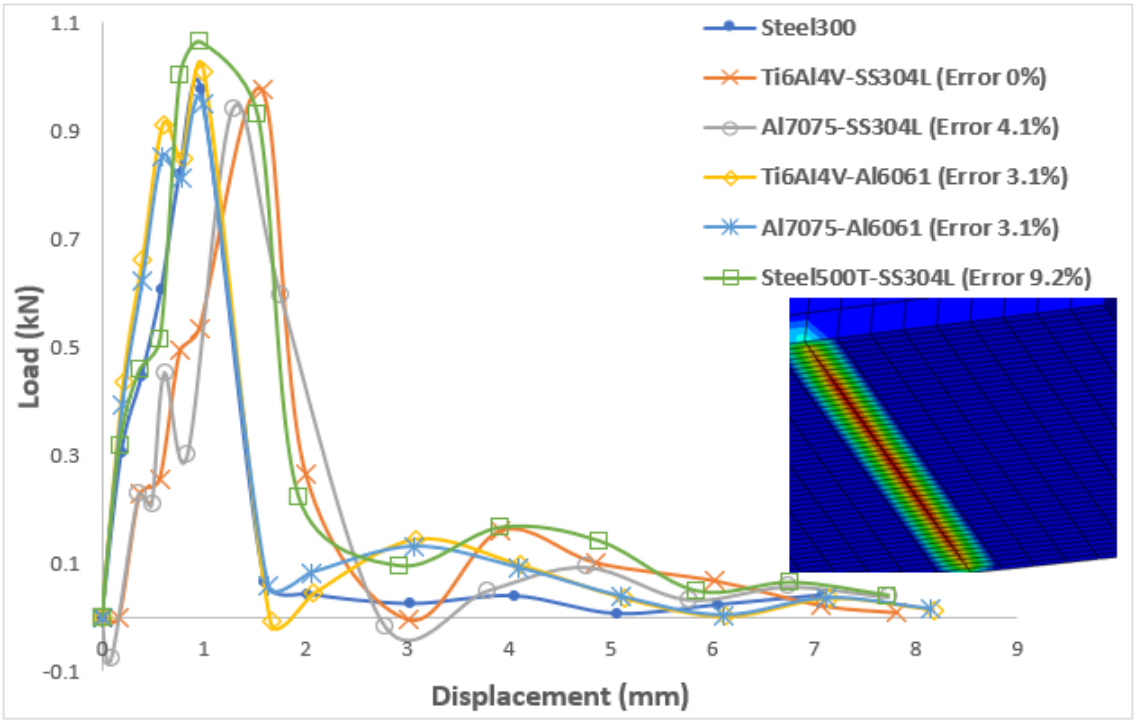
Steel300
Ti6Al4V-SS304L (Error 0%)
Al7075-SS304L (Error 4.1%)
Ti6Al4V-Al6061 (Error 3.1%)
Al7075-Al6061 (Error 3.1%)
Steel500T-SS304L (Error 9.2%)
Load (kN)
Displacement (mm)
1.1
0.9
0.7
0.5
0.3
0.1
-0.1
0
1
2
3
4
5
6
7
8
9

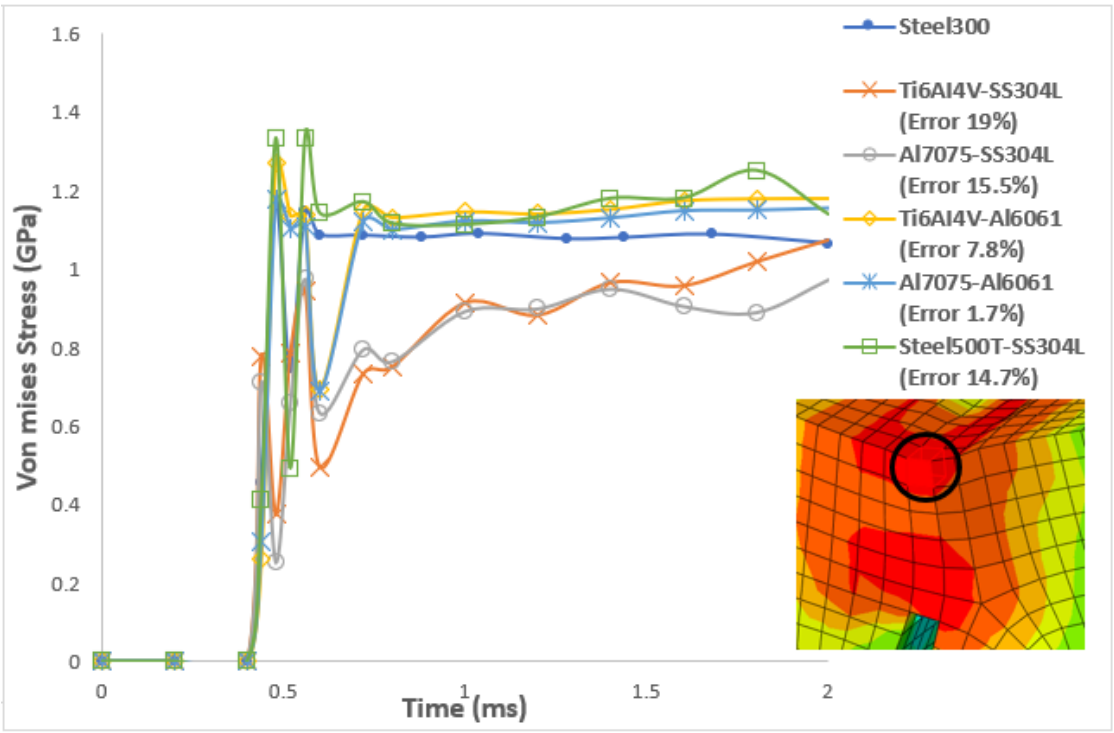
Steel300
Ti6Al4V-SS304L (Error 19%)
Al7075-SS304L (Error 15.5%)
Ti6Al4V-Al6061 (Error 7.8%)
Al7075-Al6061 (Error 1.7%)
Steel500T-SS304L (Error 14.7%)
Von mises Stress (GPa)
Time (ms)
1.6
1.4
1.2
1
0.8
0.6
0.4
0.2
0
0
0.5
1
1.5
2

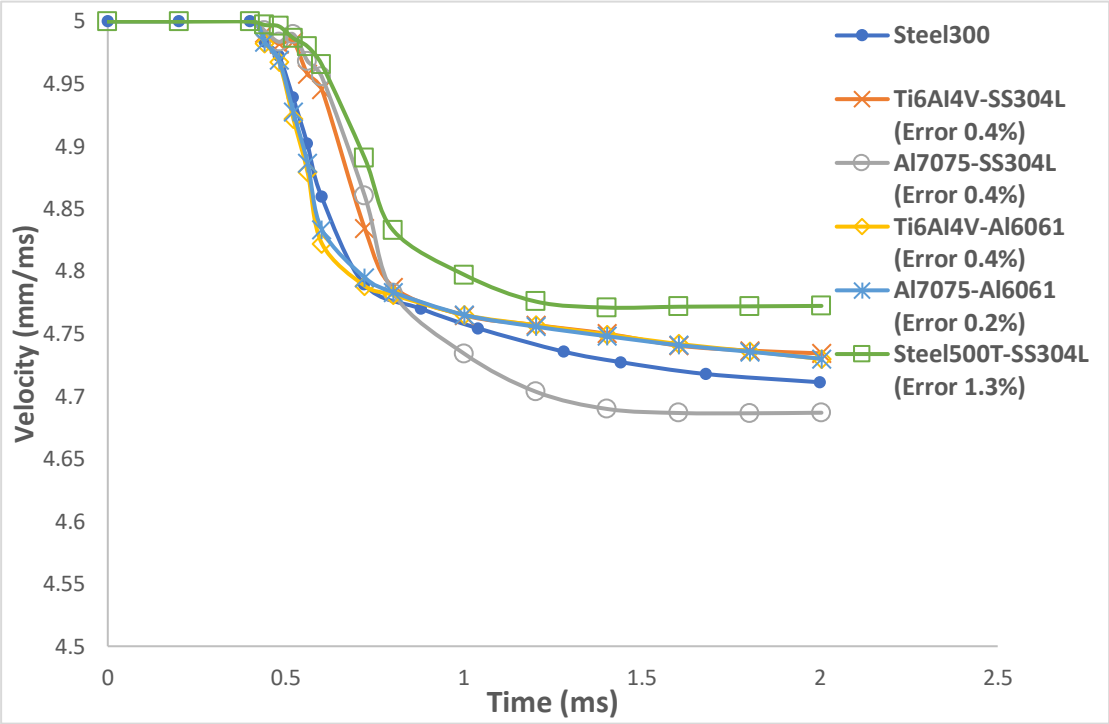

Figure 5.5 Striker velocity returned by first-order theory in comparison with full-scale result.

First-order results are presented in Fig. 5.5 based on the identities listed in Table 5.1, with errors listed in Table 5.5, where the differences between zeroth and first order are exposed. For the criterion of the error is 5%, not all combinations provide good outcomes as might be anticipated. Results of the zeroth-order theory are most not acceptable, except with Steel500T. However, it shows a particular case that material performs well in zeroth-order theory but cannot produce better results in the first order. It is because Steel500T's properties significantly differ from both physical material and the other trial material, but it can still be acceptable in zeroth-order simulation. Al6061 provides nearly acceptable results, which can be generally improved with other materials in first-order theory. Note the response of the non-steel combination Al7075-Al6061. The good accuracy returned by this combination indicates that it is a potential candidate for practical studies. Although the first-order theory does not provide an expression for energy (being of higher order) the energy absorbed by the specimen can nevertheless be obtained from the striker velocity, as indicated in Fig. 5.5. According to the results in the figures, steel500T and Al6061 are selected for zeroth-order and first-order simulation, respectively.

Table 5.5 Result comparison at critical point of curves presented in Fig. 5.

Physical		Peak load (kN)	Displacement (mm)	Maximum von mises stress (GPa)	Maximum strain	Final Velocity (mm/ms)
Steel300		0.98	7.79	1.16	0.189	4.71
Trial mat. 1 ($\beta_1 = 0.5$	Trial mat. 2 $\beta_2 = 0.25$	Peak load (kN) (Error%)	Displacement (mm) (Error%)	Maximum von mises stress (GPa) (Error%)	Maximum strain (Error%)	Final Velocity (m/s) (Error%)
Steel500T	-	0.92 (6%)	7.77 (0.3%)	1.13 (2.6%)	0.204 (7.9%)	4.69 (0.4%)
Ti6Al4V	-	0.72 (27%)	7.85 (7.7%)	0.88 (24.1%)	0.198 (4.8%)	4.76 (1.1%)
Al7075	-	0.7 (29%)	7.79 (0%)	0.85 (26.7%)	0.182 (3.7%)	4.73 (0.4%)
-	304LSS	0.56 (37%)	7.91 (1.5%)	1.06 (8.6%)	0.189 (0%)	4.82 (2.3%)
-	AL6061	0.87 (11%)	7.99 (2.6%)	1.08 (6.9%)	0.196 (3.7%)	4.73 (0.4%)
Steel500T	304LSS	1.07 (9.2%)	7.72 (0.9%)	1.33 (14.7%)	0.209 (10.6%)	4.77 (1.3%)
Ti6Al4V	Al6061	1.01 (3.1%)	7.97 (1%)	1.27 (7.8%)	0.199 (5.3%)	4.73 (0.4%)
Ti6Al4V	304LSS	0.98 (0%)	7.81 (0.3%)	0.94 (19.0%)	0.202 (6.9%)	4.73 (0.4%)
Al7075	304LSS	0.94 (4.1%)	7.74 (0.6%)	0.97 (15.5%)	0.178 (5.8%)	4.69 (0.4%)
Al7075	Al6061	0.95 (3.1%)	7.93 (1.8%)	1.18 (1.7%)	0.194 (2.6%)	4.72 (0.2%)

5.3 Application in external impact processes

Armed with the preliminary findings of Section 5.3 for a selection of material combinations, and the favoured parameter selection procedure, it is of interest to explore a practical case study involving impact on a pressure vessel. The analysis is performed with the commercial finite element software package Abaqus explicit, which is particularly well suited to impact studies.

5.3.1. Pressure vessel and the test process

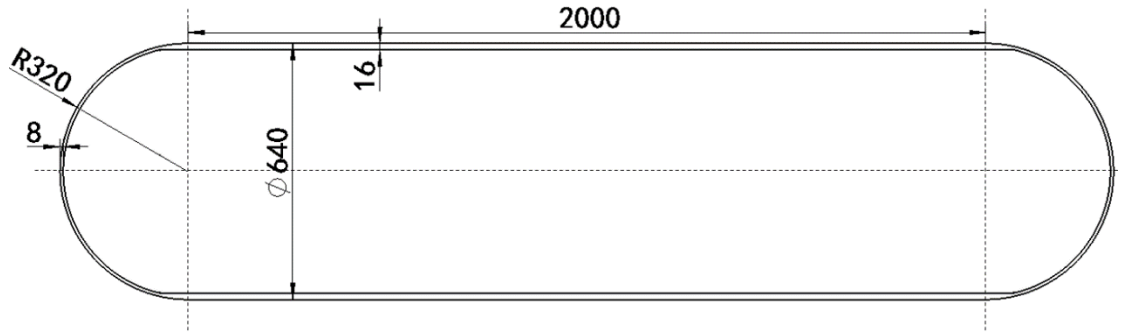

Figure 5.6 Cross-section view and dimensions for a pressure vessel residing in the physical space.

The pressure vessel of interest is depicted in Fig. 5.6 and is thin-walled and designed in accordance with the pressure vessel design manual [172]. The pressure vessel dimensions in the physical space are presented in Fig. 5.6 and is furnished with a tetrahedral mesh in preparation for finite element analysis as depicted in Fig. 5.7. A global element size of 20mm is applied with a finer mesh of 1mm at 10mm*10mm area around the target point of the projectile detailed in Fig. 5.7. A total of 89890 C3D10M elements are utilised with the bullet (projectile) and supports for the pressure vessel set to be rigid but nonetheless meshed with 2mm sized elements. The simulation of a high-velocity impact on the pressure vessel follows that presented in ref [173], with identical parameters and bullet velocity applied in the physical space. The setting for the projectile penetration test is shown in Fig. 5.7(b) with the pressure vessel bonded to two supports, which are fixed on the floor, and the projectile is targeted at the middle of the vessel. Dimensions of the projectile as applied in the physical space is detailed in Fig. 5.7(c). Note however, these features are expected to change in the trial space models with bullet mass, size and velocity adjusted according to the similitude rules. The initial bullet velocity is defined to be the velocity at that instant when the bullet touches the pressure vessel. For the Abaqus simulation the change in bullet velocity is of principal concern along with stress and equivalent strain at the damaged site.

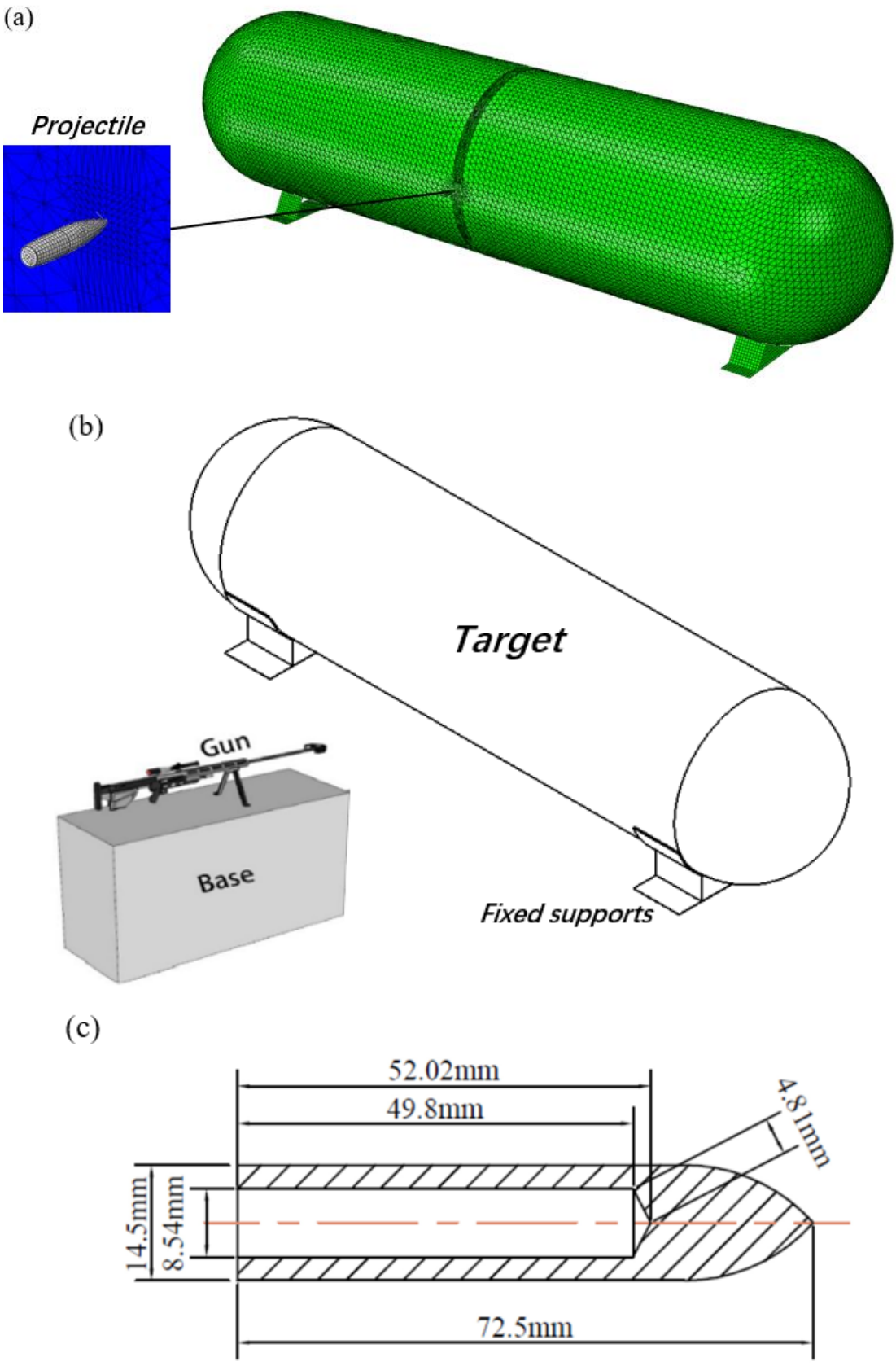

Figure 5.7 Impact loading of a pressure vessel with (a) meshed details of the vessel, (b) setting of the high-rate impact test, and (c) dimensions of the projectile in the physical space. [173]

Table 5.6 Parameters of projectiles for different scales and materials.

Scale	Material	Mass of projectile $M\ (g)$	Initial velocity of projectile $v_i\ (mm/ms)$	Period of the impact process $(10^{-4}s)$	Internal pressure of vessel (MPa)
Physical	Steel300	54.2	950	1	20
Trial 1 $(\beta_1 = 0.5)$	Steel300	6.8	962.17	0.4937	20.5
	Ti6Al4V	4.0	1545.2	0.3074	29.3
	Al7075	2.3	1662.7	0.2857	20.7
	Steel500T	6.8	1045.8	0.4542	24.2
Trial 2 $(\beta_2 = 0.25)$	Steel300	0.85	974.19	0.2438	21
	Al6061	0.29	926.88	0.2562	6.5

5.3.2. Application of first-order theory

To make use of the data presented in Table 5.3 the length scale factors β_1 and β_2 are once again set to 0.5 and 0.25, respectively for trial models. The materials identified in Section 5.3 are applied here also with the important information recoded in Table 5.6. Note that the internal pressure for the pressure vessel in the physical space is set to 20MPa and the period of penetration is 0.1ms, which is the time taken for the bullet to completely pass through the front shell. The process of penetration is depicted in Fig. 5.8 along with corresponding projectile velocities and times. The exact same analysis is repeated for the trial models with the initial velocity satisfying the zeroth order condition $\boldsymbol{v}_1 = g\beta^{-1}\boldsymbol{v}_{ts}$ as logged in Table 5.6. For the different models the bullet velocity is plotted against displacement as show in Fig. 5.9 to provide a means to contrast the different responses.

The impact test selects materials based on the results in the Charpy impact test for accurate and acceptable results, which makes the criterion of validation in this test

different and specific. Referring to the results in Fig 5.5, the criterion of velocity change should be less than 1%, and for the stress field result, it can be 7.8%.

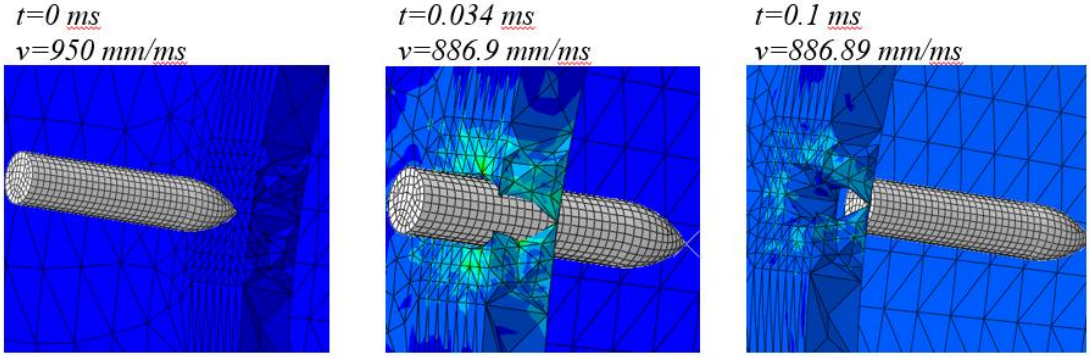

Figure 5.8 Penetrating process of the physical model.

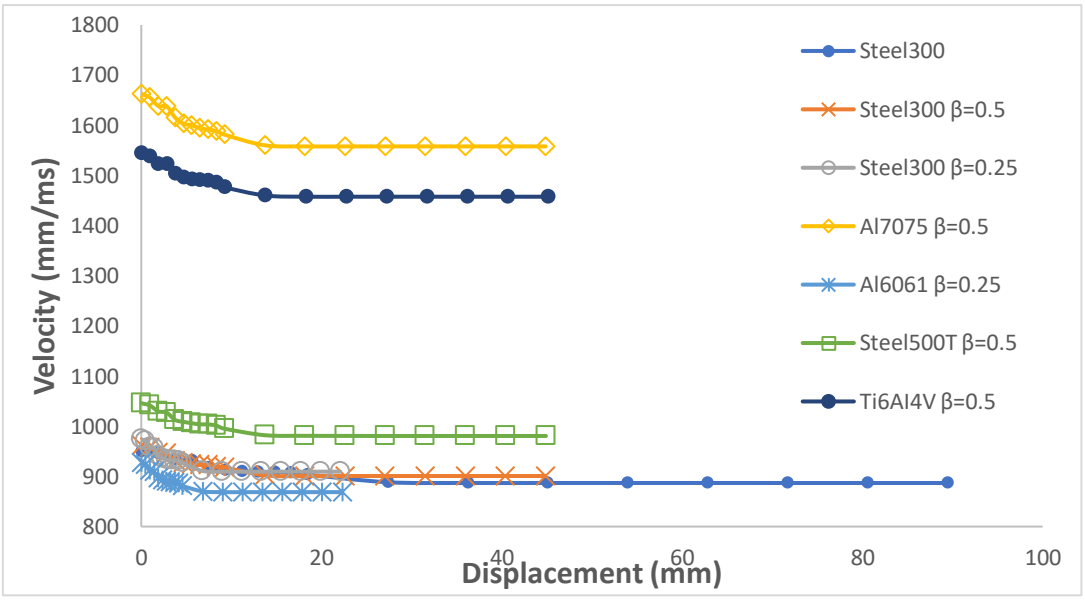

Figure 5.9 Velocity changes through displacement for all models.

Application of the zeroth order relationship condition $\boldsymbol{v}_{ps} = g\beta^{-1}\boldsymbol{v}_{ts}$ and condition $t_{ps} = g^{-1}t_{ts}$ and viewing of the results in the physical space provide the graphs in Fig. 5.10. Zeroth order provides a reasonable approximation in most cases with Ti6Al4V performing worst, so accordingly this material is taken forward (along with Al5075) for improvement with the first-order theory. Cases 1.5 and 1.8 shown in Table 5.3 are considered with velocity satisfying the first-order relationship in Table 5.1. The results for two first-order models are depicted in Fig. 5.11, where the increase in accuracy returned by a two-experiment material model is revealed. The

errors in the prediction of the final velocity of the bullet are recorded in Table 5.7, where an 8-fold improvement in accuracy is reported for Ti6Al4V.

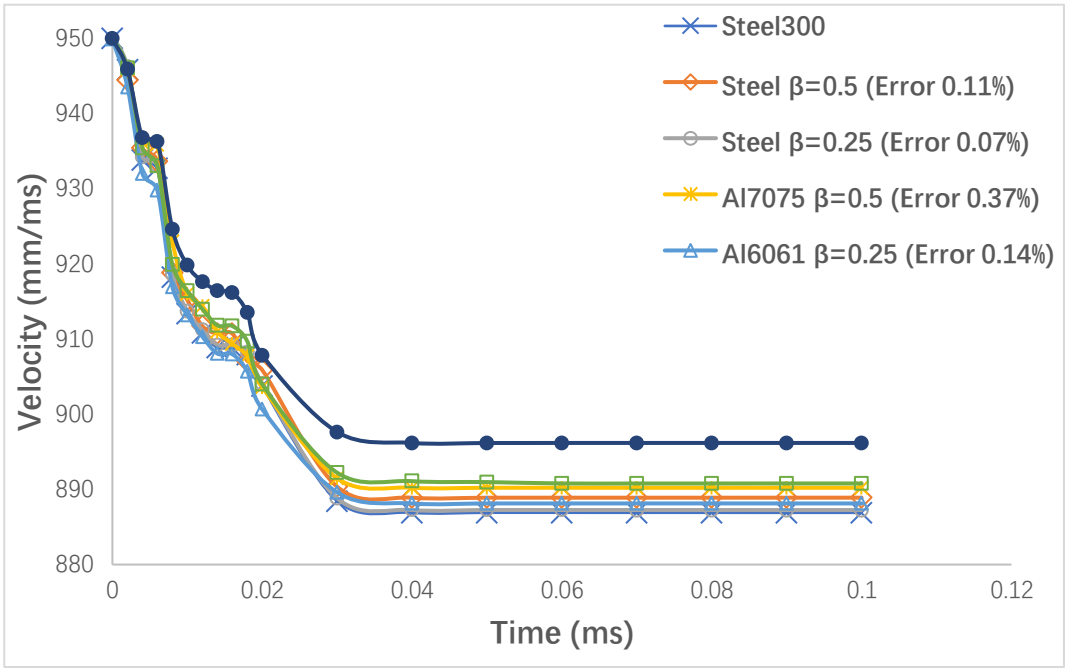

Figure 5.10 Temporal response of bullet velocity as viewed by all models in the physical space.

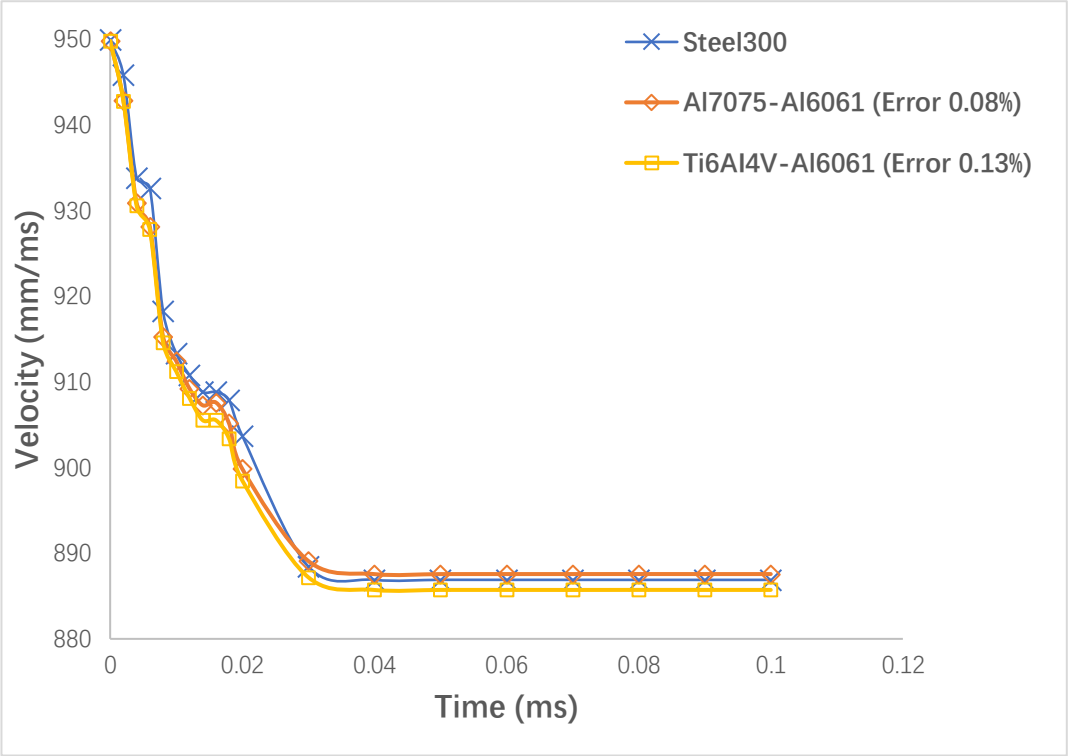

Figure 5.11 Temporal response of bullet velocity as viewed in the physical space for two first-order models.

Table 5.7 Final bullet velocity with errors recorded for zeroth and first-order models.

Physical material		Final Velocity (mm/ms)	
Steel300		886.89	
Trial material 1 ($\beta_1 = 0.5$)	Trial material 2 ($\beta_2 = 0.25$)	Final velocity (mm/ms)	Error
Steel300	-	887.89	0.11%
-	Steel300	887.25	0.07%
Steel500T	-	890.79	0.44%
Al7075	-	890.21	0.37%
Ti6Al4V	-	896.18	1.04%
-	Al6061	888.13	0.14%
Al7075	Al6061	887.57	0.08%
Ti6Al4V	Al6061	885.71	0.13%

It is of interest to explore other physical fields to ascertain whether the first-order theory can reproduce other behaviours. The von mises stress field in the vicinity of the localised damage zone is recognised to be complex and therefore challenging to capture exactly. A path and the von mises stress are recorded along this path are presented in Fig. 5.12. The stresses shown are residual stresses remaining at the damaged site following full penetration by the projectile. The path is located at the edge of the finer mesh zone and sufficiently far away from the hole to avoid obliteration by the bullet. Although not every feature of the curve for Steel300 is captured, nevertheless, the two first-order models Ti6Al4V-Al6061 and Al7075-Al6061 provide a reasonable account and give significantly better results than models based on Ti6Al4V and Al7075 alone.

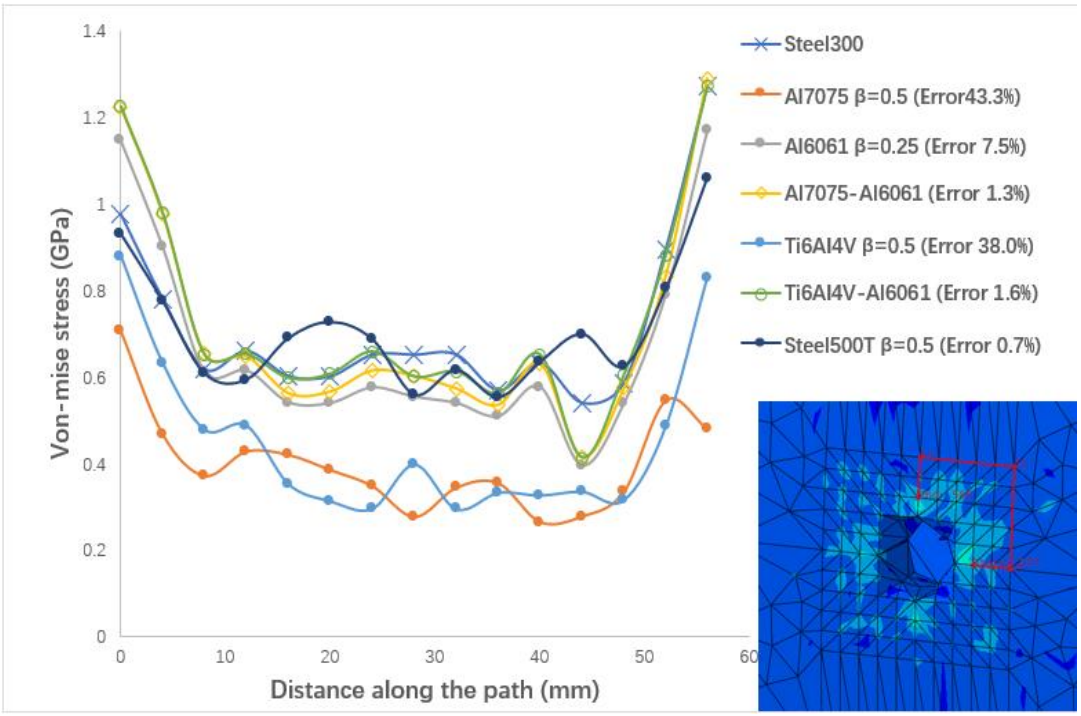

Figure 5.12 Von mises stress in the vicinity of localised damage along the path.

The change in bullet velocity is captured reasonably well by the zeroth-order theory although improved upon with first order. This is not too unexpected since the cylindrical-vessel wall is relatively thin and consequently the bullet passes through relatively quickly providing little scope for large deviations. Greater complexity is apparent in the vessel stress field local to the damage zone being influenced more by material response and type. The errors presented in Fig. 12 are average errors and it is evident from the undulations present in the curves that perfect replication of Steel300 is not achieved. However, despite the complexity involved the two first-order models Ti6Al4V-Al6061 and Al7075-Al6061 provide a good account and give significantly better results than models based on Ti6Al4V and Al7075 alone.

5.3.3. Practical constraints

Zeroth-order similitude rules have been applied in the study above to specify the mass and initial velocity of the bullet, but practical considerations impinge on this freedom. Available bullet types and mass necessitate the introduction of alternative dimensional scaling factors. Listed in Table 5.8 are a selection of available rifle cartridges, which

are to be contrasted against a 12.7mm NATO bullet [174] used in the physical space. In selecting a bullet for a trial model, the zeroth-order rules applied to the NATO bullet provide the desired dimensions and mass. Representative dimensions are given priority with mass dictated by availability. The initial bullet velocity is arranged to be higher than 920 m/s for all trial models and is set equal to 920 m/s for the tests. The geometric features of the bullet types listed in Table 8 are presented in Fig. 5.13 and are also referred to in ref [175].

Table 5.8 Bullets used in the different models.

β_i	Supposed Mass of projectile (g)	Supposed initial velocity (m/s)	Type of bullet applied (mm)	Applied Mass of projectile (g)	Applied initial velocity (m/s)	Period of the process $(10^{-4}s)$	Internal pressure of vessel (MPa)
1	50	908	12.7	45	908	1	20
0.6	10.8	916	8.0	12	920	0.6	20
0.5	6.25	920	6.5	7	920	0.5	20
0.4	3.2	923	5.0	3.4	920	0.4	21
0.3	1.35	928	4.0	1.8	920	0.3	21

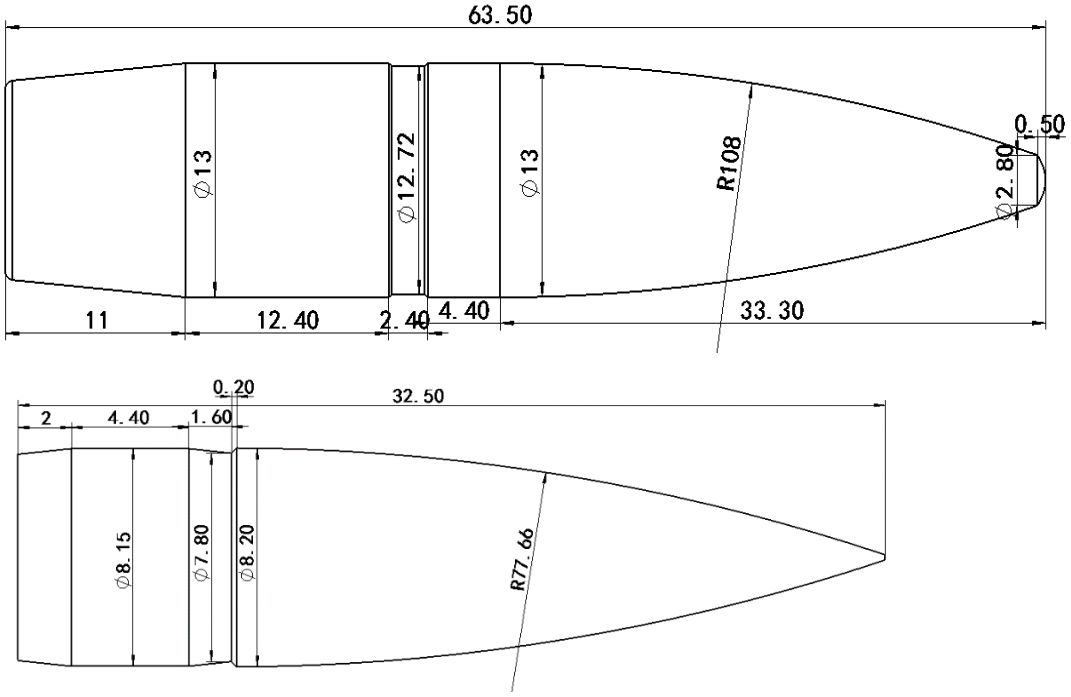

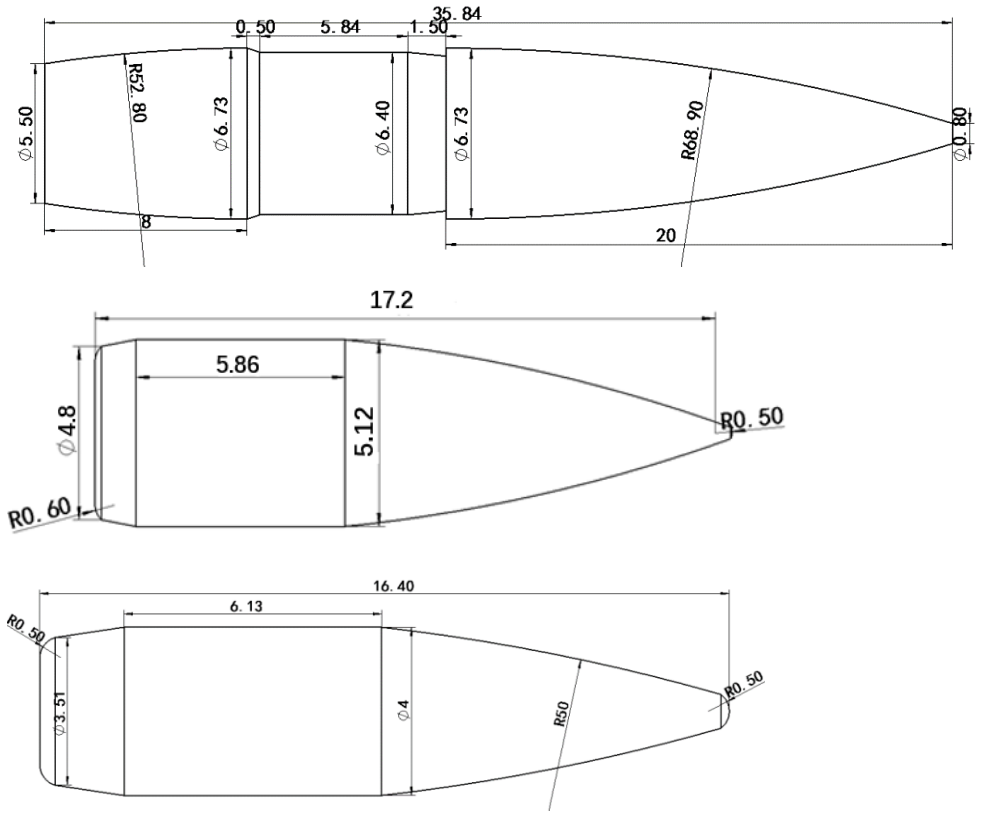

Figure 5.13 Bullet configurations with classifications 12.7mm, 8.0mm, 6.5mm, 5mm and 4mm respectively presented from top to bottom.

The setup in Fig 5.7 again applies, and scaling factors are calculated as outlined above although g_1 and g_2 are not critically set exactly equal to the values provided by Eqs. (5.8). An additional consideration is the velocity synchronization of the initial velocity between trial and physical models. However, since the applied velocity and the required velocity are close any change in g_1 and g_2 will have limited impact. Repeating the analysis above, identical materials are applied to all models and zeroth-order results are presented in Fig 5.14. Examination of this figure reveals significant disparities in the results due to mismatch in bullet mass. The mass is generally higher than the desired value (as indicated in Table 5.8) and consequently provides greater momentum and higher final velocities as indicated in Fig 5.14. Although there exist bullets with the correct mass, these possess smaller dimensions, which allows them to penetrate the pressure vessel shell wall much more easily.

Table 5.9 Scaling factor in Case study 2.

Case	β_1	β_2	g_1	g_2	α_1^ρ	α_2^ρ	R_1
3.1	0.5	0.3	0.4935	0.2961	8	37.037	1.42

3.2	0.5	0.4	0.4935	0.3948	8	15.625	3.2
3.3	0.6	0.3	0.5922	0.2961	14.1761	37.037	0.77
3.4	0.6	0.4	0.5922	0.3948	14.1761	15.625	1.31

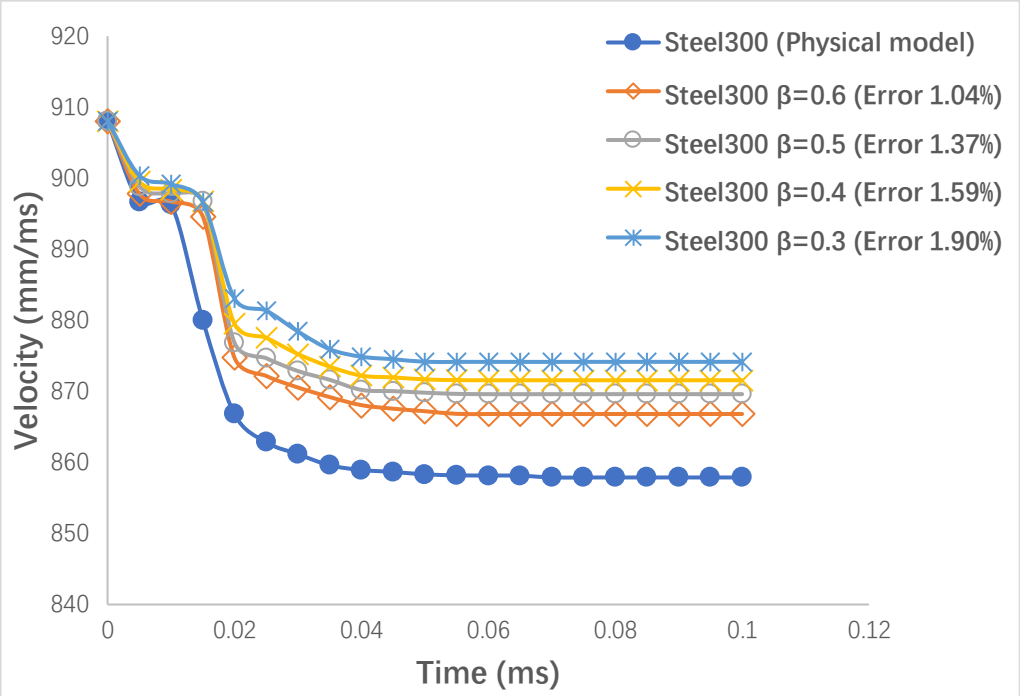

Figure 5.14 Trial and physical space results are viewed in the physical space with Steel300 used in all models.

To improve on the results presented in Fig. 5.14 the first-order theory is next considered applying the velocity expression in Table 5.1, with results returned in Fig. 5.15. A significant improvement in the results is apparent, which are quantified explicitly in Table 5.10 for the final velocity for both zeroth and first-order predictions. Taking into consideration the data in Table 5.8, it is apparent that lower β values produce larger errors with zeroth-order scaling. results, Although the initial velocities are identical the errors are due to the difference between the required mass and the actual mass of the bullets, and additionally smaller models are invariably more sensitive to this difference. The mass error for trial model $\beta = 0.4$ is lower than trial model $\beta = 0.5$ (6% to 12% respectively) yet the error associated with the smaller projectile is larger. The application of two-experiment physical modelling provides the flexibility to counter such errors as revealed by the improvement recorded in Fig. 5.15.

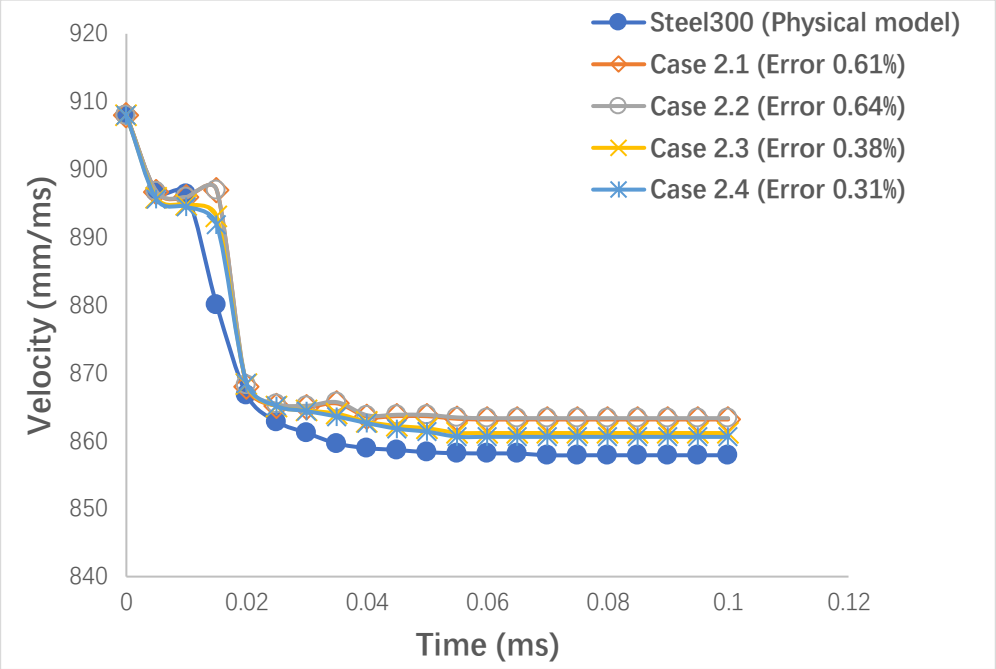

Figure 5.15 Trial and physical space first-order results are viewed in the physical space for replica scaling.

Table 5.10 Final velocity and the error of all models in case study 2.

β_1 (Steel300)	β_2 (Steel300)	Final velocity (mm/ms)	Error (%)
1	-	857.89	0
0.6	-	866.82	1.04
0.5	-	869.61	1.37
0.4	-	871.57	1.59
0.3	-	874.16	1.90
0.5	0.3	863.15	0.61
0.5	0.4	863.35	0.64
0.6	0.3	861.16	0.38
0.6	0.4	860.59	0.31

5.4 Application in internal explosive loading test

An alternative loading type important for of pressure vessels is shock loading arising from an internal blast, which is a commonly used test and safety measure for testing resistance to overpressure. A respected approach for the simulation of explosive blast loading using the finite element method is the conventional weapons effect program (Conwep) first developed for military purposes. This approach can be used to simulate several types of explosions involving the production of a shock wave by the sudden release of energy from an explosive core. The critical parameters in a Conwep model are converted to mass of Trinitrotoluene (TNT), type of blast, location of detonation, and the applied surfaces.

5.4.1. Model and the input parameters.

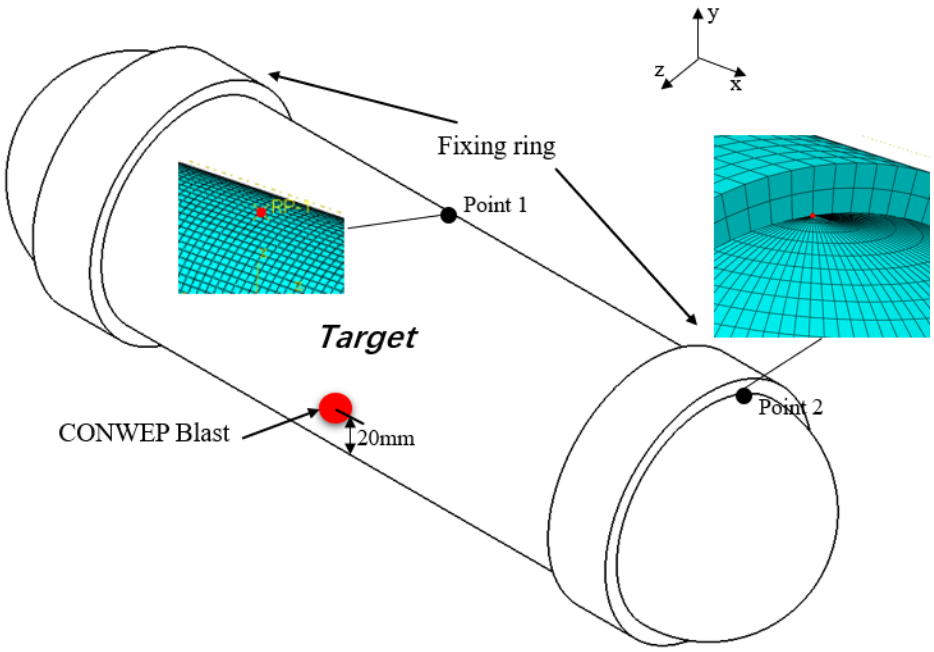

Figure 5.16 Pressure vessel model subjected to the internal blast.

The details of the pressure vessel and model can be found in Fig. 5.16 and is based on the analysis performed by Barsoum et al. [176] in that it involves the same pressure vessel, penetration test, and two fixing rings at the ends of vessel. The rings feature to ensure that the vessel does not split and is able to withstand the internal blast both statically and dynamically. The explosive loading acts over all the inner surfaces of the pressure vessel making it unnecessary for a targeted fine meshed so a global mesh size of 10mm is applied to the physical model. A shell model consisting of 60600 S4R

shell elements is adopted in this study as opposed to a solid model. A shell model is selected here because it better suited to capture the nonlocalized loading and response of the pressure vessel model and consequently provides for greater stability and accuracy. The source of the explosion (TNT) is located at the middle of the pressure vessel 20mm from the bottom surface as shown in Fig. 5.16. A 1kg mass of TNT is used as the source of the Conwep blast in the physical model; this is sufficient to ensure that the shell is damaged under explosive loading. Identified points of interest in this study are points 1 and 2 labelled in Fig. 5.16. The materials considered in this study are titanium for the physical model, along with aluminium, steel and stainless steel for the trial models. Here the material order is changed due to the engineering practice, which can also prove that the material order in finite similitude theory will hardly affect the results. The scaling parameters for the new material combinations are shown in Table 5.11. For the tests to comply with the analysis performed in Section 5.3 the dimensional scaling factors are once again set to be equal to $\beta_1 = 0.5$ and $\beta_2 = 0.25$. The pertinent parameters for the models are logged in Table 5.12, where the mass of TNT in each model is determined on scaling of the explosive mass with size. Note that internal blast loading differs from the previous loading case (i.e., external impact with an impactor) in the sense that the source mass is most critical as opposed to the loading rate. Consequently, the mass of TNT and the period of the loading process in the trial space are not dictated by the time scalar g per se, but by the scale of the model.

Table 5.11 Scaling parameters for materials in the internal explosion study.

Case	Trial material 1 ($\beta_1 = 0.5$)	Trial material 2 ($\beta_2 = 0.25$)	g_1	g_2	α_1^ρ	α_2^ρ	R_1
3.1	Ti-6Al-4V	Ti-6Al-4V	0.4978	0.2478	8	64	1
3.2	Steel300	SS 304L	0.8041	0.3287	4.4355	36.3487	-0.5482
3.3	AL7075	AL6061	0.4632	0.4140	13.1259	104.6199	-0.6215

Table 5.12 Input parameters for the explosive loading model.

Scale	Material	Mass of TNT $M\ (g)$	Period of the impact process (ms)	Distance from explosion to the surface (mm)
Physical	Steel300	1000	2	20
Trial 1 ($\beta_1 = 0.5$)	Steel300	125	1	10
	Ti-6Al-4V	125	0.96	10
	AL7075	125	0.94	10
Trial 2 ($\beta_2 = 0.25$)	Steel300	15.625	0.5	5
	AL6061	15.625	0.48	5

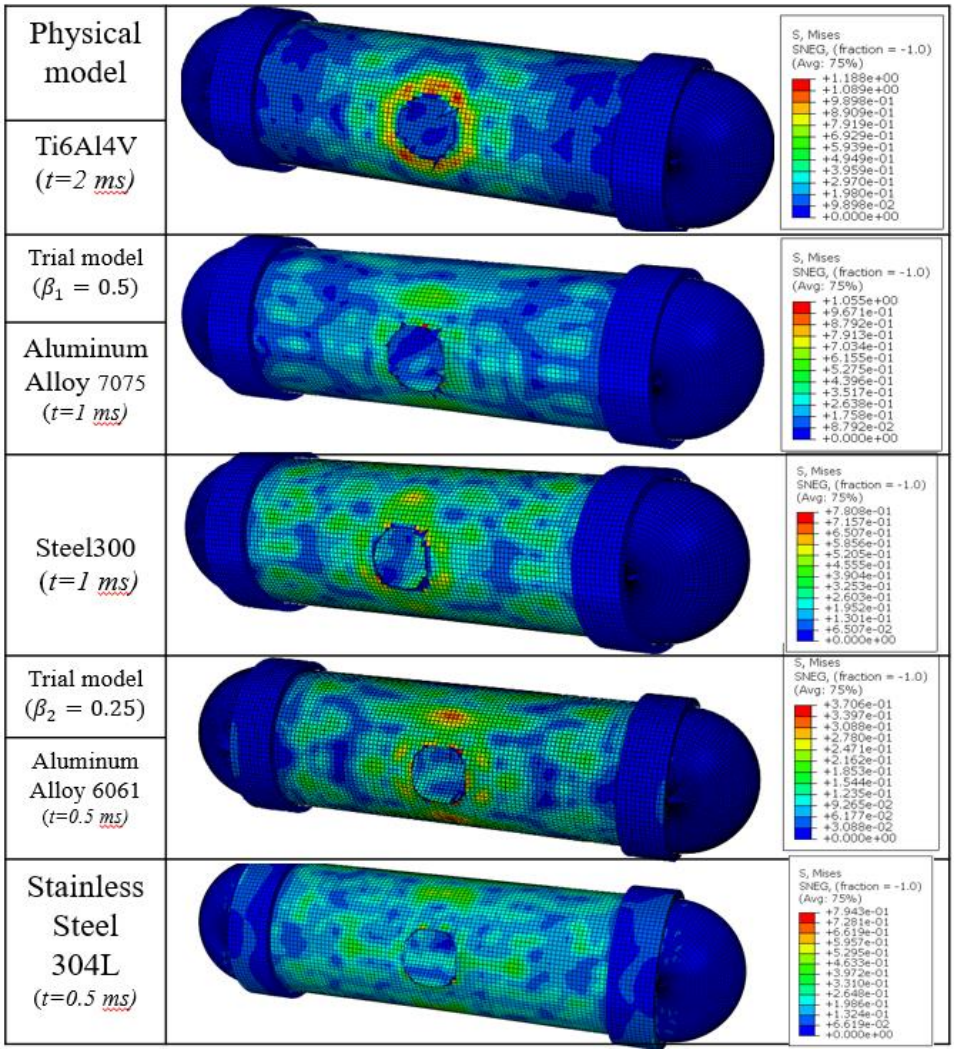

Figure 5.17 Von mises stress levels of the models for different materials.

5.4.2. Application of first-order theory

Von mises stress levels returned on performing a Abaqus analysis are presented in Fig.

5.17 for a steel physical model, and aluminium and titanium alloy trial models. The damaged area local to the charge is similar in each model but stress levels are significantly different. However, the temporal variation of pressure on the inner surface of the vessel at the damage site as viewed in the physical space (see Fig. 5.18), confirm that the TNT masses are appropriate in the zeroth-order models. Note how the pressure both rises and falls rapidly in accordance with the expected behaviour of a Conwep blast and damaged model.

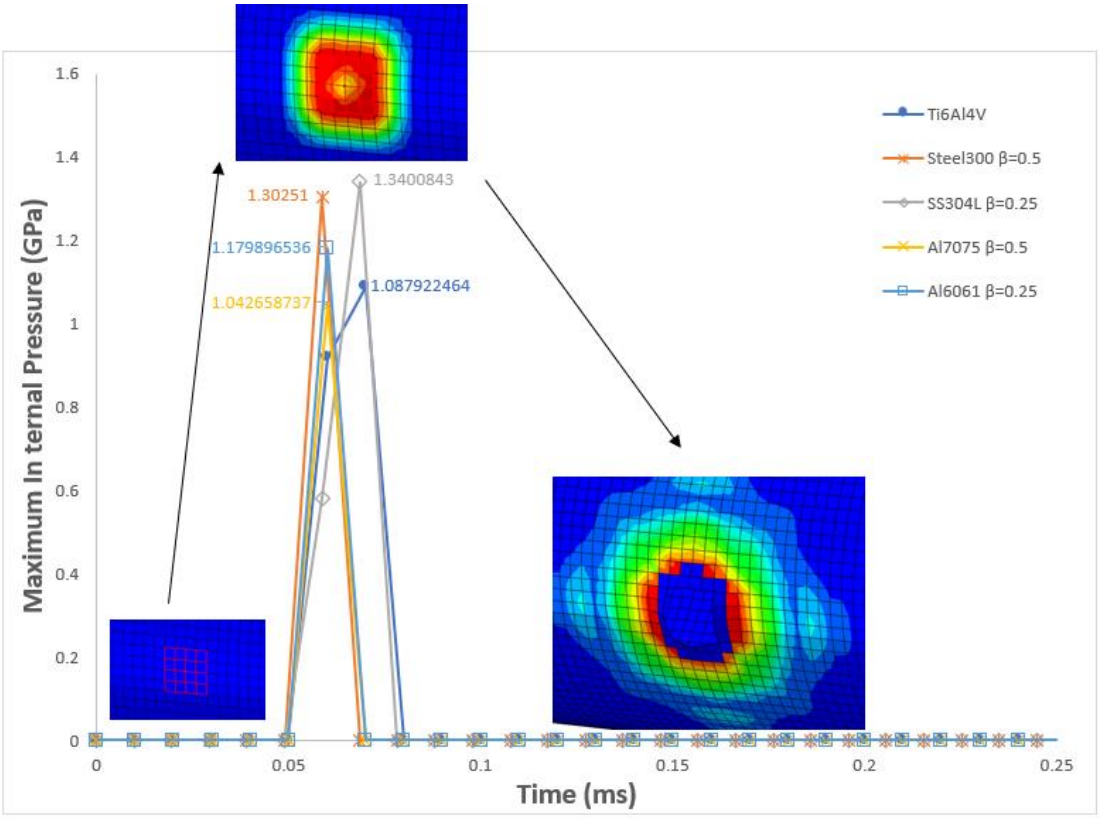

Figure 5.18 Temporal variation of pressure on the inner surface of the pressure vessel for the trial and physical spaces as viewed in the physical space.

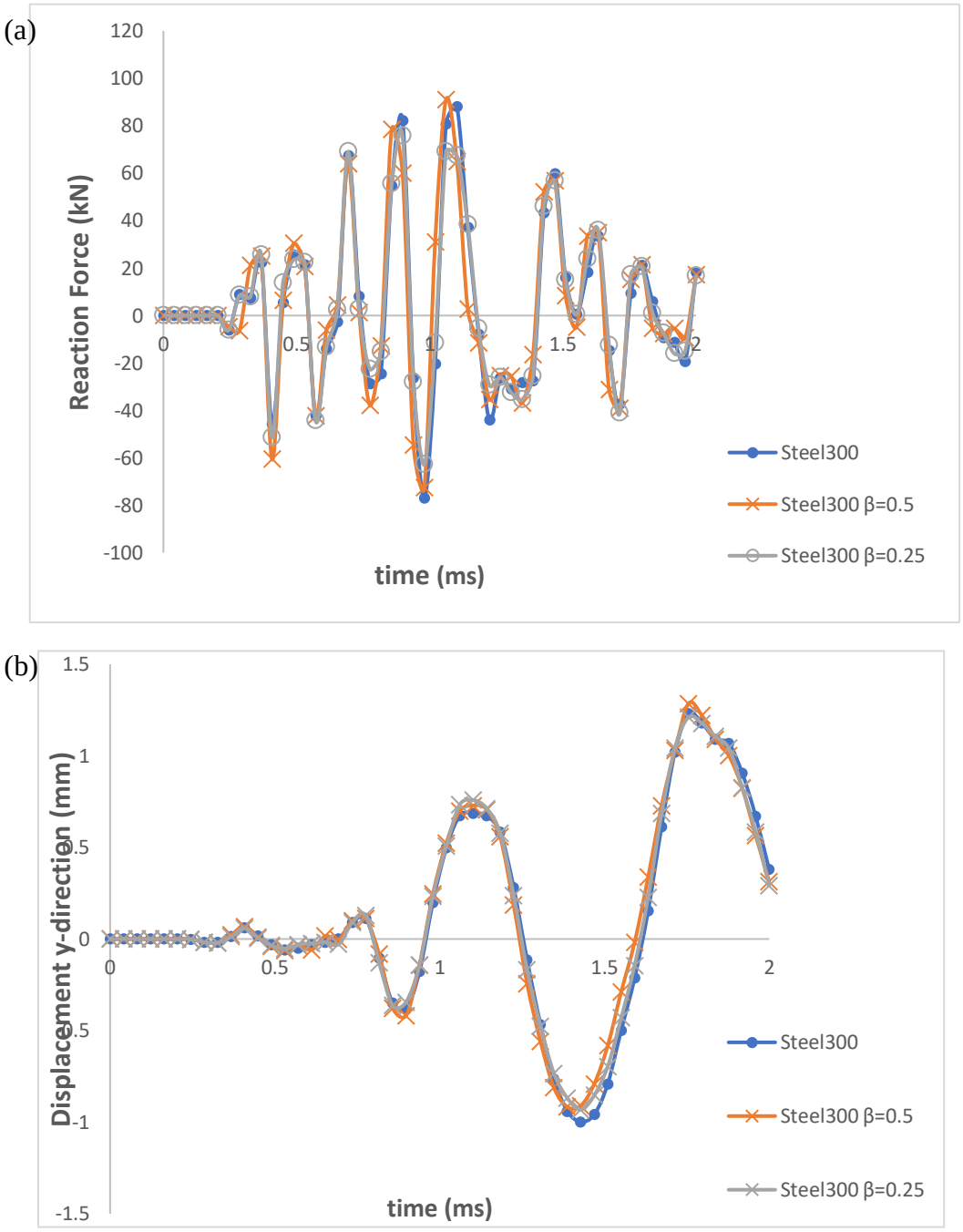

Figure 5.19 Trial and physical space zeroth-order results as viewed in the physical space for identical material showing (a) the reaction force at point 2, (b) the displacement in y direction at point 1 (see Fig. 5.16).

Zeroth-order results for replica scaling (i.e., using the same material throughout) are presented in Fig. 5.19. The close conformity of the results rules out the need for the application of the first-order theory. However, the focus here is on physical modelling and the ability of the first-order theory to rectify the differences in the individual models produced with different materials. Presented in Figs. 5.20 and 5.21 are results

returned on application of the first-order theory plotted alongside those returned with zeroth order. The percentage errors recorded are based on the areas under the curves, as the same criterion of error will be used here. Examination of Figs 5.20 and 5.21 reveal significant differences with greatest deviation resulting in the single experiment models. The first-order models although not providing perfect replication improve the predictions markedly. The frequency of vibration is represented to good accuracy, but amplitudes deviate at certain instances. Overall, however the first-order approach has been confirmed to significantly enhance the prediction even when in the presence of widely deviating zeroth-order results.

(a)

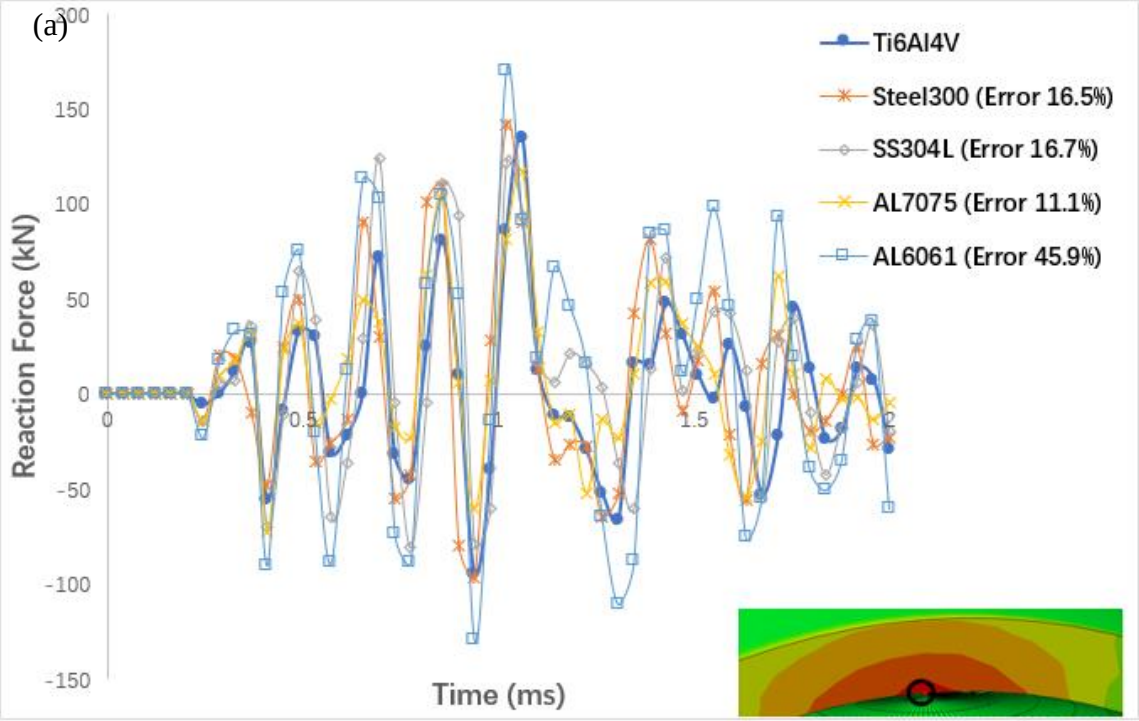

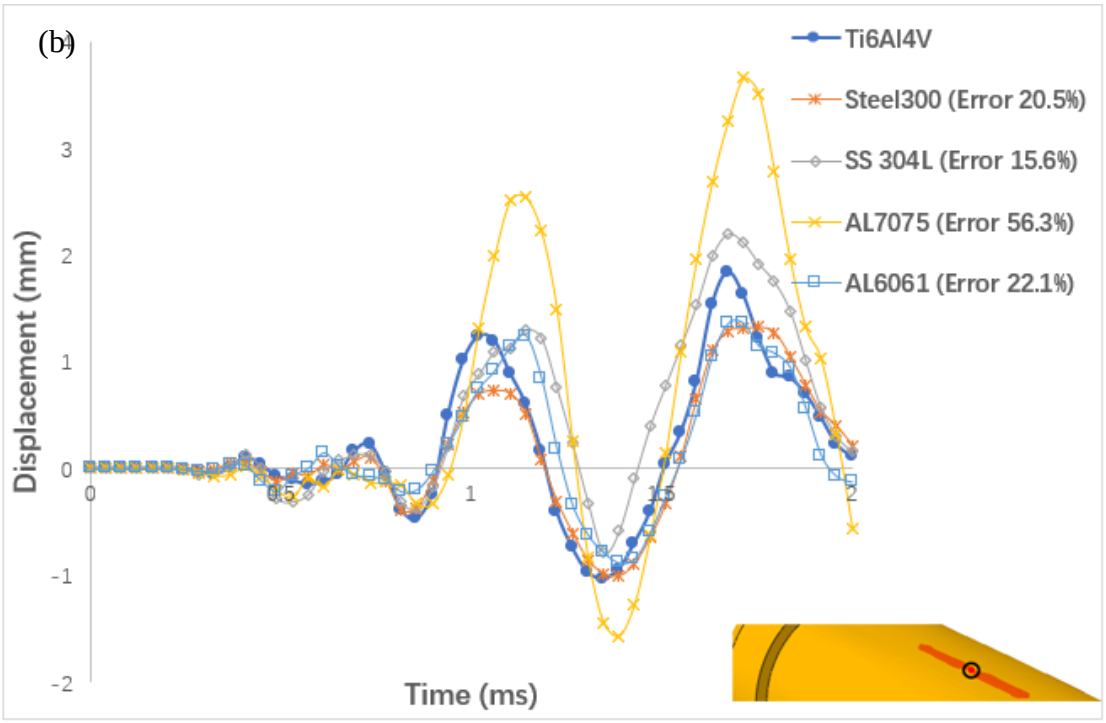

Figure 5.20 Zeroth order results as viewed in the physical space for explosive impact test, showing (a) the reaction force at point 2, (b) the displacement in y direction at point 1(see Fig. 16).

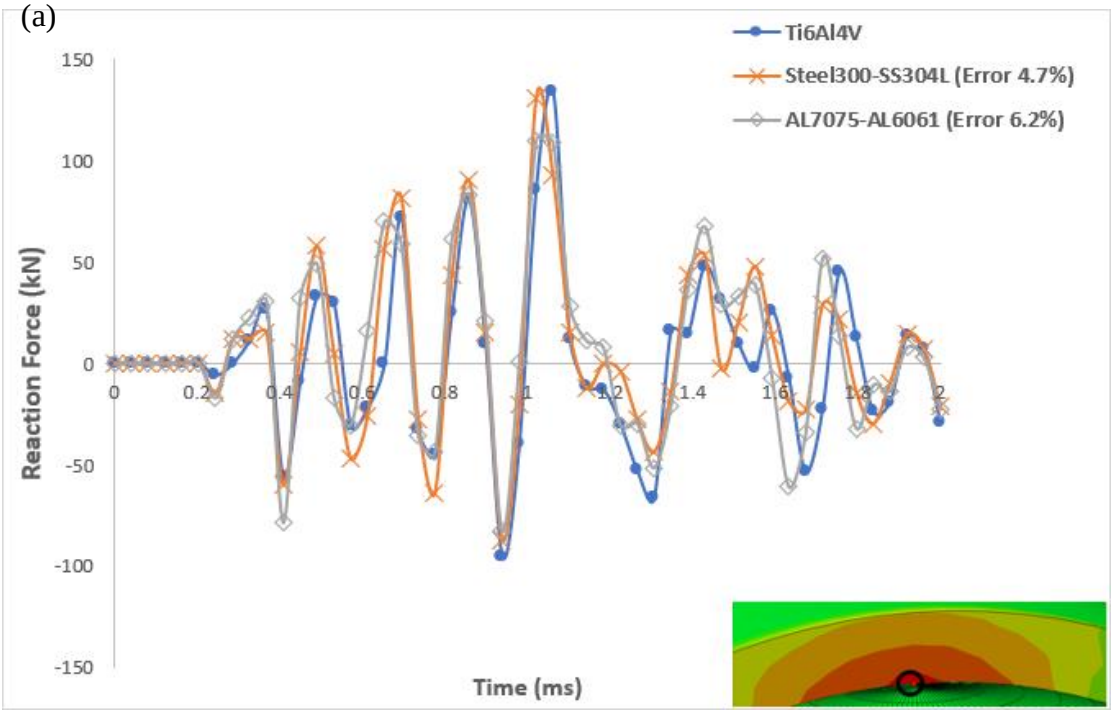

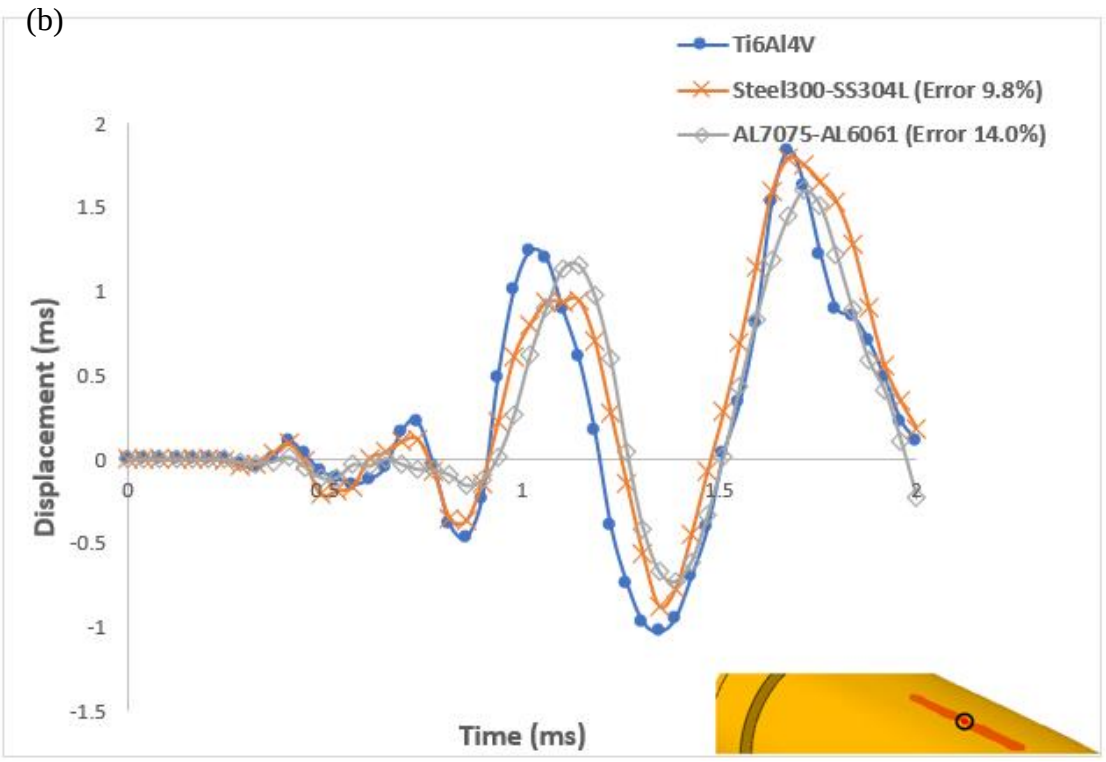

Figure 5.21 First-order results as viewed in the physical space for explosive impact test, showing (a) the reaction force at point 2, (b) the displacement in y direction at point 1(see Fig. 16).

The study provided a significant challenge with internal pressure and the load rate being related nonlinearly to that mass of the TNT and distance between the explosion source and shell [177]. This meant that a single scaled model was unable to replicate full-scale behaviour as is readily revealed in Fig. 5.18. The added flexibility provided by the first-order theory although insufficient to achieve perfect replication returned acceptable results as presented in Fig. 5.21.

5.5 Conclusion

The Chapter introduces and re-examines the place of physical modelling for practical impact studies in the light of a new two-experiment scaling theory. It is shown in the chapter how two-experiment studies can be initiated through the analysis of a standard impact test (the Charpy impact test was considered) to assess material suitability before moving on to practical investigations. Pressure-vessel related studies were trialled to assess the practical value of the new approach with loading through impact and explosion testing. Models founded on the Johnson-Cook constitutive and damage

laws were applied in the finite element models and a procedure was established to set the free parameters that appear in the scaling theory. This was achieved by capturing key features of the Johnson-Cook laws through integration over the process-parameter window pertinent to the studies. The theory developed is applied to the practical test cases, and the following conclusions can be drawn from the results obtained:

- Zeroth order, involving one scaled experiment, and first order involving two, have roles to play in physical modelling in impact studies. If zeroth order proves sufficient, then first order is not required but inaccuracy in zeroth order can generally be improved with application of the first-order theory.
- The first-order theory provides significant scope for combining unlikely material behaviours at scale to capture to good accuracy full-scale behaviours. Materials ruled out as unsuited by zeroth-order theory (single experiment study) now have the potential to play a part in a two-experiment analysis.
- It was confirmed that a standard test and specifically the Charpy impact test can be used to assess the suitability of materials for physical modelling in single and two experiment impact studies. The optimum choices for material combinations remained the best choices for the practical studies.
- The benefit of two scaled experiments were revealed in both the penetration and internal blast test with the application of dissimilar materials to capture to good accuracy full-scale behaviours, providing significant enhancement over a single experiment using a dissimilar material.

Specifically, to the case studies:

- Scaling experiments of the Charpy impact test are not entirely acceptable since some errors are higher than expected, especially stress change. Unlike other data, the stress is evaluated from an individual element rather than a whole model, which presents that this kind of result is more variable and challenging to synchronize. On the other hand, it again strengthens the importance of material selection for finite similitude theory. This is a criterion or limitation of applying finite similitude with different materials.

- Based on the material selection in the Charpy impact test, the projectile penetration test produces better results. It proves that the scaling of rate through finite similitude theory is correct in the dynamic process. Moreover, results in Figs. 5.14 and 5.15 present that the scaling experiment's boundary condition can be flexible, though it still needs to obey a common law.
- The internal explosive test produces more challenges to the scaling theory. A particular point of the test is that both load and loading rate are controlled by one factor, the mass of the explosion source. It is hard to decide the load and its rate by the transport equations since they have different non-linear relationships with the mass. It scales the mass by size for all models to ensure the same frequency between different materials. It makes the shape of curves similar, but the results are not quite matched, though the first-order theory can improve the accuracy. (See in Fig. 5.21) In this case, it is recommended to use identical material in the scaling experiment when the boundary conditions cannot be regularly controlled.

Chapter 6 Conclusion and Future work

The purpose of the work presented in the thesis is to assess the feasibility and efficacy of the finite similitude scaling theory for application in fracture mechanics. The finite similitude theory provides a systematic approach for the representation of scale effects, and it was envisaged at the start of the work that this would provide tangible benefits in fracture mechanics with improved accuracy from scaled experimentation. The following conclusions can be drawn from the body of work presented in the thesis:

6.1 Overall Conclusion

- The results presented provide strong evidence that the finite similitude theory can offer real benefits to fracture-mechanics studies. It is applicable to both LEFM and EPFM and can be applied to investigate critical values or fracture processes. For LEFM the theory has been confirmed correct by both analytical and numerical evaluation of stress intensity factors. For EPFM, it has been confirmed through numerical case studies, with representative virtual models, that standard ASTM tests can be accurately represented by scaled models over a range of scales, confirming the absence of scale effects.
- Apart from the simulations of LEFM, which can be done by finite similitude theory in different ways, EPFM should be the main objective to assess the efficacy of finite similitude, especially the first-order theory. As it could be founded during the process of research, errors of scaling for zeroth-order theory always appear between different materials, or in plastic behaviour of identical material. It is shown that these errors can be solved by the application of first-order theory, by associating the results in zeroth order. In fact, first-order theory cannot completely vanish these errors, even when dealing with the errors of plasticity by size effect, it could be explained by the no-linearity in plastic section, and the application of the transport equations are finally linear with the outputs.

- Though the results of plasticity or different are not perfectly matched in scaling, it still provides an accurate agreement of the predictions under first-order theory. The key factor would be the synchronization of material properties and size scale before analysis, it could be founded in the test of numerical study, with virtual material. The scaling factors are developed by the transport equations based on space scaling, which aims to synchronize different material and scales, From the matched results between virtual material and the real physical material, it proves that the scaling theory can successfully transfer the material or size in a virtual case, though it cannot be used in practical experiment.
- As for the application in real test, for example the ASTM tests or dynamic impact test, the results are also matched as supposed, which can be concluded by the performance of material in virtual cases. As the outputs of specimens reflecting the material behaviour, which has a same meaning of 'material properties', the behaviour can be consequently synchronized as the properties. The finite similitude theory can be regarded as a transfer system between scale experiments, that inputs (material properties) are used to obtain the scaling factors and transport equations, and then these will be used to predict the outputs (material behaviours), and it can also be applied oppositely.
- Identical material applied in different scale experiments can clearly show the size effect, in this case, stress field and displacement field are scale independent, which causes the errors in zeroth-order prediction. It was previous matched with linearly dependency of displacement field. The error can be regarded as the scale effect, which is then improved by applying first-order theory. The error is caused by the invariance properties reversing from trial space to physical space (displacement field), and solved with the first-order transformation of the properties (see Fig 4.4), which again returns to the properties-to-behaviours reflection in finite similitude theory.
- It could find that first-order theory can minimize the error caused by zeroth-order theory, by associating two distinct scale experiments. In this case, many

limitations by zeroth-order theory can be freed, which leads to more choice of scaling experimentation, for example size independent and property independent. It then gives encouragement when applying scaling theory that results with error can be synchronized to get a more accurate result with higher-order finite similitude theory.

- Based on the encouragement of first-order theory, it starts to try more choices and unknowns by applying finite similitude theory in dynamic impact model, with Johnson-Cook damage model. The dynamic loading tests are different with quasi-static experiment, here time scale needs to be considered which will also affect the result significantly. Synchronization of J-C material models and strain hardening curves are similar because they are both from the stress-strain behaviour of tensile test. From these experiences it can conclude that to synchronize the plastic material behaviour, which is not linear, determining the scaling factors with mean component is an effective approach.
- For the application in the practical study, from the study in Section 3.6, zeroth-order theory can obtain a good prediction in LEFM. In EPFM, it is necessary to use first-order theory. Solutions for size effect, different material, and inexact boundary conditions are provided in the first-order theory. Compared with other scaling theories, it can consider the constraint effects in fracture mechanics. However, the restrictive condition of the scaling experiment is a crucial limitation in reality. With one scaled experiment it should be possible to control most parameters like temperature, velocity, pressure, load, size, and geometry. These must of course be controlled and correctly synchronized when two scaled experiments are involved.

6.2 Conclusion based on case studies

- There is an analytical simulation with pure mathematical calculation in Section 3.6, which proves that in LEFM, the theory can transfer the outputs between different materials. The process shows that the calculation links several linear

equations, where the critical material properties obtain the scaling parameters to simulate output in the same order. The perfectly matched results show that the transported equations are applicable. However, this test displays a restriction on the size scale β_i for the selected material. Though it can control the influence of size-dependent factors, the critical value of structure size is always a significant limitation of a scaling theory.

- Elastic-plastic J-integral tests are developed in Sections 3.7 to 3.8. The finite similitude theory is applied to the material properties. Then it shows its applicability by comparing the outputs numerically since the J-integral value cannot be directly synchronised with the scaling theory. It provides a good trend between input and output, showing the theory's rationality and availability. The first-order theory first makes significant improvements by adding a trial experiment. The test proves the efficacy of finite similitude theory in fracture mechanics, and offers a standard of material selection, but it is not very meaningful, especially for practical experiments. It ignores the size effect since the comparison is between the same model between physical and virtual materials. Furthermore, for a scaling experiment, it is intended that physically measurable outputs are compared.
- In Section 4.4, a new approach of finite similitude theory is applied, using scale invariance with identical material. The figures of synchronised load-displacement, J-Δa shows high-accuracy simulation as intended, which means the size effect can be solved in this approach. It proves that the two-experiment theory can minimise the influence of the size effect during scaling experiments; it is also available for practical problems with the complex scale variance parameters, and the tests with different materials.
- Apart from the problem of individual element evaluation, dynamic fracture mechanics study must consider additional parameters like time, loading rate and strain rate and synchronise them to be identical between different models. Load and energy results in Fig.5.4 show the timing error between different materials

(different displacement or time of the peak load/energy). It can further restrict material selection in dynamic and practical experiments.

- From the projectile penetration test (Chapter 5) and the fracture toughness test (Chapter 4), an incorrect input is not forbidden in the scaling theory. However, the two-experiment theory is necessary to vanish the error in the one-experiment theory. Investigating Figs. (4.8) and (5.14) can find that the scaled models have a common trend compared to the physical model. For example, in Fig (4.8), all the scaled specimens appear harder to fail with decreasing size; in Fig (5.14), the velocity resistance is less with β_i since they have heavier projectiles than expected. To conclude, an additional experiment in first-order theory can solve the identical and regular error trend.
- Finally, the procedure of finite similitude theory applying to a practical experiment can be:
  1. Clarify the objective's detail, including diameters, geometry, material, boundary conditions like applied load, stress or velocity, and the required outputs.
  2. Create the scaled specimens with satisfied diameters and materials. The shape/geometry of the scaled specimens should be the same as the prototype. It is best to use the same material if possible, or materials close to the original material are recommended.
  3. Calculate the necessary scaling parameters by the β and material properties, including g, α^{ρ}, α^{v} and R_1. For the study involving plasticity, the mean value of material properties should be considered to calculate these parameters. Then define the transported equations that will be used for the required outputs.
  4. Determine the boundary conditions of the scaling experiments by their scaling parameters and the original boundary conditions.
  5. Generate the experiment with the scaled specimens and collect the results individually.

6. Take two-specimen combinations and synchronise their results with the transport equations, and then the analytical results of each group are obtained.
7. Create a numerical study with the given diameter and material for the prototype, then compare the analytical results and numerical results to see if they have good agreement.

6.3 Future works recommendations

- Firstly, some of the case studies already done in the thesis can be improved with additional jobs. The numerical study with virtual material in EPFM can be simulated again with actual materials, and synchronize the outputs then compare the results of, for example, load-displacement or J-integral (which needs to be calculated indirectly) between the calculated one and physical one.

  Some typical tests, for example, ASTM E1820 tests and Charpy impact test, are suggested to be tested experimentally. These tests are not too complex but can be more direct to view the performance of specimens and make the research more convincible, which is not done due to some condition factors. It is better to generate the scaling experiment with one of the specimens and synchronize the results, then compare them to the numerical results. Considering the strain rate and time-scale effect in fracture mechanics studies is also essential. As the loading rate in ASTM E399 and E1820 tests is already suggested, scaling the loading rate should be considered as the study in the dynamic process.

  It has been introduced another way to determine $g_1$and g_2 by the functions of stress and displacement, which will finally get $\alpha_0^v g \quad = \beta^{-3}$. Stress is dominantly related to strain for the material modes involved in this thesis, so this approach has not been tested. It can be assumed that $g_1$and g_2 determined by stress and displacement fields is available for the model or method related between them, which would be cohesive zone model, with traction separation method. So furtherly, the scaling test of fracture mechanics with CZM can be evaluated with this method.

- Singular fracture value like fracture toughness and critical J-integral have been investigated in this thesis. The two-parameter fracture mechanics should also be tested with finite similitude theory, which was introduced in ref [48-49]. It can use the original specimens of J-value evaluation in this thesis, such as CT and TPB models. The *J*-*Q* theory will be further considered for the critical value, which can be represented by $J_c = J_0(1 - \frac{Q\sigma_Y}{\sigma_c})^{n+1}$, as J_0 is the *J* value of singular fracture mechanics. In this case study, two different parameters should be synchronised respectively for the results, where J_0 can follow the same procedure in a singular fracture test. *Q* value is related to the stress field, which be calculated by stress of small-scale yield and hoop stress. Essentially, this experiment aims to obtain accurate prediction for both load-displacement data and different stress fields around the crack.
- It can see that applying finite similitude theory in different fields gives more experience to the scaling theory. The suggestion will continue this way. The application method and ability of finite similitude can become more mature with further scale experiments. The expanded study can consist of two directions; one is evaluating the theory in different kinds of experiments—for example, the penetration test of the solid model (see ref [178]). Compared to the thin-wall penetration test, it provides a broader range of strain rate and markedly rate change of the impactor. In addition, the influence of material properties of the penetrated target will be more significant, which can test finite similitude theory more effectively. The investigation outputs will be the velocity change, reaction force change over time and displacement. As the test uses a solid or thick-wall objective, the duration of the change will be extended until the kinetic energy drops to zero. In this process, the results will be more mature and different materials will make higher differences, which needs the synchronisation of first-order theory, so it is a good choice for the test or improvement of the theory. In detail, the experiments can prepare several solids in different materials, which are penetration targets. These solids do not need to be scaled since they are always

significantly larger than the projectile. In the beginning, the test can be done with the same-size projectile and different materials of the solids. The material of the target solid should determine the mass and initial velocity. Then the size of projectiles can be scaled by β. The primary objective of this experiment is not for the scaling test but for the synchronisation of material behaviour between different materials.

- The dynamic internal blast test on cracked pressure vessels is also exciting and worth trying (see ref [159]), combining two practical tests and displaying another way of dynamic fracture mechanics. This test will include predicting fracture mechanics (stress intensity factor and J-integral) under vibration caused by an explosion. As the results of the explosive loading test in this thesis, the synchronisation of vibration from the explosion is not perfectly matched between different materials. This test can firstly do with identical material to investigate the effect of fracture parameters due to the vibration and whether the first-order theory can resolve that. According to ref [159], it evaluates the crack propagation under the sudden impact caused by the explosion, for example, crack growth and cracks growth rate over time, which is different from the smooth and constant internal pressure. As it could find that internal blast loading is a particular case for scaling, it can be a new challenge for finite similitude theory to predict the material behaviour under the blast. In detail, thin-wall pressure vessels of different sizes and the same material will be used, with the scale-mass TNT as an explosion source. A pre-crack should be located far from the TNT, which is intended to propagate after the explosion. The investigation outputs should include the elastic-plastic J-integral, the crack extension rate and the J-R curve under explosion.
- Finite similitude is a scaling theory which is not only the method for material evaluation for reducing finical cost. The theory can also apply in the scale experiment to some industrial products. For example, a failure assessment for a pressure vessel is necessary for safety factors [179]. It can test the scaling of

maximum allowed pressure, failure assessment diagram, and the S-N curve. Here the practical test can do with the vessels under internal pressure. In a practical test, pressure vessels can be designed to have different sizes and materials and then evaluate the critical value of pressure causing damage. The finite similitude theory can use here to synchronise the pressure between different models.

It was mentioned in the review that structures will still fail even if it never reaches any failure criterion after working for a long time, which is known as fatigue. So, a scale experiment of a product under a low cyclic load is necessary. For some simple components, for example, a beam or a bar, the investigation of these components can focus on the scaling of fatigue life. It can test between different materials, which can make the application of theory more flexible. The test can design to have compact tension models or bending models of different sizes and materials subjected to cyclic loads, which are determined by the material. It can investigate the scaling theory for the fracture process, for example, stress intensity factor along with the cycles, crack initiation point, and the S-N curve.

References

1. Hossdorf, H. (1974). ‘Model analysis of structures’, Van Nostrand Reinhold Company.
2. Galileo, G., Weston, J. (1730). ‘Mathematical Discourses concerning Two new sciences relating to Mechanical and local motion: in four dialogues’. John Hooke, London.
3. Rayleigh, L. (1915). ‘The principle of similitude’. Nature, 95, pp. 66-68
4. Goodier, J.N. and Thomson, W.T. (1944). ‘Applicability of similarity principles to structure models’. National Advisory Committee for Aeronautics, Washington, DC, Report No. CR-4068
5. Goodier, J.N. (1950). ‘Dimensional Analysis’. Wiley, New York.
6. Singer, J., Arbocz, I. and Weller, T. (1997). ‘Bulking experiments’. Wiley, Chickester, UK
7. Baker, W.E., Westine, P.S. and Dodge, F.T. (1991). ‘Similarity method in Engineering dynamics: theory and practice of scale modeling’. Revised Ed, Elsevier, Amsterdam, the Netherlands
8. Sonin, A.A. (2001). ‘The physical basis of Dimensional Analysis’. Department of Mechanical Engineering, MIT, Cambridge, MA.
9. Griffith, A.A. (1921). VI. The phenomena of rupture and flow in solids. Philosophical Transactions of the Royal Society of London. Series A, Containing Papers of a Mathematical or Physical Character, 221(582-593), pp.163–198.
10. Irwin, G.R. (1958) Fracture, Elasticity and Plasticity. Springer, Berlin, 551-590.
11. Miller, J.D. and Jennett, W.B. (1968). Complications of Depressed Skull Fracture. The Lancet, 292(7576), pp.991–995.
12. Irwin, G.R. (1957) Analysis of stresses and strains near the end of a crack traversing a plate. Journal of Applied Mechanics, 24: 361-64

13. Rice, J.R. (1968). A Path Independent Integral and the Approximate Analysis of Strain Concentration by Notches and Cracks. Journal of Applied Mechanics, 35(2), pp.379–386.

14. Bažant, Z. P. and Pfeiffer, P. A. (1987). Determination of Fracture Energy from Size Effect and Brittleness Number. *ACI Materials Journal*, 84(6). doi:10.14359/2526.

15. Bažant, Z. P. (1984). Size effect in blunt fracture: concrete, rock, metal. *f. of Engrg. Mech.,* ASCE, 110,518-535

16. Carpinteri, A. and Chiaia, B. (1995). Multifractal nature of concrete fracture surfaces and size effects on nominal fracture energy. *Materials and Structures*, 28(8), pp.435–443. doi:10.1007/bf02473162.

17. Carpinteri, A., Chiaia, B. and Ferro, G. (1995). Size effects on nominal tensile strength of concrete structures: multifractality of material ligaments and dimensional transition from order to disorder. *Materials and Structures*, 28(6), pp.311–317. doi:10.1007/bf02473145.

18. Ray, S. and Chandra Kishen, J.M. (2011). Fatigue crack propagation model and size effect in concrete using dimensional analysis. *Mechanics of Materials*, 43(2), pp.75–86. doi:10.1016/j.mechmat.2010.12.002.

19. Belytschko, T. and Black, T. (1999). Elastic crack growth in finite elements with minimal remeshing. *International Journal for Numerical Methods in Engineering*, 45(5), pp.601–620.

20. Melenk, J.M. and Babuška, I. (1996). The partition of unity finite element method: Basic theory and applications. *Computer Methods in Applied Mechanics and Engineering*, 139(1-4), pp.289–314.

21. Hearn, E.J. (1997). Theories of Elastic Failure, *Mechanics of materials. 1, An introduction of the mechanics of elastic and plastic deformation of solids and structural materials*. Oxford: Butterworth-Heinemann, 1, pp. 401-429

22. Aliabadi, M.H. (2003). Boundary Element Methods in Linear Elastic Fracture Mechanics. *Comprehensive Structural Integrity*, 3, pp.89–125.
23. Irwin, G. R. (1957). Relation of stresses near a crack to the crack extension force, *in: Proceedings of the International Congresses of Applied Mechanics*, Vol. VIII, University of Brussels, pp. 245-251
24. Cherepanov, G. P. (1967). The propagation of cracks in a continuous medium, *Journal of Applied Mathematics and Mechanics*, 31(3), pp. 503–512.
25. Rice, J.R. and Rosengren, G.F. (1968). Plane strain deformation near a crack tip in a power-law hardening material, *J. Mech. Phys. Solids*, vol. 16, no. 1, pp. 1–12.
26. Hutchinson, J.W. (1968) Singular behaviour at the end of a tensile crack in a hardening material, *J. Mech. Phys. Solids*, vol. 16, no. 1, pp. 13–31.
27. McMeeking, R.M. and Parks, D.M. (1979). On criteria for J-dominance of crack-tip field in large-scale yielding. In: Elastic-plastic fracture. ASTM STP 668. American Society for Testing and Materials. p. 175-94
28. Begley, J. A., & Landes, J. D. (1972). The J Integral as a Fracture Criterion. *National Symposium on Fracture Mechanics*, Part II, ASTM STP 514, 1-20.
29. Kobayashi, A. S., Chiu, S. T., and Beeuwkes, R. (1973). A Numerical and Experimental Investigation on the Use of J-Integral. *Engineering Fracture Mechanics*, Vol. 5, 293-305.
30. ASTM E399-09e2 (2011). Standard test method for linear-elastic plane strain fracture toughness KIc of metallic materials. American Society for Testing and Materials.
31. Srawley, J.E., Brown, W.F. (1965). Fracture toughness testing methods. In: Fracture toughness testing and its applications. ASTM STP 381. American Society for Testing and Materials; p. 133–96.
32. Brown, W.F., Srawley, J.E. (1966). In: Plane strain crack toughness testing of high strength metallic materials. ASTM STP 410. American Society for Testing

and Materials; p. 1–65.

33. Anon.(1960). ASTM special committee on fracture testing of high strength materials. ASTM Bulletin, January 1960. p. 29–40.
34. Srawley, J.E., Jones, M.H. and Brown, W.F. (1967). Determination of plane strain fracture toughness. Material research and standards, vol. 7. American Society for Testing and Materials; p. 261–6.
35. McCabe, D.E. (1972) Evaluation of the compact tension specimen for determining plane-strain fracture toughness of high strength materials. J Mater, 7:449–542.
36. Heyer, R.H., McCabe, D.E. (1970) Evaluation of a test method for plane-strain fracture toughness using a bend specimen. In: Review of developments in plane strain fracture toughness testing. ASTM STP 463. American Society for Testing and Materials; p. 22–41.
37. Wallin, K.R.W. (2005) Critical assessment of the standard ASTM E399. J ASTM Int;2:JAI12051.
38. Joyce, J.A. and Smudz, R. (1992). Evaluation of elastic intensity using J-integral specimen geometries. J Test Evaluat; 20:1–5.
39. Joyce, J.A. (1998) Experimental justification for proposed changes to the measurement of KIc using ASTM E399. J Test Evaluat; 26:455–62.
40. ASTM E1820-11 (2011). Standard test method for measurement of fracture toughness. American Society for Testing and Materials.
41. Merkle, J.G. and Corten, H.T. (1974). A J integral analysis for the compact specimen considering axial force as well as bending effects. J Press Ves Technol; 96:286–92.
42. Sumpter, J.D.G. and Turner, C.E. (1976). Method for laboratory determination of JC (contour integral for fracture analysis). In: Cracks and fracture. ASTM STP 601. American Society for Testing and Materials.
43. Clarke, G.A0 and Landes, J.D. (1979). Evaluation of the J-integral for the compact specimen. J Test Evaluat; 7:264–9.
44. McClintock, F.A. (1979). Plasticity aspect of fracture. In: Liebowitz H, editor.

Fracture: an advanced treatise, vol. 3. London: Academic press. p. 47-225

45. Williams, M. L. (1957). On the Stress Distribution at the Base of a Stationary Crack, *Journal of Applied Mechanics*, Vol. 24, pp. 109-114.

46. Sherry, A.H., France, C.C. and Goldthorpe, M.R. (1995). COMPENDIUM OF T-STRESS SOLUTIONS FOR TWO- AND THREE-DIMENSIONAL CRACKED GEOMETRIES. *Fatigue & Fracture of Engineering Materials and Structures*, 18(1), pp.141–155. doi:10.1111/j.1460-2695. 1995.tb00148. x.

47. O'Dowd, N. P. and Shih, C. F. (1992). Two-Parameter Fracture Mechanics Theory and Applications. *Naval Surface Warfare Centre*, Bethesda, MD 20084-5000.

48. Sumpter, J. D. G. and Forbes, A. T. (1992). Constraint Based Analysis of Shallow Cracks in Mild Steel, Proceedings of TWI/EWI/IS International Conference on Shallow Crack Fracture Mechanics Test and Applications. Cambridge, UK.

49. Kirk, M. T., Koppenhoefer, K. C., and Shih, C. F. (1998). Effect of Constraint on Specimen Dimensions Needed to Obtain Structurally Relevant Toughness Measures. *To appear in ASTM-STP*

50. Buckingham, E. (1914). "On physically similar systems; illustrations of the use of dimensional equations". *Physical Review*. **4** (4): 345 -376.

51. Jones, N. (2012). *Structural Impact*' 2nd ed. Cambridge.

52. Cherepanov, G.P. (1979). 'Mechanics of brittle fracture' McGraw-Hill international book company.

53. Carpinteri, A. (1982). 'Notch sensitivity in fracture testing of aggressive material' Engineering fracture mechanics, 16, 467-481.

54. Carpinteri, A. (1991). 'Size-scaling transition from ductile to brittle failure: structural response vs crack growth resistance curve' Int. J. Fracture, 51, 175-186

55. Barenblatt, G.I. (1993). 'Some general aspect of fracture mechanics.' Modeling of Defects and Fracture Mechanics, Herrman G ed. Springer-Verlag

56. Barenblatt, G.I. (1993). 'Micromechanics of fracture'. Theoretical and Applied Mechanics 1992, Bodner SR et al. eds. Elsevier Science Publisher B.V

57. Zhao, Y.P. (1996). ‘Irwin number and ductile-brittle fracture transition.’ Int. J. Fracture, 75, R17-R21
58. Zhao, Y.P. (1997). ‘On some dimensionless numbers in fracture mechanics’. Int. J. Fracutre. 83, L7-L13
59. Zhao, Y.P. (1998). ‘Suggestion of new dimensionless number for dynamic plastic response of beam and plates’, Arch. Appl. Mech., 68, 524-538
60. Zhao, Y.P. (1998). ‘On the similarity methods in fracture mechanics’, Forschung im Ingenieurwesen., 64, 257-648
61. Barenblatt, G.I. (2003). ‘Scaling, self-similarity, and intermediate asymptotics’. Cambridge texts in applied mechanics. Cambridge University Press. ISBN 987-0-521-53394-2
62. Skoglund, V. (1967). ‘Similitude: theory and application’ International Textbook Co.;
63. Decius, J. (1948). ‘Dimensional analysis: an approach from transformation theory and a criterion for scaling model experiments’. J Frankl Inst 245(5):379-387
64. Coutinho, C.P., Baptista, A.J. and Rodrigues, J.D. (2016). ‘Reduced scaling model based on similitude theory: are view up to 2015’. Eng Struct.; 119: 81-94
65. Atkins, A. (1999). ‘Scaling laws for elastoplastic fracture’. Int J Fract 95(1-4):51-66.
66. Bažant, Z.P. (2000). ‘Size effect’. Int J Solid Struct 37(1-2):69-80.
67. Drazetic, P., Ravalard, Y., Darcheux, F., and Marguet, B. (1994). ‘Applying no-direct similitude technique to dynamic bending collapse of rectangular section tubes. Int J Impact Eng; 15(6): 797-814.
68. Carpinteri, A. and Paggi, M. (2011). ‘Dimensional analysis and fractal modeling of fatigue crack growth’. ASTM Special Publication Volume 1546:3-19.
69. Ajiboye, J.S., Jung, K.-H. and Im, Y.-T. (2010). Sensitivity study of frictional behavior by dimensional analysis in cold forging. *Journal of Mechanical Science and Technology*, 24(1), pp.115–118.

70. Ezra, A.A. and Penning, F.A. (1962). Development of scaling laws for explosive forming. *Experimental Mechanics*, 2(8), pp.234–239.

71. Weibull, W. (1939). The phenomenon of rupture in solids. *Proc., Royal Swedish Institute of Engineering Research* (Ingenioersvetenskaps Akad. Handl.) **153**, Stockholm, 1--55.

72. Weibull, W. (1949). A statistical representation of fatigue failures in solids. *Proc., Roy. Inst. of Techn.* No. **27**.

73. Weibull, W. (1951). A statistical distribution function of wide applicability. *J. of Applied Mechanics ASME,* Vol. **18**.

74. Bažant, Z. P. and Chen, E. P. (1997). Scaling of structural failure. *Applied Mechanics Reviews ASME* 50 (10), 593—627

75. Bažant, Z. P. and Novák, D. (2000). Energetic-statistical size effect in quasibrittle failure at crack initiation. *ACI Materials Journal* 97 (3), 381—392.

76. Bažant, Z. P. (1983). Fracture in concrete and reinforced concrete. *IUTAM Prager Symp. on Mechalllcs of Geomalenals: Rocks, Concretes, Soils.* Z. P. Bazant, cd., Northwestern Univ., Evanston, 111.,281-316

77. Sornette, D. (1998). Discrete-scale invariance and complex dimensions. Phys. Reports, 297, 239-270

78. Bažant, Z. P.(1984). Scaling laws in mechanics of failure. *f. of Engrg. Mech.*, ASCE, 110,1828-1844

79. Invernizzi, S., Lacidogna, G. and, Carpinteri, A. (2009). Numerical simulation of cracking and AE scaling in quasi-brittle materials, Int. Conference. Fracture 2: 1394-1403

80. Kirane, K. and Bažant, Z. P. (2016). Size effect in Paris law and fatigue lifetimes for quasi-brittle materials: Modify theory, experiment and micro-modeling. Int. J. Fatigue 83:209-220.

81. Carpinteri, A. and Corrado, M. (2018). Experimental evidence and numerical simulation of size effects on the ductile fracture of metallic materials. Int. J. Fracture 211(1-2): 43-59
82. Bažant, Z. P. (2019). Design of quasi-brittle materials and structures to optimize strength and scaling at probability tail: An apercu. Proceedings of the Royal Society A: Mathematical, Physical and Engineering Sciences. 475(2224).
83. Drazetic, P., Ravalard, Y., Dacheux, F. and Marguet, B. (1994). Applying non-direct similitude technique to the dynamic bending collapse of rectangular section tubes. *International Journal of Impact Engineering*, 15(6), pp.797–814.
84. Mazzariol, L.M., Oshiro, R.E. and Alves, M. (2016). A method to represent impacted structures using scaled models made of different materials. *International Journal of Impact Engineering*, 90, pp.81–94.
85. Alves, M. and Oshiro, R.E. (2006). Scaling the impact of a mass on a structure. *International Journal of Impact Engineering*, 32(7), pp.1158–1173.
86. Mazzariol, L.M. and Alves, M. (2019). Similarity laws of structures under impact load: Geometric and material distortion. *International Journal of Mechanical Sciences*, 157–158, pp.633–647.
87. Mazzariol, L.M. and Alves, M. (2019). Experimental verification of similarity laws for impacted structures made of different materials. *International Journal of Impact Engineering*, 133, p.103364.
88. Neuberger, A., Peles, S. and Rittel, D. (2007). Scaling the response of circular plates subjected to large and close-range spherical explosions. Part I: Air-blast loading. *International Journal of Impact Engineering*, 34(5), pp.859–873.
89. Neuberger, A., Peles, S. and Rittel, D. (2007). Scaling the response of circular plates subjected to large and close-range spherical explosions. Part II: Buried charges. *International Journal of Impact Engineering*, 34(5), pp.874–882.
90. Grossmann, S. and Lohse, D. (2000). Scaling in thermal convection: a unifying theory. *Journal of Fluid Mechanics*, [online] 407, pp.27–56. Available at: https://research.utwente.nl/en/publications/scaling-in-thermal-convection-a-

unifying-view [Accessed 20 Apr. 2020].

91. Kneller, B. and Buckee, C. (2000). The structure and fluid mechanics of turbidity currents: a review of some recent studies and their geological implications. *Sedimentology*, 47, pp.62–94.
92. Mohamed, M.S., Foster, A.D., Lin, J., Balint, D.S. and Dean, T.A. (2012). Investigation of deformation and failure features in hot stamping of AA6082: Experimentation and modelling. *International Journal of* Machine Tools and Manufacture 53(1), pp. 27-38.
93. Simitses, G.J. and Rezaeepazhand, J. (1995). Structural Similitude and Scaling Laws for Buckling of Cross-Ply Laminated Plates. *Journal of Thermoplastic Composite Materials*, 8(3), pp.240–251.
94. Cheng, Y.-T. and Cheng, C.-M. (2004). Scaling, dimensional analysis, and indentation measurements. *Materials Science and Engineering: R: Reports*, 44(4–5), pp.91–149.
95. Brinell. J.A. (1901) Congres International des M des de Construction (Paris), tome 2, 83-94.
96. Le, J.-L., Manning, J. and Labuz, J.F. (2014). Scaling of fatigue crack growth in rock. *International Journal of Rock Mechanics and Mining Sciences*, 72, pp.71–79.
97. Ray, S. and Chandra Kishen, J.M. (2011). Fatigue crack propagation model and size effect in concrete using dimensional analysis. *Mechanics of Materials*, 43(2), pp.75–86.
98. Davey K, Darvizeh R, Al-Tamimi A. (2017). Scaled Metal Forming Experiments: A Transport Equation Approach. International Journal of Solids and Structures, 125, pp. 184–205.
99. Sadeghi, H., Davey, K., Darvizeh, R. and Darvizeh, A. (2019). A scaled framework for strain rate sensitive structures subjected to high rate impact loading. International Journal of Impact Engineering, 125, pp.229–245.
100. Sadeghi, H., Davey, K., Darvizeh, R. and Darvizeh, A. (2019). Scaled models for failure under impact loading. International Journal of Impact Engineering, 129,

pp.36–56.

101. Davey, K. and Darvizeh, R. (2016). Neglected transport equations: extended Rankine–Hugoniot conditions and J -integrals for fracture. *Continuum Mechanics and Thermodynamics*, 28(5), pp.1525–1552.

102. Gurtin, M.E. (1995). The nature of configurational forces. *Archive for Rational Mechanics and Analysis*, 131(1), pp.67–100.

103. Gewin, V. (2008). Shock physics. *Nature*, 454(7200), pp.134–134.

104. Al-Tamimi, A., Darvizeh, R. and Davey, K. (2018). Experimental investigation into finite similitude for metal forming processes. Journal of Materials Processing Technology, 262, pp.622–637.

105. Ochoa-Cabrero, R., Alonso-Rasgado, T. and Davey, K. (2018). Scaling in biomechanical experimentation: a finite similitude approach. Journal of The Royal Society Interface, 15(143), p.20180254.

106. Moghaddam, M., Darvizeh, R., Davey, K. and Darvizeh, A. (2018). Scaling of the powder compaction process. *International Journal of Solids and Structures*, 144–145, pp.192–212.

107. Davey, K., Sadeghi, H., Darvizeh, R., Golbaf, A. and Darvizeh, A. (2021). A Finite Similitude Approach to Scaled Impact Mechanics. International Journal of Impact Engineering, 148, p.103744.

108. Department of Defense. Military Standardization Handbook: Metallic Materials and Elements for Aerospace Vehicle Structures MIL-HDBK-5E, Volume 2. June 1987.

109. Holmquist, T.J. and Johnson, G.R. (2011). A Computational Constitutive Model for Glass Subjected to Large Strains, High Strain Rates and High Pressures. *Journal of Applied Mechanics*, 78(5).

110. Nicholas. T. (1980). Material behavior at high strain rates. Report AFWAL-TR-80-4053, USAF Wright Aeronautical Laboratories, Wright-Patterson Air Force Base, OH, USA.

111. Antusch, S., Armstrong, D.E.J., Britton, T.B., Commin, L., Gibson, J.S.K.-L.,

Greuner, H., Hoffmann, J., Knabl, W., Pintsuk, G., Rieth, M., Roberts, S.G. and Weingaertner, T. (2015). Mechanical and microstructural investigations of tungsten and doped tungsten materials produced via powder injection molding. *Nuclear Materials and Energy*, 3–4, pp.22–31.

112. Salih, S., Davey, K. and Zou, Z. (2016). Rate-dependent elastic and elasto-plastic cohesive zone models for dynamic crack propagation. *International Journal of Solids and Structures*, 90, pp.95–115.

113. ANSYS, Inc, (2019) ANSYS Users' manual, Swanson Analysis System.

114. Marie, S., and Nédélec, M. (2007). A New Plastic Correction for the Stress Intensity Factor of an Under-Clad Defect in a PWR Vessel Subjected to a Pressurised Thermal Shock. Int. J. Pressure Vessels Piping, 84(3), pp. 159–17

115. Shlyannikov, V. (2016). Nonlinear stress intensity factors in fracture mechanics and their applications. *Procedia Structural Integrity*, 2, pp.744–752.

116. Horstman, R., Peters, K., Meltzer, R., Bruce Vieth, M., Irwin, G. and de Wit, R. (1983). A Summary of Fracture Mechanics Concepts. Journal of Testing and Evaluation, 11(1), p.56.

117. Fazil Erdogan and Pa (1995). Fracture mechanics. 25, [25th National Symposium on Fracture Mechanics: New Trends in Fracture Mechanics, held in Bethlehem, Pennsylvania on 28 June - 1 July 1993]. Philadelphia, Pa.: Astm.

118. Cotterell, B. (2002). The past, present, and future of fracture mechanics. Engineering Fracture Mechanics, 69(5), pp.533–553.

119. ASTM E1823-10a (2011). Standard terminology relating to fatigue and fracture testing. American Society for Testing and Materials.

120. ASTM E561-10 (2011). Standard test method for K–R curve determination. American Society for Testing and Materials.

121. ASTM E1290-08e1 (2011). Standard test method for crack-tip opening displacement (CTOD) fracture toughness measurement. American Society for Testing and Materials.

122. ASTM E2472-06e1 (2011). Standard test method for determination of

resistance to stable crack extension under low-constraint conditions. American Society for Testing and Materials.

123. Joyce, J.A. and Link, R.E. (1997). Application of two parameter elastic-plastic fracture mechanics to analysis of structures. Engineering Fracture Mechanics, 57(4), pp.431–446.

124. Mitchell, D. and Landes, J. (2006). Evaluation of the ASTM J Initiation Procedure Using the EURO Fracture Toughness Data Set. Journal of Testing and Evaluation, 34(3), p.12596.

125. Schwalbe K.H., Landes J.D., Heerens J. (2007). Classic fracture mechanics methods. Germany

126. Zhu, X. (2009). J-integral resistance curve testing and evaluation. Journal of Zhejiang University-SCIENCE A, 10(11), pp.1541–1560.

127. Zhu, X.K. and Joyce, J.A. (2012). Review of fracture toughness (G, K, J, CTOD, CTOA) testing and standardization. Engineering Fracture Mechanics, [online] 85, pp.1–46. Available at: https://digitalcommons.unl.edu/cgi/viewcontent.cgi?article=1096&context=usnavyresearch [Accessed Jan. 2021].

128. Drazetic, P., Ravalard, Y., Dacheux, F. and Marguet, B. (1994). Applying non-direct similitude technique to the dynamic bending collapse of rectangular section tubes. International Journal of Impact Engineering, 15(6), pp.797–814.

129. Popper, K.R. (1977). The Logic of Scientific Discovery. Systematic Zoology, 26(3), p.361.

130. Sadeghi, H., Davey, K., Darvizeh, R., Rajabiehfard, R. and Darvizeh, A. (2020). An investigation into finite similitude for high-rate loading processes: Advantages in comparison to dimensional analysis and its practical implementation. International Journal of Impact Engineering, 140, p.103554.

131. Ochoa-Cabrero, R., Alonso-Rasgado, T. and Davey, K. (2020). Zeroth-order finite similitude and scaling of complex geometries in biomechanical experimentation. Journal of The Royal Society Interface, 17(167), p.20190806.

132. Harmanci, Y. (2019). Test independent identification of fracture parameters of plain concrete based on a cohesive XFEM formulation. Proceedings of the 10th International Conference on Fracture Mechanics of Concrete and Concrete Structures.

133. Chen, X., Nanstad, R.K. and Sokolov, M.A. (2014). J-R Curve Determination for Disk-Shaped Compact Specimens Based on the Normalization Method and the Direct Current Potential Drop Technique, in , ed. M. Sokolov and E. Lucon (West Conshohocken, PA: ASTM International, 2014), 1-18.

134. Özdemir, U. and Yeni, Ç. (2012). Determination of Elastic Plastic Fracture Toughness Parameters for a Compact Tension Specimen Using the Finite Element Method. Materials Testing, 54(6), pp.408–415.

135. Balakrishnan, V., Roshan, P., Goel, S., Jayaganthan, R. and Singh, I.V. (2017). Experimental and XFEM Simulation of Tensile and Fracture Behavior of Al 6061 Alloy Processed by Severe Plastic Deformation. Metallography, Microstructure, and Analysis, 6(1), pp.55–72.

136. Belytschko, T. and Black, T. (1999). Elastic crack growth in finite elements with minimal remeshing. International Journal for Numerical Methods in Engineering, 45(5), pp.601–620.

137. Melenk, J.M. and Babuška, I. (1996). The partition of unity finite element method: Basic theory and applications. Computer Methods in Applied Mechanics and Engineering, 139(1-4), pp.289–314.

138. Sharma, V.M.J., Diwakar, V., Sree Kumar, K., Nageswara Rao, B. and Pathak, S.D. (2006). A Simple J-integral Approach for Fracture Toughness Assessment on Invalid Test Data of Standard CT Specimens. Trends in Applied Sciences Research, 1(2), pp.132–143.

139. Hearn, E.J. (1997). Theories of Elastic Failure, Mechanics of materials. 1, An introduction of the mechanics of elastic and plastic deformation of solids and structural materials. Oxford: Butterworth-Heinemann, 1, pp. 401-429

140. Aliabadi, M.H. (2003). Boundary Element Methods in Linear Elastic Fracture Mechanics. Comprehensive Structural Integrity, 3, pp.89–125.

141. Qian, Y. and Zhao, J. (2019). Fracture Toughness Calculation Method Amendment of the Dissimilar Steel Welded Joint Based on 3D XFEM. Metals, 9(5), p.509.

142. Yang, Z., Zhou, C., Dai, Q. (2014) Elastic-plastic crack propagation based on extended finite element method. J. Nanjing Tech Univ. (Nat. Sci. Ed.) 36, 50–57. (In Chinese)

143. Booth E, Collier D, Miles J. (1983) Impact scalability of plated steel structures. In: Jones N, Wierzbicki T, editors. Structural crashworthiness. London: Butterworths;. p.136–74.

144. Jiang, P., Tian, C.J., Xie, R.Z. and Meng, D.S. (2006). Experimental investigation into scaling laws for conical shells struck by projectiles. *International Journal of Impact Engineering*, 32(8), pp.1284–1298.

145. Noam, T., Dolinski, M. and Rittel, D. (2014). Scaling dynamic failure: A numerical study. *International Journal of Impact Engineering*, 69, pp.69–79.

146. Oshiro, R.E. and Alves, M. (2004). Scaling impacted structures. *Archive of Applied Mechanics*, 74(1-2), pp.130–145.

147. Oshiro, R.E. and Alves, M. (2007). Scaling of cylindrical shells under axial impact. *International Journal of Impact Engineering*, 34(1), pp.89–103.

148. Oshiro, R.E. and Alves, M. (2009). Scaling of structures subject to impact loads when using a power law constitutive equation. *International Journal of Solids and Structures*, 46(18-19), pp.3412–3421.

149. Mazzariol, L.M., Oshiro, R.E. and Alves, M. (2016). A method to represent impacted structures using scaled models made of different materials. *International Journal of Impact Engineering*, 90, pp.81–94.

150. Alves, M. and Oshiro, R.E. (2006). Scaling impacted structures when the prototype and the model are made of different materials. *International Journal of Solids and Structures*, 43(9), pp.2744–2760.

151. Trimiño, L.F. and Cronin, D.S. (2014). Non-direct similitude technique applied to the dynamic axial impact of bonded crush tubes. *International Journal of Impact Engineering*, 64, pp.39–52.

152. Ramu, M., Prabhu Raja, V. and Thyla, P.R. (2013). Establishment of structural similitude for elastic models and validation of scaling laws. *KSCE Journal of Civil Engineering*, 17(1), pp.139–144.

153. Cao, Y., Zhen, Y., Song, M., Yi, H., Li, F. and Li, X. (2020). Determination of Johnson–Cook parameters and evaluation of Charpy impact test performance for X80 pipeline steel. *International Journal of Mechanical Sciences*, 179, p.105627.

154. Musteață, A.E., Pirvu, C., Deleanu, L. and Georgescu, C. (2019). Simulation of Charpy test for different impact velocities. *IOP Conference Series: Materials Science and Engineering*, 514(1), p.012011.

155. Madhusudhan, D., Chand, S., Ganesh, S. and Saibhargavi, U. (2018). Modeling and simulation of Charpy impact test of maraging steel 300 using Abaqus. *IOP Conference Series: Materials Science and Engineering*, 330, p.012013.

156. Børvik, T., Hopperstad, O.S., Langseth, M. and Malo, K.A. (2003). Effect of target thickness in blunt projectile penetration of Weldox 460 E steel plates. *International Journal of Impact Engineering*, 28(4), pp.413–464.

157. İrhan, B., Ožbolt, J. and Ruta, D. (2015). 3D finite element simulations of high velocity projectile impact. *International Journal of Solids and Structures*, 72, pp.38–49.

158. Nilakantan, G., Wetzel, E.D., Bogetti, T.A. and Gillespie, J.W. (2013). A deterministic finite element analysis of the effects of projectile characteristics on the impact response of fully clamped flexible woven fabrics. *Composite Structures*, 95, pp.191–201.

159. Ma, L., Xin, J., Hu, Y. and Zheng, J. (2013). Ductile and brittle failure assessment of containment vessels subjected to internal blast loading. *International Journal of Impact Engineering*, 52, pp.28–36.

160. Romero, C., Benner, J.C. and Berkbigler, L.W. (1997). Experimental and numerical correlation of a scaled containment pressure vessel subjected to an internal blast load. [online] 1997 ASME Pressure Vessel & Piping Conference Structure under Extreme Load Conditions. Orlando FL. Available at: https://www.osti.gov/servlets/purl/484526 [Accessed 22 Dec. 2021].

161. Elek, P.M., Jaramaz, S.S., Micković, D.M. and Miloradović, N.M. (2016). Experimental and numerical investigation of perforation of thin steel plates by deformable steel penetrators. *Thin-Walled Structures*, 102, pp.58–67.

162. ASTM E23 (2018). Standard Test Method for Notched Bar Impact Testing of Metallic Materials.

163. Norris, D.M. (1979). Computer simulation of the Charpy V-Notch toughness test. *Engineering Fracture Mechanics*, 11(2), pp.261–274.

164. Johnson, G.R. and Cook, W.H. (1985). Fracture characteristics of three metals subjected to various strains, strain rates, temperatures and pressures. *Engineering Fracture Mechanics*, 21(1), pp.31–48.

165. Peirs, J., Verleysen, P., Van Paepegem, W. and Degrieck, J. (2011). Determining the stress–strain behaviour at large strains from high strain rate tensile and shear experiments. *International Journal of Impact Engineering*, 38(5), pp.406–415.

166. Tham, C.Y., Tan, V.B.C. and Lee, H.P. (2008). Ballistic impact of a KEVLAR® helmet: Experiment and simulations. *International Journal of Impact Engineering*, 35(5), pp.304–318.

167. Lesuer, D.R. (2000) Experiment investigations of material models for Ti-6Al-4V titanium and 2024-T3 aluminum, Technical report.

168. Steinberg, D.J. (1996). Equation of State and Strength Properties of Selected Materials. *Lawrence Livermore National Laboratory.*

169. Flores-Johnson, E.A., Shen, L.M., Guiamatsia, I. and Nguyen, G.D. (2014). Finite-Element Modelling of the Impact Behaviour of Aluminium Nacre-Like Composite. *Applied Mechanics and Materials*, 566, pp.457–462.

170. Xuan, H., Hu, Y., Wu, Y. and He, Z. (2018). Containment Ability of Kevlar 49 Composite Case under Spinning Impact. *Journal of Aerospace Engineering*, 31(2), p.04017096.

171. Saxena, A., Kumaraswamy, A., Dwivedi, S.P., Srivastava, A.K. and Maurya, N.K. (2020). Experimental and computational investigation on dynamic fracture toughness (J) behavior of multi-pass SMA armor steel weldments. *Theoretical and Applied Fracture Mechanics*, 106, p.102502.

172. Bednar, H.H. (1986). *Pressure vessel design handbook*. New York ; Wokingham: Van Nostrand Reinhold.

173. Feng, J., Gao, X., Li, J., Dong, H., Yao, W., Wang, X. and Sun, W. (2019). Influence of fiber mixture on impact response of ultra-high-performance hybrid fiber reinforced cementitious composite. *Composites Part B: Engineering*, 163, pp.487–496.

174. Barnes, F.C. (2019). *Cartridges of the World, 16th Edition : A Complete and Illustrated Reference for over 1,500 Cartridges.* Krause Publications.

175. Daniau, E. (2016). *Towards a " 600 m " lightweight General Purpose Cartridge, part I*. Emeric DANIAU, DGA Techniques Terrestres, Bourges.

176. Barsoum, I., Lawal, S.A., Simmons, R.J. and Rodrigues, C.C. (2018). Failure analysis of a pressure vessel subjected to an internal blast load. *Engineering Failure Analysis*, 91, pp.354–369.

177. Karlos, V. and Solomos, G. (2013). Calculation of Blast Loads for Application to Structural Components. *JRC Technical Report*. doi:10.2788/61866.

178. Wan, W., Yang, J., Xu, G. and Liu, Y. (2021). Determination and evaluation of Holmquist-Johnson-Cook constitutive model parameters for ultra-high-performance concrete with steel fibers. *International Journal of Impact Engineering*, 156, p.103966.

179. Nageswara Rao, B. and Acharya, A.R. (1998). Failure assessment on M300 grade maraging steel cylindrical pressure vessels with an internal surface crack. *International Journal of Pressure Vessels and Piping*, 75(7), pp.537–543.

Appendix: Publications

Journal paper

Published

1. Davey, K., Darvizeh, R. and Zhang, J. (2021). Finite similitude in fracture mechanics. *Engineering Fracture Mechanics*, 245, p.107573.

2. Davey, K., Zhang, J. and Darvizeh, R. (2022). Fracture mechanics: A two-experiment theory. *Engineering Fracture Mechanics*, 271, p.108618. doi: 10.1016/j.engfracmech.2022.108618.

3. Zhang, J., Davey, K., Darvizeh, R. and Sadeghi, H. (2022). A two-experiment approach to physical modelling: damage and failure under high-rate loading. *Thin-Walled Structures*, 179, p.109589. doi: 10.1016/j.tws.2022.109589.